Climate Change Impact on Air Quality in California

REPORT TO THE

CALIFORNIA AIR RESOURCES BOARD

Project # 04-349

Prepared by:

Dr. Michael J. Kleeman[1]
Dr. Shu-Hua Chen[2]
Dr. Robert A. Harley[3]

[1]Department of Civil and Environmental Engineering
[2]Department of Land, Air, and Water Resources
University of California, Davis
One Shields Avenue, Davis, CA, 95616

[3]Department of Civil and Environmental Engineering
University of California, Berkeley
Berkeley, California 94720

June 2010

DISCLAIMER

The statements and conclusions in this report are those of the contractor and not necessarily those of the California Air Resources Board. The mention of commercial products, their source, or their use in connection with material reported herein is not to be construed as actual or implied endorsement of such products.

This report was prepared by the University of California at Davis as an account of work partially sponsored by the United States Environmental Protection Agency (USEPA). This research has not been subject to the Agency's required peer and policy review and therefore does not necessarily reflect the reviews of the Agency and no official endorsement should be inferred.

ACKNOWLEDGEMENTS

We thank Nehzat Motallebi (CARB) for project management support and for help obtaining datasets used for statistical downscaling of ozone concentrations. We thank Dan Cayan, Mary Tyree, Martha Coakley and Josh Shiffrin (UCSD) for data processing and analyses related to the downscaling of meteorological variables.

We gratefully acknowledge the U.S. Department of Energy's (DOE) Office of Science (BER) Accelerated Climate Prediction Initiative (ACPI) project for supplying global climate model simulations. We thank Stephen Zelinka (CARB, Sonoma Technology Inc.) for providing observation data to evaluate WRF results. Thanks also go to the National Typhoon and Flood Research Institute and National Central University, Taiwan, which provided computer clusters for part of the WRF simulations. We thank Kemal Gurer(CARB) and Dr. Jian-Wen Bao (NOAA) for help in the early stage of the WRF downscaling.

The work described in this report was primarily accomplished by UC Davis graduate students Abdullah Mahmud, Mark Hixson, and Zhan Zhao and UC Berkeley graduate student Dev Millstein. Additional help was provided by UC Davis graduate student Jianlin Hu and UC Davis postdoctoral scholar James Chen.

TABLE OF CONTENTS

ACKNOWLEDGEMENTS 3
LIST OF TABLES 7
LIST OF FIGURES 9
LIST OF ACRONYMS 18
ABSTRACT 21
EXECUTIVE SUMMARY 22
1.0 INTRODUCTION 29
1.1 Motivation 29
1.2 Previous Analysis for Climate Effects on Air Quality in California 29
1.3 Research Objectives 31
1.4 Scope of the Current Study 33
2.0 A PRELIMINARY ASSESSMENT OF THE SENSITVITY OF AIR QUALITY IN CALIFORNIA TO GLOBAL CHANGE 35
2.1 Introduction 35
2.2 Background 35
2.3 Model Description 36
2.4 Model Application 37
2.5 Results 39
2.6 Discussion 54
2.7 Conclusions 56
3.0 IMPACT OF CLIMATE CHANGE ON PHOTOCHEMICAL AIR POLLUTION IN SOUTHERN CALIFORNIA 57
3.1 Introduction 57
3.2 Methods 58
3.3 Results and Discussion 62
3.3.1 Base Case Model Evaluation 62
3.3.2 Effects of Climate Change 64
3.3.3 Effects of Emission and Inflow Boundary Condition Changes 66
3.3.4 Combined Effects 67
3.3.5 Temporal Patterns of Ozone Change 69
3.3.6 Future Temperature Change 71
3.4 Summary and Recommendations 74
4.0 STATISTICAL DOWNSCALING OF CLIMATE CHANGE IMPACTS ON OZONE CONCENTRATIONS IN CALIFORNIA 75
4.1 Introduction 75
4.2 Data and Methods 76
4.3 Results 77
4.4 Conclusion 95
5.0 THE IMPACT OF CLIMATE CHANGE ON AIR QUALITY RELATED METEOROLOGICAL CONDITIONS IN CALIFORNIA – PART I: PRESENT TIME SIMULATION ANALYSIS 96
5.1 Introduction 96
5.2 Methodology and Model Description 98
5.2.1 Methodology 98
5.2.2 PCM model 99

5.2.3 WRF model and the interface between WPS and PCM *99*
5.2.4 WRF basic configuration *100*
5.3 Tests of different physics schemes in WRF..... 101
5.3.1 Numerical experiments design *101*
5.3.2 Results analysis *102*
5.4 Downscaling Results Analysis..... 104
5.4.1 Downscaling results driven by PCM vs. GFS data..... *104*
5.4.2 Surface comparison between simulation results and observation data..... *110*
5.4.3. Low PBLH during summer *116*
5.5 Conclusions..... 121
6.0 THE IMPACT OF CLIMATE CHANGE ON AIR QUALITY RELATED METEOROLOGICAL CONDITIONS IN CALIFORNIA – PART II: PRESENT VERSUS FUTURE TIME SIMULATION ANALYSIS 123
6.1 Introduction..... 123
6.2 Model configurations and methodology 124
6.3 Results..... 125
6.3.1. Stagnation Event Analysis..... *125*
6.3.2. Future changes of air quality related meteorological fields *127*
6.3.3 Climate change impacts on land-sea breeze..... *134*
6.3.4 Significance Test *138*
6.4 Conclusions..... 140
7.0 CLIMATE IMPACT ON AIRBORNE PARTICULATE MATTER CONCENTRATIONS IN CALIFORNIA USING SEVEN YEAR ANALYSIS PERIODS..... 141
7.1 Introduction..... 141
7.2 Methods 142
7.3 Results..... 148
7.4 Summary and Conclusions 162
8.0 CLIMATE IMPACT ON POPULATION-WEIGHTED AIRBORNE PARTICULATE MATTER CONCENTRATIONS IN CALIFORNIA DURING SHORT AND LONG TIME PERIODS 164
8.1 Introduction..... 164
8.2 Methods 165
8.3 Results and discussion 167
8.3.1 Annual Average PM Concentrations *167*
8.3.2 Extreme Events..... *173*
8.4 Conclusions..... 179
9.0 CLIMATE IMPACT ON PARTICULATE MATTER (PM) IN CALIFORNIA FOR EMISSIONS PROJECTED IN 2050..... 180
9.1 Introduction..... 180
9.2 Emissions Projections 180
9.3 Results..... 182
9.4 Conclusions..... 198
10.0 COMBINED IMPACT OF CLIMATE CHANGE AND EMISSIONS CONTROLS ON PARTICULATE MATTER (PM) IN CALIFORNIA 199
10.1 Introduction..... 199

10.2 Methods 199
10.3 Results..... 200
10.4 Conclusions..... 209
11.0 SUMMARY AND CONCLUSIONS 210
11.1 A Preliminary Assessment of the Sensitivity of Air Quality in California to Global Change 210
11.2 Impact of Climate Change on Photochemical Air Pollution in Southern California 210
11.3 Statistical Downscaling of Climate Change Impacts on Ozone Concentrations in California 211
11.4 The Impact of Climate Change on Air Quality Related Meteorological Conditions in California – Part I: Present Time Simulation Analysis 212
11.5 The Impact of Climate Change on Air Quality Related Meteorological Conditions in California – Part II: Present versus Future Time Simulation Analysis 212
11.6 Climate Impact on Airborne Particulate Matter Concentrations in California Using Seven Year Analysis Periods 213
11.7 Climate Impact on Population-Weighted Airborne Particulate Matter Concentrations in California during Short and Long Time Periods 213
11.8 Climate Impact on Particulate Matter (PM) in California for Emissions Projected in 2050 214
11.9 Combined Impact of Climate Change and Emissions Controls on Particulate Matter in California 215
11.10 Future research..... 215
Reference 217

LIST OF TABLES

Table 2-1: Lateral boundary conditions used during model simulations..... 37

Table 2-2: Air quality episodes to be studied with sensitivity analysis..... 38

Table 2-3: Emissions summary for the air quality episodes described in Table 2-2.. 38

Table 2-4: Relative change in composition for O3, hydroxyl radical (OH), total reactive nitrogen (RN), and various forms of reactive nitrogen at 1500 PST on September 9, 1993 caused by a +5 K temperature perturbation. PN is particulate nitrate. 41

Table 2-5: Relative change in composition for O3, hydroxyl radical (OH), total reactive nitrogen (RN), and various forms of reactive nitrogen at 1500 PST on September 25, 1996 caused by a +5K temperature perturbation. PN is particulate nitrate. 41

Table 2-6: Relative change in composition for O3, hydroxyl radical (OH), total reactive nitrogen (RN), and various forms of reactive nitrogen at 1500 PST on January 6, 1996 caused by a +5K temperature perturbation. PN is particulate nitrate. 41

Table 3-1: Domain-wide emission totals (tons/day)..... 59

Table 3-2: AVOC, BVOC and NOx, base case and future emissions by county. Emissions are reported in tons/day for Thursday July 14th..... 61

Table 3-3: Average weekday ozone (ppb) at 1500 h LT (local time): base case levels and differences between specified run and base case 68

Table 3-4: Average weekday 8-h ozone (ppb) at 1000 h – 1800 h LT (local time): base case levels and differences between specified run and base case..... 68

Table 4-1: Variables that were perturbed during the Monte Carlo simulations of ozone formation..... 82

Table 4-2: Temperature (T850) increase (^{o}C) in 2070-2099 relative to 1961-1990 projected for the SoCAB and SJAB by various climate models under the IPCC A2 and B1 emissions scenario..... 90

Table 4-3: Summary of predicted decadal median daily 1-hr maximum ozone concentrations under IPCC A2 and B1 global emissions scenarios at Upland (SoCAB) and Parlier (SJVAB). Note that the underlying assumption for this prediction is that the emissions in CA remain at the 1990-2004 level. 94

Table 5-1: Simulation cases for normal and leap years..... 99

Table 5-2. Six suites of physics schemes for WRF simulations..... 101

Table 7-1: Domain-averaged initial concentrations of major model gas and particle species at the surface..... 145

Table 7-2: Average boundary concentrations of various model gas and particle species concentrations along the western boundary of the modeling domain..... 146

Table 9-1: County-specific growth factors between 2029/2030 and 2050 based on Department of Finance population projections. 182

LIST OF FIGURES

Figure 1: Average weekday ozone (ppb) at 1500 h LT (local time) for a SoCAB episode in 2005: base case levels and differences between specified run and base case..... 23

Figure 3: The number of days per year conducive to forming 1-hr maximum ozone of 90 ppb or more at Upland, CA under the Intergovernmental Panel on Climate Change (IPCC) emissions scenarios: A2 (top panel) and B1 (bottom panel). Note that the underlying assumption for this prediction is that the criteria emissions in CA remain at the 1990-2004 level. Uncertainty bars represent the third and the first quartiles of the predicted number of days..... 25

Figure 4: Changes in annual average $PM_{2.5}$ mass concentrations and corresponding p-values in CA likely to occur in the future (2047-53) due to climate change from the present-day (2000-06). The p-value quantifies the likelihood that average future concentrations are equal to present day concentrations..... 26

Figure 5: Future (2047-53) minus present (2000-06) change in population-weighted $PM_{2.5}$ total mass, components, and primary source categories for (a) annual averages and (b) 99th percentile extreme pollution events. Results are averaged across the entire state of California. The error bars represent the 95% confidence interval. 27

Figure 2-1: Basecase O_3 concentration at 1500 PST on September 9, 1993 (panel a) and sensitivity of O_3 concentration to (b) +5 K temperature change with constant absolute humidity, (c) +2 K temperature change with constant absolute humidity, (d) +5 K temperature change with constant relative humidity, (e) +50% increase in mixing depth, and (f) + 5K temperature change with constant relative humidity and increase in background O_3 from 30 ppb to 60 ppb..... 43

Figure 2-2: Basecase $PM_{2.5}$ concentration on September 9, 1993 (panel a) and sensitivity of $PM_{2.5}$ concentration to (b) +5 K temperature change with constant absolute humidity, (c) +2 K temperature change with constant absolute humidity, (d) +5 K temperature change with constant relative humidity, (e) +50% increase in mixing depth, and (f) + 5K temperature change with constant relative humidity and increase in background O_3 from 30 ppb to 60 ppb..... 46

Figure 2-3: Basecase O_3 concentration at 1500 PST on September 25, 1996 (panel a) and sensitivity of O_3 concentration to (b) +5 K temperature change with constant absolute humidity, (c) +2 K temperature change with constant absolute humidity, (d) +5 K temperature change with constant relative humidity, (e) +50% increase in mixing depth, and (f) + 5K temperature change with constant relative humidity and increase in background O_3 from 30 ppb to 60 ppb..... 47

Figure 2-4: Basecase $PM_{2.5}$ concentration on September 25, 1996 (panel a) and sensitivity of $PM_{2.5}$ concentration to (b) +5 K temperature change with constant absolute humidity, (c) +2 K temperature change with constant absolute humidity, (d) +5 K temperature change with constant relative humidity, (e) +50% increase in mixing depth, and (f) + 5K temperature change with constant relative humidity and increase in background O_3 from 30 ppb to 60 ppb..... 48

Figure 2-5: Basecase O_3 concentration at 1500 PST on January 6, 1996 (panel a) and sensitivity of O_3 concentration to (b) +5 K temperature change with constant absolute humidity, (c) +2 K temperature change with constant absolute humidity, (d) +5 K temperature change with constant relative humidity, (e) +50% increase in mixing depth, and (f) + 5K temperature change with constant relative humidity and increase in background O_3 from 30 ppb to 60 ppb. 49

Figure 2-6: Basecase $PM_{2.5}$ concentration on January 6, 1996 (panel a) and sensitivity of $PM_{2.5}$ concentration to (b) +5 K temperature change with constant absolute humidity, (c) +2 K temperature change with constant absolute humidity, (d) +5 K temperature change with constant relative humidity, (e) +50% increase in mixing depth, and (f) + 5K temperature change with constant relative humidity and increase in background O_3 from 30 ppb to 60 ppb. 53

Figure 2-7: Summary of pollutant response to meteorological perturbations when background O3 concentrations are 60ppb during pollution episodes that occurred in (a) Southern California September 9, 1993, (b) Southern California September 25, 1996, and (c) the San Joaquin Valley January 6, 1996. The bars represent the range of concentration change at any location in the modeling domain in response to the indicated perturbation. The circles represent the concentration change at the location of the maximum concentration for each pollutant. AH is absolute humidity and RH is relative humidity. 55

Figure 3-1: Map of southern California study domain used for air quality modeling in the present study. Locations highlighted from left to right: Central Los Angeles, Anaheim, Pomona, Riverside, and Palm Springs. 62

Figure 3-2: Comparison of base case model output (blue) to ozone measurements (red) at five sites..... 63

Figure 3-3: Difference between future and base case temperatures, and resulting changes in weekday-average ozone concentrations at 1500 h LT. The locations shown are from left to right, Central Los Angeles, Pomona/Claremont, and Riverside. 64

Figure 3-4: Difference between future and base case biogenic emissions, and resulting changes in weekday-average ozone concentrations at 1500 h LT. The locations shown are from left to right, Central Los Angeles, Pomona/Claremont, and Riverside. 65

Figure 3-5: Differences between future and base case O3 concentrations on weekdays at 1500 h LT. The locations shown are from left to right, Central Los Angeles, Pomona/Claremont, and Riverside. (a) Future inflow boundary condition scenario, (b) Future anthropogenic emissions, (c) Future climate perturbations (increased temperature, absolute humidity, biogenic emissions), (d) all perturbations (a-c) combined together. 65

Figure 3-6: Difference between future and base case absolute humidity and ozone concentrations on weekdays at 1500. 66

Figure 3-7: Peak ozone semi-normalized sensitivity to NOx (left) and VOC (right). 69

Figure 3-8: Difference between base case and future ozone concentrations (ppb) by time at five locations. (All perturbations scenario). 70

Figure 3-9: Difference between future and base case ozone concentrations on weekdays at 0300 h LT (left panels) and 1500 h LT (right panels). Compare right panel here vs. Figure 3-2 where T increase was applied uniformly throughout the day instead of most mostly at night. The locations shown are from left to right, Central Los Angeles, Pomona/Claremont, and Riverside. 71

Figure 3-10: Difference between base case and future ozone concentrations (ppb) by time at five locations. (Future temperature scenario with future temperature change adjusted by time of day)..... 72

Figure 3-11: Difference between future and base case biogenic emissions and ozone concentrations on weekdays at 300 (top panels) and 1500 (bottom panels). Biogenic emissions in the scenario are based on temperature changes that have been adjusted by time of day. 73

Figure 4-1: (a) Observed daily 1-hr max ozone versus the corresponding temperature at 850 mbar (T850), and (b) linear correlation between the ozone quartile boundaries and the corresponding daily max T850 at Upland, CA for the months May-October over the period 1980-2004. 79

Figure 4-2: The frequency distributions of the observed daily 1-hr max ozone corresponding to T850 of 302 K (a) and 284 K (b) at Upland, CA, between May-October over the time period from 1980 to 2004. 80

Figure 4-3: Three-day back trajectories for air parcel arriving at 3:00 pm on September 09, 1993 at Claremont, CA. Each trajectory path reflects random variations in wind speed and direction..... 81

Figure 4-4: Predicted frequency distribution of the daily 1-hr maximum ozone concentration corresponding to a T850 of 302 K at Claremont, CA. Different ozone values were generated by random perturbations in the input meteorological parameters, emissions, and initial conditions as summarized in Table 1. Panel (a) corresponds to a base emission inventory appropriate for 1993, panel (b) corresponds to base emission inventory appropriate for 1987, and panel (c) represents the sum of (a) and (b)..... 84

Figure 4-5: Comparison of observed and predicted reductions in ozone concentrations in 1990's relative to 1980's for the South Coast Air Basin (SoCAB) based on changes to the emissions inventory. 85

Figure 4-6: The linear correlation between the median of the observed daily 1-hr maximum ozone and the corresponding daily maximum T850 at Upland, CA, as a function of decade..... 86

Figure 4-7: Seasonal correlation between 1-hr maximum ozone and 1-hr maximum T850 at Upland, CA, for the years between 1990 and 2004. Diamonds correspond to quartile 3 (Q3), squares correspond to quartile 2 (median; Q2), triangles correspond to quartile 1 (Q1)..... 88

Figure 4-8: Seasonal correlation between 1-hr maximum ozone and 1-hr maximum T850 at Parlier, CA, for the years between 1990 and 2004. Diamonds correspond to

quartile 3 (Q3), squares correspond to quartile 2 (median; Q2), triangles correspond to quartile 1 (Q1). 89

Figure 4-9: The number of days per year conducive to forming 1-hr maximum ozone of 90 ppb or more at Upland, CA under the Intergovernmental Panel of Climate Change (IPCC) emissions scenarios: A2 (top panel) and B1 (bottom panel). Note that the underlying assumption for this prediction is that the emissions in CA remain at the 1990-2004 level. Uncertainty bars represent the third and the first quartiles of the predicted number of days. 91

Figure 4-10: The number of days per year conducive to forming 1-hr maximum ozone of 90 ppb or more at Parlier, CA under the Intergovernmental Panel of Climate Change (IPCC) emissions scenarios: A2 (top panel) and B1 (bottom panel). Note that the underlying assumption for this prediction is that the emissions in CA remain at the 1990-2004 level. Uncertainty bars represent the third and the first quartiles of the predicted number of days. 92

Figure 4-11: Number of days per decade conducive to the formation of daily 1-hr max ozone ≥90 ppb for 2046 – 2055 and 2091 – 2100 at Upland (SoCAB) and Parlier (SJVAB). Note that the underlying assumption for this prediction is that the emissions in CA remain at the 1990-2004 level. 93

Figure 5-1: Nested domains for WRF simulations. The black dot shows the location of the observation station 'VIS'. The line in domain 3 (d3) crossing 'VIS' indicates the location of the vertical cross session in Figure 5-14. 100

Figure 5-2: Seasonal RMSE of model simulated U10, V10, T2 and RH2 with the six suites of physics schemes compared to observation data averaged over all stations in CA. The six suites are listed in order in the plots. 103

Figure 5-3: Persistent scores: percentage with which each suite performed the best with respect to RH2, T2, U10 and V10. The total counts for T2, RH2, and wind component comparisons are 55833, 45837 and 14883, respectively..... 103

Figure 5-4: Spatial distribution of differences between 7-year averaged WRF results driven by PCM and GFS data (PCM-WRF – GFS-WRF) for T2 (units are in °K) during (a) summer and (b) winter; wsp10 (units are in ms^{-1}) during (c) summer and (d) winter; and PBLH (units are in m) during (e) summer and (f) winter 106

Figure 5-5: Seven-year averaged PBLH from GFS-WRF simulation during (a) summer and (b) winter. Units are in m. 107

Figure 5-6: Spatial distribution of 7- year averaged T2 (shading, units in °K), sea level pressure (contour lines, units in mb) and wind vectors of (a) PCM data for summer, (b) GFS data for summer, (c) PCM data for winter, (d) GFS data for winter; and T2 difference between PCM data and GFS data (PCM – GFS) for (e) summer and (f) winter. 109

Figure 5-7: Seven year averaged 500mb height field of PCM (left) and GFS (right) data during summer. Units are in m. 110

Figure 5-8: Seven-year averaged T2 bias over (a) SoCAB and (b) SJV for each simulation case driven by GFS and PCM data. 112

Figure 5-9: (a) and (b) are the same as Figures 5-6a and 5-6b, respectively, but during case 7..... 113

Figure 5-10: Same as Figure 5-8, but for 10-m wind speed. 114

Figure 5-11: 7-year averaged model (a) bias and (b) RMSE with respect to observed wind speed in SoCAB..... 116

Figure 5-12: Three year (2004-2006) averaged daily maximum PBLH from observations (light gray solid line), PCM-WRF simulations (dark gray dashed line), and GFS-WRF simulations (dark gray solid line) at station VIS. 118

Figure 5-13: Daily maximum PBLH averaged over 2004-2006 (gray solid line) and during 2000 (black dashed line). The encircled part is from case 6 simulation. 119

Figure 5-14: Vertical cross sections of positive w (black solid lines), negative w (black dashed lines) and potential temperature (gray solid lines) at 4 PM on (a) August 7, 2000 and (b) March 28, 2000 passing VIS (shown as black dot on x axis). The plotting range is indicated in Figure 5-1. The interval of the potential temperature and negative wind velocity in the plots is 1° K and 0.03ms^{-1}, respectively. A contour interval multiplier of 3 (i.e. 1cms^{-1}, 3cms^{-1}, 9cms^{-1}, etc.) was applied to the positive wind velocity due to the strong upward motion in the mountain region. 120

Figure 5-15: SJV averaged 3km vertical velocity at 4 PM during simulation case 6 (summer) and case 3 (spring)..... 121

Figure.6-1: Normalized seasonal stagnation days from different WRF simulations: GFS-WRF, PCM_WRF_pres. (PCM-WRF runs for 2000 to 2006) and PCM_WRF_fut. (PCM-WRF runs for 2047 to 2053). 126

Figure 6-2: Same as Figure 6-1, but for SJV wide averaged ventilation rate during the stagnation events. Units are m^2 s^{-1}. 127

Figure 6-3: Predicted change (future-present) in annual average surface wind speed (units in m s^{-1}), 2-m temperature (units in °K) and PBLH (units in m) during summer and winter..... 129

Figure 6-4: (a) Present and (b) future seven year averaged summertime surface temperature (shading) and sea level pressure (contours). Units are ^{o}K for temperature and hPa for sea level pressure..... 130

Figure 6-5: Predicted change (future-present) in 2-m surface temperature during (a) summer and (b) winter by the Parallel Climate Model (PCM). Units are ^{o}K..... 132

Figure 6-6: Present-day seven year averaged (2000-06) PBLH during (a) summer and (b) winter. Units are m..... 133

Figure 6-7: Spatial distribution of future change for surface temperature and southwesterly wind component at 2pm and 2am during summer. Units are ^{o}K..... 137

Figure 6-8: Corresponding p-values of the plots in Figure 6-3. The p-value quantifies the likelihood that average meteorological conditions are identical in the present (2000-2006) and future (2047-2053). Note that smaller p-values represent bigger climate change signals. 139

Figure 7-1: Flow Chart of the climate downscaling and air quality modeling systems. 143

Figure 7-2: Panels (a)-(f) show changes in annual average values in meteorological parameters likely to occur due to climate change in the future (2047-53) from the present-day (2000-06). 149

Figure 7-3: Annual average Particulate Matter 2.5 ($PM_{2.5}$) concentrations (μg m^{-3}) in CA for the present day (2000-06) (a) total mass, (b) elemental carbon, (c) organic carbon, (d) nitrate, (e) ammonium, and (f) sulfate. 152

Figure 7-4: Comparison between modeled and observed 7-year average $PM_{2.5}$ (a) total mass, (b) elemental carbon, (c) organic carbon, (d) nitrate, (e) ammonium, and (f) sulfate concentrations at different sites in California: (1) CELA-central Los Angeles North Main St, (2) SJ4-San Jose 4th St, (3) FSF-Fresno 1st St, (4) M14-Modesto 14th St, (5) VCS-Visalia Church St, and (6) S13-Sacramento T St. 154

Figure 7-5: Predicted variations around the 7-year average $PM_{2.5}$ total mass concentration at four sites in California: (a) Riverside-Rubidoux (RIVR), (b) Central Los Angeles (CELA), (c) Bakersfield (BFK), and (d) Fresno (FSF) 156

Figure 7-6: Changes in annual average total mass and primary $PM_{2.5}$ concentrations (μg m^{-3}), and their corresponding p-values in CA likely to occur in the future (2047-53) due to climate change from the present-day (2000-06). The p-value quantifies the likelihood that average future concentrations are equal to present day concentrations. 159

Figure 7-7: Changes in annual average secondary $PM_{2.5}$ concentrations (μg m^{-3}), and their corresponding p-values likely to occur in the future (2047-53) due to climate change from the present-day (2000-06). The p-value quantifies the likelihood that average future concentrations are equal to present day concentrations. 161

Figure 8-1: Three major air basins in California: (1) Sacramento Valley Air Basin (SV), (2) San Joaquin Valley Air Basin (SJV), and (3) South Coast Air Basin (SoCAB) 167

Figure 8-2: Future (2047-53) change in population-weighted concentrations of $PM_{2.5}$ total mass, primary and secondary components, trace metal and source categories contributing to the total mass from present-day (2000-06). Panels (top-down) show California state-wide average, Sacramento Valley (SV) air basin average, San Joaquin Valley (SJV) air basin average, and South Coast Air Basin (SoCAB) average results. The error bars represent the 95% CI. 170

Figure 8-3: Future (2047-53) change in population-weighted concentrations of $PM_{0.1}$ total mass, primary and secondary components, trace metal and source categories contributing to the total mass from present-day (2000-06). Panels (top-down) show California state-wide, Sacramento Valley (SV) air basin, San Joaquin Valley (SJV) air basin, and South Coast Air Basin (SoCAB) average results. The error bars represent the 95% CI. 171

Figure 8-4: Future (2047-53) change in population-weighted concentrations of PM_{10} total mass, primary and secondary components, trace metal and source categories

contributing to the total mass from present-day (2000-06). Panels (top-down) show California state-wide average, Sacramento Valley (SV) air basin average, San Joaquin Valley (SJV) air basin average, and South Coast Air Basin (SoCAB) average results. The error bars represent the 95% CI. 172

Figure 8-5: Frequency distribution of 24-hr average population-weighted $PM_{2.5}$ total mass concentrations for California under the (a) present-day (2000-2006) and (b) future (2047-2053) climate conditions. The shaded regions encompass values higher than the 99th percentile value of each distribution. 173

Figure 8-6: Average of worst 24-hr average $PM_{2.5}$ total mass concentrations (μg m^{-3}) corresponding to days with population-weighted concentrations above the 99th percentile values as illustrated in Figure 8-3 for California under the (a) future (2047-2053), and (b) present-day climate (2000-2006) conditions. Panel (c) shows the difference between the future (a) and present-day (b). 174

Figure 8-7: Climate change effects on 24-hr average population-weighted concentrations of $PM_{0.1}$ total mass and component species, and contributions from various sources to the total mass using average data above the 99th percentile value in the 7-year data distribution in the present-day and future periods..... 176

Figure 8-8: Climate change effects on 24-hr average population-weighted concentrations of $PM_{2.5}$ total mass and component species, and contributions from various sources to the total mass using average data under the shaded regions illustrated in Figure 8-6..... 177

Figure 8-9: Climate change effects on 24-hr average population-weighted concentrations of PM_{10} total mass and component species, and contributions from various sources to the total mass using average data above the 99th percentile values in the 7-year data distribution in the present-day and future periods. 178

Figure 9-1: Annual average fine particulate matter ($PM_{2.5}$) concentrations in CA for the present day (2000-06) utilizing the emissions control projected for 2050: (a) total mass, (b) elemental carbon, (c) organic carbon, (d) nitrate, (e) ammonium, and (f) sulfate. 184

Figure 9-2: Changes in annual average total mass and primary $PM_{2.5}$ concentrations (μg m^{-3}), and their corresponding p-values in CA likely to occur in the future (2047-53) due to climate change and projected emissions control for 2050 from the present-day (2000-06). The p-values were calculated for a one-tailed student t-distribution from annual average concentrations at 95% confidence interval. 186

Figure 9-2 continued: Changes in annual average secondary $PM_{2.5}$ concentrations (μg m^{-3}), and their corresponding p-values in CA likely to occur in the future (2047-53) due to climate change and projected emissions control for 2050 from the present-day (2000-06). The p-values were calculated for a one-tailed student t-distribution from annual average concentrations at 95% confidence interval. 187

Figure 9-3: Future change (2047-53 vs. 2000-06) in population-weighted concentrations of $PM_{2.5}$ total mass / components / primary source contributions. Panels (top-down) show California state-wide average, Sacramento Valley (SV) air

basin average, San Joaquin Valley (SJV) air basin average, and South Coast Air Basin (SoCAB) average results. 189

Figure 9-4: Future change (2047-53 vs. 2000-06) in population-weighted concentrations of PM_{10} total mass / components / primary source contributions. Panels (top-down) show California state-wide average, Sacramento Valley (SV) air basin average, San Joaquin Valley (SJV) air basin average, and South Coast Air Basin (SoCAB) average results. 190

Figure 9-5: Future change (2047-53 vs. 2000-06) in population-weighted concentrations of $PM_{0.1}$ total mass / components / primary source contributions. Panels (top-down) show California state-wide average, Sacramento Valley (SV) air basin average, San Joaquin Valley (SJV) air basin average, and South Coast Air Basin (SoCAB) average results. 191

Figure 9-6: Frequency distribution of 24-hr average population-weighted $PM_{2.5}$ total mass concentrations for California under the (a) present-day (2000-2006) and (b) future (2047-2053) climate conditions. The shaded regions encompass values higher than the 99th percentile value of each distribution. 192

Figure 9-7: Average of the highest 24-hr average $PM_{2.5}$ total mass concentrations (μg m^{-3}) corresponding to days with population-weighted concentrations above the 99th percentile values as illustrated in Figure 9-3 for California under the (a) future (2047-2053), and (b) present-day climate (2000-2006) conditions. Panel (c) shows the difference between the future (a) and present-day (b). 193

Figure 9-8: Future change (2047-53 vs. 2000-06) in population-weighted 99th percentile concentrations of $PM_{0.1}$ total mass / components / primary source contributions. Panels (top-down) show California state-wide average, Sacramento Valley (SV) air basin average, San Joaquin Valley (SJV) air basin average, and South Coast Air Basin (SoCAB) average results. 194

Figure 9-9: Future change (2047-53 vs. 2000-06) in population-weighted 99th percentile concentrations of $PM_{2.5}$ total mass / components / primary source contributions. Panels (top-down) show California state-wide average, Sacramento Valley (SV) air basin average, San Joaquin Valley (SJV) air basin average, and South Coast Air Basin (SoCAB) average results. 196

Figure 9-10: Future change (2047-53 vs. 2000-06) in population-weighted 99th percentile concentrations of PM_{10} total mass / components / primary source contributions. Panels (top-down) show California state-wide average, Sacramento Valley (SV) air basin average, San Joaquin Valley (SJV) air basin average, and South Coast Air Basin (SoCAB) average results. 197

Table 10-1: Summary of climate and emissions cases analyzed. 199

Figure 10-1: Annual average PM 2.5 mass difference (2047 to 2053) using 2050 emissions vs. (2000 – 2006) using 2000 emissions. 200

Figure 10-2: PM2.5 population-weighted concentration differences by chemical component. The first two bars of each group show the climate signal, the second two bars show the emissions signal, and the final bar shows the combined signal.

Uncertainty bars represent the 95% confidence interval based on the inter-annual variability. The crustal signal has been removed from the (2050-2000) emissions comparisons (3rd – 5th bars) for all locations except the SoCAB to remove a bias in the calculation. 202

Figure 10-3: PM0.1 population-weighted concentration differences by chemical component. The first two bars of each group show the climate signal, the second two bars show the emissions signal, and the final bar shows the combined signal. Uncertainty bars represent the 95% confidence interval based on the inter-annual variability. The crustal signal has been removed from the (2050-2000) emissions comparisons (3rd – 5th bars) for all locations except the SoCAB to remove a bias in the calculation. 203

Figure 10-4: PM10 population-weighted concentration differences by chemical component. The first two bars of each group show the climate signal, the second two bars show the emissions signal, and the final bar shows the combined signal. Uncertainty bars represent the 95% confidence interval based on the inter-annual variability. The crustal signal has been removed from the (2050-2000) emissions comparisons (3rd – 5th bars) for all locations except the SoCAB to remove a bias in the calculation. 204

Figure 10-5: PM2.5 population-weighted concentration differences by primary source contribution. The first two bars of each group show the climate signal, the second two bars show the emissions signal, and the final bar shows the combined signal. Uncertainty bars represent the 95% confidence interval based on the inter-annual variability. The dust and miscellaneous (Misc) signals have been removed from the (2050-2000) emissions comparisons (3rd – 5th bars) for all locations except the SoCAB to remove a bias in the calculation. 206

Figure 10-6: PM0.1 population-weighted concentration differences by primary source contribution. The first two bars of each group show the climate signal, the second two bars show the emissions signal, and the final bar shows the combined signal. Uncertainty bars represent the 95% confidence interval based on the inter-annual variability. The dust and miscellaneous (Misc) signals have been removed from the (2050-2000) emissions comparisons (3rd – 5th bars) for all locations except the SoCAB to remove a bias in the calculation. 207

Figure 10-7: PM10 population-weighted concentration differences by primary source contribution. The first two bars of each group show the climate signal, the second two bars show the emissions signal, and the final bar shows the combined signal. Uncertainty bars represent the 95% confidence interval based on the inter-annual variability. The dust and miscellaneous (Misc) signals have been removed from the (2050-2000) emissions comparisons (3rd – 5th bars) for all locations except the SoCAB to remove a bias in the calculation. 208

LIST OF ACRONYMS

AB32 - California State Assembly Bill 32
ACPI - Accelerated Climate Prediction Initiative
AIM - Aerosol Inorganic Model
AR3 - Third Assessment Report of the IPCC
AR4 - Fourth Assessment Report of the IPCC
ARW - Advanced Research WRF
AVOC - anthropogenic volatile organic compounds
BAU - Business as Usual
BCs - boundary conditions
BenMAP - Benefits Mapping model from USEPA
BVOC - biogenic volatile organic compounds
CACM - Caltech Atmospheric Chemistry Model
CARB - California Air Resources Board
CCAQS - California Ambient Air Quality Standards
CCSM - Community Climate System Model
CI - confidence interval
CIT - California Institute of Technology
CM3 - Climate Model version 3
CMAQ - Community Multiscale Air Quality model from USEPA
CNRM - Centre National de Recherches Meteorologiques
DJF - December January February
DOE - Department of Energy
EC - elemental carbon
EMFAC - Emissions Factor Model maintained by CARB
ENSO - El-Nino Southern Oscillation
FDDA - Four Dimensional Data Assimilation
GBHP - Great Basin High Pressure
GCM - Global Climate Model / General Circulation Model
GFDL - Geophysical Fluid Dynamics Laboratory
GFS - Global Forecast System
GISS - Goddard Institute for Space Studies
ICs - initial conditions
IPCC - Intergovernmental Panel on Climate Change
JJA - June July August
KF - Kain- Fritsch scheme
LAC - Los Angeles County
MABL - Marine Atmospheric Boundary Layer
MAM - March April May
MIROC3.2 - Model for Interdisciplinary Research on Climate version 3.2
MM5 - Mesoscale Meteorological Model version 5
MPI-ECHAM5 - Max Planck Institute for Meteorology ECHAM version 5
MYJ - Mellor-Yamada-Janjic TKE scheme
NAAQS - National Ambient Air Quality Standards

NATL - North American Thermal Low
NCAR - National Center for Atmospheric Research
NCEP - National Center for Environmental Prediction
NH4+ / N(-III) - ammonium ion
NO3- / N(V) - nitrate
NOAA - National Oceanic and Atmospheric Administration
NOx - oxides of nitrogen
O3 - ozone
OC - organic carbon
OH - hydroxyl radical
PBLH - Planetary Boundary Layer Height (mixing depth)
PCM - Parallel Climate Model
PM0.1 - Airborne particle mass with aerodynamic diameter less than 0.1 Âµm.
PM10 - Airborne particle mass with aerodynamic diameter less than 10.0 Âµm.
PM2.5 - Airborne particle mass with aerodynamic diameter less than 2.5 Âµm.
PM - Airborne particulate matter
PN - particulate nitrate
POP - Parallel Ocean Program
PSH - Pacific Subtropical High
RASS - Radio Acoustic Sounding System
RCM - Regional Climate Model
RH2 - relative humidity at 2 m above the ground
RMSE - Root Mean Square Error
RN - reactive nitrogen
RRTM - Rapid Radiation Transfer Model
SCAQMD - South Coast Air Quality Management District
SCAQS - Southern California Air Quality Study
SJV - San Joaquin Valley Air Basin
SO42- / S(VI) - sulfate
SoCAB - South Coast Air Basin
SON - September October November
SOP - Standard Operating Procedure
SRES - Special Report on Emissions Scenarios from the IPCC
SST - Sea Surface Temperature
SV - Sacramento Valley Air Basin
T2 - temperature at 2 m above the ground
T850 - temperature at an elevation of 850 millibars
TKE - Turbulent Kinetic Energy
U10 - X component of wind at height of 10 m above the ground.
UCB - University of California at Berkeley
UCD - University of California at Davis
UCSD - University of California at San Diego
USEPA - United States Environmental Protection Agency
UV - Ultraviolet radiation
V10 - Y component of wind at height of 10 m above the ground
VIS - Visalia

VOC - volatile organic compounds
WPS - WRF Preprocessing System
WRF - Weather Research and Forecast
WSM6 - WRF single-momentum 6-class scheme
Wsp10 - wind speed at height of 10 m above the ground
YSU - Yonsei University

ABSTRACT

This report explores how climate change will influence air quality in California through changes to meteorology and emissions. The report addresses the challenging nature of the high spatial resolution needed to represent California's air basins and the long analysis periods needed to capture El-Nino Southern Oscillation (ENSO) meteorological cycles. Previous studies have not adequately addressed these issues for California.

Three study methods were employed: (i) model perturbations (O_3 and PM), (ii) statistical downscaling (O_3), and (iii) dynamic downscaling (PM). Model perturbation studies for historical ozone episodes suggest that concentrations increase when maximum daytime temperatures increase, and that the climate change penalty will offset much of the benefit from future emissions control programs. Perturbation studies also suggest that ozone concentrations are relatively insensitive to changes in nighttime temperatures. Nighttime temperatures in California have increased more than daytime temperatures over the past several decades, but the majority of GCMs predict that daytime temperatures will increase in the future in California. For example, daytime temperatures at a height of ~1.5 km (T850) over the San Joaquin Valley (SJV) and South Coast Air Basin (SoCAB) are predicted to increase according simulations performed with the Geophysical Fluid Dynamics Laboratory (GFDL) model developed at Princeton. The statistical relationship between the 1-hr maximum measured ozone concentrations and historical daytime maximum T850 values combined with the GFDL predictions suggest that by the year 2050 California would experience an additional 22-30 days year^{-1} and 6-13 days year^{-1} with ozone concentrations ≥90 ppb under the IPCC A2 and B1 emissions scenarios, assuming criteria pollutant emissions in California remain at 1990-2004 levels.

Climate impacts on ground level airborne particulate matter (PM) concentrations were analyzed by dynamic downscaling of global models. The air quality simulations were carried out with a resolution of 8 km for the entire state of California for the years 2000-06 (present climate) and 2047-53 (future climate). Each period was evaluated using emissions for the year 2000 and for the year 2050. Predictions from over 4000 simulation days suggest that the ENSO signal causes inter-annual variability that is greater than the average shift in PM concentrations between present and future climate conditions. Statistically significant decreases in annual-average $PM_{2.5}$ concentrations (0.5-1.0 μg m^{-3}) over coastal regions of California were predicted due to increased future wind speed during the winter season. Changes to the summer sea breeze system did not have a major impact on coastal PM concentrations. The dynamic downscaling further predicted that extreme 99th percentile PM concentrations will increase (10-20 μg m^{-3}) in the Sacramento Valley (SV) and SJV due to stronger stagnation conditions.

Climate change reduced annual-average population-weighted concentrations of $PM_{0.1}$, $PM_{2.5}$, and PM_{10} in the SoCAB using either year 2000 or year 2050 emissions. Conversely, climate change increased extreme 99th percentile primary $PM_{0.1}$, $PM_{2.5}$, and PM_{10} concentrations in the SV and SJV. Emissions controls such as diesel particle filters or bans on residential wood combustion are effective methods to offset the climate penalty for $PM_{2.5}$ during extreme pollution events.

EXECUTIVE SUMMARY

Background: California has persistent air quality problems that affect the health of millions of residents. Global climate change will modify long-term weather patterns in California with direct consequences to air quality and public health. California's diverse emissions sources located inside air basins bordered by mountain ranges require analysis at fine spatial resolution (<10km) while at the same time the long-term El-Nino Southern Oscillation (ENSO) patterns require 7-8 year analysis periods for meaningful analysis. Rigorous evaluations that address both of these issues are needed to accurately assess climate impacts on air quality in California.

Jacob and Winner [1] recently reviewed studies seeking to quantify climate change impacts on regional air quality. They identify three major classes of study methods: (i) statistical downscaling, (ii) model perturbations, and (iii) dynamic downscaling. Statistical downscaling uses historical relationships between meteorology and air quality to predict future changes in ozone (O_3) and airborne particulate matter (PM) concentrations based on changes to meteorology alone. Model perturbation studies alter the meteorological inputs used in regional air quality models in a manner that is consistent with future climate change. Full dynamic downscaling uses Global Climate Model (GCM) predictions as initial/boundary conditions for regional weather models that are then coupled to air quality models to more accurately balance the simultaneous modifications to meteorological variables that are likely to occur because of climate change. Each of these study designs has strengths and weaknesses for ozone and PM analysis in California.

Methods: The three study methods identified by Jacob and Winner [1] were employed to analyze climate change impacts on ground-level O_3 and PM concentrations in California (see Table 1).

Table 1: Summary of methods employed to study climate impacts on California air quality and the chapters documenting results.

	Pollutant	
Study Method	O_3	PM
Statistical Downscaling	Chapter 4	Not Applicable
Perturbation Studies	Chapters 2,3	Chapter 2
Dynamic Downscaling	Not Applicable	Chapters 5-10

Statistical downscaling studies for PM concentrations could not be carried out because robust linear relationships between meteorological variables and PM concentrations do not exist for California's air basins. Dynamic downscaling studies for O_3 could not be carried out because summertime wind speed was over-predicted by the downscaling methods, leading to excess ventilation and under-predicted basecase O_3 concentrations. This issue does not severely impact annual-average PM predictions because summer-time PM concentrations are typically much lower than concentrations in other seasons.

Model perturbation studies based on changing the meteorology during historical episodes were feasible for both O_3 and PM and so these studies were used for a preliminary analysis of climate effects on air quality in California. Statistical downscaling was then used to transform results from the GFDL Global Climate Model into an O_3 assessment between the years 2000 – 2100. The foundation for this analysis was the strong correlations between surface ozone concentrations and the air temperature at a height of 850 millibars (T850). Dynamic downscaling of the PCM Global Climate Model using the Weather Research Forecast (WRF) meteorological model, the UCD/CARB/SCAQMD emissions system, and the UCD air quality model was then used for the future PM assessment. Climate-induced changes to PM concentrations were calculated regionally and using population-weighted concentrations. The uncertainty of the comparison between current and future climate was quantified using the inter-annual variability within the same climate periods.

Ozone Results: Perturbation studies for historical O_3 episodes suggest that concentrations increase when maximum daytime temperatures increase. Since the majority of Global Climate Models predict that future climate will be warmer than current climate in California, a "climate penalty" exists for ground level O_3 concentrations as summarized in Figure 1 for the South Coast Air Basin (SoCAB).

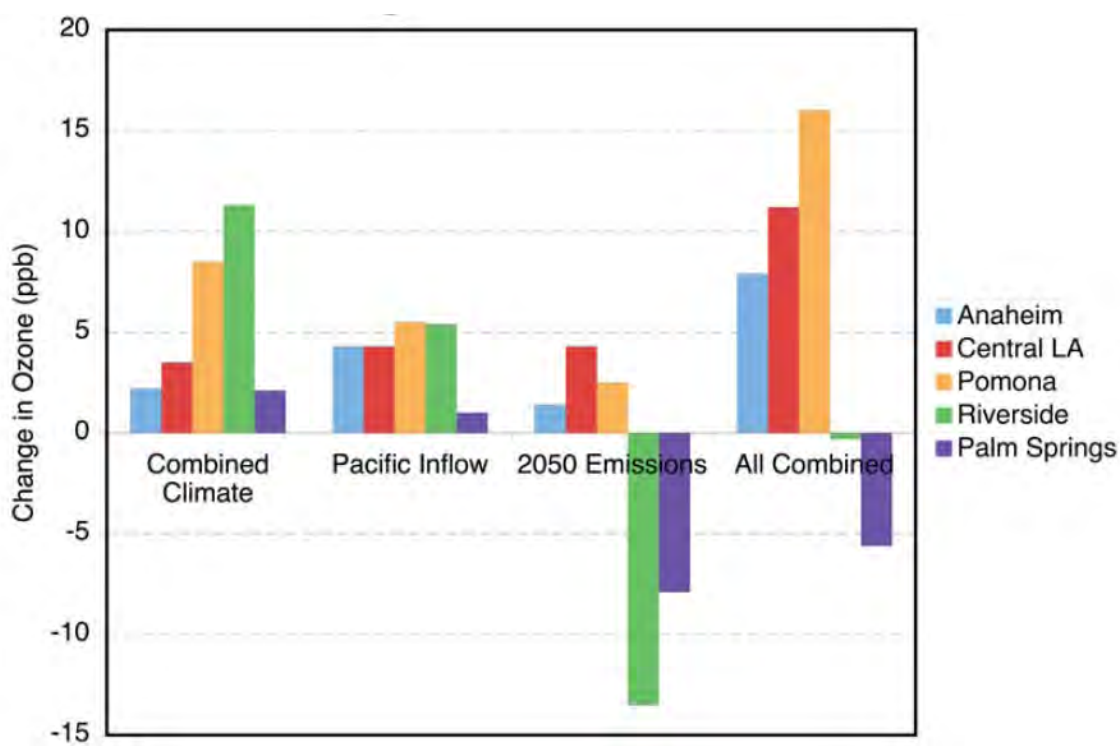

Figure 1: Average weekday ozone (ppb) at 1500 h LT (local time) for a SoCAB episode in 2005: base case levels and differences between specified run and base case.

Both statistical downscaling and model perturbation studies confirm that the magnitude of the climate penalty for O_3 depends on the base emissions year used for the evaluation, with larger penalties calculated for more reactive emissions (older episodes) and smaller

penalties for less reactive emissions (newer episodes) as shown in Figure 2 for the SoCAB.

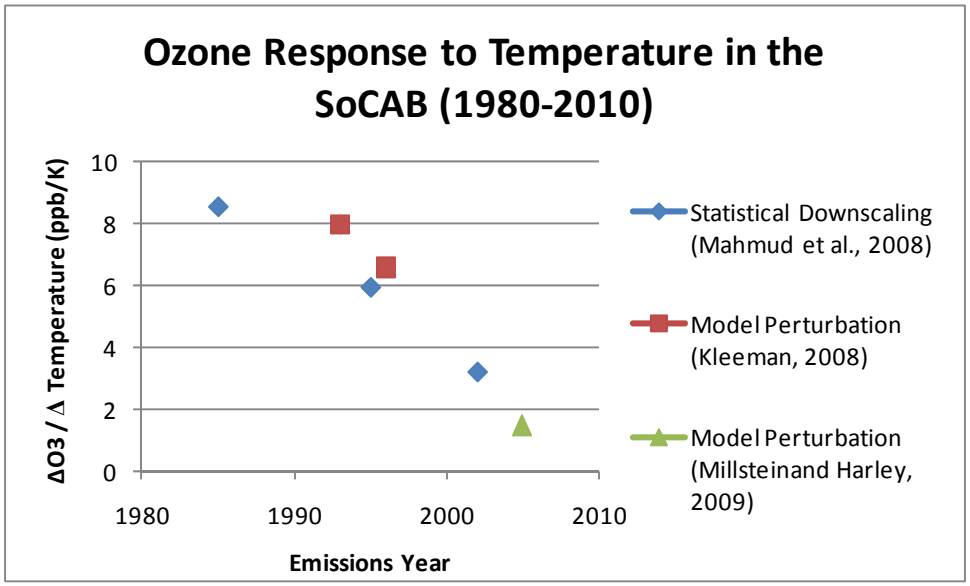

Figure 2: Evolution of the O_3 climate penalty over time due to changes in the emissions inventory in the South Coast Air Basin (SoCAB).

Perturbation studies also show that O_3 concentrations are insensitive to changes in nighttime temperatures. Nighttime temperatures in California have increased more than daytime temperatures over the past several decades, but future changes may not follow this pattern. Maximum daytime temperatures at a height of ~1.5 km (T850) over the San Joaquin Valley (SJV) and South Coast Air Basin (SoCAB) are predicted to increase according to most Global Climate Models, including the Geophysical Fluid Dynamics Laboratory (GFDL) model developed at Princeton. The correlation slope between surface O_3 concentrations and T850 is robust under fixed emissions conditions. Statistical downscaling suggests that by the year 2050 California would experience an additional 22-30 days year^{-1} and 6-13 days year^{-1} with ozone concentrations ≥90 ppb under the IPCC A2 and B1 emissions scenarios (assuming emissions of criteria pollutants in California remained at 1990-2004 levels). Note that ENSO cycles introduce inter-annual variability in these results, but the upward trend over several decades is

unmistakable.

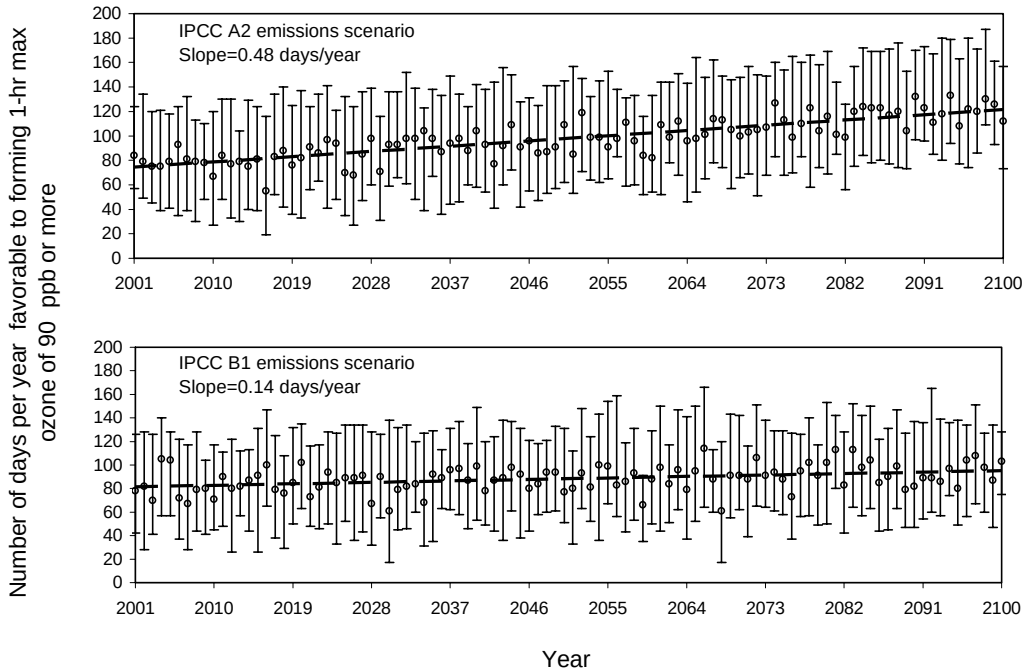

Figure 3: The number of days per year conducive to forming 1-hr maximum ozone of 90 ppb or more at Upland, CA under the Intergovernmental Panel on Climate Change (IPCC) emissions scenarios: A2 (top panel) and B1 (bottom panel). Note that the underlying assumption for this prediction is that the criteria emissions in CA remain at the 1990-2004 level. Uncertainty bars represent the third and the first quartiles of the predicted number of days.

PM Results: Model perturbation studies for PM concentrations in California were inconclusive. Increasing temperature increases the production rate of semi-volatile reaction products but decreases partitioning to the condensed phase. Increased humidity and ozone concentrations generally promote increased condensation of ammonium nitrate but increased precipitation events quickly scavenge airborne particulate matter. These competing trends clearly point out the need for full dynamic downscaling of model predictions.

Dynamic downscaling of PCM global results to 4 km resolution over California predicts that average surface air temperatures over California will increase by 1-2K between 2047-53 and 2000-06 ($p<0.05$). Average wind speeds are predicted to increase during the winter in coastal regions of California ($p<0.1$) but change little in other seasons or locations. The strength of the atmospheric stagnation events is predicted to increase in the future during all seasons except for spring.

Model predictions for $PM_{2.5}$ mass and component concentrations between the years 2000-06 were biased ~30% lower than measurements because the wind speeds predicted by WRF were biased high by 2-3 ms^{-1} during stagnation events. Positive wind speed bias largely results from excessive transfer of momentum into the surface layer, compounded by the fact that the predictions cannot be constrained by assimilation of actual

measurements (that do not exist for climate simulations). Overall, the bias introduced by the wind speed over-prediction should be consistent between present and future analysis periods so that the comparison between periods is meaningful.

Average $PM_{2.5}$ mass concentrations are predicted to decrease in coastal California but increase slightly in the northern SJV between 2000-06 and 2047-53. A corresponding analysis of the inter-annual variability indicates that only the changes in the coastal areas are significant at the 95% confidence level, meaning that other regions may experience little impact on $PM_{2.5}$ mass due to climate change.

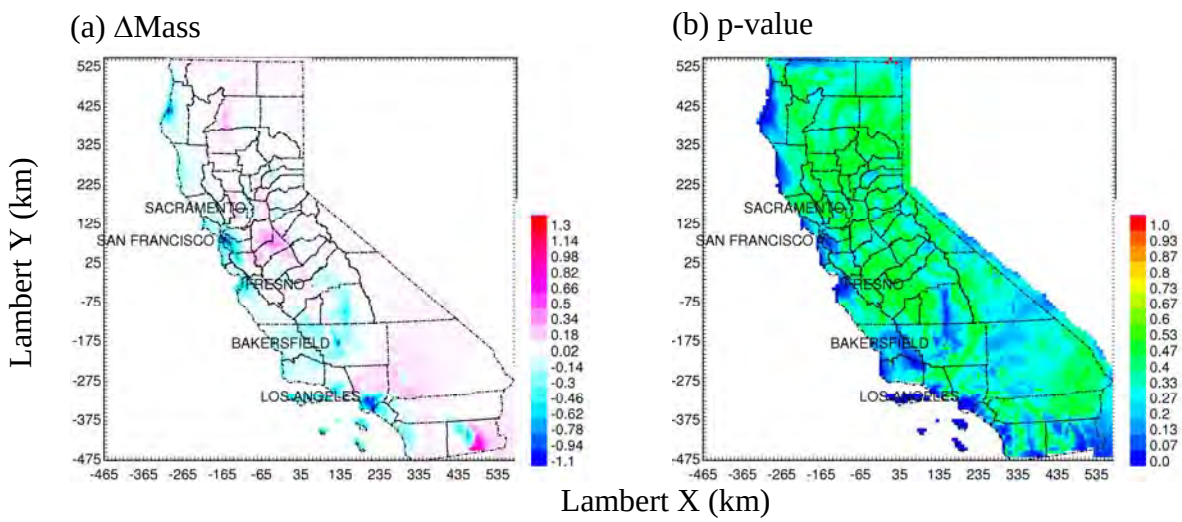

Figure 4: Changes in annual average $PM_{2.5}$ mass concentrations and corresponding p-values in CA likely to occur in the future (2047-53) due to climate change from the present-day (2000-06). The p-value quantifies the likelihood that average future concentrations are equal to present day concentrations.

The majority of the decreased average $PM_{2.5}$ concentrations were associated with reductions in primary PM constituents (due to increased average ventilation) and secondary ammonium nitrate (due to increased ventilation and increased temperature).

Annual-average population-weighted $PM_{2.5}$ mass differences between 2047-53 and 2000-06 are small relative to the uncertainty introduced by inter-annual variability. Individual source contributions to PM mass do respond to climate in a statistically significant manner (95% CI does not overlap zero). Future population-weighted annual-average primary $PM_{2.5}$ from shipping and combustion of high sulfur fuel both decrease by ~6% in response to climate change.

Extreme $PM_{2.5}$ mass concentrations (predicted on the 1% of days with the highest overall concentrations) are predicted to increase by 7-20 $\mu g\ m^{-3}$ in the SJV between 2000-06 and 2047-53 due to the increased strength of future stagnation events. The inter-annual variability of the $PM_{2.5}$ mass during extreme events is large, leading to broad confidence intervals on the climate signal for total PM mass. Once again, climate signals are more evident for primary source contributions that contribute to overall mass. Extreme 99th

percentile population-weighted $PM_{2.5}$ primary source contributions from diesel engines increase by 28% response to future climate change. Emissions controls such as diesel particle filters or bans on residential wood combustion are effective methods to offset the climate penalty for $PM_{2.5}$ during extreme pollution events.

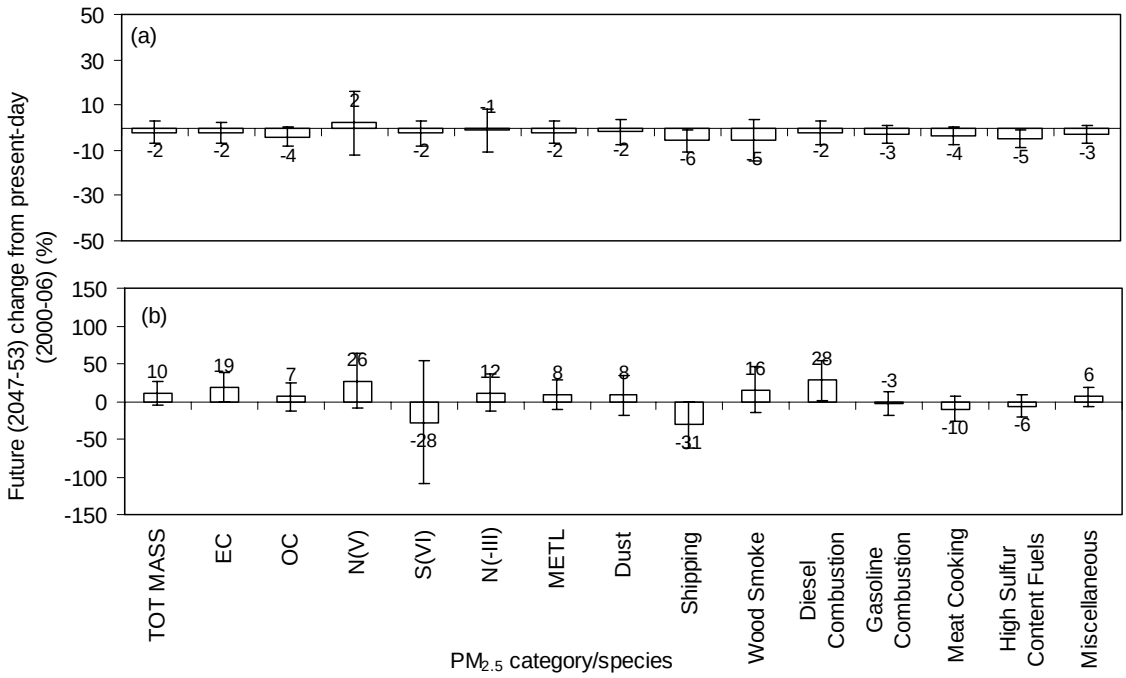

Figure 5: Future (2047-53) minus present (2000-06) change in population-weighted $PM_{2.5}$ total mass, components, and primary source categories for (a) annual averages and (b) 99th percentile extreme pollution events. Results are averaged across the entire state of California. The error bars represent the 95% confidence interval.

Conclusions: Statistical downscaling and model perturbation studies for ozone consistently indicate that climate change will produce conditions more conducive to ozone production in California. The magnitude of the "climate penalty" for ozone is decreasing over time due to the changes occurring in the criteria pollutant emissions inventory. Additional emissions controls are currently needed to offset the climate "penalty". The magnitude of the additional emissions controls needed in the future depends on our progress towards achieving air quality standards.

Dynamic downscaling techniques indicate that the effect of climate change on PM concentrations is likely to be smaller than the inter-annual variability experienced during any seven year analysis window. Longer analysis times are needed to quantify a climate signal different from zero with 95% confidence across a broad array of PM metrics.

Evidence from over 4000 simulated days in the current study suggests that climate change will reduce annual-average primary PM_{10} / $PM_{2.5}$ / $PM_{0.1}$ concentrations but

increase extreme 99th percentile primary PM_{10} / $PM_{2.5}$ / $PM_{0.1}$ concentrations in the state of California.

Future Work: The economic consequences of known climate impacts in California are estimated to be $31-57B [2], with another $8B of estimated costs needed to offset potential air quality impacts [2]. The model perturbation analysis for ozone that is summarized in this final report provides part of the foundation for this latter estimate, but significant uncertainty remains about the economic costs associated with changes to extreme PM concentrations. Future studies should quantify the economic impacts associated with extreme concentration events in California.

The 7 year analysis periods for dynamic downscaling exercises should be expanded to ~10 years to reduce the uncertainty bounds of the climate signal on PM concentrations in California. Furthermore, an ensemble of simulations should be conducted using different models to fully quantify the uncertainty in the calculation (which is larger than the inter-annual variability predicted by a single modeling system).

The shortcomings in the meteorological models that prevent accurate downscaling during winter months without data assimilation should be corrected so that dynamic downscaling studies can be carried out for ozone concentrations in California.

Future studies should incorporate emissions reductions associated with California Assembly Bill 32 (AB32) into the future inventories and take care to properly scale power generation, chemical processing, and goods movement sources as a function of economic condition.

1.0 INTRODUCTION

1.1 Motivation

The Intergovernmental Panel on Climate Change (IPCC) Fourth Assessment Report (AR4) (2007) projected that the global mean surface air temperature is likely to increase between 1.8 °C and 4 °C in 2090 – 2099 relative to 1980 – 1999 under the IPCC Special Report on Emissions Scenarios (SRES) B1 (lowest) and A2FI (highest) emissions scenarios, respectively. At the regional scale, the annual mean surface air temperature in North America is estimated to increase between 3.7 °C (25% quartile) and 5.2 °C (75% quartile) in 2080 – 2099 relative to 1980 – 1999 under the A1B SRES emissions scenario ([3]). Because of this climate warming, the frequency, duration, and intensity of conditions conducive to forming air pollution events are also likely to increase ([4]). It is widely recognized that maintaining safe atmospheric levels of various pollutants such as ozone (O_3), carbon monoxide (CO), nitrogen oxides (NO_x), particulate matter (PM) and other toxic chemicals depends on both emissions and meteorological conditions ([5]).

Previous studies have shown that there is an association between high concentrations of surface ozone and adverse public health (see for example,[6], [7], [8]). Exposure to elevated concentrations of airborne particles with aerodynamic diameter less than 2.5 µm ($PM_{2.5}$) also has serious health consequences (see for example, [9], [10], [11]). Climate change may affect exposure to these pollutants by modifying weather, anthropogenic emissions, and biogenic emissions ([12]).

California has two of the most polluted air basins in the United States that consistently violate the National Ambient Air Quality Standards (NAAQS): the San Joaquin Valley air basin (SJV) with a population of ~3 million, and the South Coast Air basin (SoCAB) with a population of ~15 million. California has a complex topography that includes mountains, valleys, deserts and ocean. These features combine with typical weather conditions to create a persistent air quality problem in California despite stringent control measures implemented over the previous decades. Climate change is expected to alter the long-term meteorological patterns in California, with unknown consequences for air quality and human health.

1.2 Previous Analysis for Climate Effects on Air Quality in California

The relationship between climate and air quality has been studied using General Circulation Models (GCMs) coupled to chemistry calculations (see for example [13-16]). These calculations typically use grid cells that are larger than 1° (>100 km at mid latitudes), making them most appropriate for regional pollutants (such as O_3) in locations that do not have complex terrain (such as the eastern United States). Wu et al [17] summarized a list of 11 studies that examined how climate change will affect global tropospheric background ozone. Most of the summarized studies predict that climate change will reduce global tropospheric ozone concentrations due to increasing concentrations of water vapor leading to reduced ozone lifetimes in low-NOx environments. In contrast, Prather et al [13] noted that increasing global emissions of

methane and other greenhouse gases are causing net increases in global tropospheric ozone concentrations, with a 2-7 ppb increase in surface ozone over much of the northern hemisphere by 2030. Thus, the same global emissions that cause climate change are also causing increased background concentrations of ozone in North America. The changing climate somewhat mitigates this concentration increase, but the common link to global anthropogenic emissions cannot be ignored and the system must be treated as a whole. California is likely to experience higher background ozone concentrations in the future. This background ozone will combine with local ozone production during the summer months and contribute to secondary particulate matter formation during the winter months. The present study incorporates increasing concentrations of tropospheric background ozone into the boundary conditions during the analysis for California air quality.

Climate-induced changes to ozone at the regional level can be studied using statistical downscaling, perturbations of chemical transport models, or full dynamic downscaling of global through regional models. Jacob and Winner [1] recently reviewed results from each type of study, finding a consistent pattern of increased peak surface ozone concentrations in polluted regions in response to climate change. The magnitude of this "climate penalty" was found to be 1-10 ppb depending on the specific study region and the methods employed. The published versions of several chapters in the current report were incorporated into the Jacob and Winner review and so the results are inherently consistent with their meta analysis.

Dynamic downscaling from global to regional models represents the most comprehensive approach to study climate effects on regional air quality, but it can be difficult to carry out these types of studies in California. Sharp spatial gradients in California's extreme topography require high spatial resolution while proper accounting of ENSO cycles simultaneously require long analysis periods. The standard regional meteorology models used for downscaling also over-predict wind speed during summer months in California, resulting in an under-prediction of ozone concentrations. Jacob and Winner [1] identified 14 dynamic downscaling studies for ozone that were focused on domains ranging from the entire globe to continental scales. The majority of these studies employed +36 km horizontal resolution, and none of them represented California with spatial resolution on the order of < 10 km (the current standard for air quality modeling in California). The dynamic downscaling results for ozone are therefore inconclusive for California's major air basins at this time. Dynamic downscaling for ozone was not attempted in the current project.

Fewer studies have addressed the relationship between climate and $PM_{2.5}$, and those studies that did incorporate $PM_{2.5}$ into their analysis were unable to identify consistent results. Statistical downscaling studies generally find little correlation between elevated $PM_{2.5}$ concentrations and meteorological variables other than the observation that stagnation is generally a requirement for high concentrations. Perturbation studies identify competing trends with increased temperatures simultaneously promoting the gas-phase oxidation of precursor compounds and the evaporation of semi-volatile PM components. Increased humidity and ozone concentrations generally promote increased

condensation of ammonium nitrate but increased precipitation events quickly scavenge airborne particulate matter. These competing trends clearly point out the need for full dynamic downscaling of model predictions, but the time and spatial scales inherent in California once again make this difficult to accomplish. Jacob and Winner [1] summarize a total of 9 dynamic downscaling studies for PM carried out by coupling global and regional models. None of these studies simultaneously addressed spatial and time resolution needed to properly represent California's air basins. Tagaris *et al*. ([18]) used a downscaling system consisting of the GISS, MM5, CMAQ and BenMAP models to investigate the potential impact of climate change on $PM_{2.5}$ related health effects for the United States. Spatial resolution was relatively coarse (36km) and only one annual average year was simulated. According to their analysis, annual average $PM_{2.5}$ concentrations across the United States will decrease due to climate change, and California is likely to experience an average **decrease** of 186 cases of premature death with decreasing trends also in other $PM_{2.5}$-related health issues including chronic and acute bronchitis, asthma, hospital admissions, and respiratory diseases in the future. Avise et al. [19] used a downscaling system consisting of PCM, MM5, and CMAQ to predict climate impacts on July $PM_{2.5}$ concentrations across the United States. Future July $PM_{2.5}$ concentrations in EPA's Region 9 (encompassing California) were predicted to decrease by 0.5 µg m^{-3} in response to climate change, but once again this time period does not adequately represent peak PM seasons in California. Jacobson [19] used the GATOR GCM-RCM to directly examine the effects of CO_{-2}-induced climate change on $PM_{2.5}$ concentrations across the United States using +50 km spatial resolution. The July-November mean $PM_{2.5}$ concentration was reported to increase by 0.065 µg m^{-3} but the analysis time period does not correspond to the peak PM concentrations in California and the details of the basecase simulation do not appear to match measured concentration patterns in California. More recently, Jacobson [20] evaluated the direct impact of CO_2 concentrations domes around major cities on $PM_{2.5}$ concentrations, finding slight concentrations increases. This study addresses the local effects of CO_2 emissions on air quality but it does not address the effects of global climate change on pollutant concentrations.

Each of the previous studies described above has significant analysis gaps that must be addressed to properly consider climate impacts on air quality in California. The present study attempts to address these shortcomings to better quantify the climate impact on ground-level ozone and PM concentrations in California's major air basins.

1.3 Research Objectives

The overall objective of this research was to quantify and understand the impact of global climate change on regional air quality, especially on ozone and particulate matter (PM) concentrations in California. Special attention will be given to the spatial and temporal scales needed to fully characterize climate – air quality interactions in California. The research also analyzes the probable impact of climate change on health by quantifying population-weighted concentrations of PM. These objectives were achieved by analyzing

historical measurement data (1984-2004), simulating air quality for both the present-day (2000-06) and future (2047-2053) periods, and analyzing population-weighted concentrations over multiple years and during extreme events.

This report is comprised of 11 chapters, including introduction (Chapter 1) and conclusions (Chapter 11). Chapter 2 provides a preliminary assessment of climate impacts on air quality in California using a perturbation analysis during regional air pollution events.

Authors note: The work in chapter 2 has been published in the journal Climatic Change and may be cited in any future studies as "Kleeman, M.J. (2008), A preliminary assessment of the sensitivity of air quality in California to Global Change, Climatic Change 87 (Suppl1) p 273-292.

Chapter 3 provides an assessment of climate impacts on photochemical (ozone) pollution in Southern California by imposing climate-related forcing onto meteorological conditions experienced during a summer 2005 high-ozone time period.

Authors note: The work in chapter 3 has been published in the journal Atmospheric Chemistry and Physics and may be cited in any future studies as "Millstein, D.E. and R.A. Harley (2009) Impact of climate change on photochemical air pollution in Southern California, Atmospheric Chemistry and Physics, 9(11), p 3745-3754"

Chapter 4 presents a statistical down-scaling technique to quantify the impact of global climate change on daily 1-hr maximum ozone concentrations in California including a rigorous uncertainty analysis.

Authors note: The work in chapter 4 has been published in the Journal of Geophysical Research and may be cited in any further studies as "Mahmud, A., M. Tyree, D. Cayan, N. Motallebi, and M. J. Kleeman (2008), Statistical downscaling of climate change impacts on ozone concentrations in California, J. Geophys. Res., 113, D21103, doi:10.1029/2007JD009534"

Chapter 5 summarizes tests conducted with the Weather Research Forecast (WRF) model to determine the optimal configuration for dynamic climate downscaling exercises in California.

Authors note: The work of chapter 5 will be submitted to the journal Climate Change for publication and may be cited as "Zhao, Z. et al., The Impact of Climate Change on Air Quality Related Meteorological Conditions in California – Part I: Present Time Simulation Analysis, Climate Change, submitted" until accepted and published.

Chapter 6 summarizes the comparison between dynamic climate downscaling exercises in California between the years 2000-06 and 2047-53.

Authors note: The work of chapter 6 will be submitted to the journal Climate Change for publication and may be cited as "Zhao, Z. et al., The Impact of Climate Change on Air Quality Related Meteorological Conditions in California – Part II: Present versus Future Time Simulation Analysis, Climate Change, submitted" until accepted and published.

Chapter 7 contains the results of a dynamic down-scaling exercise of regional climate and air quality modeling for airborne fine particulate matter. The specific objective of this chapter was to quantify the climate impact on annual average fine particles ($PM_{2.5}$) using seven-year data for both present-day (2000-06) and future (2047-2053). The uncertainty associated with the prediction was estimated as well as the significance of the climate impact on annual mean results. Validation of the air quality model results was also part of the analysis.

Authors note: The work in chapter 7 has been published but not peer reviewed in Atmospheric Chemistry and Physics Discussions (ACPD) journal and is currently under review for publication in Atmospheric Chemistry and Physics (ACP). The work may be cited in any further studies as "A. Mahmud, M. Hixson, J. Hu, Z. Zhao, S. Chen and M. J. Kleeman, Climate impact on airborne particulate matter concentrations in California using seven year analysis periods, Atmospheric Chemistry and Physics Discussions, 10, 2985-3020, 2010" until published in ACP.

Chapter 8 includes an analysis of population-weighted particulate matter concentrations. The specific objective of this chapter was to understand the future climate change impact on public health through population-weighted annual average and extreme event concentrations of particles for California and three air basins: the Sacramento Valley air basin (SV), the San Joaquin Valley air basin (SJV) and the South Coast Air Basin (SoCAB).

Authors note: The work of chapter 8 will be submitted to Environmental Science and Technology (ES&T) journal for publication and may be cited as "Mahmud, A., Hixson, M., and Kleeman, M., J. 2010, Environmental Science and Technology, submitted" until accepted and published.

Chapter 9 repeats the analysis conducted in Chapters 7 and 8 using the emissions projected for the year 2050 instead of emissions for the year 2000. The results of this chapter determine if any non-linear chemical transformations influence the conclusions from the previous chapters.

Chapter 10 compares the effects of climate change and emissions changes between the years 2000-06 and 2047-53.

1.4 Scope of the Current Study

The computational burden associated with dynamic downscaling for analysis of air pollution concentrations is significant. Several simplifying assumptions are commonly applied by researchers studying climate-air quality interactions. Climate feedback effects

from the air pollution system on local meteorology (rain shadows, modified temperature structure, modified wind structure, etc) were not considered. Climate feedback effects from the air pollution system on cloud cover were not considered. Climate feedback effects from the air pollution system on land-cover (amount and type of vegetation) were not considered. The possible increase in random events such as wildfires due to climate change was not considered. Feedback effects between the capacity of transportation facilities and land-use policies that influence the growth of cities were not fully considered when allocating the spatial distribution of future emissions growth in California. An ensemble of GCM/RCM/CTM (chemical transport models) to fully quantify the uncertainty in the calculations was not considered.

Each of the feedback effects described above adds complexity and computation burden to the problem. While several models have attempted to address one or two of these issues, no modeling system to date has systematically demonstrated the ability to comprehensively simulate all feedback effects with comparison to measurements as validation. Furthermore, such models are prohibitively burdensome and could not be used to analyze ENSO periods in the current and future climate with a reasonable amount of computational resources. All of the simplifying assumptions listed above were used in the current study to enable a climate-air quality analysis at high spatial resolution needed for California's extreme topography spanning the multi-year periods needed to fully analyze ENSO signals.

Future studies funded by CARB and other agencies should continue to address inter-annual variability while at the same time considering feedback effects, especially as computational power continues to increase and new measurements provide reasonable datasets that can be used to evaluate model performance on feedback simulation.

2.0 A PRELIMINARY ASSESSMENT OF THE SENSITVITY OF AIR QUALITY IN CALIFORNIA TO GLOBAL CHANGE

2.1 Introduction

California's combination of large urban populations situated in confined air basins that are subject to severe air pollution events causes significant public health concerns. Ozone (O_3) and airborne particles with diameter smaller than 2.5 µm ($PM_{2.5}$) are two of the main ingredients of the photochemical "smog" that can form when atmospheric mixing is low, causing pollutants to be trapped near the earth's surface. The South Coast Air Basin and the San Joaquin Valley in California are the two air basins with the highest "smog" concentrations in the United States and they have a combined population greater than 15M. The adverse health effects of O_3 and $PM_{2.5}$ are widely acknowledged, and reducing the concentrations of these pollutants is an important objective for the State of California.

Changes in global population, economic development, energy consumption, and technology can have consequences for air quality in California. It is generally acknowledged that global consumption of fossil fuels has changed the earth's atmosphere in a way that will lead to sustained changes in regional meteorological patterns (ie. Climate Change) [22]. The severity of air pollution events in California is largely determined by the strength of atmospheric stagnation events that are driven by these regional-scale meteorological patterns. Thus, global change can influence air quality in California. As a second effect, atmospheric pollutants can be directly transported between countries and even between continents [23, 24] leading to increased "background" concentrations for both O_3 and $PM_{2.5}$. Background concentrations currently account for approximately 33% of the National Ambient Air Quality Standard (NAAQS) for O_3 [24] and 25% of the annual-average NAAQS for $PM_{2.5}$ in California [25]. Future changes in meteorology and background concentrations will influence the local actions that must be taken in California to reduce the concentration of O_3 and $PM_{2.5}$ to acceptable levels.

The purpose of this study was to investigate the sensitivity of present-day air quality in California to changes in meteorological conditions and background pollutant concentrations. Three air quality episodes were studied that span the full range of pollution conditions that commonly occur in California. The individual effect of each variable on O_3 and $PM_{2.5}$ concentrations was identified, and preliminary conclusions were made about the likely effect of global change on air quality in California.

2.2 Background

The relationship between climate and air quality can be studied using General Circulation Models (GCMs) coupled to chemistry calculations (see for example [13-16]). These calculations use grid cells that are larger than 1° (>100 km at mid latitudes), making them most appropriate for regional pollutants (such as O_3) in locations that do not have complex terrain (such as the eastern United States). The majority of these studies predict

that O_3 concentrations will increase in the future due to a combination of factors related to climate and emissions [13]. Finer spatial scales can be resolved by dynamically downscaling meteorology and coupling to a regional air quality model. Calculations for the eastern United States [26] and Europe [27] generally show that climate change will have a strong influence on surface O_3 concentrations.

Simulating the relationship between climate and $PM_{2.5}$ + O_3 in the western United States is difficult because the complex topography in this region results in sharper spatial gradients. A few studies have been performed to dynamically downscale meteorological predictions [28, 29] but these results have not yet been combined with chemical transport models. Perturbation studies can be used to identify the mechanistic response of pollutant concentrations to meteorological variables even when the full dynamics of the system are not completely known. Previous studies have examined the effect of temperature change on tropospheric O_3 concentrations in the eastern U.S. [30, 31], soil moisture change on O_3 and $PM_{2.5}$ concentrations in the western U.S.[32], and temperature change on O_3 and $PM_{2.5}$ concentrations in the western U.S. [33]. The present study will build on this previous work by conducting a rigorous sensitivity analysis of three separate air quality episodes that span the full range of conditions experienced in California.

2.3 Model Description

The UCD-CIT air quality model is a reactive chemical transport model that predicts the concentration of primary and secondary pollutants in the gas and particle phase in the presence of emissions, transport, deposition, chemical reaction, and phase change. Model calculations are initialized with measured concentrations and then allowed to evolve according to the governing equations for the system while enforcing boundary conditions at the edges of the model domain. Table 2-1 summarizes the lateral boundary conditions used during the current study. Previous studies [34-37] have described the formulation of the UCD/CIT source-oriented air quality model, and so only those aspects that differ for the current project are discussed here.

SJV Simulations

The gas-phase chemical mechanism used to model episodes in the SJV is based on the SAPRC90 [38] mechanism with extensions to predict the formation of 10 semi-volatile organic compounds [39]. The partitioning of semi-volatile organic species to the particle phase is calculated using an absorption model calibrated using surrogate species that have representative properties for the 10 lumped model compounds [40]. The temperature dependence of the surrogate species is estimated using the Classius Clapyron equation based on a literature survey of available thermodynamic data [33].

SoCAB Simulations

The Caltech Atmospheric Chemistry Model (CACM) [41, 42] was integrated into the UCD/CIT framework with several modifications. Ethane was tracked as an individual species so that an appropriate rate constant could be specified for reaction with hydroxyl radical. The thermodynamic data describing the equilibrium concentration of semi-volatile reaction products above the condensed aqueous phase [42, 43] was adapted to

work with the dynamic (non-equilibrium) treatment used in the UCD/CIT air quality model. A single subroutine was created to dynamically partition inorganic and organic species between the gas and particle phases. The method of Kusik and Meissner [44] was used to predict activity coefficients for inorganic species while the UNIFAC model [45] was used to predict activity coefficients for organic species. The vapor pressure of water above the particle surface was adjusted to account for organic and inorganic solutes. Water exchange between the gas and liquid phases was calculated as a dynamic process using equations described by Kleeman et al. [46].

Table 2-1: Lateral boundary conditions used during model simulations.

Pollutant	Lateral Boundary Concentration	Notes
CO	200 ppb	Interpolated value from measurements used in surface cells
CO2	332 ppb	
SO2	1 ppb	
NO2	1 ppb	0 ppb used on North boundary during Sept 7-9, 1993 simulation
NO	1 ppb	0 ppb used on North boundary during Sept 7-9, 1993 simulation
O3	30 ppb	0 ppb used on North boundary during Sept 7-9, 1993 simulation
RHC	7 ppb	0 ppb used on North boundary during Sept 7-9, 1993 simulation
HCHO / CCHO / RCHO	0 – 5 ppb	Exact value depends on measurements during episode
HNO3 / HCl / NH3		Interpolated from measurements during episode
PM Species		Interpolated from measurements during episode

2.4 Model Application

Calculations were performed for the air pollution episodes that occurred in the South Coast Air Basin (SoCAB) on September 7-9, 1993, in the SoCAB on September 23-25, 1996, and in the San Joaquin Valley (SJV) on January 4-6, 1996. The extensive meteorological, emissions, and air quality information needed to support detailed modeling of each episode has been assembled previously, and base-case modeling studies have validated the performance of air quality models used to simulate the formation of pollutant concentrations [34-37, 47-51]. Table 2-2 summarizes the focus pollutants used in each episode and the published studies describing those episodes. Table 2-3 summarizes the total emissions of oxides of nitrogen (NOx), volatile organic compounds (VOC), and particles with diameter smaller than 10 µm (PM_{10}) within the SoCAB and SJV during each air pollution episode.

Table 2-2: Air quality episodes to be studied with sensitivity analysis.

		Location	
		SoCAB	SJV
Focus Pollutant	O_3	Date: September 7-9, 1993 References: [47, 48]	Footnote a.
	PM	Date: September 23-25, 1996 References: [34, 37, 52]	Date: January 3-5, 1996 References: [35, 36, 50, 51]

a. Sensitivity analysis of O3 response to climate change in the SJV is being conducted as part of a separate project funded by the US EPA at UC Berkeley.

SoCAB September 7-9, 1993: Daytime surface temperatures exceeded 35°C at inland locations and a strong elevated temperature inversion formed. Light surface winds followed the land-sea breeze pattern with onshore flow during the day and stagnation at night. Upper level winds originated from the north – north west of the modeling domain (over land). Measured O_3 concentrations exceeded 250 ppb, while 3-hr average $PM_{2.5}$ concentrations reached 90 µg m^{-3}.

SoCAB Septembr 23-25, 1996: Temperatures at inland locations were moderate with peak daytime values reaching 25°C. Winds were light onshore during the day and stagnant during the evening. The total time required for air parcels to traverse the study region from west to east was calculated to be greater than 3 days. Peak O_3 concentrations were generally less than 100 ppb while $PM_{2.5}$ concentrations measured at Riverside between the hours of 1400-1700 PST exceeded 75 µg m^{-3}.

SJV January 4-6, 1996: Temperatures ranged between 0°C at night to 10-15°C during the day. O_3 concentrations were less than 40 ppb, reflecting the low photochemical activity during winter pollution events in the SJV. Regional particulate nitrate concentrations built up to high levels during the stagnation event. Local emissions of carbonaceous aerosol also develop around urban areas. Measured PM_{10} concentrations during the episode reached 150 µg m^{-3} during the evening hours, with the majority of that material in the $PM_{2.5}$ size range.

Table 2-3: Emissions summary for the air quality episodes described in Table 2-2.

	NOx (tons day^{-1})	VOC (tons day^{-1})	PM10 (tons day^{-1})
SoCAB Sept 7, 1993	1066	1828	529
SoCAB Sept 23, 1996	929	1219	381
SJV, Jan 6, 1996	526	447	187

Perturbations: Temperature perturbations +2K and +5K were considered during the sensitivity analysis (air temperature only, ground temperature and sea surface temperature are not used in the simulation). These values span the range of IPCC projections for global mean surface temperature rise over the next 100 years. Humidity perturbations were coordinated with temperature to avoid artificially specifying an atmosphere with RH>100%. Each temperature perturbation was evaluated once with no change to absolute humidity and once with no change to relative humidity. Perturbations in mixing depth considered in this study were chosen to be +50%. Mixing depth perturbations were carried out without changes to air temperature even though this is a highly artificial case. The sensitivity to mixing depth by itself reveals the effect of dilution separately from the effect of temperature on reaction rates.

Perturbations to wind speed were not considered in the present study. Although wind speed is expected to change in concert with other meteorological parameters, the appropriate direction and level of perturbation is not obvious. One recent study suggests that higher soil moisture content leads to decreased wind speed in Los Angeles[32], but future trends in soil moisture are also not known.

Long term trends in O_3 concentrations are currently being studied by many researchers. The weight of preliminary evidence suggests that background O_3 concentrations will increase from approximately 30 ppb to 60 ppb in the next 50 to 100 years [24]. In the current study, perturbations of background O_3 concentrations were chosen to simulate a doubling of global background O_3 concentrations to approximately 60 ppb.

2.5 Results

Figure 2-1 (a) shows the predicted regional pattern of 1hr-average O3 concentrations on September 9, 1993 at 1500 PST. A band of high O3 concentrations occurs along a line connecting Claremont, Riverside, and Perris, with the highest predicted concentrations reaching 290 ppb at Perris. Regional concentrations of O3 over the entire modeling domain are large during the episode, approaching 90 ppb. Predicted O3 concentrations in the region immediately downwind of Central Los Angeles are slightly lower than the regional average because they are suppressed by emissions of fresh NOX.

Figures 2-1 (b) and (c) show the predicted increase in regional O3 concentrations at 1500 PST on September 9, 1993 when temperature is uniformly perturbed at all times and locations by +5 K and +2 K, respectively. O3 concentrations along the line connecting Claremont, Riverside, and Perris increase by approximately 18 – 40 ppb in response to this change. Regional O3 concentrations at other locations increase by 4 - 14 ppb. Small regions with a ~1 - 3 ppb decrease are also observed, but these effects are minor compared to increases at other locations.

The underlying cause for the increase in O3 concentrations at hotter temperatures can be diagnosed by looking at the speciation of nitrogen compounds. Table 2-4 shows the

relative change to the concentration of O3, hydroxyl radical (OH), total reactive nitrogen (RN), and various forms of reactive nitrogen at locations in the SoCAB at 1500 PST on September 9, 1993 in response to a +5 K temperature perturbation. O3 concentrations at these locations increase by 3-22% in response to the temperature change. The locations with the largest increase in O3 concentrations (in the eastern end of the SoCAB) also have significant increases in hydroxyl radical (OH) concentrations. OH reacts with NO to form HONO. HONO further reacts with OH to form NO2 or it can decomposes in the presence of sunlight to yield 90% NO and 10% NO2. The net decrease in HONO concentrations evident in Table 2-4 suggests that the reaction with OH is more significant. Under either scenario, the enhanced OH concentrations convert NO to NO2 leading to increased O3 concentrations.

Table 2-4: Relative change in composition for O3, hydroxyl radical (OH), total reactive nitrogen (RN), and various forms of reactive nitrogen at 1500 PST on September 9, 1993 caused by a +5 K temperature perturbation. PN is particulate nitrate.

	O_3	OH	RN	NO	NO_2	NO_3	N_2O_5	HONO	HNO_3	HNO_4	PAN	PN
LGBH	1.04	0.96	0.99	0.93	1.02	1.3	0.71	0.87	1.01	0.53	0.36	0.65
CELA	1.03	0.99	1.00	0.94	1.03	1.27	0.76	0.92	0.99	0.58	0.42	0.34
AZUS	1.22	1.20	0.97	0.79	1.01	1.80	0.86	0.93	1.04	0.84	0.76	0.38
CLAR	1.15	1.16	0.96	0.81	0.99	1.58	0.98	0.93	1.02	0.76	0.72	0.36
PERI	1.12	1.08	0.94	0.91	1.07	1.43	0.88	1.00	0.95	0.69	0.66	0.47

Table 2-5: Relative change in composition for O3, hydroxyl radical (OH), total reactive nitrogen (RN), and various forms of reactive nitrogen at 1500 PST on September 25, 1996 caused by a +5K temperature perturbation. PN is particulate nitrate.

	O_3	OH	RN	NO	NO_2	NO_3	N_2O_5	HONO	HNO_3	HNO_4	PAN	PN
LGBH	1.03	0.89	0.99	0.94	1.02	1.25	0.68	0.87	1.07	0.47	0.31	0.78
CELA	1.03	1.03	0.98	0.91	1.01	1.29	0.69	0.92	1.13	0.57	0.47	0.64
AZUS	1.06	1.09	1.00	0.91	1.02	1.36	0.75	0.96	1.15	0.64	0.57	0.28
CLAR	1.06	1.11	1.02	0.92	1.03	1.36	0.75	0.98	1.20	0.65	0.61	0.26

Table 2-6: Relative change in composition for O3, hydroxyl radical (OH), total reactive nitrogen (RN), and various forms of reactive nitrogen at 1500 PST on January 6, 1996 caused by a +5K temperature perturbation. PN is particulate nitrate.

	O_3	RN	NO	NO_2	NO_3	N_2O_5	HONO	HNO_3	HNO_4	PAN	PN
FEI	1.19	1.00	0.83	1.05	1.73	0.96	0.87	1.59	0.73	0.62	0.23
KWR	1.19	1.01	0.96	1.23	1.75	1.17	1.09	3.64	0.75	0.72	0.88

Large relative increases are observed in the concentration of nitrate radical (NO3) at hotter temperatures, but NO3 constitutes only a minor fraction of total reactive nitrogen. The concentration of nitric acid (HNO3) is also enhanced at several locations when temperature is increased partially due to the reaction of increased OH concentrations with NO2 and partly due to the evaporation of particulate nitrate (PN). All the reactive nitrogen species that undergo thermal decomposition reactions (N2O5, HNO4, PAN, PN) have reduced concentrations at hotter temperatures as shown in Table 2-4. PAN concentrations summarize the net effect of all PAN-like species in the calculation. Many of these compounds decompose to form NO2, but the resulting increase in NO2 concentrations (-1 to + 7%) is smaller than the decrease in NO concentrations (-6 to -21%) suggesting that the effect of increased hydroxyl radical concentrations is more significant than the thermal decomposition of various reactive nitrogen compounds. Total reactive nitrogen concentrations change by up to 6% because the different forms of reactive nitrogen have different loss rates.

Figure 2-1 (d) shows the change in predicted regional O3 concentrations at 1500 PST on September 9, 1993 when temperature is uniformly perturbed by +5 K with no change to relative humidity. Basecase inland absolute humidity concentrations at 1500 PST are on the order of 15-20 ppth (parts per thousand) yielding relative humidity that ranges from 30-70%. When temperature is increased without adjusting absolute humidity, the relative humidity decreases. Given the proximity of the SoCAB to the Pacific Ocean, relative humidity may stay constant as temperature increases, leading to an effective increase in absolute humidity. The results in Figure 2-1 (d) can be compared to Figure 2-1 (b) which applied a +5 K temperature perturbation with no change to absolute humidity. The spatial distribution of increased O3 concentrations shown in Figure 2-1 (d) matches that shown in Figure 2-1 (b), but the magnitude of the predicted concentration increase is 67 ppb (vs. 40 ppb for the case with lower humidity). The increase in O3 concentrations associated with higher concentrations of water vapor is caused by the production of hydroxyl radical from H2O.

Figure 2-1 (e) shows the change in predicted regional O3 concentrations at 1500 PST on September 9, 1993 in response to a uniform increase in mixing depths of +50%. The increased mixing depth leads to an increase in predicted O3 concentrations in the western portion of the model domain by 75 ppb and a decrease in predicted O3 concentrations in the eastern portion of the model domain by 36 ppb. Increased mixing depth reduces the concentration of primary pollutants such as oxides of nitrogen (NOx). Reduced NOx concentrations can promote higher O3 concentrations in regions where there is an over abundance of NOx. The location of the maximum concentration increase differs slightly from the location of the predicted O3 maximum in the base-case simulation, and so the net effect of the increased mixing depth is to slightly increase the maximum O3 concentrations predicted during the episode and to increase the size of the region experiencing those maximum concentrations. The relationship between increased mixing depth and higher O3 concentrations during severe photochemical episodes in the SoCAB has been noted previously during simulations of the Southern California Air Quality Study (SCAQS) [39].

Figure 2-1 (f) shows the change in predicted regional O3 concentrations at 1500 PST on September 9, 1993 in response to a +5 K temperature perturbation with no changes to relative humidity when background O3 concentrations are increased from 30 ppb to 60 ppb. This result can be directly compared to Figure 2-1 (d) to view the effect of increased background O3 concentrations. The additional 30 ppb of background O3 increases regional O3 concentrations by approximately 30 ppb but maximum O3 concentrations are increased by approximately 46 ppb.

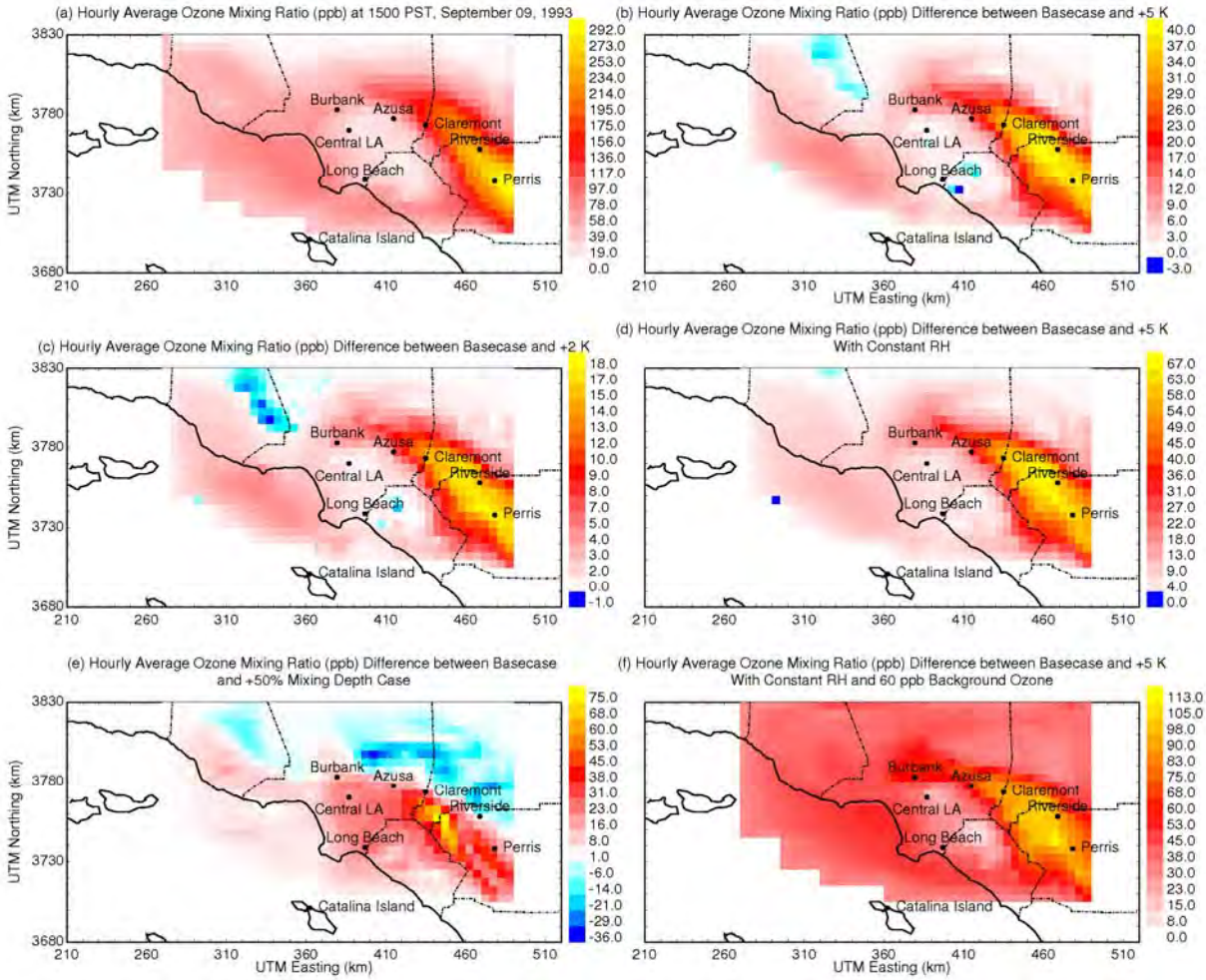

Figure 2-1: Basecase O_3 concentration at 1500 PST on September 9, 1993 (panel a) and sensitivity of O_3 concentration to (b) +5 K temperature change with constant absolute humidity, (c) +2 K temperature change with constant absolute humidity, (d) +5 K temperature change with constant relative humidity, (e) +50% increase in mixing depth, and (f) + 5K temperature change with constant relative humidity and increase in background O_3 from 30 ppb to 60 ppb.

Figure 2-2 (a) shows the predicted regional pattern of 24-hr average PM2.5 concentrations on September 9, 1993. The largest PM2.5 concentration of 194 µg m-3 is predicted to occur in the region west of Riverside where ammonia concentrations are very large leading to enhanced formation of particulate ammonium nitrate. The predicted concentration of PM2.5 at most other locations in the inland portion of the modeling

domain is 70-90 µg m-3. The hot base-case temperatures during the current episode suppress the formation of large regions of particulate nitrate, since increasing temperature encourages nitrate evaporation [15].

Figures 2-2 (b) and (c) show the predicted change in regional PM2.5 concentrations on September, 1993 when temperature is uniformly perturbed by +5 K and +2 K, respectively, at all times and locations. PM2.5 concentrations in the region east of Riverside decrease by 14 to 31 µg m-3 in response to this change. The majority of this reduction is associated with the volatilization of particulate ammonium nitrate as temperature increases. The location west of Riverside with the highest base-case concentration of particulate nitrate (see Figure 2-2a) does not experience the largest reduction in PM2.5 concentrations because regions with higher excess gas-phase ammonia concentrations respond less strongly to increased temperature than regions with lower excess gas-phase ammonia [15]. Figures 2-2 (b) and (c) also show that regional average PM2.5 concentrations are predicted to decrease by 3 to 15 µg m-3 in response to the +2 K and +5 K temperature perturbations. Once again, this change is caused by the partitioning of semi-volatile species to the gas phase at hotter temperatures, with particulate ammonium nitrate being the largest contributor to this effect. The region around the Long Beach harbor experiences a 0.2 µg m-3 increase in PM2.5 concentrations in response to a +2 K temperature perturbation. Increased temperature promotes the oxidation of SO2 emissions in this region to form sulfuric acid. Sulfur acid is essentially non-volatile at all ambient temperatures, and so this species partitions to the particle phase regardless of temperature perturbation.

Figure 2-2 (d) shows the change in predicted regional PM2.5 concentrations on September 9, 1993 when temperature is uniformly perturbed by +5 K with no changes to relative humidity. This figure can be compared to Figure 2-2 (b) which applied a +5 K temperature perturbation with no changes to absolute humidity. Maintaining relative humidity will maintain the amount of particle-phase water, leading to enhanced partitioning of water-soluble semi-volatile species. The reductions in particulate matter mass apparent in Figure 2-2 (b) are caused by the combined effect of increased temperature and reduced particle water content while the reductions in particulate matter mass shown in Figure 2-2 (d) are only caused by temperature. The region immediately west of Riverside experiences no decrease in PM2.5 concentrations when temperature is increased by +5 K with no change to relative humidity, and one grid cell (5km*5km area) even experiences a 2 µg m-3 increase PM2.5 concentrations. The effect of temperature on particulate ammonium nitrate evaporation is moderated in regions with extremely high ammonia concentrations [15]. The area east of Riverside still experiences a decrease of PM2.5 concentrations by approximately 19 µg m-3, but this is moderated from the decrease of 36 µg m-3 predicted in the case with lower humidity. The reduction in regional average PM2.5 concentrations in response to a +5 K increase in temperature is also moderated when relative humidity is maintained. Most inland regions experience a decrease in predicted PM2.5 concentrations of 1 to 7 µg m-3, with slight increases predicted in the region around the Long Beach Harbor, and the Los Angeles International Airport. The regional increases in PM2.5 at these locations are once again associated with the enhanced production of sulfate aerosol from SO2 emissions.

Figure 2-2 (e) shows the change in predicted regional PM2.5 concentrations on September 9, 1993 in response to a uniform increase in mixing depth of +50%. The maximum increase in PM2.5 concentrations in response to this change is 5 µg m-3 in the region that experienced the largest increase in O3 concentrations (see Figure 2-1e). Predicted PM2.5 concentrations in the region to the east of Riverside are reduced by 9 µg m-3 as the plume of enhanced nitrate is diluted by the increased mixing depth.

Figure 2-2 (f) shows the change in predicted PM2.5 concentrations on September 9, 1993 in response to a +5 K temperature perturbation with no change to relative humidity when background O3 concentrations are increased from 30 ppb to 60 ppb. This result can be directly compared to Figure 2-2 (d) to view the effect of increased background O3 concentrations. Increased background O3 concentrations lead to increased PM2.5 concentrations through the production of additional particulate nitrate via the formation of N2O5 at night. The results illustrated in figure 2-2 (f) show that a 30 ppb increase in background O3 concentrations in the presence of a +5 K uniform temperature perturbation with no change to relative humidity leads to +5 to +8 µg m-3 increase in PM2.5 concentrations near the Long Beach harbor and a +10 to +21 µg m-3 increase in PM2.5 concentrations west of Riverside. Concentrations in other parts of the domain still decrease by -3 to -13 µg m-3 in the presence of the +5 K temperature perturbation (despite the increased background O3).

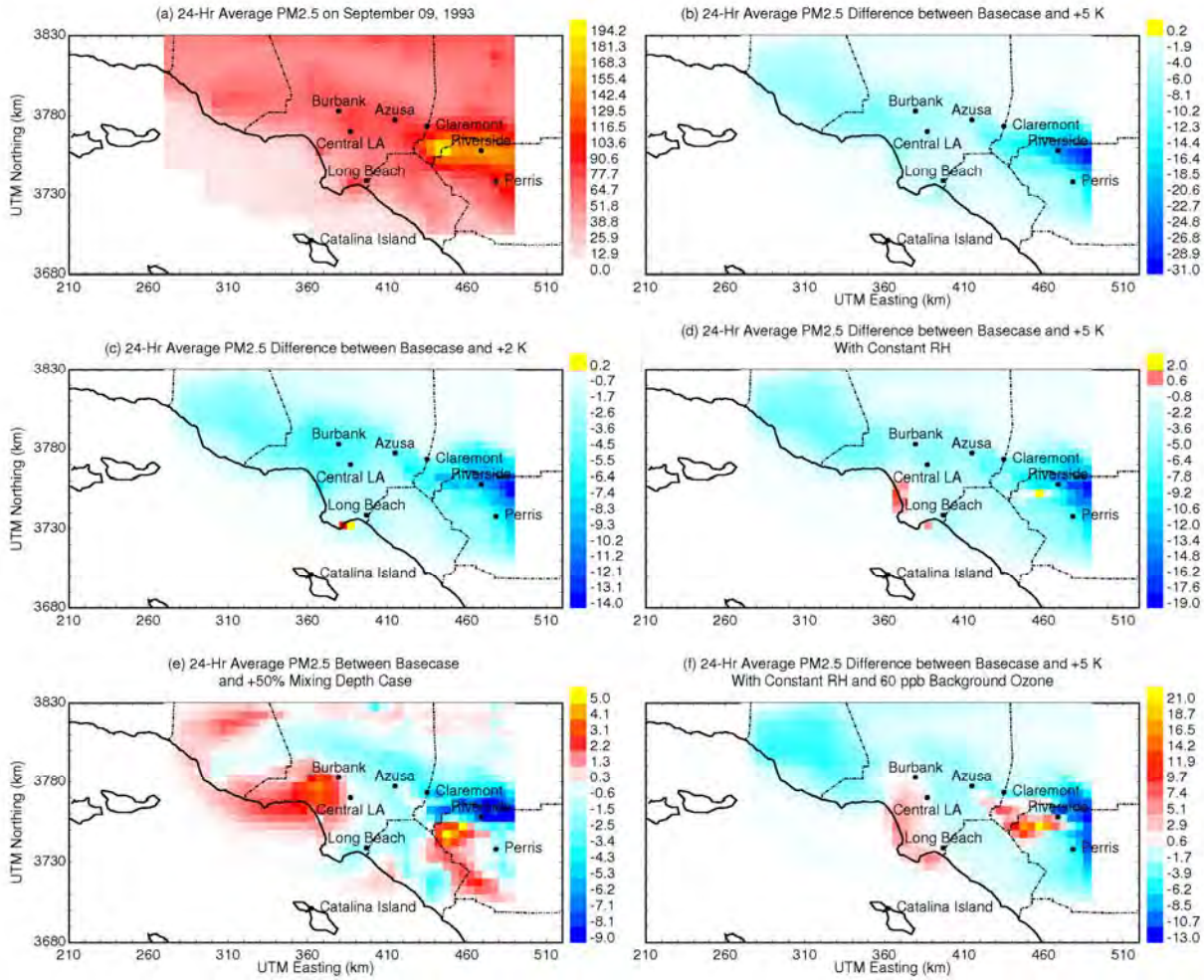

Figure 2-2: Basecase $PM_{2.5}$ concentration on September 9, 1993 (panel a) and sensitivity of $PM_{2.5}$ concentration to (b) +5 K temperature change with constant absolute humidity, (c) +2 K temperature change with constant absolute humidity, (d) +5 K temperature change with constant relative humidity, (e) +50% increase in mixing depth, and (f) + 5K temperature change with constant relative humidity and increase in background O_3 from 30 ppb to 60 ppb.

Figures 2-3 and 2-4 illustrate the predicted effect of temperature, humidity, and mixing depth perturbations on O3 and PM2.5 concentrations in the SoCAB on September 25, 1996. The format used in Figures 2-3 and 2-4 is identical to the format of Figures 2-1 and 2-2. Figure 2-3(a) shows that the highest predicted 1hr-average O3 concentration on September 25, 1996 at 1500 PST is 120 ppb in the northeast corner of the domain that is downwind of the major emissions sources during this event. Concentrations immediately downwind of central Los Angeles are once again slightly lower than the regional average because they are suppressed by emissions of fresh NOx. Maximum predicted O3 concentrations in this region are 70-80 ppb. Figure 2-4(a) shows that the largest basecase 24-hr average PM2.5 concentrations of 125 µg m-3 are predicted to occur in the region west and northeast of Riverside where ammonia concentrations are very large leading to

enhanced formation of particulate ammonium nitrate. The predicted concentration of PM2.5 at most other locations in the inland portion of the modeling domain is 40-80 µg m-3 on September 25, 1996. The moderate base-case temperatures during the current episode allow for the formation of significant quantities of particulate ammonium nitrate throughout the study region.

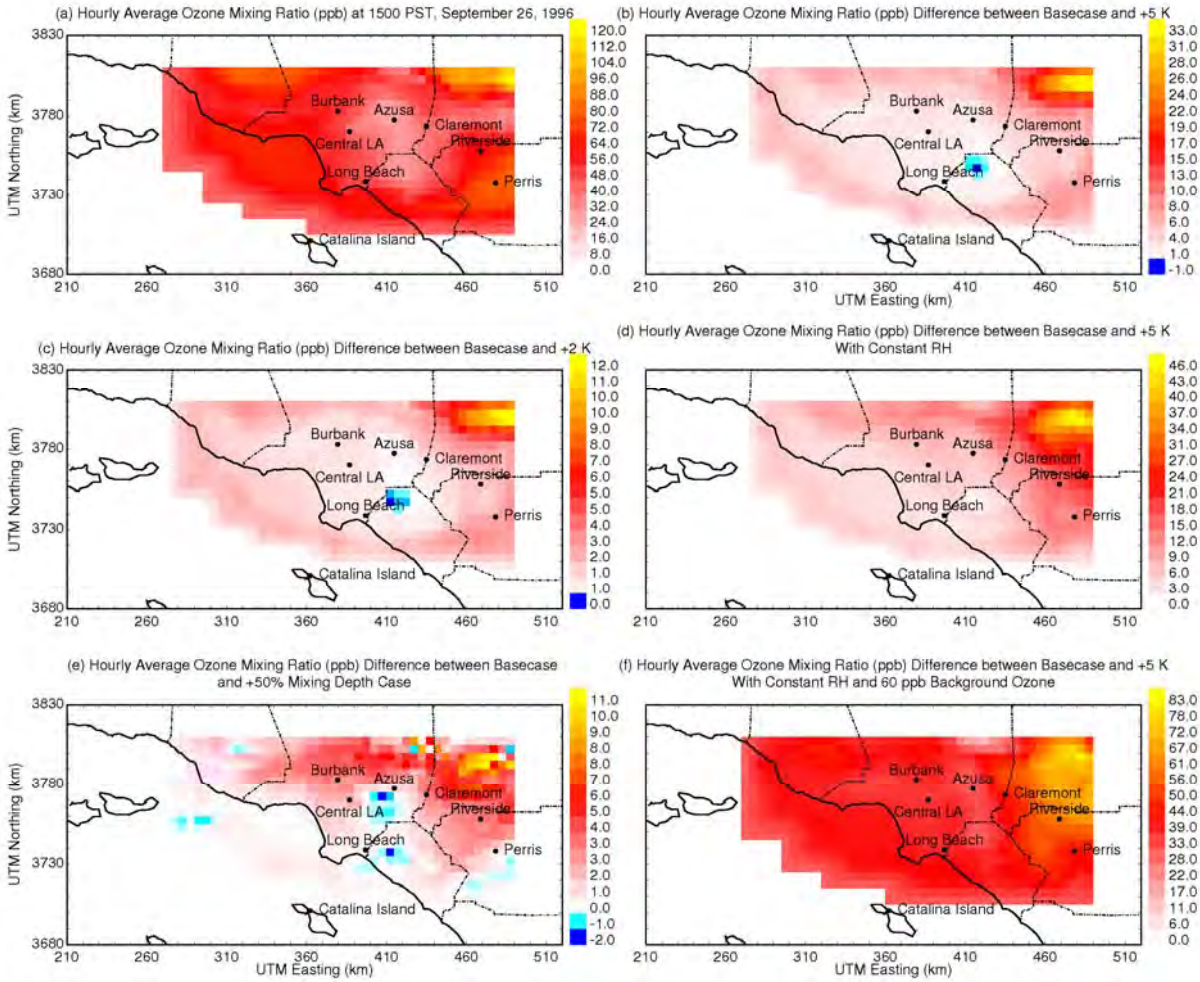

Figure 2-3: Basecase O_3 concentration at 1500 PST on September 25, 1996 (panel a) and sensitivity of O_3 concentration to (b) +5 K temperature change with constant absolute humidity, (c) +2 K temperature change with constant absolute humidity, (d) +5 K temperature change with constant relative humidity, (e) +50% increase in mixing depth, and (f) + 5K temperature change with constant relative humidity and increase in background O_3 from 30 ppb to 60 ppb.

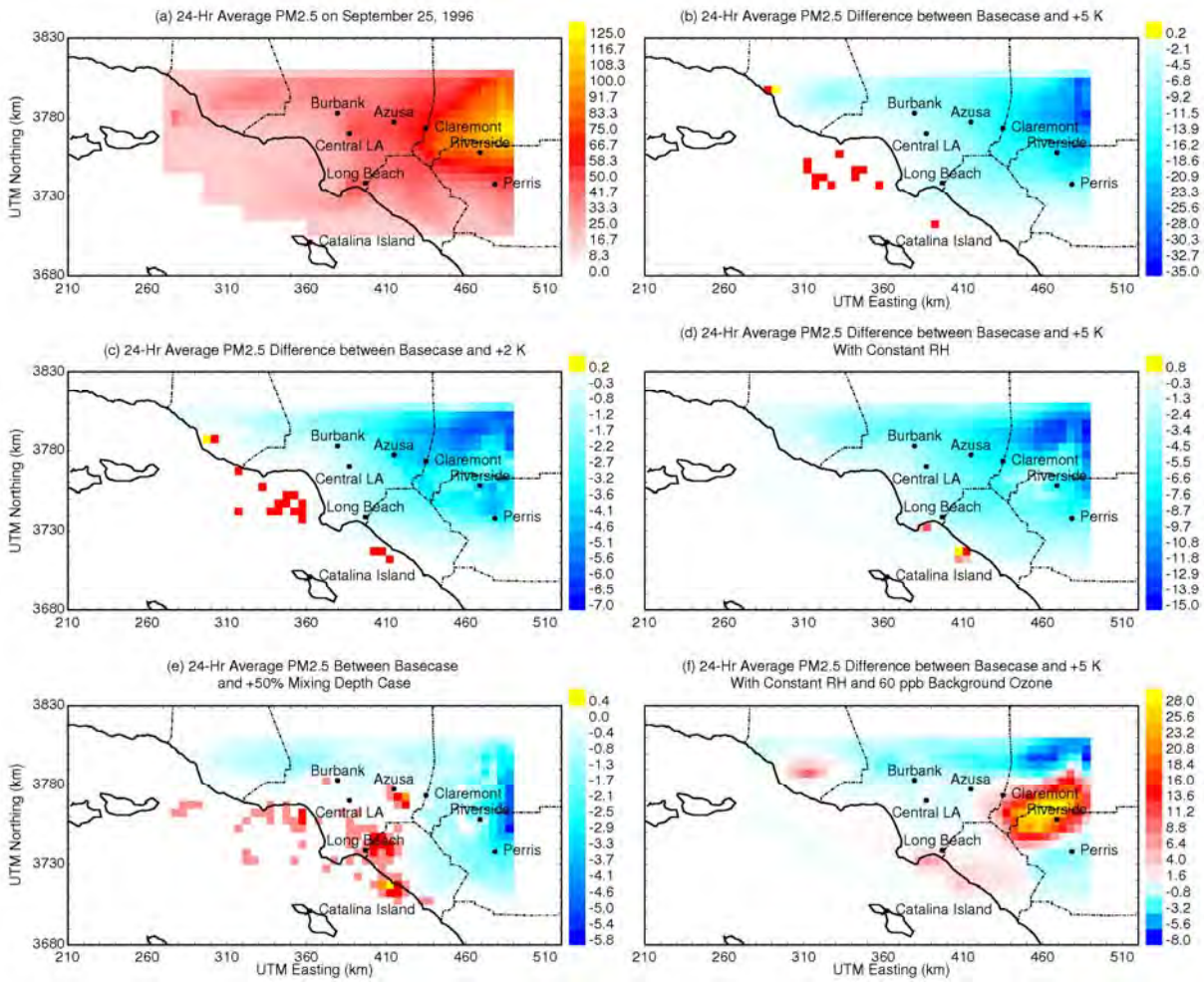

Figure 2-4: Basecase $PM_{2.5}$ concentration on September 25, 1996 (panel a) and sensitivity of $PM_{2.5}$ concentration to (b) +5 K temperature change with constant absolute humidity, (c) +2 K temperature change with constant absolute humidity, (d) +5 K temperature change with constant relative humidity, (e) +50% increase in mixing depth, and (f) + 5K temperature change with constant relative humidity and increase in background O_3 from 30 ppb to 60 ppb.

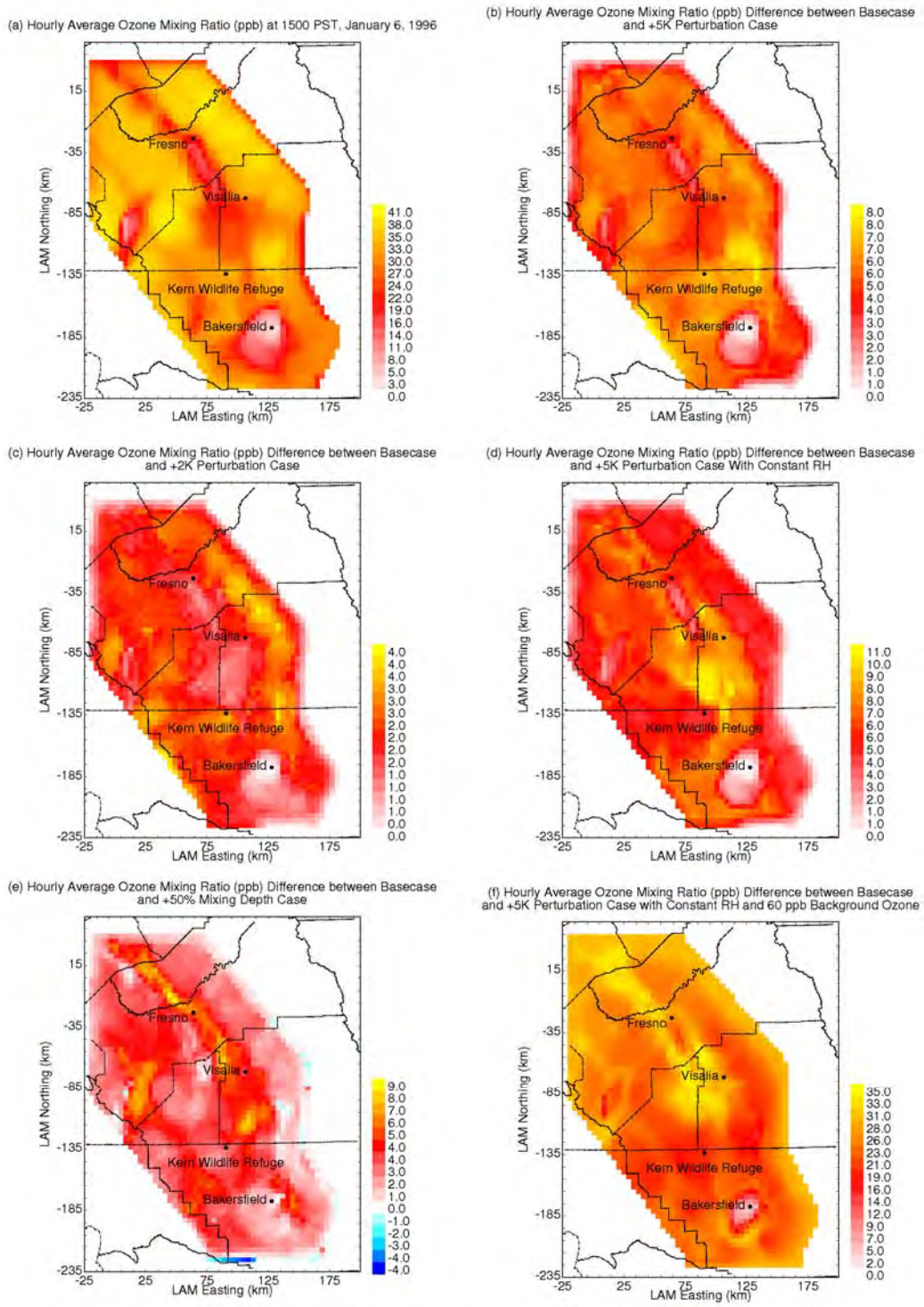

Figure 2-5: Basecase O_3 concentration at 1500 PST on January 6, 1996 (panel a) and sensitivity of O_3 concentration to (b) +5 K temperature change with constant absolute humidity, (c) +2 K temperature change with constant absolute humidity, (d) +5 K temperature change with constant relative humidity, (e) +50% increase in mixing depth, and (f) + 5K temperature change with constant relative humidity and increase in background O_3 from 30 ppb to 60 ppb.

The predicted changes in O3 and PM2.5 concentrations in response to changes in meteorological variables and background O3 is shown in Figures 2-3 (b-f) and 2-4(b-f) for September 25, 1996. In all cases, the qualitative behavior of O3 and PM2.5 on September 9, 1993 (Figures 2-1 and 2-2) and September 25, 1996 (Figures 2-3 and 2-4) are similar. Increased temperature results in higher predicted peak O3 concentrations and lower predicted peak PM2.5 concentrations (Figures 2-3b,c; Figures 2-4b,c). Increased humidity below the saturation threshold results in higher predicted peak O3 and PM2.5 concentrations (Figure 2-3d; Figure 2-4d). The magnitude of the positive humidity effect on PM2.5 concentrations was generally smaller than the negative temperature effect. Increased mixing depth produced mixed results: O3 and secondary PM22.5 increased in regions with excess NO while primary PM2.5 and O3 in regions without excess NO decreased (Figure 2-3e; Figure 2-4e). The magnitude of the effect caused by mixing depth was smaller on September 25, 1996 than September 9, 1993 because basecase mixing depths were larger during the 1996 episode. Increased background O3 produced higher peak concentrations of O3 and PM2.5 inside the SoCAB (Figure 2-3f; Figure 2-4f). The magnitude of the positive effect on PM2.5 caused by background O3 was greater than the negative effect caused by a +5K temperature perturbation.

Table 2-5 shows the relative change in O3, hydroxyl radical (OH), total reactive nitrogen (RN), and various forms of reactive nitrogen in response to a +5 K temperature perturbation on September 25, 1996. The trends illustrated in Table 2-5 (September 1996) are similar to those shown in Table 2-4 (September 1993) but the magnitude of the changes are smaller. O3 concentrations increase by 3-6%, largely due to a decrease in the concentration of NO by 6-9%. The apparent cause for the decrease in NO concentrations is an increase in OH that favors the production of NO2 and HNO3.

Figure 2-5 (a) shows the regional distribution of 1hr-average O3 concentrations in the SJV at 1500 PST on January 6, 1996. Peak O3 concentrations are 41 ppb across a wide portion of the study domain except in regions with large NOx emissions where the O3 concentrations are titrated to very low values. The O3 suppression associated with the Highway 99 transportation corridor connecting Fresno, Visalia, and Bakersfield is clearly visible in this plot. Previous studies have noted that the excess NOx in the emissions inventory around Bakersfield appear to contradict measured concentrations in the region [18, 40]. Results in the area around Bakersfield are likely incorrect, but results for the remainder of the domain agree well with measurements and should be accurate. Figure 2-6 (a) shows the regional distribution of 24-hr average PM2.5 concentrations in the SJV on January 6, 1996. Peak PM2.5 values reach 95 µg m-3 around the urban locations of Fresno and Bakersfield due to the accumulation of wood smoke and other combustion particles combined with a regional background of ammonium nitrate particles peaking close to Visalia [18, 37].

Figures 2-5(b-f) illustrate the predicted change in O3 concentrations in the SJV on January 6, 1996 in response to changes in meteorological parameters. The qualitative behavior of the SJV system shown in Figures 2-5 matches the predicted behavior of the SoCAB illustrated in Figures 2-1 and 2-3. Hotter temperatures enhance predicted local

O3 formation (Figure 2-5b,c) as does increased humidity below the saturation threshold (Figure 2-5d). Increased mixing depths produces higher O3 concentrations in regions with transportation corridors that have an excess of fresh NO emissions (Figure 2-5e). Higher concentrations of background O3 directly increased the O3 concentrations within the SJV (Figure 2-5f).

Figures 2-6(b-f) illustrate the predicted change in PM2.5 concentrations in the SJV on January 6, 1996 when meteorology is perturbed. Once again, the qualitative behavior of the SJV system is similar to that observed in the SoCAB (compare Figure 2-6 with Figures 2-2 and 2-4). Hotter temperatures reduce predicted PM2.5 concentrations due to the evaporation of NH4NO3 (Figure 2-6b,c) The region immediately south of Visalia does not experience a large decrease in PM2.5 concentrations because NH3 emissions in this region are very large, reducing the sensitivity of NH4NO3 to temperature. Increased humidity acted in the opposite direction as temperature because higher humidity increased the liquid water content of airborne particles which in turn promoted particulate NH4NO3 formation. Maintaining RH in the presence of a +5K temperature perturbation produced increased PM2.5 concentrations in the region with the highest NH3 emissions (Figure 2-6d). In the region immediately south of Visalia, an 8 µg m-3 increase in PM2.5 concentrations is predicted to occur when relative humidity is constant and temperature increases by 5 K. The base temperature is low in the winter conditions during the current study, reducing the sensitivity of ammonium nitrate to temperature increases. The increase of temperature south of Visalia increases the formation rate of nitric acid faster than it increases the volatility of ammonium nitrate aerosol, leading to higher predicted PM2.5 concentrations. It should be noted that the location of the maximum increase is slightly south of the maximum base-case concentrations. The net effect of this temperature increase is to expand the region of maximum PM2.5 concentrations during the current study. Other locations in the SJV with lower amounts of excess gas-phase ammonia experience a decrease in PM2.5 concentrations of 4.6 µg m-3 in response to a +5 K temperature perturbation even when relative humidity remains constant.

Table 2-6 shows the relative change in O3, hydroxyl radical (OH), total reactive nitrogen (RN), and various forms of reactive nitrogen in response to a +5 K temperature perturbation on January 6, 1996. Once again, the increased temperature changes the speciation of reactive nitrogen, leading to decreased concentrations of NO and increased concentrations of NO2. O3 concentrations at Fresno (FEI) and Kern Wildlife Refuge (KWR) both increase by 19%, but at Fresno the change is largely driven by a decrease in NO while at Kern Wildlife Refuge the change is largely driven by an increase in NO2 concentrations. This difference in behavior is likely caused by the fact that Fresno is an urban city while Kern Wildlife Refuge is a remote location. The fresh emissions at the urban location result in behavior that matches the trends observed in the South Coast Air Basin (see Tables 2-4 and 2-5).

Figure 2-6 (e) shows the change in predicted regional PM2.5 concentrations on January 6, 1996 in response to a uniform increase in mixing depths of +50%. Predicted PM2.5 concentrations immediately north of Bakersfield increase by +4.6 µg m-3 in response to the increased mixing depth because the diluted NOx concentrations form more nitric acid

which interacts with the ammonia plume just north of that location. As noted previously, the high NOx emissions in the Bakersfield region are an artifact of the emissions inventory used in the current study, and so this increase in concentrations is likely also an artifact. PM2.5 concentrations at locations farther north in the domain are predicted to undergo slight decreases or increases associated with the enhanced mixing of pollutants aloft to the surface.

Figure 2-6 (f) shows the change in predicted regional PM2.5 concentrations on January 6, 1996 when background O3 concentrations are increased from 30 ppb to 60 ppb while temperature is uniformly increased by 5 K with no changes in relative humidity. The formation of particulate nitrate via the nighttime reaction of N2O5 is particularly important during winter SJV episodes, and so the PM2.5 concentrations respond strongly to background O3. The entire central portion of the study domain is predicted to experience a +5 to +20 µg m-3 increase in PM2.5 concentrations under these conditions. The largest increase occurs near Visalia where ammonia concentrations are large.

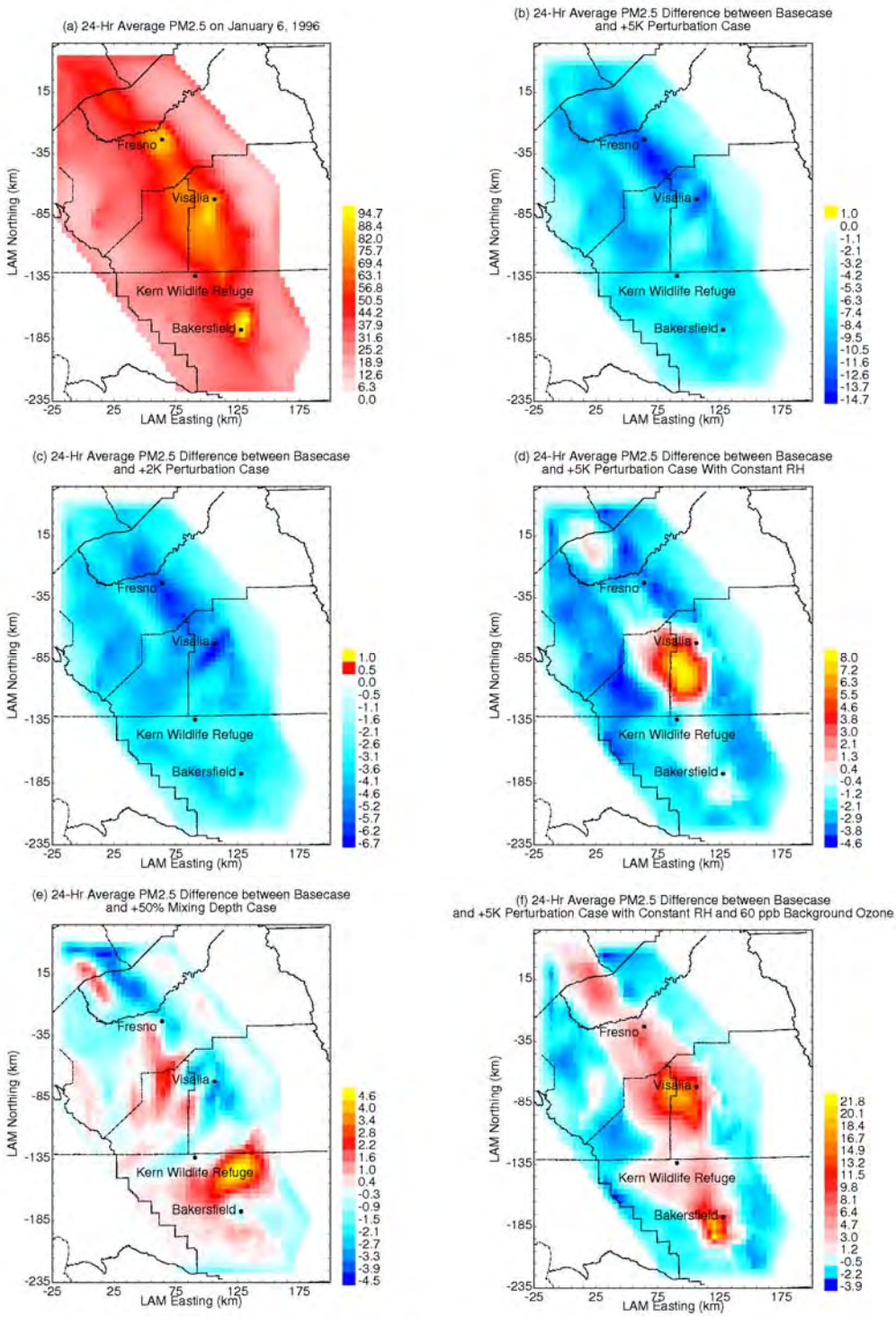

Figure 2-6: Basecase $PM_{2.5}$ concentration on January 6, 1996 (panel a) and sensitivity of $PM_{2.5}$ concentration to (b) +5 K temperature change with constant absolute humidity, (c) +2 K temperature change with constant absolute humidity, (d) +5 K temperature change with constant relative humidity, (e) +50% increase in mixing depth, and (f) + 5K temperature change with constant relative humidity and increase in background O_3 from 30 ppb to 60 ppb.

2.6 Discussion

Figure 2-7 summarizes the range of changes in predicted O3 and PM2.5 concentrations resulting from all the meteorological perturbations considered in the current study when background O3 concentrations are set equal to 60 ppb (approximately double present-day conditions). The bars shown in Figure 2-7 illustrate the largest change in pollutant concentrations predicted anywhere in the domain, while the circles illustrate the change in the maximum concentrations. When the circles are located close to the extreme values of the bars, it shows that the greatest change in concentration occurs at the location of maximum concentration.

Figure 2-7 shows that increasing temperature with no change in absolute humidity generally increases peak O3 concentrations in all the episodes studied. PM2.5 concentrations decrease in some parts of the study domain, but peak concentrations generally increase during all of the episodes studies, largely because the the temperature effect (reducing PM2.5 formation) is overwhelmed by the effect of background O3 (promoting PM2.5 formation). Increasing temperature with no change to relative humidity increases predicted O3 concentrations even further due to the enhanced production of hydroxyl radical. The increased humidity also mitigates the reduction in PM2.5 concentrations leading to greater increases, especially in the SJV in regions with large excesses of gas-phase ammonia and cooler basecase temperatures.

Figure 2-7 generally shows that increasing mixing depths usually increases surface O3 concentrations because the extra volume allows for increased dilution of fresh NOx emissions, reducing the titration of surface O3 concentrations. This effect may not be significant at the location of maximum O3 concentration. The increased mixing depth also usually reduces primary PM2.5 concentrations through increased dilution. Secondary PM2.5 can increase as mixing depth rises due to the same chemistry that enhances O3 formation under these conditions. The effect of mixing depth on PM2.5 concentrations is generally smaller than the effect of background O3, which promotes enhanced PM2.5 concentrations.

Emissions of NOx, VOC, and particulate matter in California have been reduced over the last several decades in an attempt to control ambient O3 and airborne particulate matter concentrations to protect public health. The emissions totals summarized in Table 2-3 for the SoCAB reflect the predicted effects of emissions control programs between 1993 and 1996. Similar downward emissions trends are predicted for the SJV. The effectiveness of future emissions control programs will be determined by the competition between projected increases in population vs. improved efficiency or other technological advances that reduce emissions per unit of activity. Even if emissions are reduced to levels that achieve the National Ambient Air Quality Standards (NAAQS), meteorology will still affect air pollutant concentrations in California. The SJV already has significantly lower emissions than the SoCAB and the predicted response of O3 and PM2.5 to changes in temperature, humidity, and mixing depth in the SJV are qualitatively similar to those in the SoCAB. The results of the present analysis suggest that meteorological conditions that enhance the formation of O3 and PM2.5 will require stricter emissions control

programs than would otherwise have been required to achieve the NAAQS. Further research is needed to quantify the magnitude of this effect.

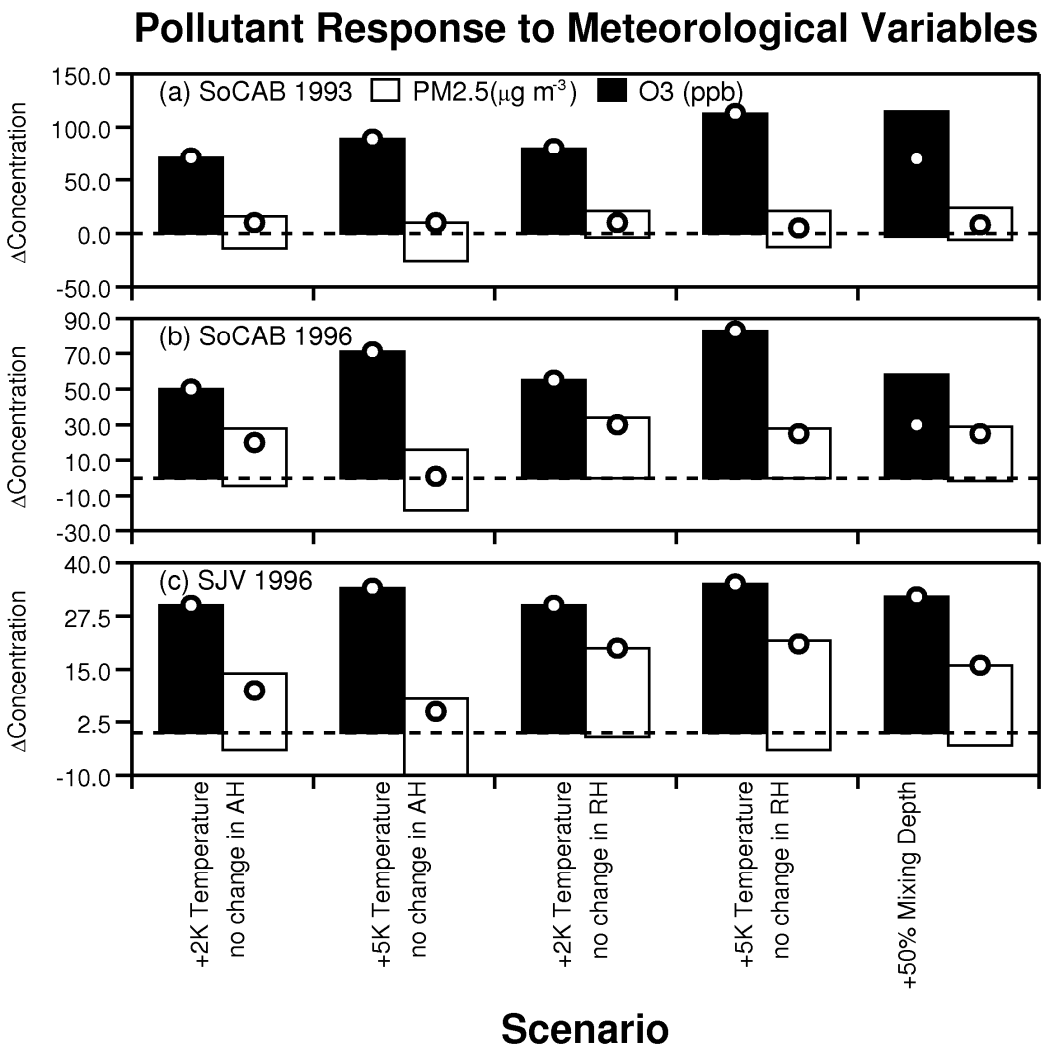

Figure 2-7: Summary of pollutant response to meteorological perturbations when background O3 concentrations are 60ppb during pollution episodes that occurred in (a) Southern California September 9, 1993, (b) Southern California September 25, 1996, and (c) the San Joaquin Valley January 6, 1996. The bars represent the range of concentration change at any location in the modeling domain in response to the indicated perturbation. The circles represent the concentration change at the location of the maximum concentration for each pollutant. AH is absolute humidity and RH is relative humidity.

2.7 Conclusions

The trends illustrated in the previous section show that air pollution problems in California are sensitive to temperature, humidity, mixing depth, and background concentrations. Future trends for temperature, humidity, mixing depth, and background concentrations are not exactly known at this time, but the weight of scientific evidence suggests that background O3 concentrations and temperature are likely to rise. The results of the current study suggest that these changes will lead to increased O3 concentrations in California.

The PM2.5 response to global change is more complicated to diagnose because some of the likely trends act in opposite directions. Increased temperature discourages the formation of particulate ammonium nitrate, but rising concentrations of background O3 encourages the formation of this same species. PM2.5 concentrations increased in all of the episodes currently studied under the limiting scenario of a +5 K temperature increase with no change in absolute humidity and a +30 ppb increase in background O3. The effect of increased background O3 was especially important during episodes with lower basecase temperatures. PM2.5 events in the San Joaquin Valley usually occur during the winter months, and so increased background O3 concentrations have a strong positive effect on PM2.5 concentrations in this location. These results suggest that global change will increase PM2.5 concentrations in California, but more research is needed to verify this result.

3.0 IMPACT OF CLIMATE CHANGE ON PHOTOCHEMICAL AIR POLLUTION IN SOUTHERN CALIFORNIA

3.1 Introduction

Ozone air quality varies depending on meteorological conditions. A positive correlation between ozone levels and temperature is a well-known aspect of this relationship [33, 53-55]. Air quality management plans may be affected if an increase in emission control requirements is needed to offset changes in climate that increase the severity and/or frequency of air pollution episodes.

Global analyses [16, 56-59] simulate future meteorology and air quality under different climate scenarios. With climate change these studies report ozone decreases in remote areas as destruction of ozone by water vapor increases with higher temperatures. The global models do not provide a consistent picture of the response of urban ozone levels to climate change.

Regional air quality models have been used to assess local air quality effects while incorporating global-scale changes. Racherla and Adams [60] reported longer future ozone seasons and increases in summertime ozone levels in the eastern U.S. using a "unified" model that allowed them to incorporate air quality impacts from climate change that occur outside their U.S. study region. Jacobson [19] used a global model with a nested regional U.S. grid and found adverse effects on public health relating to climate change-induced air quality changes.

High-resolution air quality models are needed to study local effects on air quality, such as complex terrain, spatially resolved emissions, and fine-scale patterns of expected population growth. Studies such as Aw and Kleeman [33], Steiner et al. [5], and Kleeman [61] refine the scale of interest to focus on air quality in urban areas. These studies incorporate predictions of future temperature changes and various feedbacks that may result. Effects on ozone varied strongly by location across each air basin, highlighting the importance of using a fine-scale grid for this type of analysis.

Other studies have examined the effects on air quality of changing the frequency of stagnation events. Mickley et al. [14] report that changes in weather patterns (specifically the frequency of low-pressure systems passing through) lead to a lengthening of stagnation events across the eastern and mid-western U.S., creating longer and more severe ozone air pollution episodes. Similarly, Leung and Gustafson [62] find evidence of increasing stagnation in southern California during the fall, also leading to adverse effects on ozone air quality.

Duffy et al. [63] discuss increases in observed surface temperatures for California over the last 50 years, pointing out that increases in temperature have been higher during the nighttime than daytime. They argue that global climate models do not represent accurately the seasonal or diurnal changes in the observed temperature record in California since 1950. Duffy et al. [63] show that unmodeled forcings due to changes in

land-use and irrigation affect trends in daily maximum temperatures. Bonfils and Lobell [64] and Lobell and Bonfils [65] show that increases in irrigation have had a cooling effect on daytime temperatures during summer. Ongoing work by Lebassi et al., [66], indicate the potential for stronger sea breezes associated with climate change to cause summer daytime cooling while average seasonal temperatures continue to increase. These daytime cooling effects may have mitigated some effects of climate change on ozone air quality.

The objective of this research is to predict potential effects of future changes in climate, population, and emissions on ozone air quality in southern California. Outcomes at different locations throughout the Los Angeles area are evaluated to assess interactions among the above factors.

3.2 Methods

The effects on ozone air quality of changes in five different factors (temperature, humidity, biogenic emissions, inflow boundary conditions, anthropogenic emissions) are evaluated in southern California. Each of these factors is considered individually. In addition, the combined air quality effects of changes in temperature, biogenic emissions, and humidity represent an aggregate climate-related effect on air quality. The combined effects on air quality of future changes in anthropogenic emissions and inflow boundary conditions reflect effects of population growth and technology change, occurring locally in southern California and globally. Each of these effects on air quality is evaluated relative to a base case high-ozone episode from summer 2005.

Air pollution formation and transport is modeled for a base case period of 14-19 July 2005, when observed ozone concentrations peaked at over 100 ppb at many inland locations in southern California. This time period has been used to support control strategy design in the 2007 Air Quality Management Plan for the Los Angeles area [67]. The model domain (110×74 grid cells with 5 km horizontal resolution) is centered over downtown Los Angeles, extending west over the Pacific Ocean past the Channel Islands, and east over the Mojave Desert. The domain extends from northern Mexico to the south end of San Joaquin Valley as shown in Fig. 3-1. The vertical dimension is divided into 25 layers extending to ~15 km above sea level, with a telescoping vertical grid starting at 36 m layer thickness at ground level and increasing to 6.5 km near the tropopause.

The Community Multiscale Air Quality model (CMAQ; Byun and Schere, 2006[68]) version 4.6 is used to predict base case and future air quality. The SAPRC99 chemical mechanism [69], containing 77 model species (including lumped VOC categories) and 216 reactions, is used to describe relevant atmospheric chemistry. Boundary conditions similar to Steiner et al. [5] were used here except that the NO and NO_2 inflow (western) boundary conditions were reduced from 1 ppb each to 0.01 and 0.03 ppb, respectively, based on Nowak et al. [70]. Meteorological fields were developed by the South Coast Air Quality Management District [71] using the National Center for Atmospheric Research Mesoscale Meteorological model (MM5) version 3.6.1. Three two-way nested domains were used with spatial resolution of 45, 15, and 5 km. Only the innermost 5 km

meteorological fields were used in the present study to drive air quality model calculations. SCAQMD evaluated meteorological model predictions over the 14-19 July 2005 episode, in general finding small differences between modeled and observed temperature, wind speed, and humidity. For example, the daily average bias in wind speed ranged from –0.03 to 0.23 m/s. For temperature, most days had smaller than a -0.5°C bias compared to observation, the largest temperature bias was for July 19th, of –1.2°C. The largest bias of humidity was -5%, also for July 19th.

The base case emission inventory used here was provided by the California Air Resources Board [72]. Separate hourly and day-specific gridded estimates of mobile, point, and area source emissions were combined with biogenic emission estimates developed using the BEIGIS model [73]. Table 3-1 shows domain-wide emission totals for NO_x, non-methane organic compounds (NMOC), and CO, for each category of emissions. Table 3-1 highlights the importance of both on-road mobile emissions as well as off-road/area emission as important sources. A high degree of emission control has been achieved on large point sources such as power plants in southern California, so these sources are of relatively minor importance here.

Table 3-1: Domain-wide emission totals (tons/day)

Source	Weekday Emissions (tons/day)			Weekend Emissions (tons/day)		
	NO_x	NMOC	CO	NO_x	NMOC	CO
Area/off-road mobile	720	707	1498	612	738	2163
On-road mobile	775	353	3408	445	283	2806
Point	142	76	171	128	44	147
Biogenic		713			719	

Perturbations to the base case air quality model were developed and applied using results from a global and regional climate modeling study by Snyder et al. [74]. A doubling of pre-industrial global background CO_2 levels from 280 to 560 ppm was the basis for future climate calculations. The domain used in the regional climate model was centered on California with a horizontal resolution of 40 km. This fine resolution is needed to capture the wide variety of elevations, land cover types, and microclimates that are found within California. The regional climate model was forced using global-scale predictions from the NCAR parallel climate model for the 2× CO_2 scenario. See Snyder et al. [74] for further details. Predicted temperature increases in southern California for July range from 1.6 to 3.5°C, with larger increases predicted to occur further inland, as shown in the first panel of Fig. 3-2. Temperature changes from Snyder et al. [74] are monthly average values based on 5-year long regional scenarios and are applied evenly across all times of day and week except when otherwise specified.

Perturbations to the base case were considered separately to isolate the effects of individual variables. Temperature changes affect chemical reaction rates in the model, but these changes were not linked to other variables such as wind speed or planetary boundary layer height, which remained the same as in the base case. Temperature changes were mapped directly from the regional climate model to the air quality domain. Both climate and mesoscale meteorological models used a Lambert conformal map projection which facilitated superposition of regional climate model-derived temperature perturbations on the MM5-derived meteorological fields.

The effect of increased temperatures on biogenic emissions of volatile organic compounds was modeled as a separate effect. Biogenic emissions of isoprene and methyl-butenol are sensitive to temperature and light, whereas terpenes are sensitive to temperature but not light. For the future temperature scenario, emissions of isoprene and terpenes were scaled using algorithms described by Guenther et al. [75]. Methyl-butenol emissions were adjusted following Harley et al. [76]. These algorithms show all emissions increasing exponentially with temperature increases, but note isoprene and methyl-butenol emissions saturate at temperatures above 40°C. In this scenario, biogenic emissions were calculated for the higher temperature regime while atmospheric chemistry proceeded at temperature-dependent rates equal to those of the base case. This isolated the effects of biogenic emission changes on air quality.

Assuming relative humidity remains constant in the future climate scenario, absolute humidity was adjusted given the new (higher) temperatures. This calculation adjusts the ratio of (g water)/(kg air) to maintain the same relative humidity under future temperature conditions. Note that in the "humidity only" scenario relative and absolute humidity both increase, while temperature is held constant. For the combined climate case, relative humidity is unchanged between future and base case scenarios, as both absolute humidity and temperature increase.

Future anthropogenic emissions were estimated from current emissions, scaled to account for population growth and technology change. Population growth in California through 2050 has been forecast at the county level [77]. We assumed that improved technologies and increased regulation of air pollution sources will reduce VOC, CO, and NO_x emission factors by 80% below present-day (circa 2000, already controlled) levels. Following Steiner et al. [5], growth in NO_x emissions is estimated as double VOC growth because of expected continuing increases in the freight-transport sector. Table 3-2 shows anthropogenic and biogenic VOC and NO_x emission totals by county for Thursday, July 14th, for future conditions and base case conditions. Included are the growth factors for each county. Future domain-wide NO_x emissions decrease from the base case by 31% while anthropogenic VOC emissions decrease by roughly double this amount. This future emission scenario is based on past trends in California and does not reflect current greenhouse gas regulatory efforts that may also influence the trajectory of NO_x and VOC emission reductions.

Table 3-2: AVOC, BVOC and NOx, base case and future emissions by county. Emissions are reported in tons/day for Thursday July 14th.

County	Pop. Growth	Base Case NO_x	Future NO_x	% chg	Base Case AVOC	Future AVOC	% chg	Base Case BVOC[1]	Future BVOC[1]	% chg
Imperial	2.3	34.8	32.4	-7%	53.1	24.7	-53%	6.3	7.8	+25%
Kern	2.7	181.5	198.9	+10	90.4	49.6	-45	52.0	59.1	+14
Los Angeles	1.3	524.8	272.9	-48	377.8	98.2	-74	34.4	35.6	+3
Orange	1.3	143.8	75.4	-48	136.2	35.7	-74	7.5	6.8	-9
Riverside	2.5	145.6	145.0	-0.4	107.9	53.7	-50	25.4	30.3	+19
San Bernardino	1.9	210.3	158.1	-25	110.5	41.5	-62	20.6	27.6	+34
San Diego	1.5	162.5	96.9	-40	163.7	48.8	-70	53.1	55.3	+4
San Louis Obispo	1.4	20.9	11.8	-44	21.1	6.0	-72	26.5	25.3	-4
Santa Barbara	1.3	34.1	17.4	-49	37.1	9.5	-74	43.6	40.9	-6
Ventura	1.5	53.4	32.5	-39	46.2	14.1	-70	27.0	29.4	+9
Non-County	1.6	115.6	74.9	-35	37.5	12.2	-68	0.2	0.2	-6
Total		1627	1116	-31	1181	394	-67	296	318	+7

[1] Reported in this column are biogenic emissions of terpenes, isoprene, and methyl-butenol. Future emissions of these compounds were changed based on future temperature predictions.

Future inflow boundary conditions were adjusted following Steiner et al. [5], using increased concentrations of CO, ozone, and methane in response to emission increases in the A1B scenario between 2000 and 2050 [78]. In order to highlight the potential effects from increasing emissions in Asia, ozone concentrations were increased by roughly double the amount predicted in the A1B scenario, a scenario that predicts economic growth with market based approaches to limiting greenhouse gas emissions and assumes no single energy generation technology is dominant. Parrish et al., [79, 80], and Jaffe et al., [81] describe observed increases in ozone levels in Pacific Ocean inflow to the western United States, raising concerns about disproportionately higher impacts for ozone. Therefore in this study at the western inflow boundary, CO was increased by 30%, methane was increased by 40%, and ozone was increased by 30%.

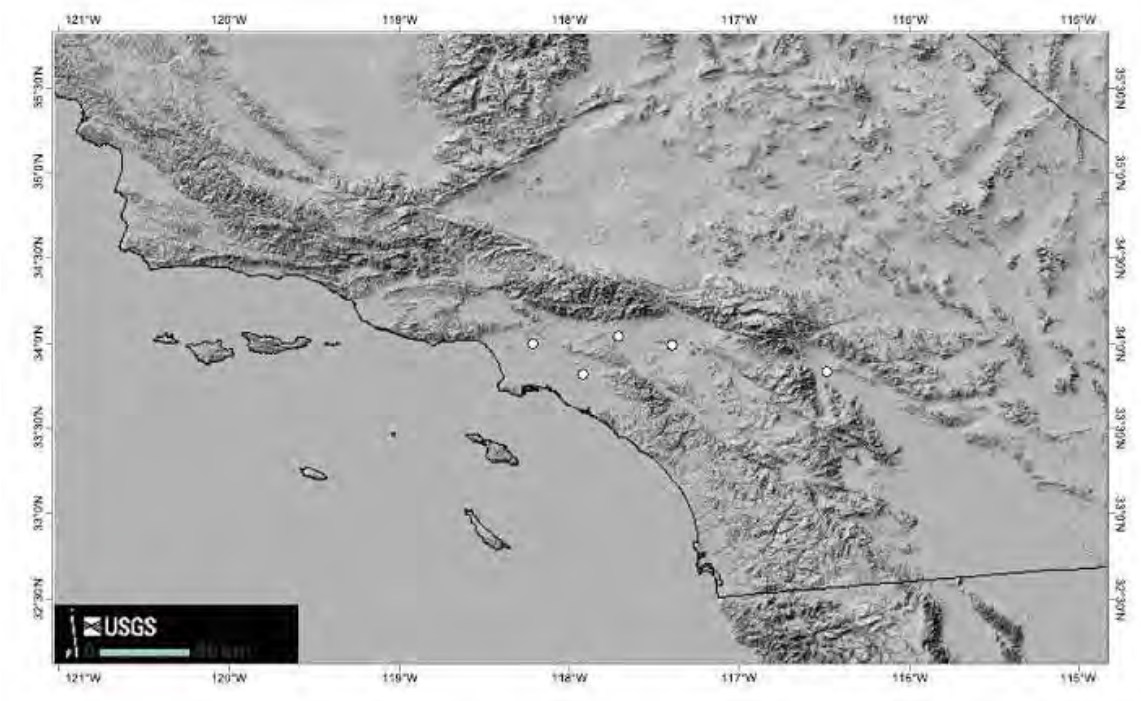

Figure 3-1: Map of southern California study domain used for air quality modeling in the present study. Locations highlighted from left to right: Central Los Angeles, Anaheim, Pomona, Riverside, and Palm Springs.

3.3 Results and Discussion

3.3.1 Base Case Model Evaluation

Ozone predictions were compared to observations at 83 surface sites. Comparing all ozone observations above 40 ppb with model predictions, a normalized bias of +3% and a normalized error of 30% were found. The spatial distribution of ozone in the model matches that seen in the observations, with the best agreement found in the urbanized areas around Los Angeles. A comparison of model output to observations at five representative locations is presented in Fig. 3-2. The modeling domain is well-suited to studying photochemical air pollution in the South Coast air basin. In contrast, both San Diego and the southern San Joaquin Valley lie at the edges of the study area used here and as such are subject to larger uncertainties due to their proximity to northern and southern boundaries of the modeling domain.

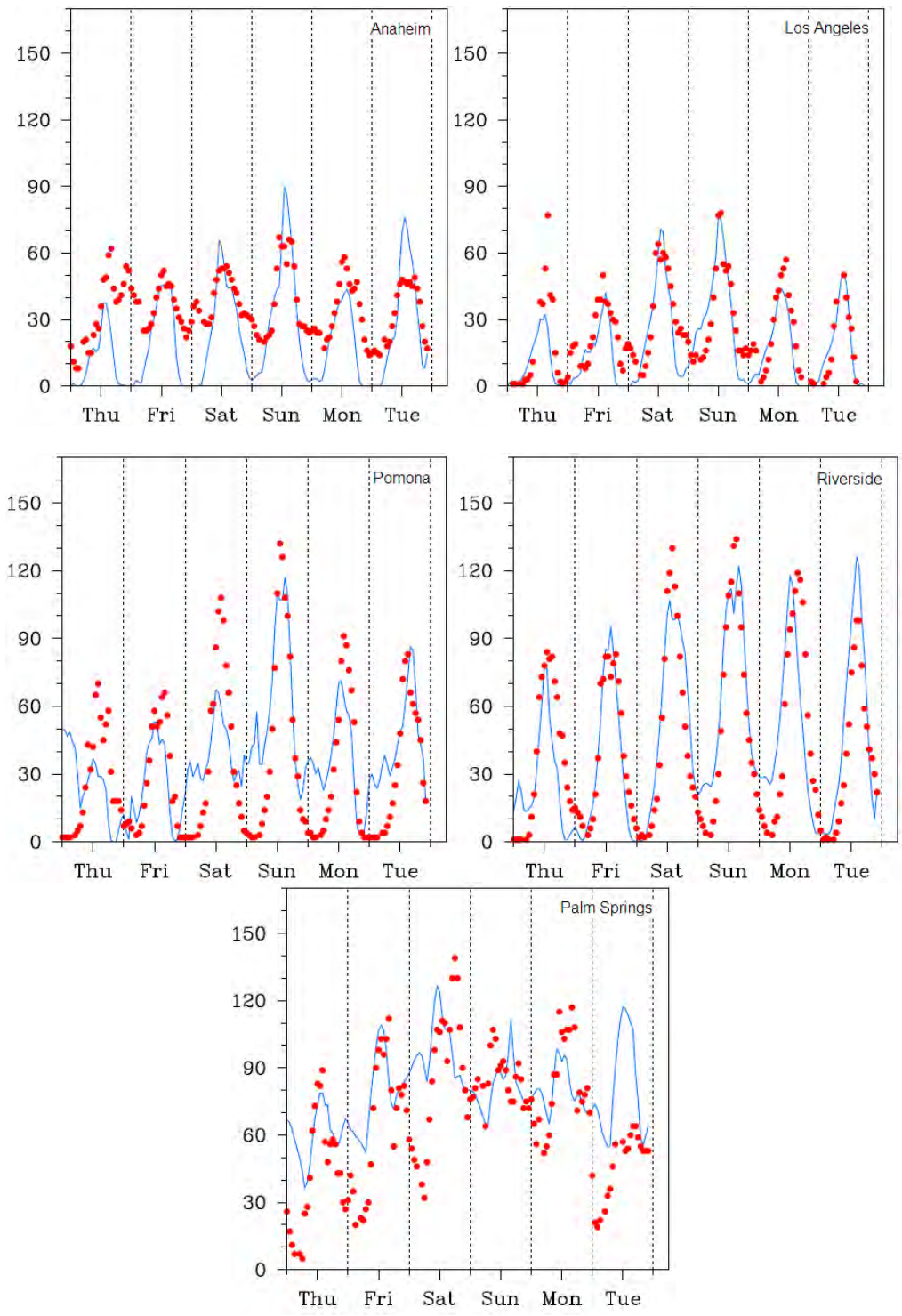

Figure 3-2: Comparison of base case model output (blue) to ozone measurements (red) at five sites.

3.3.2 Effects of Climate Change

A series of model runs was conducted to determine the sensitivity of air quality in southern California to future changes in emissions and climate. Figures 3-3, 3-4, and 3-5 show differences in input data and resulting changes in ozone air quality between various modeled perturbations and the summer 2005 base case. The spatial patterns of ozone changes are shown at 3 PM, which is a high-ozone time of day. Time series plots showing ozone changes at all times of day are discussed later.

The effect of increased temperatures on chemical reaction rates is to increase peak ozone levels across the domain. Figure 3-3 shows the change in temperature and corresponding peak ozone response. Inland areas that experience larger future temperature increases and are close enough to Los Angeles to be strongly influenced by its emissions showed the strongest ozone response to temperature changes.

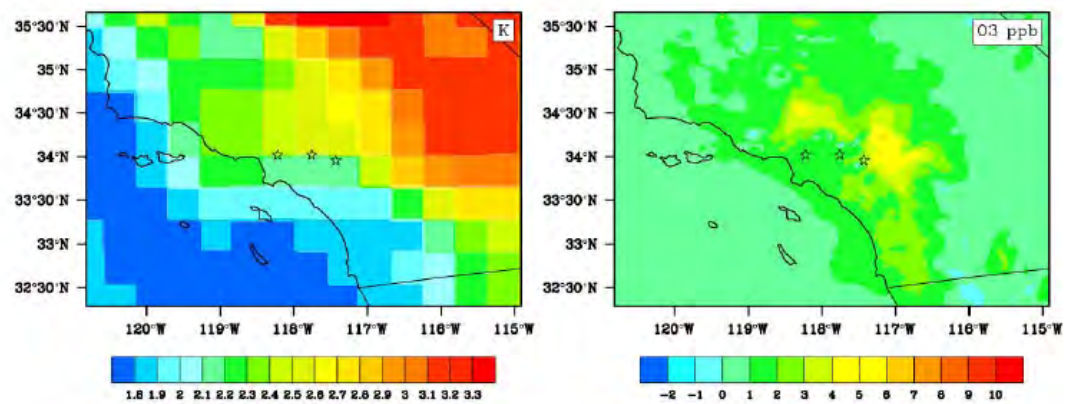

Figure 3-3: Difference between future and base case temperatures, and resulting changes in weekday-average ozone concentrations at 1500 h LT. The locations shown are from left to right, Central Los Angeles, Pomona/Claremont, and Riverside.

Figure 3-4 shows changes in biogenic emissions and the corresponding peak ozone response. Similar to the results shown in Fig. 3-3, Fig. 3-4 shows little change in ozone for the coastal areas of Orange and Los Angeles Counties and larger ozone increases further inland. The effects of biogenic emission increases are mitigated to some extent by the spatial distribution of these emissions, which occur mostly in the surrounding mountains rather than within urbanized areas. Increased biogenic emissions had the largest effects on ozone in areas north and east of Los Angeles. Over much of the domain, biogenic emissions increased by 20-35% compared to the base case as a result of higher temperatures.

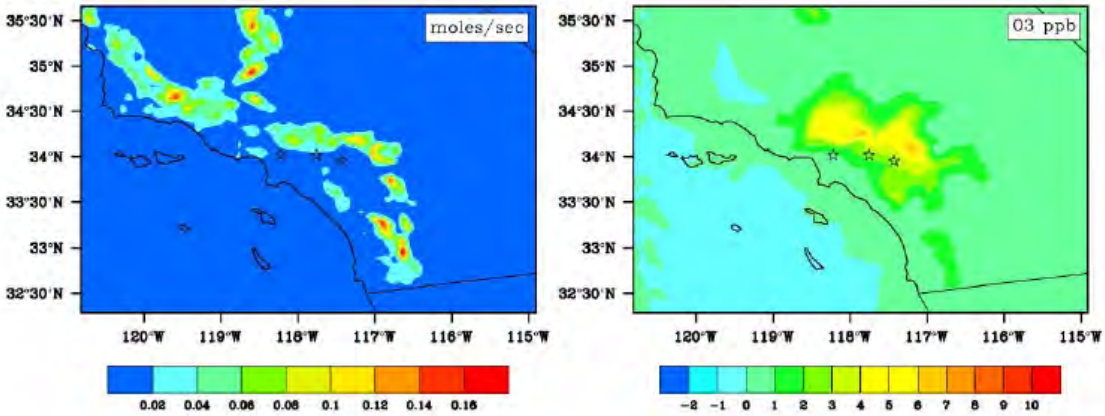

Figure 3-4: Difference between future and base case biogenic emissions, and resulting changes in weekday-average ozone concentrations at 1500 h LT. The locations shown are from left to right, Central Los Angeles, Pomona/Claremont, and Riverside.

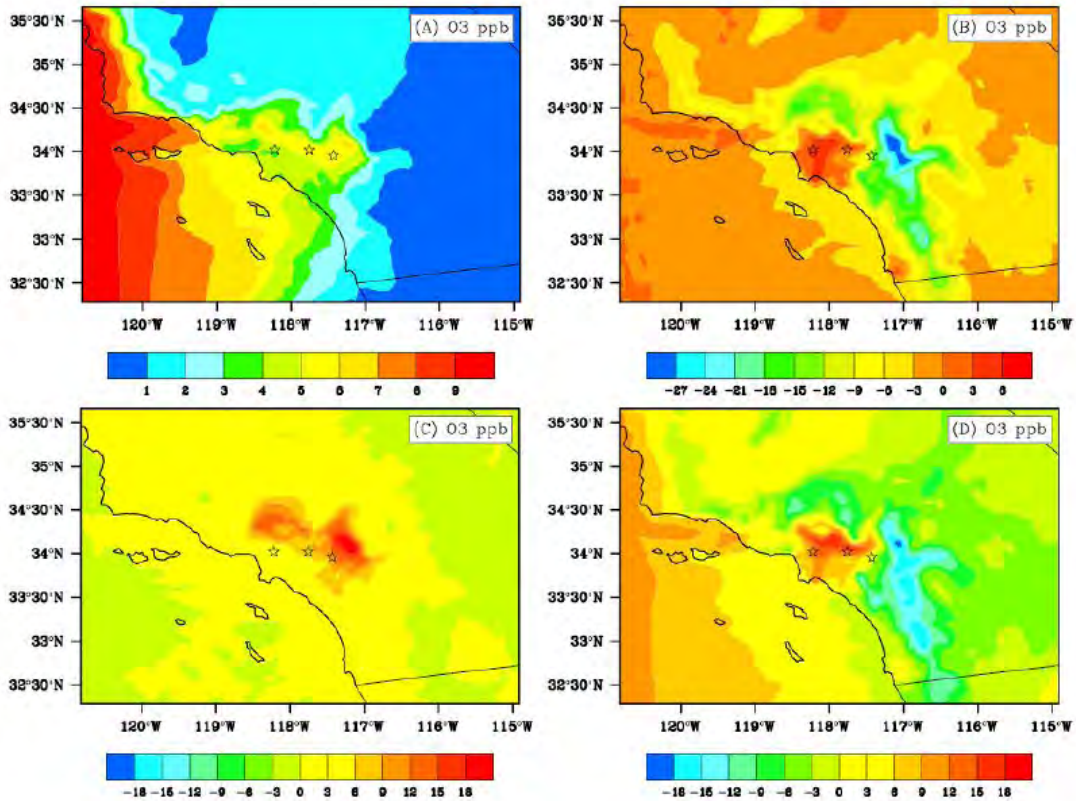

Figure 3-5: Differences between future and base case O3 concentrations on weekdays at 1500 h LT. The locations shown are from left to right, Central Los Angeles, Pomona/Claremont, and Riverside. (a) Future inflow boundary condition scenario, (b) Future anthropogenic emissions, (c) Future climate perturbations (increased temperature, absolute humidity, biogenic emissions), (d) all perturbations (a-c) combined together.

The response of peak ozone to increased humidity is positive in most urbanized areas, and can be seen in Fig. 3-6. The increase in water vapor leads to greater production of HO_x as a result of ozone photolysis, and thus increased atmospheric processing of pollutants such as NO_x and VOC. For example, in response to humidity changes, modeled afternoon NO_x concentrations in and around Pomona and Riverside decrease by an average of 3 and 6%, respectively. In these NO_x saturated regions, modeled ozone levels increase as a result. Further east, a smaller NO_x decrease is seen, for example 2% at Palm Springs, but this area is more remote and NO_x limited thus ozone concentrations decrease in response.

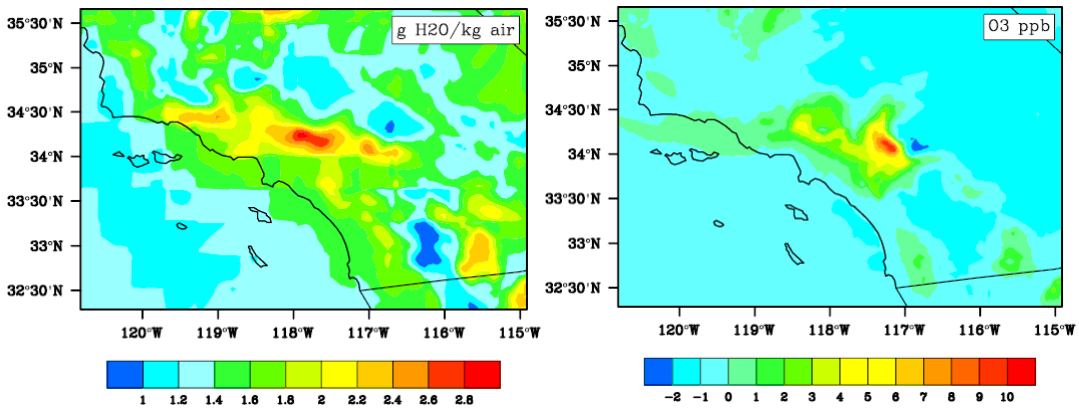

Figure 3-6: Difference between future and base case absolute humidity and ozone concentrations on weekdays at 1500.

3.3.3 Effects of Emission and Inflow Boundary Condition Changes

Increased pollutant concentrations at the western inflow boundary increase peak ozone levels consistently across all sites except Palm Springs (see Fig. 3-5a). There are large relative increases in ozone near the coast where base case ozone levels were generally lower compared to inland locations.

Under the future emission scenario, emissions of NO_x, VOC and CO decrease across the domain. Coastal areas see reductions of 35-50% in NO_x emissions and even larger reductions in VOC. The resulting effects on ozone were mixed, due to spatial differences in ozone sensitivity to VOC versus NO_x emissions as well as differences in predicted growth rates between the counties. In central Los Angeles future emissions and inflow create an increase in peak ozone levels of up to 9 ppb, whereas Riverside sees a similar sized decrease. The effects of future changes in inflow BC and local emissions taken together are shown in Fig. 3-5b (combined anthropogenic effects scenario).

3.3.4 Combined Effects

Figure 3-5c shows the ozone air quality impact of a combined climate forcing case, incorporating changes to temperatures, absolute humidity, and biogenic emissions. Increases in peak ozone are seen across the domain, ranging from 3-15 ppb, with the largest increases occurring inland near Riverside. The combined anthropogenic effects and climate change scenario shows increases in peak ozone at most locations with decreases seen only far inland (Fig. 3-5d).

Table 3-3 summarizes changes in peak 1-h ozone between each future scenario and the base case. Combined scenarios 6-8 are not linear combinations of individual scenarios 1-5, but instead represent results of additional model runs incorporating various combinations of the individual perturbations as noted in Table 3-3. Table 3-4 shows changes in peak 8-h ozone for each scenario, with results that follow closely those of the 1-h ozone changes in Table 3-3.

The locations shown in Table 3-3 were chosen to span future air quality outcomes in populated areas near Los Angeles. Figure 3-1 shows a map of the study area including the locations of these 5 sites. Anaheim is located in Orange County, south of Los Angeles. The Central Los Angeles site is located near downtown, approximately 20 km from the coast. Pomona, Riverside, and Palm Springs are located progressively further east of Los Angeles. Pomona is ~40 km east of Los Angeles and Riverside is ~40 km east of Pomona. Although the terrain becomes more complex traveling east from Los Angeles to Riverside, no major mountains are located between these locations. Palm Springs and the Mojave Desert are separated from Riverside by mountain ranges.

Overall there are large changes in peak ozone due to changes in both climate and emissions. Ozone increases across the greater Los Angeles area, and decreases east of Riverside. The changes in peak ozone range over ±17.5 ppb. More detailed forecasts of future emissions are needed, and air quality management plans may need to be adjusted to account for ozone increases that may occur due to climate change.

Table 3-3: Average weekday ozone (ppb) at 1500 h LT (local time): base case levels and differences between specified run and base case

	Anaheim	Central L.A.	Pomona	Riverside	Palm Springs
Base case O_3	44.6	39.9	51.2	82.3	91.5
1) Temperature	+1.3	+1.6	+1.5	+3.3	+2.2
2) Biogenic VOC	+0.6	+1.0	+2.8	+2.9	+0.9
3) Humidity	+0.1	+0.9	+3.4	+4.4	-1.1
4) 2050 Emissions	+1.4	+4.3	+2.5	-13.5	-7.9
5) Inflow BC	+4.3	+4.3	+5.5	+5.4	+1.0
6) Combined 1-3	+2.2	+3.5	+8.5	+11.3	+2.1
7) Combined 4-5	+6.1	+8.8	+8.3	-8.2	-6.9
8) Combined 1-5	+7.9	+11.2	+16.0	-0.3	-5.6

Table 3-4: Average weekday 8-h ozone (ppb) at 1000 h – 1800 h LT (local time): base case levels and differences between specified run and base case.

	Anaheim	Central L.A.	Pomona	Riverside	Palm Springs
Base case O_3	40.5	31.2	48.6	79.3	91.0
1) Temperature	+1.1	+0.8	+1.3	+2.4	+1.9
2) Biogenic VOC	+0.6	+0.9	+2.4	+3.3	+0.9
3) Humidity	+0.3	+0.7	+2.6	+4.2	-0.6
4) 2050 Emissions	+2.5	+6.3	+1.9	-12.9	-7.3
5) Inflow BC	+4.3	+3.9	+4.3	+5.0	+1.0
6) Combined 1-3	+2.2	+2.5	+6.8	+10.4	+2.3
7) Combined 4-5	+7.2	+10.8	+6.6	-8.4	-6.2
8) Combined 1-5	+9.1	+13.0	+12.9	-1.7	-4.3

A sensitivity analysis of the combined future emissions and climate scenario shows that urban areas from downtown Los Angeles east to Riverside remain NO_x saturated (see

Fig. 3-7). This may seem counter-intuitive as the isolated future emissions scenario showed ozone decreases in the Riverside area. However, high growth is predicted in Riverside, canceling out predicted improvements in emissions control in this scenario. Thus the isolated future emission scenario shows reduced ozone in Riverside occurring because of emission reductions elsewhere while maintaining steady emissions locally. The sensitivity analysis measures the ozone response to a uniform percentage change across the domain. The sensitivity response indicates that future NO_x control would need to be much stronger than estimated in this work in order to shift populated regions from NO_x saturated to NO_x limited regimes. Secondly, since urban areas from Los Angeles to Riverside remain NO_x saturated, ozone response to emission and climate changes in between the modeled year 2050 and present can be expected to maintain the same sign as and fall below changes predicted by the combined emission and climate scenario.

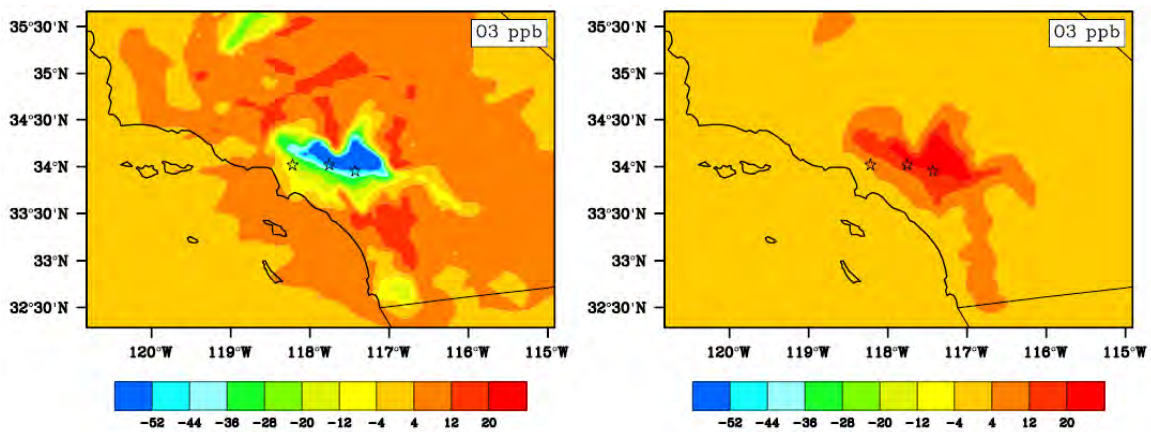

Figure 3-7: Peak ozone semi-normalized sensitivity to NOx (left) and VOC (right).

3.3.5 Temporal Patterns of Ozone Change

Riverside lies near the interface between positive and negative ozone outcomes under the combined scenario of future climate, emissions, and inflow boundary conditions. The magnitude and even the sign of the change in ozone concentrations at Riverside are time-dependent. The ozone response differs both by time of day, and for weekdays versus the weekend. Figure 3-8 shows predicted difference between base case and future scenario ozone concentrations by time of day at five locations.

Future ozone is closest to base case predictions around noon, although the sign of the change varies from day to day at Riverside. At other sites, such as Pomona and central Los Angeles, future ozone concentrations are consistently higher than in the base case. This is due to a combination of air quality penalties due to climate change and higher inflow boundary conditions, and a local effect of lower NO_x emissions on ozone in upwind areas, where the system is NO_x-saturated. Added model uncertainty exists for nighttime conditions when the observed partitioning of odd oxygen between NO_2 and O_3 in the nocturnal boundary layer is difficult to reproduce.

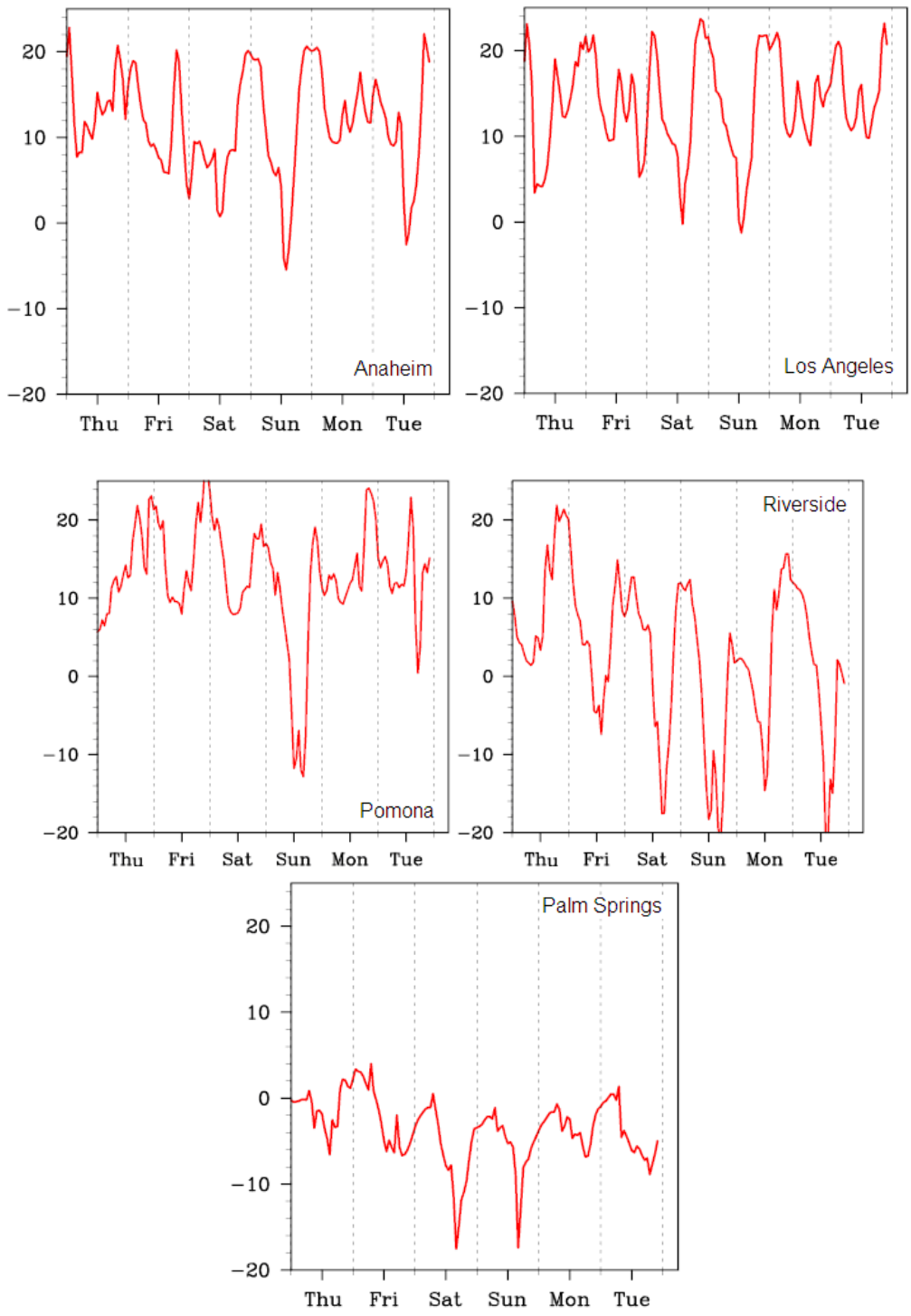

Figure 3-8: Difference between base case and future ozone concentrations (ppb) by time at five locations. (All perturbations scenario).

3.3.6 Future Temperature Change

Temperature perturbations applied here so far do not consider possible time-of-day dependence. Historically (i.e., from 1950 to present day) however, observed temperature increases during summer months have been largest at nighttime hours in many areas of California, and little increase in daytime maximum temperatures has been reported in the observed record [82]. To evaluate the effect of a diurnally-varying rather than uniform temperature increase on atmospheric chemistry and biogenic VOC emissions, an alternate form of the temperature perturbation was developed. Future temperatures were recalculated as a function of time of day:

$$T(t) = T_0(t) + \Delta T\left[1 + 0.8\cos\left(\frac{2\pi t}{24}\right)\right] \tag{1}$$

Where T_0 is the original temperature in the base case scenario, t is time in hours past midnight, and ΔT is the 24-h average increase in temperature predicted by Snyder et al. [74] for the month of the July. The amplitude of the oscillatory component (0.8) is arbitrary, but was chosen so that most but not all of the temperature increase occurs at night. Applying the past record of summer daytime cooling due to increased irrigation of 0.14 to 0.25°C per decade in California [64] to the 2050 temperature predictions by Snyder et al. removes most but not all of the daytime temperature increases and is consistent with Eq. (1).

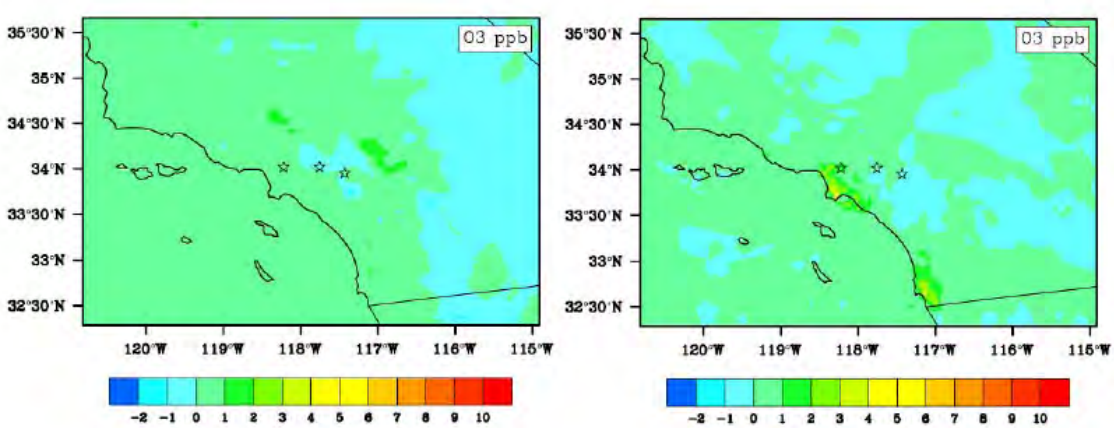

Figure 3-9: Difference between future and base case ozone concentrations on weekdays at 0300 h LT (left panels) and 1500 h LT (right panels). Compare right panel here vs. Figure 3-2 where T increase was applied uniformly throughout the day instead of most mostly at night. The locations shown are from left to right, Central Los Angeles, Pomona/Claremont, and Riverside.

The increase in peak ozone predicted above with a uniform temperature increase mostly disappears when the temperature increase occurs predominantly at night. Figure 3-9 shows the effects on ozone of increased temperature using a diurnally-varying

temperature change (Eq. 1) relative to the base case at 0300 and 1500 h LT on weekdays. More generally, ozone concentrations show little change at any time of day relative to the base case when temperature increases occur mostly at nighttime hours (see Fig. 3-10).

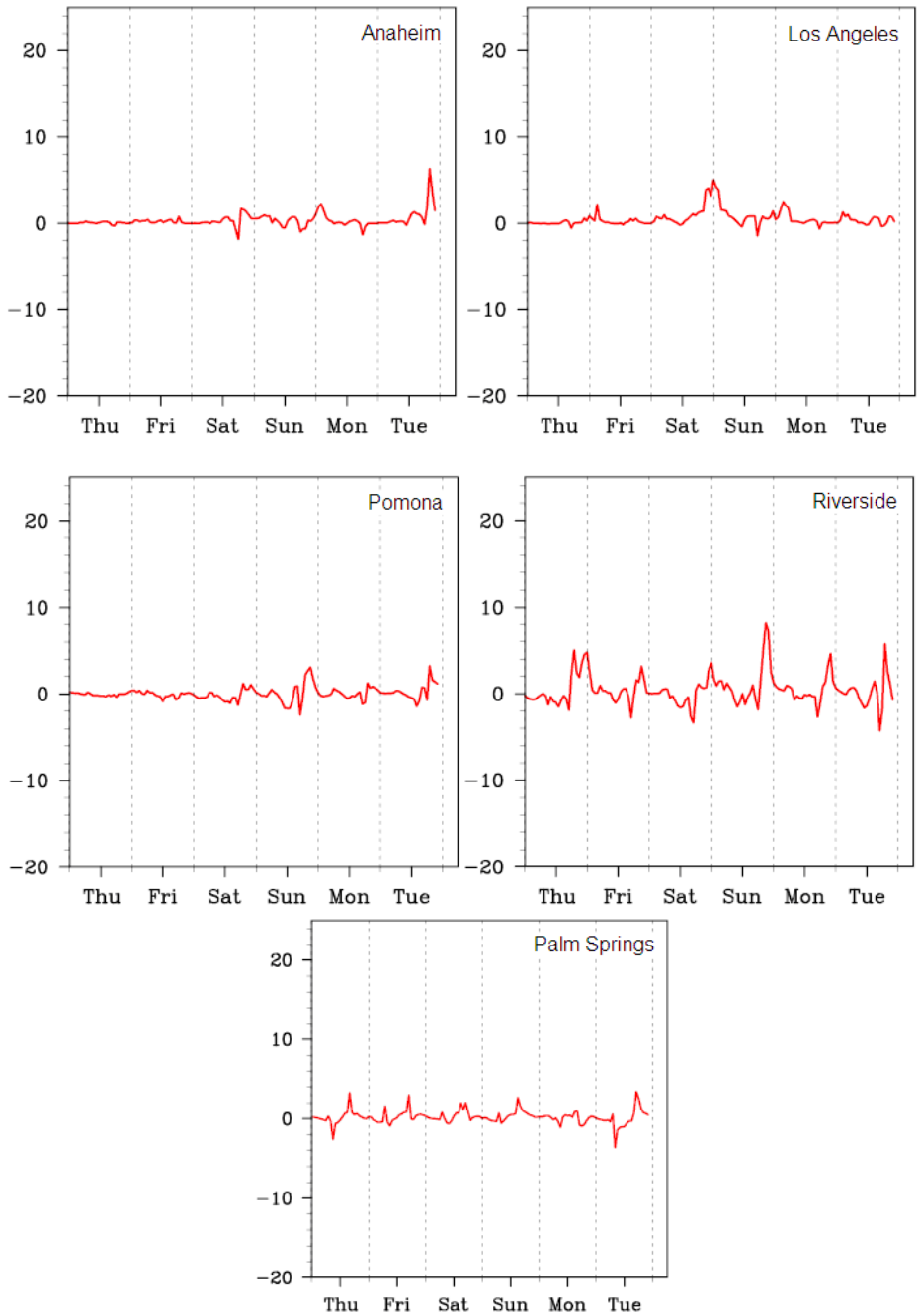

Figure 3-10: Difference between base case and future ozone concentrations (ppb) by time at five locations. (Future temperature scenario with future temperature change adjusted by time of day).

Similar results were found when biogenic emissions were recalculated using diurnally-varying temperature changes. Emissions of isoprene and methyl-butenol are both temperature and light-sensitive, and emissions of these compounds are zero at night. Nighttime temperature increases do increase terpene emissions, but the absolute effect of temperature increases on terpene emissions is reduced because baseline temperatures are lower at night. Ozone concentrations do not increase nearly as much as when temperatures were increased uniformly throughout the day. Changes in ozone at 0300 and 1500 h LT due to revised estimates of biogenic VOC emission increases are shown in Fig. 3-11.

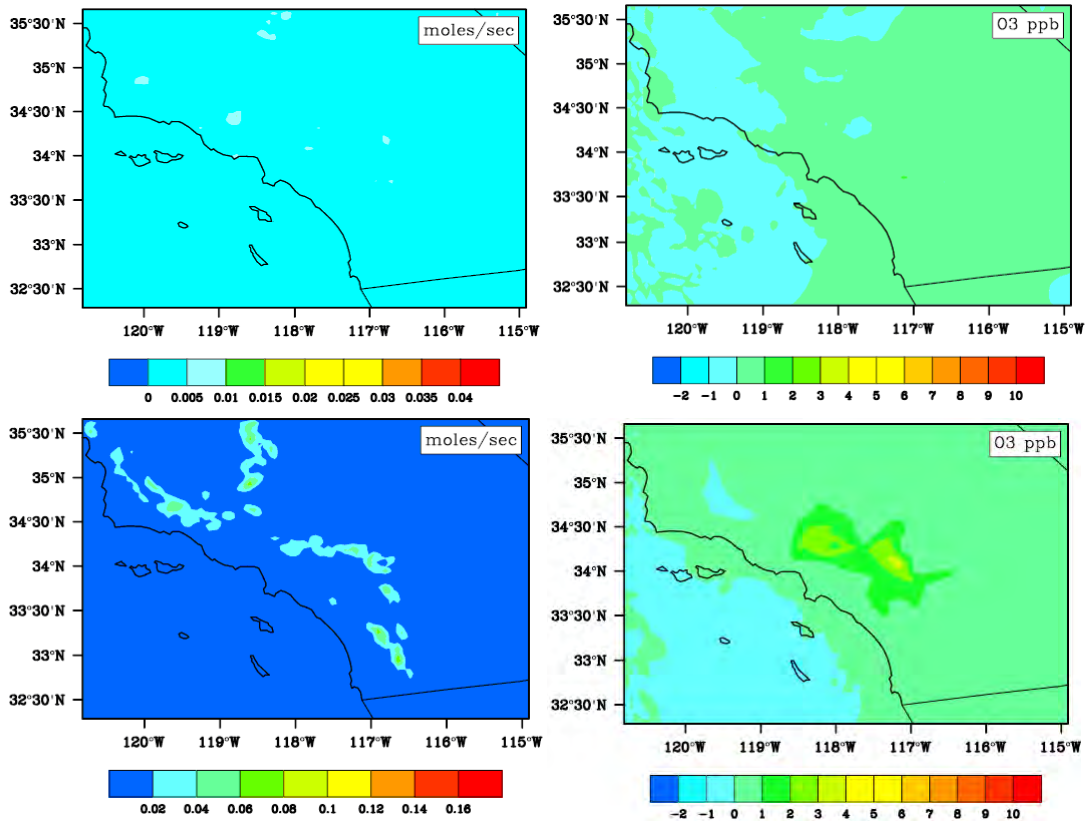

Figure 3-11: Difference between future and base case biogenic emissions and ozone concentrations on weekdays at 300 (top panels) and 1500 (bottom panels). Biogenic emissions in the scenario are based on temperature changes that have been adjusted by time of day.

The diurnal pattern of future temperature changes is important to assessments of climate change impacts on ozone air quality. Nighttime temperature increases have less effect on ozone production than similar temperature increases that occur at midday. However, the historical record of temperature increases is not necessarily a good predictor of future warming. Irrigation, which increased over the last century in California, is unlikely to continue to increase in the same manner in future years. Loss of agricultural lands to urbanization and scarcity of water may slow or reverse the expansion in irrigated lands. In fact the amount of irrigated land in California has remained relatively stable since the

1980s [64]. Thus, any past mitigating effect of increased irrigation on daytime warming is unlikely to be repeated over the next 50 years.

Other mechanisms for a diurnal pattern of future temperature change have been proposed by Lebassi et al., [66], who observed an increase in on-shore sea breezes that may have mitigated summer daytime warming relative to surrounding areas that are sheltered from these breezes. Both changes to irrigation and to sea breeze patterns have the potential to affect humidity levels as well as future diurnal temperature changes. Further research is needed to understand these effects and their interactions with air quality.

3.4 Summary and Recommendations

This study investigated ozone air quality effects of future climate change, inflow pollutant boundary conditions, and anthropogenic emissions on ozone air quality in southern California. Future temperature changes were predicted at high spatial resolution in California for a scenario of 2× pre-industrial CO_2 levels. Future emissions were predicted starting from a baseline emission inventory, factoring in expected population growth and likely advances in emission control technologies.

Globally-driven climate changes led to ozone increases throughout the study domain. In this study, climate change affected ozone levels through three mechanisms: increased temperature, increased humidity, and increased biogenic VOC emissions. These effects contribute to a climate change penalty for air quality management: additional controls on anthropogenic emissions will be needed to offset undesired effects of climate change on ozone. Likewise, future increases in pollutants, especially ozone, entering southern Calfornia via inflow from the Pacific Ocean will lead to increased mainland ozone levels, with coastal areas being especially vulnerable to this effect. The response of ozone air quality to future emission changes varied by location, with ozone increases predicted in upwind areas, and ozone decreases further downwind.

Recent commitments to control greenhouse gas emissions in California may also affect criteria pollutant emissions, and this issue requires further study. As noted above, the diurnal pattern of temperature change is important in assessing climate change effects on ozone air quality. More detailed information is needed on anticipated temperature changes as a function of time of day.

While this work focuses on how climate and future emissions influence the severity of a particular ozone episode, other investigations study factors that influence the frequency of these events. For example, Leung and Gustafson [62] consider effects such as changes in the number of stagnation events and the length of the high-ozone season. Other issues to consider include climate change effects on fine particulate matter levels, [61], and changes to other meteorological variables, such as precipitation, wind patterns, mixing and cloud cover. Finally, changes in forest fires may be an important aspect of the response to changing climate [83], with potentially serious effects on air quality.

4.0 STATISTICAL DOWNSCALING OF CLIMATE CHANGE IMPACTS ON OZONE CONCENTRATIONS IN CALIFORNIA

4.1 Introduction

Peak 1-hr average ozone concentrations in California have declined from 375 ppb during 1985 to 175 ppb in 2004 [84] due to the adoption of a long list of emissions controls. Health-based ambient air quality standards for ozone concentrations are 90 ppb (California 1-hr standard) or 85 ppb (federal 8-hr standard revised to 75 ppb in 2008) indicating that further progress is needed to protect public health. As of 2007, 35 out of California's 58 counties are designated non-attainment areas for the federal 8-hour ozone standard, affecting the health of ~30 million residents.

California has one of the largest economies in the world with correspondingly high emissions of air pollutants. The persistence of California's ozone problem is associated with warm sunny days and stagnant atmospheric conditions that trap emissions close to the surface where they have ample opportunity to undergo photochemical reactions. Climate change is expected to alter long-term meteorological patterns in California, with potential negative consequences for air quality. Surface ozone is particularly sensitive to climate change because the chemical reactions that form ozone are temperature dependent, with higher levels of ozone produced during warmer time periods [33, 55, 85] In addition, biogenic emissions and anthropogenic evaporative emissions of volatile organic compounds (VOCs), which are precursors to ozone formation, will also increase with rising temperature [4, 86-88].

Quantitative analysis of climate impacts on future ozone concentrations can be accomplished by dynamically downscaling Global Climate Model (GCM) results to regional scales using meso-scale meteorological models and regional air quality models (see for example, [5, 26, 89]). The dynamic approach incorporates a mechanistic description of atmospheric processes allowing it to extrapolate outside historical conditions. Unfortunately, the dynamic approach is also very computationally expensive in regions with severe topography such as California, so may not yield accurate results if the description of the relevant atmospheric processes is incomplete.

The statistical downscaling approach originally developed for hydrologic variables [90] provides a promising alternative technique to evaluate climate effects on ozone concentrations. The statistical downscaling method relates coarse scale meteorological variables that are available directly from GCM simulations to fine scale outcomes. The statistical approach is computationally efficient and guaranteed to capture the behavior of the historical atmospheric conditions. The disadvantage of the statistical downscaling approach is that future conditions may not follow the historical pattern due to changes in emissions, and separate statistical relationships need to be identified for each air basin of interest. Dynamic and statistical downscaling techniques are complementary and both methods should be used to evaluate future ozone trends in California.

The purpose of this chapter is to develop a statistical downscaling approach for climate effects on surface ozone concentrations in two major air basins in California: the South Coast Air Basin (SoCAB) and the San Joaquin Valley Air basin (SJVAB). Based on an extensive review of all meteorological data, the upper-air temperature at 850 millibar pressure (T850) (~1.5km altitude) will be used as the independent variable for the analysis. The variability in the measured ozone concentration at a fixed value of T850 will be explored using a perturbation analysis conducted with a mechanistic photochemical trajectory model. The verified statistical downscaling techniques will be used to evaluate climate effects on future ozone formation potential for the years between 2001 – 2100 using the output from the Geophysical Fluid Dynamics Laboratory (GFDL) coupled Climate Model (CM2.1).

4.2 Data and Methods

The daily maximum upper air temperatures at 850 millibars (T850) for the period 1980 – 2004 were obtained from the National Center for Environmental Prediction (NCEP) / National Center for Atmospheric Research (NCAR) Reanalysis1 [91] at two grid points near - (1) Upland in the South Coast Air Basin (SoCAB) and (2) Parlier in the San Joaquin Valley Air Basin (SJVAB). The NCEP/NCAR reanalysis assimilates historical measurements using the spectral statistical interpolation (SSI) scheme for the entire globe with a grid-cell size of 2.5°(longitude) x 2.5°(latitude). The resulting gridded data are saved at the beginning of each 6-hour interval (4 values saved each day). In the current project, the maximum of the 4 daily T850 values was used as the independent variable for correlation with ozone concentrations. Upper air temperature is considered to be among the most reliable data in the reanalysis dataset (class A) because it is strongly constrained by direct observations [92].

Projections of daily maximum T850 values for the period 2001 – 2100 were obtained from the Geophysical Fluid Dynamics Laboratory (GFDL) coupled climate model (CM2.1) [93]. The daily model output was available with a grid cell size of 2.5^{o} (longitude) x 4° (latitude) in 6-hour intervals. Simulated climate from GFDL CM2.1 were used in the Fourth Assessment Report of the Intergovernmental Panel on Climate Change (IPCC). GFDL CM2.1 T850 simulated under the Special Reports on Emission Scenarios (SRES) categories A2 and B1 were also of particular importance for the first assessment of climate impacts in California [92, 94], and hence these T850 predictions were used in the current study.

Daily 1-hr maximum ozone concentrations were provided by the California Air Resources Board (CARB) for two monitoring sites at: (1) Upland in the South Coast Air Basin (SoCAB) and (2) Parlier in the San Joaquin Valley Air Basin (SJVAB). The site at Upland (ARB ID: 36175, Lat: 34°6′14″, Lon: 117°37′35″, Elevation: 379 meters) is situated in a dense residential area east (downwind) of central Los Angeles. Ozone has been monitored continuously at Upland since January 01, 1973, and measurements for the period 1980 – 2004 were used in the current study. The site at Parlier (ARB ID: 10230, Lat: 36°35′50″, Lon: 119°30′15″, Elevation: 96 meters) is situated in an agricultural region southeast (downwind) of Fresno (the largest and urban center in the

SJVAB). Although Parlier is located in a relatively remote area, it experiences major air pollution events with emission signatures from the greater Fresno area. Continuous ozone measurements are available since January 01, 1983 at Parlier, and data for the period 1990 – 2004 were used in the current study.

Ozone concentrations at Upland and Parlier were measured with one of three possible instruments during the study period: a Dasibi 1003, and Dasibi 1008-AH, or an Advanced Pollution Instruments (API) 400. All monitors were regularly calibrated following a Standard Operating Procedure (SOP) so that the measurements remained accurate [SOP delivers ± 3-10% bias] and consistent over a long period of time. A test was performed in the current study to verify that the apparent relationship between upper air temperature and ozone concentrations was stable across transition periods when monitors were changed. As expected, the use of different ozone analyzers did not significantly change the relationship between temperature and ozone.

The variability in the relationship between ozone concentrations and T850 was explored in the current project using a 2-D Lagrangian (trajectory) form of the UCD/CIT photochemical airshed model [46, 52, 95-97]. The model tracks a 5km x 5km air parcel (5 vertical levels with a column height of 1100 meters) as it advects across the domain of interest. Diagnostic meteorological fields and boundary (initial) concentrations are interpolated from measurements during the current study. The model tracks the emissions of pollutants from natural and anthropogenic sources, the vertical mixing of pollutants due to turbulent diffusion, the reaction of pollutants due to photochemical processing, the condensation / evaporation of semi-volatile pollutants on primary particles, and deposition of pollutants to the surface of the earth. The Caltech Atmospheric Chemical Mechanism (CACM) [41, 48] was used in the 2-D Lagrangian model to predict the formation of ozone and other photochemical products. Previous studies have shown that CACM predictions for ozone and ozone precursors reproduce measured concentration trends at most sites in the SoCAB [98]

4.3 Results

Figure 4-1a shows the measured daily maximum 1-hr average ozone concentration as a function of the daily maximum T850 for the months May-October over the period 1980-2004 at Upland. Spring and fall months are included in the analysis even though they are outside the months that traditionally experience high ozone concentrations because climate change may increase the length of future “ozone seasons”. The scatter plot shows that the maximum observed ozone concentrations generally increased at higher temperatures, but there was significant variation at each T850 value, particularly between 281 K and 304 K. A linear correlation between ozone concentrations and the corresponding T850 is not obvious in Figure 4-1a due to the large variability in measured ozone concentrations at any given value of T850. Wind speed, wind direction, humidity, ΔT (elevated – surface) were also investigated as possible explanatory variables but they were not included in the final analysis because they did not significantly improve the regression statistics. Further study showed that the distribution of ozone concentrations at each T850 value was similar in shape but the median ozone concentration (second

quartile; Q2) increases with T850. Likewise, the first (Q1) and third (Q3) quartile ozone concentrations also increase with T850. Figure 4-1b shows linear regressions between the quartiles (Q3, Q2-median and Q1) of the measured ozone concentrations and T850. The high R^2 values (>0.80) and the good agreement over a broad range of temperatures suggest that the correlation between quartile ozone concentrations and T850 holds true at all relevant temperatures in the South Coast Air Basin (SoCAB). This relationship reflects the positive influence that temperature has on ozone concentrations, even though other factors may also influence ozone concentrations. Figure 4-1b also reveals that the relationship between ozone and T850 flattens out below T850 values of 282 K. Ozone concentrations in this range are dominated by the background value of ~30-40 ppb that is advected into the South Coast Air Basin (SoCAB).

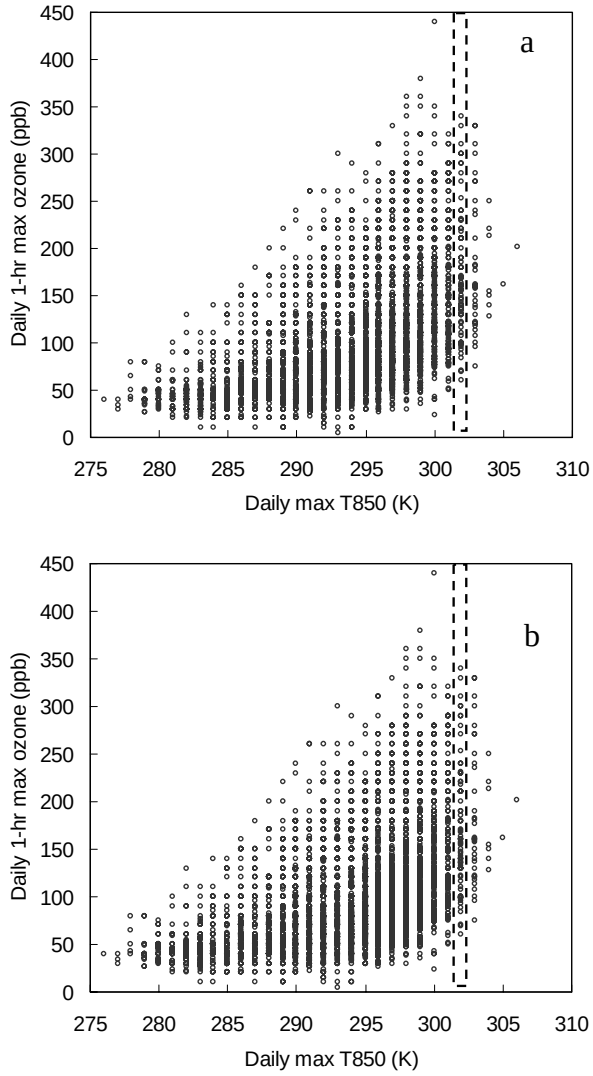

Figure 4-1: (a) Observed daily 1-hr max ozone versus the corresponding temperature at 850 mbar (T850), and (b) linear correlation between the ozone quartile boundaries and the corresponding daily max T850 at Upland, CA for the months May-October over the period 1980-2004.

Figure 4-2a shows the frequency distribution of maximum 1-hr average ozone concentrations measured at Upland when T850 was 302 K between May – October during the period 1980 – 2004. The distribution of ozone concentrations at this temperature was taken from the dashed rectangle shown in Figure 4-1a. Each ozone "bin" illustrated in Figure 4-2a shows the total number of days when maximum 1-hr average ozone concentrations reached the level indicated on the horizontal axis divided by the total number of days with T850 = 302K. Figure 4-2 therefore shows the probability distribution of ozone concentrations at this location for this meteorological condition. The probability distribution is approximately normal with a mean ozone concentration of 172 ppb, a standard deviation of 67 ppb, and slight skewness (0.65) toward higher values

of the ozone distribution. Similar probability distributions are associated with other values of T850. Figure 4-2b illustrates the probability distribution of ozone for T850 = 284K. As shown in Figure 4-1b, the median concentration of each distribution is positively correlated with temperature. The variance of the probability distribution reflects the degree to which variables other than temperature influence ozone concentrations.

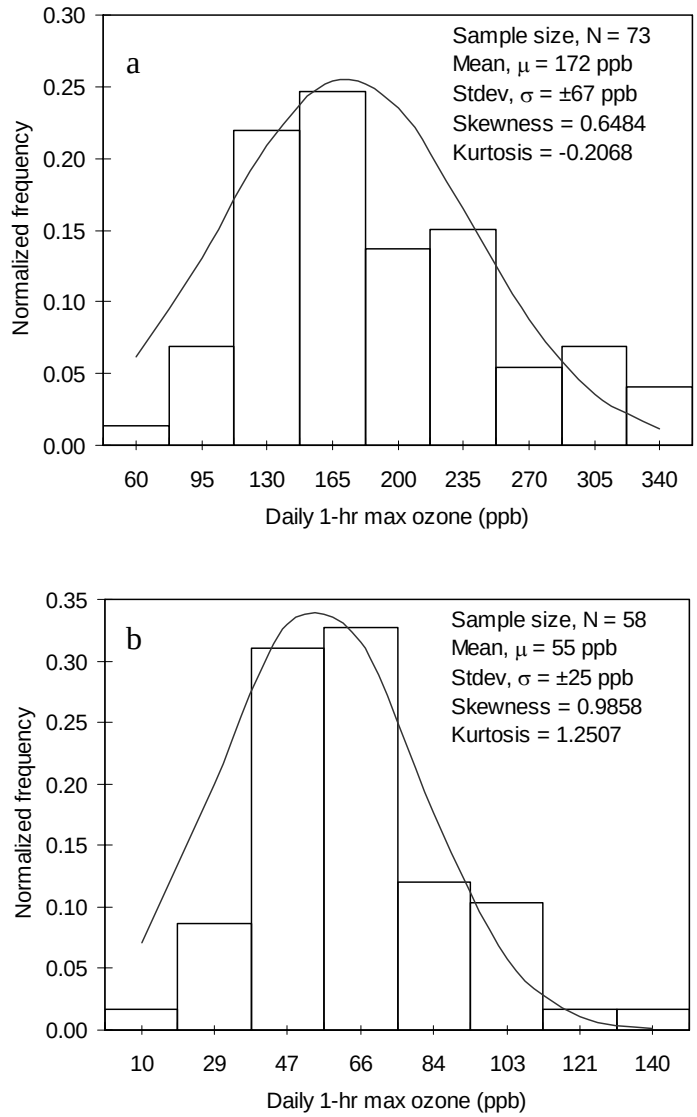

Figure 4-2: The frequency distributions of the observed daily 1-hr max ozone corresponding to T850 of 302 K (a) and 284 K (b) at Upland, CA, between May-October over the time period from 1980 to 2004.

One of the key objectives of this work was to identify the dominant sources of variability in the ozone frequency distribution that occurs at a given T850. The UCD/CIT air quality model that represents all major ozone formation processes was applied to study this question. The 2D Lagrangian form of the model was used in a Monte-Carlo simulation at Claremont, CA, on September 9, 1993 in order to understand the dominant sources that contribute to the variability of ozone concentrations at a given T850. Claremont was chosen as the receptor site because it is located in the eastern portion of the SoCAB where ozone concentrations are highest (similar to Upland) and numerous previous studies have been conducted at Claremont to validate the relevant meteorology databases and emissions inventories [95, 98, 99]. Three-day back trajectory routes for air parcel arriving at Claremont were calculated for each hour on September 9, 1993. The base case trajectory routes were then perturbed by adding stochastic bias to the wind-field [52, 100]. This method implicitly modifies dispersion coefficients, since dispersion is a function of wind speed. A total of 62 trajectory routes, including the base route were calculated for each hour of the day. Figure 4-3 shows the three-day back trajectory routes of air parcel arriving at Claremont at 3 pm on September 9, 1993, as an example.

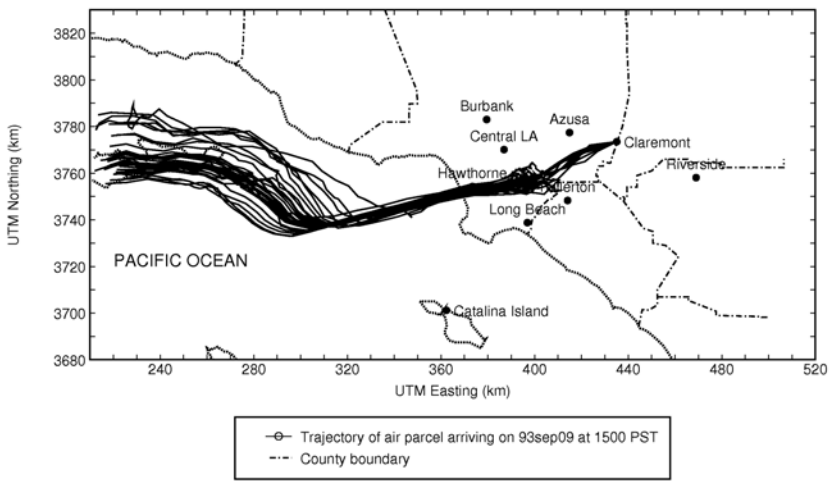

Figure 4-3: Three-day back trajectories for air parcel arriving at 3:00 pm on September 09, 1993 at Claremont, CA. Each trajectory path reflects random variations in wind speed and direction.

The Lagrangian form of the UCD/CIT air quality model was applied to each of the (5kmx5km) air parcels trajectories ending at Claremont. Perturbations (summarized in Table 1) were introduced to the meteorological parameters, initial conditions (global background concentrations), and emissions to simulate variability that could occur in the real atmosphere. The magnitude of the temperature, mixing height and relative humidity perturbations was calculated using the measured distribution of historical values in the vicinity of Claremont. The magnitude of the emissions perturbations were chosen as an extreme case to estimate the maximum sensitivity associated with this variable [97]. All perturbations were normally distributed with a mean value of zero. In addition to the emissions perturbations shown in Table 1, the base biogenic and evaporative emissions were scaled in response to changes in the perturbed temperature field. Biogenic

emissions were adjusted using an exponential relationship between temperature and emissions rates developed by [101]. Evaporative emissions from mobile sources were adjusted using a linear relationship between temperature and emissions rates (evaporative emissions scaling factor = 1 + (T-Tref)*1.34 where Tref=20°C). This approximate equation was determined by running the Emission FACtor (EMFAC) model under different temperature scenarios and then taking the average response for the entire air basin [102]. Background ozone concentrations were taken to be random values normally distributed with a mean value of 45 ppb and a standard deviation of 5 ppb. The background (initial and boundary) concentrations for volatile organic compounds (VOC), oxides of nitrogen (NO_X) and carbon monoxide (CO) were 18 ppb, 2 ppb and 200 ppb, respectively, at all model heights. The background value of methane (CH_4) was set to zero as CH_4 has no or little effect on regional-scale photochemical ozone production. To account for seasonal changes to the intensity of ultra violate (UV) radiation, the date was randomly selected between May 1 and October 31.

Table 4-1: Variables that were perturbed during the Monte Carlo simulations of ozone formation.

Variable	Variation amount
Temperature	±5 °C
Mixing height	±20%
Relative humidity	±10%
Overall emissions	±30%
Initial conditions for VOCs	±30%
Initial condition for background ozone	Between ±5 ppb
Biogenic and evaporative emissions	Temperature dependent scaling

Figure 4-4 illustrates the frequency distribution and relevant statistical properties of the predicted ozone concentrations resulting from all of the Monte Carlo simulations summarized in Table 1. Figure 4-4a shows the distribution based on the emission inventory appropriate for 1993 [41, 98]. The modeled standard deviation (44 ppb) for this level of base emissions was less than that of the observed data (67 ppb) appropriate for T850=302K. The larger variance in the observed ozone concentrations may result from the long time period over which measurements were made (1980-2004). The emissions inventory in the South Coast Air Basin (SoCAB) has changed significantly over the last three decades, but the model predictions summarized in Figure 4-4a were based exclusively on an emissions inventory appropriate for 1993. In order to partially account for the variability introduced by long-term emissions trends, the stochastic modeling summarized in Figure 4-4a was repeated for the same scenarios at Claremont but using a base emission inventory appropriate for 1987 [95, 99]. VOC emissions were projected to be 32% higher in 1987 than in 1993, while emissions of NOx were projected to be 7% lower. These changes are less than or equal to the size of the random perturbations introduced during Monte Carlo simulations, but they are applied to all emissions records uniformly. In contrast, the Monte Carlo simulations perturbed individual emissions records by ±30%, but the total emissions experienced by each air parcel from hundreds of different sources were close to the base-case values. Figure 4-4b

illustrates that when base case emissions are used from 1987, the median predicted ozone concentrations and the variance of predicted ozone concentrations are both larger than the observed statistics between 1980-2004. Figure 4-4c shows the average of cases described in Figures 4-4a and 4-4b. These results clearly indicate that the absolute value of ozone formation potential was more sensitive to the perturbations summarized in Table 1 under the emissions conditions encountered in 1987 than those in 1993. The modeling exercises conducted in the current study clearly identify long-term emissions trends as the dominant source of variability in the long term ozone record at Upland, CA.

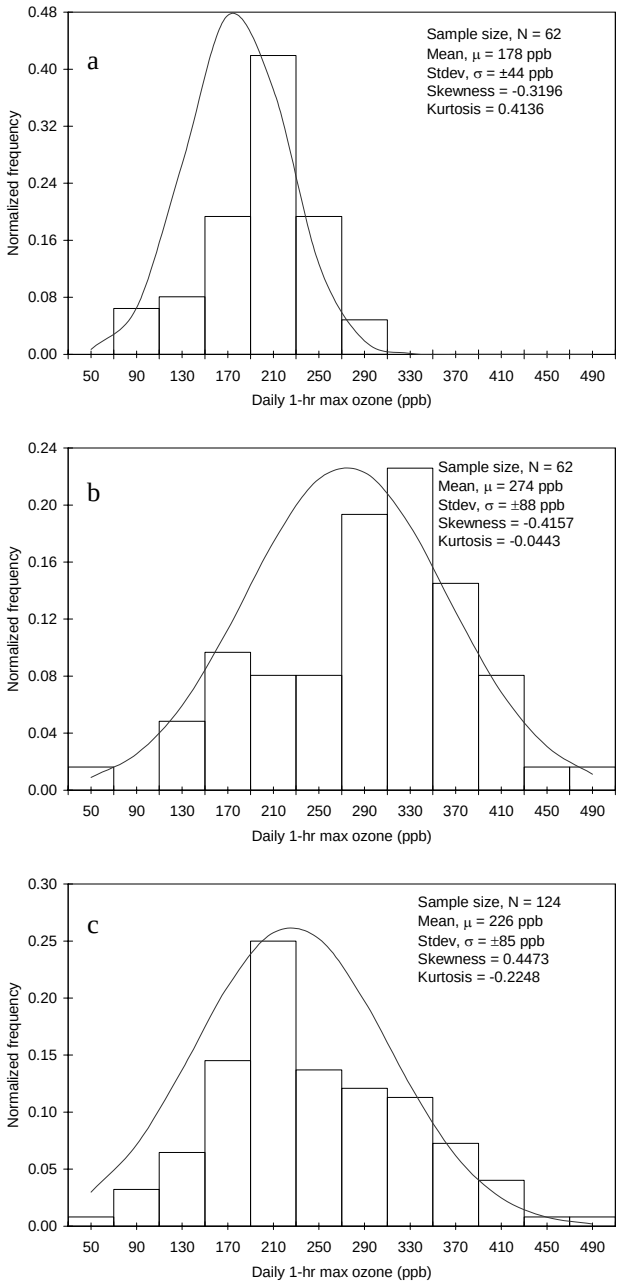

Figure 4-4: Predicted frequency distribution of the daily 1-hr maximum ozone concentration corresponding to a T850 of 302 K at Claremont, CA. Different ozone values were generated by random perturbations in the input meteorological parameters, emissions, and initial conditions as summarized in Table 1. Panel (a) corresponds to a base emission inventory appropriate for 1993, panel (b) corresponds to base emission inventory appropriate for 1987, and panel (c) represents the sum of (a) and (b).

Figure 4-5 illustrates the measured reduction in quartile ozone concentrations in the SoCAB during summer months (May-October) between the 1990's and 1980's. The

measured reduction in the median ozone concentration was 32%. Figure 4-5 also illustrates the reduction in predicted quartile ozone concentrations based on changes to the emissions inventory using the meteorological perturbations discussed above (Figure 4-4a vs. Figure 4-4b). The predicted reduction in median ozone concentrations due to changes in the emissions inventory was 37%, showing excellent agreement with measured values. This comparison once again emphasizes that long term emissions trends are the dominant source of variability in the long term ozone record at Upland, CA. Further mechanistic analysis of ozone sensitivity to meteorological variables and background concentrations in California is provided by [5, 33, 103].

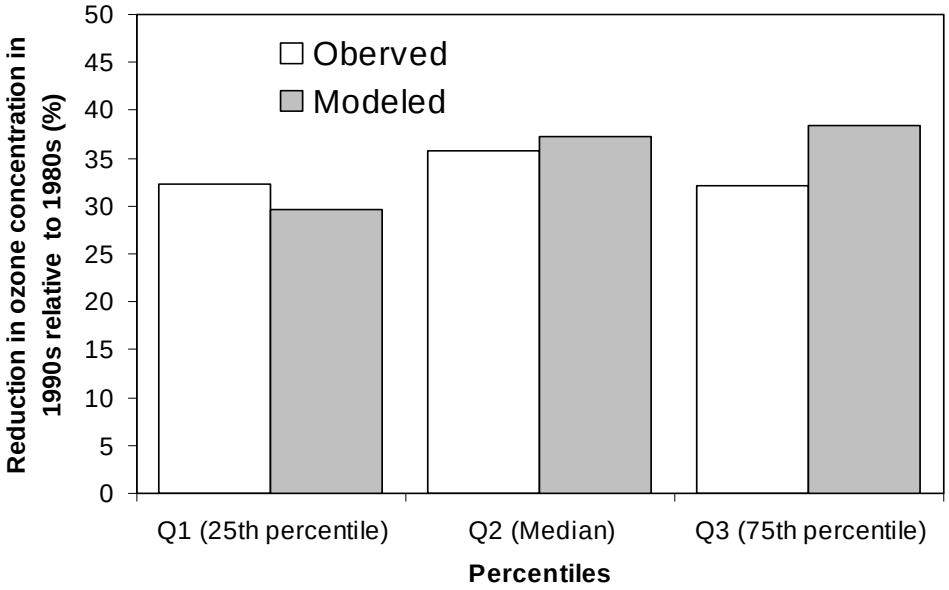

Figure 4-5: Comparison of observed and predicted reductions in ozone concentrations in 1990's relative to 1980's for the South Coast Air Basin (SoCAB) based on changes to the emissions inventory.

The effects of long-term emissions trends and seasonal variations on measured ozone concentrations were further investigated by separately analyzing different time segments of the measured ozone data record. The complete data record was segregated into three time periods: 1980-1989, 1990-1999 and 2000-2004, and into separate months between May-October. The variability in the long-term ozone records is shown in Figure 4-6 as the correlation between the median ozone concentration and the corresponding T850 at Upland for the three different decades. The correlation slope (sensitivity) decreases from 8.6 ppb K^{-1} for the period 1980-1989, to 6 ppb K^{-1} for the period 1990-1999, and 3.2 ppb K^{-1} for the period 2000-2004. The trend for 1990-1999 is in excellent agreement with the results from mechanistic modeling studies for 1993 and 1996 that predicted an ozone response to surface temperature of 2-9 ppb K^{-1} depending on location in the SoCAB [103]. The results in Figures 4-5 and 4-6 confirm the ability of the mechanistic model to capture climate effects on air quality and re-enforce the conclusion that long-term changes to the emissions inventory have decreased the sensitivity of absolute ozone concentrations to meteorological perturbations.

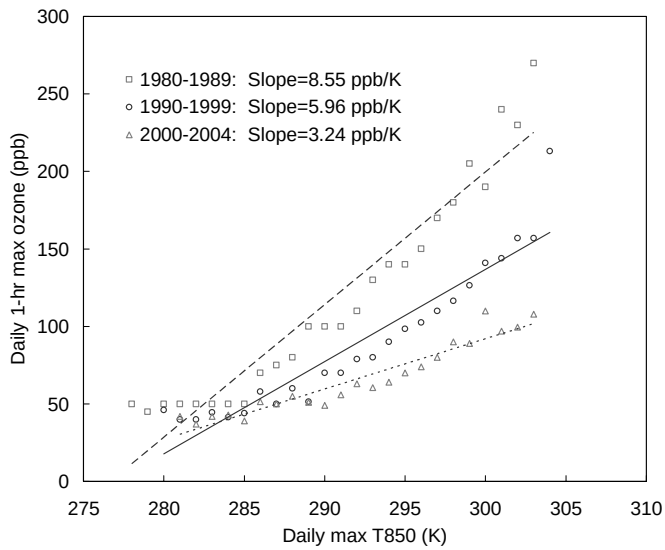

Figure 4-6: The linear correlation between the median of the observed daily 1-hr maximum ozone and the corresponding daily maximum T850 at Upland, CA, as a function of decade.

The sensitivity of relative ozone concentrations to T850 changes as a function of the absolute ozone concentration (since the absolute sensitivity is linear over a range of ozone values). The relative sensitivity (% K^{-1}) at a fixed temperature can be calculated by dividing the constant value of the absolute sensitivity (ppb K^{-1}) by the ozone concentration (ppb) at the temperature of interest. Analysis of the data shown in Figure 4-6 reveals that the sensitivity of relative ozone formation at T850≥300K is approximately constant at ~4.3 % K^{-1} across each of the time periods that were studied. When T850<300K the calculated relative ozone sensitivity is influenced more strongly by the ~30-40ppb of background ozone that is transported into the air basin. Averaged across the entire range of temperatures illustrated in Figure 4-6, the relative sensitivity of

ozone to temperature decreased from 6% K^{-1} in 1980-89 to 5.5% K^{-1} in 1990-99 and 4.3% K^{-1} in 2000-04. Overall, the sensitivity of relative ozone formation appears to be constant at hotter temperatures and decreasing at cooler temperatures across the different time periods and emissions conditions studied.

Ozone precursor emissions have decreased from 1980-1989 levels due to improved technology and stringent emission control measures, producing a decreasing trend in observed ozone concentrations [84]. Future emissions changes may continue this downward trend, or they may rebound as population growth overtakes the effects of increased efficiency. In either case, emissions will be considered to be static at 1990-2004 levels for the remainder of the current study to allow for a direct analysis of climate change on ozone formation potential.

Figure 4-7 shows the linear regression between ozone concentrations and reanalysis T850 separately for different summer months during the period 1990-2004 at Upland. The equations presented in the panels of Figure 4-7 represent the linear models based on the quartile ozone data. In each panel, the solid line represents the correlation based on the median ozone concentration and the upper and lower dashed lines indicate the correlation based on Q3 and Q1, respectively. The R^2 values (>0.75) indicate that the aggregated statistics of the ozone concentration distribution and T850 are well correlated. Importantly, different slopes are observed during different seasons. These reveal that ozone responds less strongly to temperature during the early spring (May – June) and late summer (September – October) months. Ozone concentrations respond most strongly to temperature during the middle of summer (July – August). The seasonal ozone response to T850 at Upland was also reanalyzed with a subset of the data points that have T850 between 291K-301K. Values of T850 in this range were measured in all months June-September within the historical dataset, and so this analysis removes any potential bias associated with temperature extremes experienced in one month but not other months. The ozone response within the common temperature range at Upland was still stronger in July-August vs. June or September, suggesting that some other seasonal factor besides temperature is influencing the results. Monthly average mixing height measured between 1984-1991 at Oakland, CA (at the coast upwind of the SJVAB) varied from 660 ± 80m (June), 550 ± 75m (July), 620 ± 74m (August), and 660 ± 150m (September). Mixing depth can influence ozone production [103], but the inclusion of the best-available mixing depth information in the current study did not add skill to the statistical model. Another possible seasonal factor is trends in biogenic emissions as vegetation follows a seasonal growth cycle (see for example [104]).

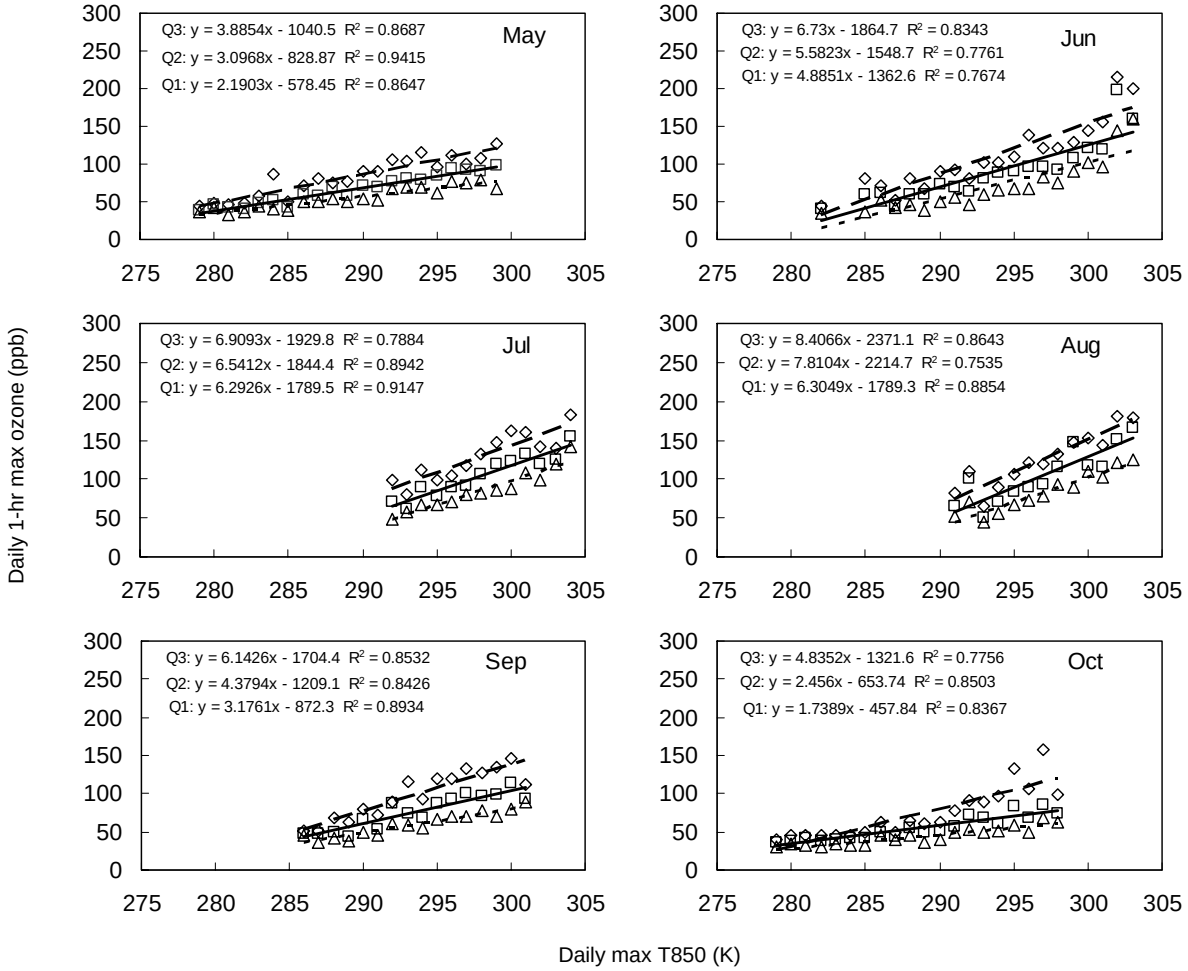

Figure 4-7: Seasonal correlation between 1-hr maximum ozone and 1-hr maximum T850 at Upland, CA, for the years between 1990 and 2004. Diamonds correspond to quartile 3 (Q3), squares correspond to quartile 2 (median; Q2), triangles correspond to quartile 1 (Q1).

Figure 4-8 shows the linear regression of quartile ozone concentrations from Reanalysis T850 at Parlier in the SJVAB for each month between May – October. Ozone trends in the SJVAB are qualitatively similar to those in the SoCAB, but the magnitude of the change induced by temperature is different because the underlying emissions inventories for the two air basins are not the same. Increased temperature still enhances ozone concentrations in the SJVAB, but the magnitude of the change is smaller than that observed in the SoCAB. As exhibited by the Upland analyses, July and August had the largest values of the regression slopes between ozone and T850 compared to other months.

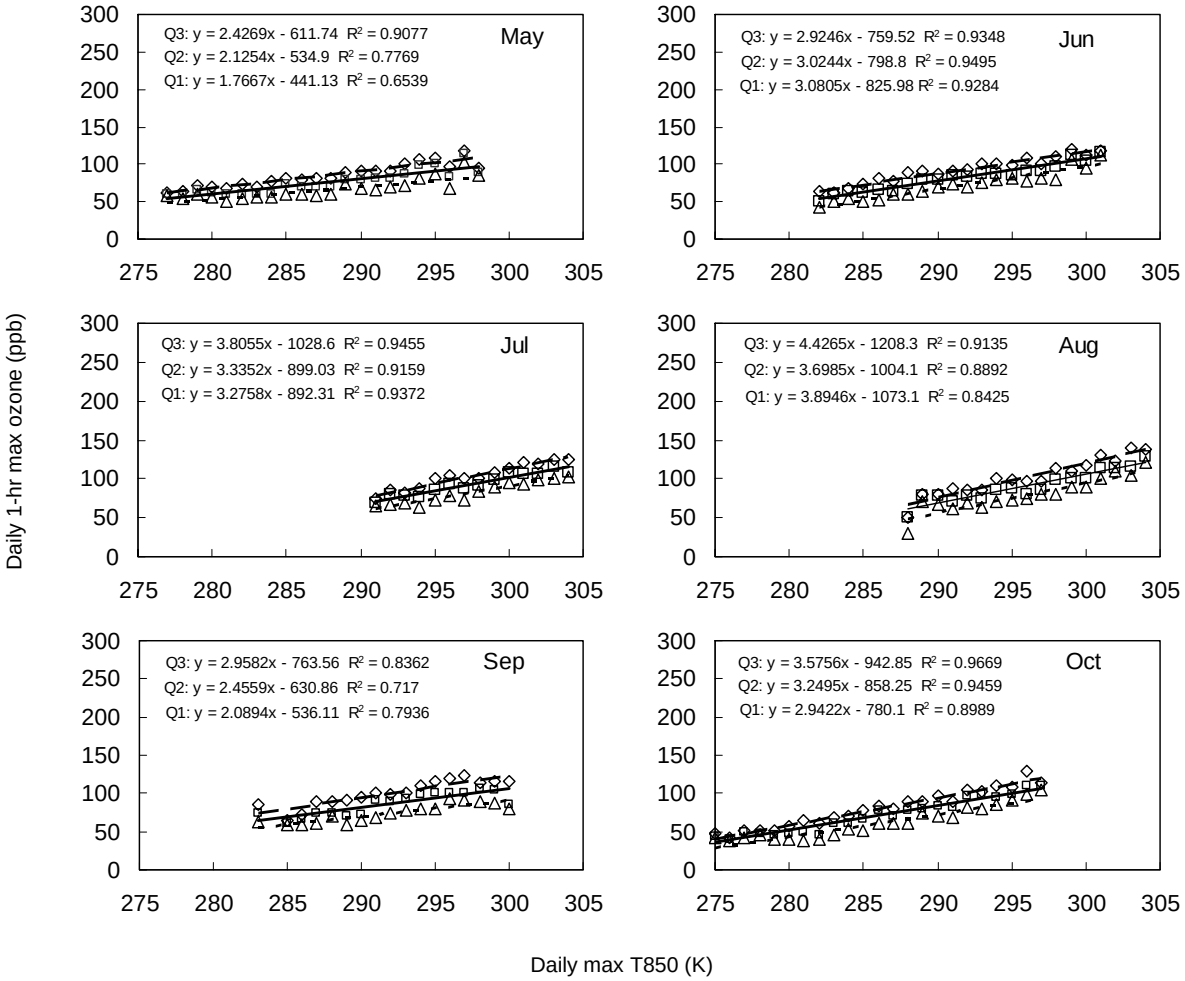

Figure 4-8: Seasonal correlation between 1-hr maximum ozone and 1-hr maximum T850 at Parlier, CA, for the years between 1990 and 2004. Diamonds correspond to quartile 3 (Q3), squares correspond to quartile 2 (median; Q2), triangles correspond to quartile 1 (Q1).

Future trends in upper air temperature are simulated by Global Climate Models (GCMs) in response to global change. There are several climate models currently available in the scientific community including the National Center for Atmospheric Research Parallel Climate Model version 1 (NCAR-PCM1), the NCAR-Community Climate System Model version 3 (NCAR-CCSM3), the Geophysical Fluid Dynamics Coupled Model version 2.1 (GFDL CM2.1), the Centre National de Recherches Meteorologiques Climate Model version 3 (CNRM-CM3) (French climate model), the Max Planck Institute for Meteorology ECHAM version 5 (MPI-ECHAM5) (German climate model), and the Model for Interdisciplinary Research on Climate version 3.2 (MIROC3.2) (medium resolution) (Japanese climate model). In the current study, the GFDL CM2.1 model was used to provide simulated T850 over a global domain, including California, for the years

2001 – 2100 based on several IPCC greenhouse gas emissions scenarios. Table 2 summarizes the temperature (T850) increase in California over the period 2070-2099 relative to 1961-1990 predicted by all of the GCMs described above. Decadal average results for all models are similar with a temperature increase of 4-5°C (A2 highest emission scenario) or 3-4°C (B1 lowest emissions scenario) during the summer ozone season in both the SJVAB and the SoCAB. The daily GFDL CM2.1 values of T850 simulated at coarse scale from model locations over the SoCAB and the SJVAB under the A2 and the B1 scenarios were used to estimate the potential for ozone formation in California. Ozone concentrations at Upland and Parlier were calculated based on the projected values of T850 for each day and the monthly statistical relationships between ozone and T850 illustrated in Figures 4-7 and 4-8 for the period 1990 - 2004. The median (Q2) ozone-T850 relationship in Figures 4-7 and 4-8 were used to obtain a baseline estimate, while Q1 and Q3 were used to obtain upper and lower bounds. In addition to the summer months (May – Oct), the correlations found in May and October were applied to each month of the periods February – April, and November – January, respectively. After calculating the daily 1-hr max quartile (Q1, Q2 and Q3) ozone concentrations with the projected temperature values for each year, the number of days with 90 ppb or more ozone was calculated for each month and an aggregate yearly result was derived under the assumption that emissions remained at 1990-2004 levels. The constant emissions reference of ozone precursors point was chosen to separately identify the projected effect of climate change on ozone concentrations.

Table 4-2: Temperature (T850) increase (^{o}C) in 2070-2099 relative to 1961-1990 projected for the SoCAB and SJAB by various climate models under the IPCC A2 and B1 emissions scenario.

	SoCAB				SJVAB			
	Jan-Mar		Jul–Sep		Jan-Mar		Jul-Sep	
Model	A2	B1	A2	B1	A2	B1	A2	B1
GFDL CM2.1	4	2	5	3	3	2	5	3
CNRM CM3	3	2	4	2	3	2	4	2
MIROC3.2 (med)	4	3	7	4	4	3	7	4
MPI ECHAM5	3	3	4	3	4	3	4	3
NCAR CCSM3	3	2	5	2	3	2	4	3
NCAR PCM1	2	2	2	1	2	2	3	2

Figures 4-9 and 4-10 show the number of days in each year that would be likely to exceed the 90 ppb threshold of the daily maximum 1-hr average ozone concentrations at Upland and Parlier respectively, if emissions remained at the 1990-2004 level. The circle represents the number of days based on the median ozone estimate, and the top and bottom bars represent the number of days based on the Q3 and Q1 correlations, respectively. As can be seen in these figures, the upper and lower bars represent the breadth of the distribution of the number of days likely to exceed the daily ozone threshold of 90 pbb for each year due to increasing temperature effects. Data are presented for years between 2001 – 2100. In both the SoCAB and the SJVAB, future values of T850 are projected to increase under both the IPCC A2 and B1 emissions

scenarios, leading to more days each year when ozone concentrations would exceed 90 ppb (under the assumption that emissions remain at 1990-2004 level). The rate of increase is higher (0.5-0.7 days yr^{-1}) for the A2 emissions scenario than the B1 emissions scenario (0.2-0.3 days yr^{-1}) because greater temperature increases are predicted under the A2 emissions scenario.

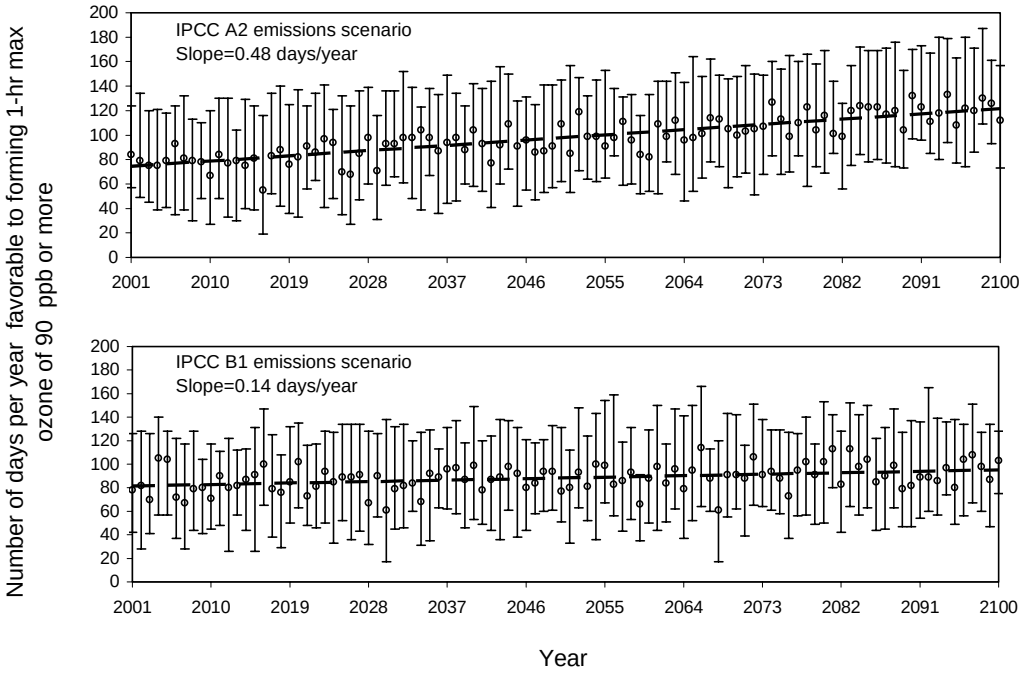

Figure 4-9: The number of days per year conducive to forming 1-hr maximum ozone of 90 ppb or more at Upland, CA under the Intergovernmental Panel of Climate Change (IPCC) emissions scenarios: A2 (top panel) and B1 (bottom panel). Note that the underlying assumption for this prediction is that the emissions in CA remain at the 1990-2004 level. Uncertainty bars represent the third and the first quartiles of the predicted number of days.

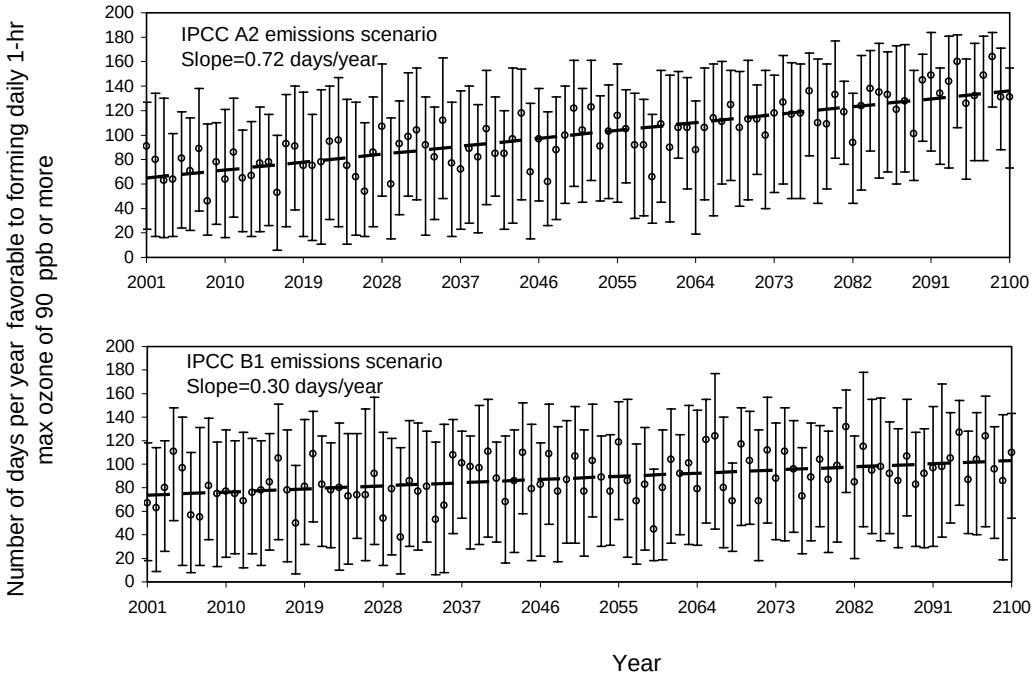

Figure 4-10: The number of days per year conducive to forming 1-hr maximum ozone of 90 ppb or more at Parlier, CA under the Intergovernmental Panel of Climate Change (IPCC) emissions scenarios: A2 (top panel) and B1 (bottom panel). Note that the underlying assumption for this prediction is that the emissions in CA remain at the 1990-2004 level. Uncertainty bars represent the third and the first quartiles of the predicted number of days.

The rate of increase for the number of days exceeding the 90 ppb ozone threshold at Parlier (SJVAB) is greater than at Upland (SoCAB) despite the fact that historical ozone concentrations are less sensitive to temperature at Parlier during all months but October (compare Figure 4-7 to Figure 4-8). These apparently contradictory trends can be explained by examining the total number of days exceeding 90 ppb of ozone during each month of the years 2046-2055 and 2091-2100 assuming emissions remained at 1990-2004 levels. Figure 4-11 illustrates that the months of July and August become "saturated" after ~2050 with continued increases occurring mainly in May-June and September-October. The annual growth at Parlier (SJVAB) is greater than Upland (SoCAB) primarily due to increases during the month of October. These trends reflect the greater lengthening of the "ozone season" in the SJVAB compared to the SoCAB assuming emissions remained constant at 1990-2004 levels.

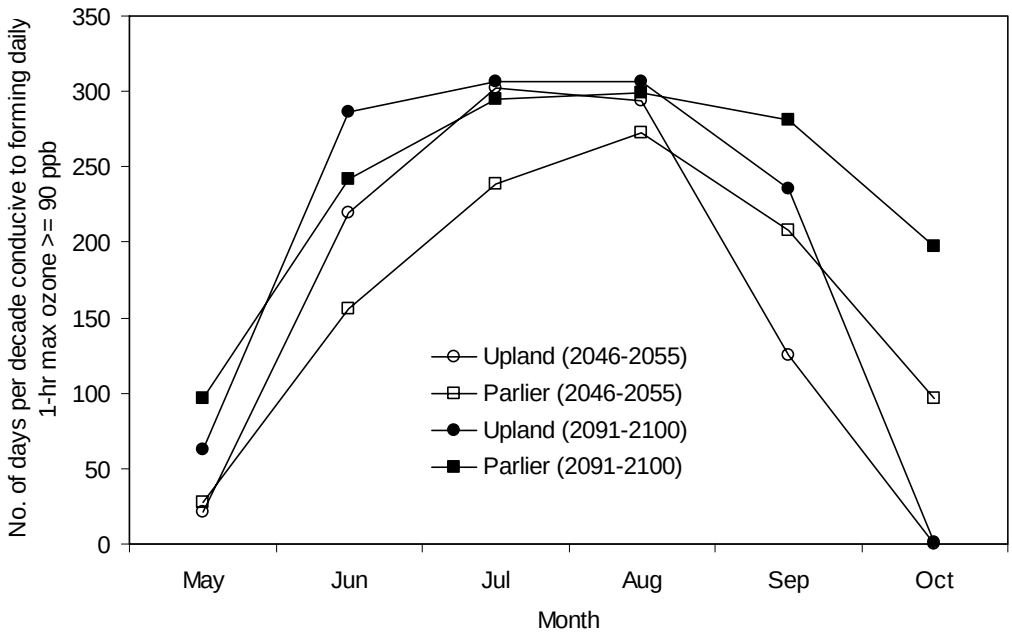

Figure 4-11: Number of days per decade conducive to the formation of daily 1-hr max ozone ≥90 ppb for 2046 – 2055 and 2091 – 2100 at Upland (SoCAB) and Parlier (SJVAB). Note that the underlying assumption for this prediction is that the emissions in CA remain at the 1990-2004 level.

Table 3 illustrates the predicted seasonal (May – October) median daily 1-hr ozone concentration for each decade over the period 2001 – 2100 at Upland (SoCAB) and Parlier (SJVAB) under the IPCC A2 and B1 emissions scenarios. Generally, the predicted median ozone increases in both the SoCAB and SJVAB over time. The seasonal median daily 1-hr ozone concentration would exceed 90 ppb as early as in 2031-2040 under the warming induced by the A2 global emissions scenario assuming emissions in California remain at the 1990-2004 level. Global Climate Models are not expected to accurately represent the weather during any given year but they should capture the meteorology over a period of decades. The GFDL CM2.1 model results were obtained for the period 1990–2000 and the T850 values were used to predict ozone concentrations based on the correlations derived in the current study. The average value of the 1-hr maximum daily ozone concentration was 84 ppb (predicted) vs. 97 ppb (measured) in the SoCAB and 83 ppb (predicted) vs. 85 ppb (measured) in the SJVAB for this period indicating that the statistical downscaling method developed in this study can effectively be used to project ozone concentrations in the future for a given air basin.

Table 4-3: Summary of predicted decadal median daily 1-hr maximum ozone concentrations under IPCC A2 and B1 global emissions scenarios at Upland (SoCAB) and Parlier (SJVAB). Note that the underlying assumption for this prediction is that the emissions in CA remain at the 1990-2004 level.

	Median ozone concentration (ppb)			
	Upland (SoCAB)		Parlier (SJVAB)	
Decade	A2	B1	A2	B1
2001-2010	84	84	86	87
2011-2020	84	87	87	87
2021-2030	86	86	88	86
2031-2040	92	87	90	89
2041-2050	90	87	90	89
2051-2060	92	87	92	88
2061-2070	97	89	93	91
2071-2080	100	91	96	90
2081-2090	105	92	97	91
2091-2100	111	91	101	92

4.4 Conclusion

The daily maximum upper air temperature at an altitude of 850 millibar pressure (T850) taken from coarse scale global model locations nearest to California's two most polluted air basins can be used to model daily 1-hr maximum surface ozone concentrations in those air basins. Other explanatory variables including wind speed, wind direction, humidity, and mixing depth did not add skills to the statistical model. There is not a one-to-one correlation between ozone and T850 extracted from the global Reanalysis dataset, but the value of T850 can be used to predict the statistical properties of the possible range of ozone concentrations. These ozone concentration distributions are approximately normal and their 25%, 50% and 75% quartile concentrations are linearly correlated with temperature. By constructing separate linear regression models for each month of the year, the effects of seasonal changes on the ozone – T850 relationship can be represented. The response of ozone to T850 is strongest in July and August and weaker in spring, early summer and fall. The sensitivity of absolute ozone concentrations to T850 has decreased over the past several decades because of changes in anthropogenic emissions. Future anthropogenic emissions trends in California will depend on the balance between population growth vs. energy conservation and the further development of efficient technologies.

The statistical relationship between coarse-scale T850 and fine scale ozone concentrations provides an efficient technique to downscale global model circulation structure to local air basin ozone concentrations. The effect of climate on future ozone concentrations can be evaluated using average emissions levels between 1990 – 2004 as a constant reference point. Projections of future temperature made by the GFDL CM2.1 global climate model combined with the historical ozone trends suggest that, by the year 2050, the number of days with conditions likely to encourage ozone concentrations greater than 90 ppb would increase by 22 - 30 days yr^{-1} under the IPCC SRES A2 emissions scenario and 6 - 13 days yr^{-1} under the B1 emissions scenario. Warmer future temperatures will require the implementation of additional emissions controls in California to offset this climate 'penalty'.

5.0 THE IMPACT OF CLIMATE CHANGE ON AIR QUALITY RELATED METEOROLOGICAL CONDITIONS IN CALIFORNIA – PART I: PRESENT TIME SIMULATION ANALYSIS

5.1 Introduction

California (CA) is more vulnerable to climate change than other areas in the United States due to its geographical location, complex topography, diverse ecosystems, intricate meso-scale meteorological features, and significant pre-existing air pollution problems ([74]; [62]). CA has been working to overcome serious summer ozone and winter particulate matter (PM) problems for multiple decades, especially in the San Joaquin Valley (SJV) and the South Coast Air Basin (SoCAB). The mountains surrounding the SJV and the SoCAB make these air basins vulnerable to air pollution problems when atmospheric conditions inhibit mixing. Atmospheric stagnation events, featuring a shallow mixing layer and low surface wind, occur in the SJV during winter and summer seasons associated with the Great Basin High Pressure (GBHP) system. The development of the atmospheric boundary layer in the SJV is also suppressed by the subsiding air associated with the valley wind during summer. In the SoCAB, a marine atmospheric boundary layer (MABL) inversion often forms due to the heated subsiding air associated with Pacific Subtropical High (PSH) and the upwelling near the coast. Each of these meteorological conditions acts to reduce atmospheric mixing, leading to stagnant conditions that trap pollutants close to the surface where they cause serious air pollution problems.

It is important to explore the future meteorology and air quality conditions in CA in order to assess the possible public health threat posed by climate change. By downscaling Global Climate Model (GCM) simulations to high-resolution outputs, previous studies have shown that climate change could induce changes in temperature, humidity, precipitation, boundary layer mixing depth, etc. on regional scales that consequently could alter regional air quality.

Mahmud et al. [103] applied statistical downscaling methods as an efficient technique to study climate impacts on ozone concentration in CA. Statistical downscaling methods ([90]) translate GCM variables directly to finer resolution outcomes with much higher efficiency than dynamically downscaling. The statistical techniques require a robust relationship between the coarse-scale variables that can be obtained directly from GCM simulations and the fine-scale variable of interest. A suitable statistical correlation between temperature at 850 millibars (T850) and surface level ozone was identified by [103]but no such relationship could be identified for PM. A full analysis of climate effects on PM must therefore be carried out using dynamic downscaling techniques.

Caldwell et al. [105] used the Weather Research and Forecasting (WRF) model to dynamically downscale Community Climate System Model ver. 3 (CCSM3) data to 12km horizontal resolution for a 40 year current period in CA with fixed greenhouse gas concentrations. Their analyses focused on precipitation, surface temperature, and snowpack, and the results show that the WRF model has an internal problem with

accurately predicting precipitation in this region, but the surface temperature predictions match the observations well. Both Bell et al. [106] and Leung and Ghan [107] studied the regional climate change in CA corresponding to double CO_2 concentration. The former study indicated a precipitation decrease in CA (and the latter study focused on temperature and precipitation extremes) and predicted more (less) frequent hot (cold) days. Duffy et al. [29] compared downscaling results from four combinations of Regional Climate Models (RCMs) and GCMs for the western US, and found that the spatial distribution of the meteorological variables can vary substantially among different RCMs due to different physics processes and surface forcing. All these studies showed that downscaled biases are largely inherited from the driving GCM. California has particularly complex topography which interacts with large-, meso-, and micro-scale flow patterns. Therefore, it is relatively difficult to capture such comprehensive meso-scale features with a regional climate model (RCM) with such coarse resolutions (i.e. greater than 12km). In order to improve the RCM downscaling results in this region, simulations with finer spatial resolution are required.

In this study, the WRF model was applied to dynamically downscale PCM ([108]) outputs under a Business As Usual (BAU) emissions scenario to 4km resolution in CA. To the best of our knowledge, there are no other dynamical downscaling studies using the WRF model with such a fine resolution to explore the climate change impacts in this region. Two seven year periods (2000-2006 and 2047-2053) were chosen to study the influence of climate change projections. It has been reported that PCM has low sensitivity to increased atmospheric CO_2 ([109], [29]). Thus a time interval of approximately 50 years was set between the current and future simulations in this study. The ultimate goal of this study is to investigate future air quality in CA, thus the analyses are focused on air quality related variables, such as wind, temperature, relative humidity, mixing layer depth, stagnation events, etc. As mentioned previously, the error of the RCM downscaling results partially succeed from GCM bias. To assess the effect of PCM data bias on the WRF downscaling results, a counterpart of the present simulations (2000-2006) is conducted with the same model configuration but driven by Global Forecast System (GFS) reanalysis data. This chapter focuses on the analysis of the current 7-year climate (2000-2006) and statistics, inter-comparisons between GFS and PCM data, and their downscaling results for the highly-polluted SoCAB and SJV. During the analysis, it was noticed that the summertime PBLH is exceptionally shallow in the SJV. This phenomenon was studied and the possible reasons were explored. Consistent with previous studies, the analysis of the present years' simulations show that the downscaling results inherit the biases of the driving GCMs through the lateral boundary conditions. In order to improve the performance of WRF downscaling, an ensemble of GCMs (CCSM3 and HadCM3, for instance) or PCM bias corrections are required which we leave for future work. The present versus future simulations driven by PCM data will be analyzed, and the climate change impacts on the air quality related meteorological conditions, including land-sea breeze, in CA will be investigated in chapter 6 of this report.

The present chapter is organized as follows: the methodology and numerical models are described in Section 5.3.2. The numerical simulations, run with six different suites of physics schemes in order to choose the best combination for the regions of interests, are

presented in Section 5.3.3. Section 5.3.4 contains the comparison of the present years' simulation results driven by PCM and GFS data, together with the investigation of summertime low PBLH phenomenon in SJV. Finally, conclusions and remarks are addressed in the end.

5.2 Methodology and Model Description

5.2.1 Methodology

Dynamical downscaling refers to a method of using an RCM to obtain regional-scale, fine-resolution climate change information from a coarse-resolution GCM (i.e., GCM data provide the initial and lateral boundary conditions for the RCM). This method retains the large-scale features of the climate projection from the GCM with a more detailed depiction of meso-scale features ([110]). Dynamic downscaling is one way to investigate the climate change impacts on meteorology and air quality in specific areas. In this study, the Weather Research and Forecasting (WRF) model ([111]), a community meso-scale meteorology model, is applied to dynamically downscale PCM data under the Business As Usual (BAU) scenario (IPCC Emissions Scenario, 2000) to investigate the meteorological conditions in CA, especially in the SJV and SoCAB. As described in the introduction, the air quality in SJV and SoCAB are largely influenced by meso-scale systems (i.e. valley wind, stagnation events, and MABL etc.), which could not be resolved in PCM due to the coarse spatial (2.8°x2.8°) and temporal resolution (6 hourly). The WRF simulations with much finer resolution add substantive meso-scale details to the driving PCM, which are crucial to study the air quality conditions in the SJV and SoCAB. Hourly averaged WRF outputs were calculated within the model and saved every hour for three-dimensional (3D) meteorological variables needed for air pollution calculations, such as wind, temperature, and humidity, and two-dimensional variables, such as the mixing layer height, precipitation, etc. These hourly averaged variables were used to evaluate WRF performance, as most observation data are hourly averaged from field experiments, and they were used as the meteorological inputs for air quality calculations. Two seven-year periods, 2000-2006 and 2047-2053, were chosen to include approximately one El Niño cycle for present and future conditions. The dynamical downscaling approach is computationally expensive and it is not necessary to simulate every day of the seven-year period to capture the essence of the El-Nino Southern Oscillation (ENSO) signal. In the current study, the computation burden was reduced by simulating two weeks out of every six weeks (as shown in Table 1) within the 21 years that were studied (e.g., 14 years with PCM data and 7 years with GFS data). A three day "spin-up" period was requested for air quality analysis to minimize the impact of initial conditions on final results, and so each simulation period was expanded to 17 rather than 14 days. Due to the fact that PCM only has 28 days' simulation for February in leap years, there is a one day shift between the cases for normal years and leap years to avoid February 29th in leap years.

GFS reanalysis data have been widely used for meso-scale meteorology simulations and are available every six hours with a horizontal resolution of 1°x1°. The data set assimilated many observations, including satellite data and, in general, is good quality.

Therefore, identical simulations were carried out using GFS reanalysis data for 2000-2006 to compare results produced by GCM initial / boundary conditions and actual initial / boundary conditions. By comparing the downscaling results between simulations driven by PCM data and GFS data, as well as the climatology from these two global datasets, the PCM data bias can be estimated and the degree to which the GCM data bias is passed to the downscaling results can be identified.

Table 5-1: Simulation cases for normal and leap years.

	Case1	Case2	Case3	Case4	Case5	Case6	Case7	Case8	Case9
Normal years	01/01-01/18	02/12-03/ 01	03/26-04/12	05/07-05/24	06/18-07/05	07/30-08/16	09/10-09/27	10/22-11/08	12/03-12/20
Leap years	01/01-01/18	02/11-02/28	03/25-04/11	05/06-05/23	06/17-07/04	07/29-08/15	09/09-09/26	10/21-11/07	12/02-12/19

5.2.2 PCM model

PCM is a fully coupled GCM. It is comprised of the NCAR Community Climate Model version 3 (CCM3), the Los Alamos National Laboratory Parallel Ocean Program (POP), the sea ice model from the Naval Postgraduate School, and the land surface biophysics model ([112]; [108]). The atmosphere component of PCM has a T42 horizontal resolution, which is approximately 2.8 degree in latitude and longitude, and 18 vertical hybrid sigma-pressure levels. The ocean component of PCM has a higher resolution than most other GCMs near the equator, which leads to stronger El Niño signal and inter-annual tropical climate variability ([108]). PCM simulations have been conducted under different greenhouse gas scenarios. In this study, the atmospheric component of the BAU B06.44 simulation, which spans the period of 1995-2099 with CO_2 increasing by 1% per year, were used to provide initial and boundary conditions for WRF downscaling.

5.2.3 WRF model and the interface between WPS and PCM

WRF is a community meso-scale meteorology model, which is suitable for both operational forecasting and atmospheric research needs. The development of WRF has been a collaborative work among several research institutes. The Advanced Research WRF core (ARW) version 2.2 ([111]; [113]) was adopted in this study. The fluid in WRF ARW is treated as fully compressible and non-hydrostatic. WRF uses terrain following vertical coordinates and the variables are horizontally staggered on an Arakawa C-grid. The governing equations are written in flux form so that mass and dry entropy are conserved. The third order Runge-Kutta scheme with time splitting technique is used for temporal integration, and the 3rd and 5th order advection schemes were chosen for the vertical and horizontal directions, respectively.

The WRF Preprocessing System (WPS), which reads in the global data and interpolates information to the WRF simulation grid, could not process PCM output data directly. Therefore, an interface program was developed to bridge PCM and WPS. The 3D variables, such as wind and temperature, were interpolated to twenty one fixed pressure levels; 2-m temperature and humidity, and 10-m wind were attained by vertically

interpolating the corresponding surface and the lowest level of 3D variables. For snow and soil related variables, daily data were available only from PCM and were used to derive 6-hourly data for WRF simulations.

5.2.4 WRF basic configuration

Three domains with two-way nesting were configured for the WRF simulations. The horizontal resolutions for domains 1-3 were 36 km, 12 km and 4 km (Figure 5-1), respectively, and the vertical direction had 31 stretched sigma levels. The time step for domain 1 was 180 seconds. The finest resolution (4km) domain (i.e., domain 3), which encompasses the entire state of CA, increases the model's capability to capture meso-scale features under complex topography and intricate flow patterns in this area. In order to choose the most suitable physics parameters for this study, simulations for year 2000 with six different suites of physics schemes were examined and compared with observations, which will be described in the next section. To avoid the drifting of larger scale features after long-term integration, Four Dimensional Data Assimilation (FDDA) was applied to domain 1 using the driving global data (PCM or GFS) during the 17 days' integration. The sea surface temperature (SST) was updated every two days for domain 1.

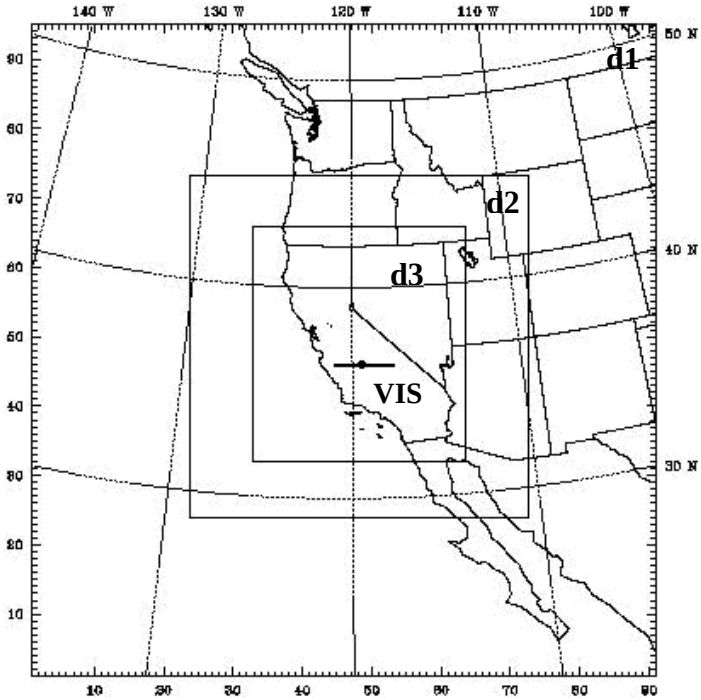

Figure 5-1: Nested domains for WRF simulations. The black dot shows the location of the observation station 'VIS'. The line in domain 3 (d3) crossing 'VIS' indicates the location of the vertical cross session in Figure 5-14.

5.3 Tests of different physics schemes in WRF

5.3.1 Numerical experiments design

The various physics schemes available in WRF perform differently depending on the domain topography and the overall meteorological conditions being simulated. In this section, six suites of physics schemes (Table 2), in combination with various planetary boundary layer (PBL) parameterization, cumulus parameterization, and microphysics, were tested for the whole year 2000 driven by GFS data. The temperature and moisture flux profiles in the boundary layer are primarily determined by the PBL parameterization, thus this physics component is crucial for the simulation of air pollution within the boundary layer. Precipitation, which is mainly handled by cumulus parameterization and microphysics, is another main factor affecting the regional air quality as rainfall can scavenge air-borne pollutants and potentially modify low-level meteorology conditions due to changes in soil moisture.

GFS reanalysis data, instead of PCM data, were used for these simulations because GFS data more closely represents conditions in California due to the assimilation of measured meteorological parameters. As a result, the best model configurations selected from the simulations driven by GFS data are more reliable and more likely to reflect the actual WRF performance for our focus regions.

The PBL parameterizations studied included the Yonsei University (YSU) scheme ([114]) and the Mellor-Yamada-Janjic TKE scheme (MYJ) ([115]; [116]); the cumulus parameterizations compared included the Kain- Fritsch (KF) ([117]) scheme and the Grell-Devenyi ([118]) scheme; and the microphysics parameterizations studied included the Thompson scheme ([119]) and WRF single-momentum 6-class scheme (WSM6) ([120]). There was no cumulus parameterization for the 3rd domain due to its fine resolution. All simulations used the Rapid Radiation Transfer Model (RRTM) long-wave ([121]) and the Dudhia short-wave radiation scheme ([122]). Other model configurations were described in Section 5.2.

GFS - WRF simulations were carried out for each day of the year 2000, with each month split into two runs. The first run included the first 15 days of the month, and the second run included the rest of the month. No aforementioned extra 3 days were added into the integration period in these simulations since the results were only used to select the optimum configuration for WRF, not to drive air quality simulations.

Table 5-2. Six suites of physics schemes for WRF simulations

	Suite 1	*Suite 2*	*Suite 3*	*Suite 4*	*Suite 5*	*Suite 6*
PBL	*YSU*	*YSU*	*MYJ*	*MYJ*	*YSU*	*MYJ*
Cumu.	*KF*	*Grell*	*KF*	*Grell*	*Grell*	*Grell*
Micro.	*Thomp.*	*Thomp.*	*Thomp.*	*Thomp.*	*WSM6*	*WSM6*

5.3.2 Results analysis

The GFS – WRF simulation results from the 3rd domain were compared with hourly observations collected from the stations operated by the California Air Resource Board (CARB) during the year 2000 to evaluate WRF performance with the six physics suites. The number of observation stations varies depending on the variable of interest; there were approximately forty stations for surface temperature and humidity, and ten stations for surface wind. Figure 5-2 shows the state-wide averaged seasonal Root Mean Square Error (RMSE) of WRF simulated results (10-m x-component wind (U10), 10-m y-component wind (V10), 2-m temperature (T2), and 2-m relative humidity (RH2)) compared with measurements. In general, the wind error in summertime is larger than that in wintertime, while the thermodynamic fields (e.g., temperature and moisture) show the opposite trend. It is noticed that with the YSU PBL scheme (suite1, 2 and 5), the model performs better for the surface wind and relative humidity in terms of RMSE. Suite 5 performs the best for simulated winter surface temperature, but not for the other three seasons.

The results were further evaluated using another method, which is named "persistent score": For each observed variable (e.g., 2-m T), the suite with the best performance at each station, for each time point was identified and given one point, while all other suites were given zero. The suites' final scores for each variable were divided by the total number of comparisons (i.e., the total number of records for each variable), which gives the percentage of the persistent significance for each suite, ranging from 0 to 1, as shown in Figure 5-3. The persistent score helps confirm the relative performance (station-wise and time-wise) of the six suites. It was seen that WRF with suite 5 physics schemes systematically performed better for the relative humidity and surface wind, which are important to air pollution studies; however, results for T2 were not superior to others when evaluated by either method. It is interesting to see that results from suites 1 and 2 were not better than those from suites 3, 4, and 6, while the RMSEs were much better. This might be due to a relatively small portion of excellent results (i.e., extremely small errors for those data) that brought down the total RMSE (Figure 5-2), but the simulations were not consistently better all the time (Figure 5-3).

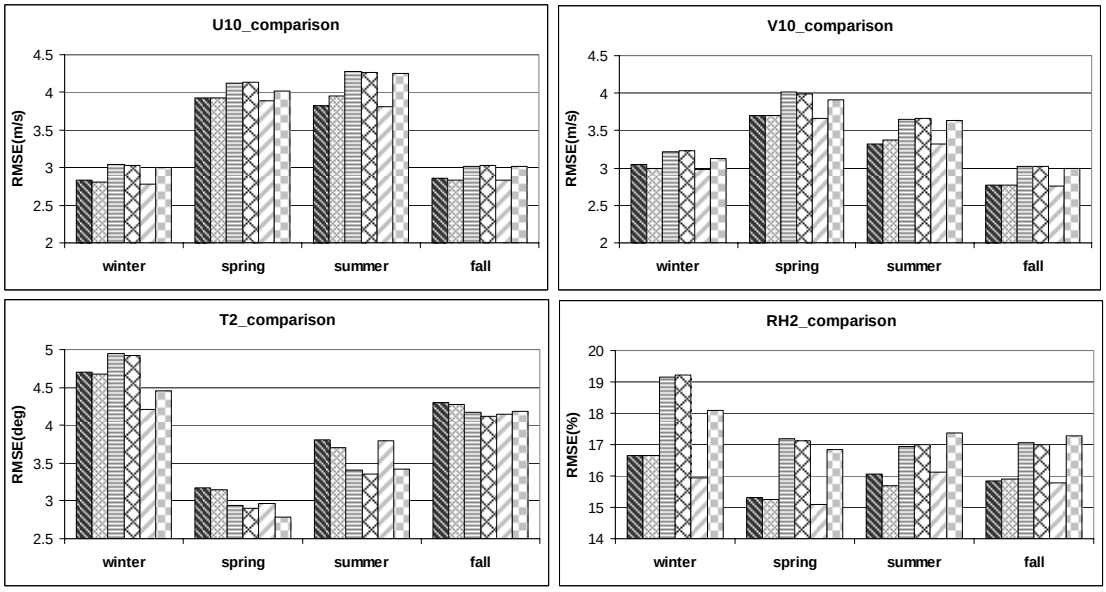

Figure 5-2: Seasonal RMSE of model simulated U10, V10, T2 and RH2 with the six suites of physics schemes compared to observation data averaged over all stations in CA. The six suites are listed in order in the plots.

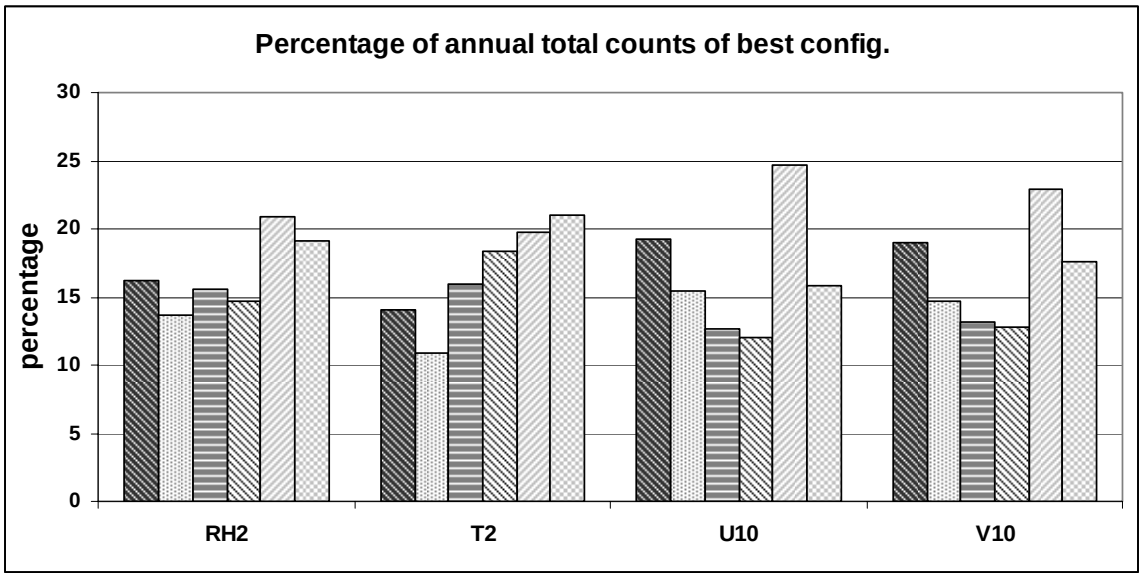

Figure 5-3: Persistent scores: percentage with which each suite performed the best with respect to RH2, T2, U10 and V10. The total counts for T2, RH2, and wind component comparisons are 55833, 45837 and 14883, respectively.

Both RMSE and the persistent score suggest that suite 5 is the best physics combination for the CA area. Results from simulated upper-air data, such as 500mb winds and height, 850mb temperature and water vapor mixing ratio, were compared to the GFS reanalysis using both comparison methods as well (plots not shown), and the same conclusion was

obtained. Therefore, the physics schemes in suite 5 were applied to the later simulations in this study.

5.4 Downscaling Results Analysis

5.4.1 Downscaling results driven by PCM vs. GFS data

After ten years spin-up time and fifty years adjustment period, the fully coupled PCM integrated for ~100 years to establish the B06.44 BAU emissions scenario data, which was used to drive WRF simulations in this study. There was no adjustment to observations during the hundred years' PCM simulation. The difference between PCM data and NCEP's GFS reanalysis data can be significant. Likewise, the downscaling results driven by these two different types of global data can also vary substantially. GFS data are treated as unbiased in this subsection, so that the PCM data and the downscaling results can be evaluated by comparison with their GFS counterparts. The analysis further assumes that systematic WRF errors (i.e., biases) are consistent between both downscaling runs.

T2, 10-m wind speed (wsp10) and PBLH of the downscaling results were averaged over seven years (2000-2006) for summer (=simulation cases 5 & 6; see Table 1) and winter (=simulation cases1, 2 & 9). The differences of the seasonal means between PCM-WRF and GFS-WRF results were calculated and are shown in Figure 5-4. The analyses focused on summer and winter since these seasons account for the majority of the ozone and PM episodes in CA.

Figure 5-4a shows that surface temperature from the PCM-WRF downscaling results were overestimated over the Pacific Ocean, the coastal region (especially southern CA), and most of the San Francisco Bay Area, whereas surface temperature was underestimated inland. The under prediction is slightly smaller in the Central Valley than other areas in CA. Land-sea temperature contrast is the most important factor for the formation of land-sea breeze, which is an evident phenomenon along the CA coastline that plays a major role in weather and air quality, especially during the summer. The disparity in T2 difference between the coast region of CA and the adjacent ocean shown in Figure 5-4a suggests that these two sets of simulations predict dissimilar land-sea breezes. The summertime wsp10 differences along the coastline, as shown in Figure 5-4c, also indicate a difference in the land-sea breeze. More details of land-sea breeze in CA and its future changes will be explored in chapter 4. During winter, PCM-WRF simulations underestimated T2 for almost the entire analysis domain, except for the adjacent Pacific Ocean of Southern CA and Mexico. The negative bias increased with distance inland and was as great as -4° to -5° in some regions. The underestimation of surface temperature overland was opposite from what was found from the WRF simulation for the present time period in [105], which was proven to be inherited from the driving CCSM3.

In regard to surface wind speed, an obvious overestimation (~3m/s) appeared in the ocean area off the coast of northern CA during summer (Figure 5-4c). There were no strong

wind speed differences in the Central Valley for summer (Figure 5-4c), while a slight overestimation occurred during winter in this region (Figure 5-4d). Evident wind speed over prediction appeared in most parts of SoCAB, particularly during winter. Overall, the surface wind speed bias from the PCM-WRF simulation was more significant during winter than summer for the inland part of the analysis domain, taking into account that the surface wind is generally weaker in winter than in summer in CA

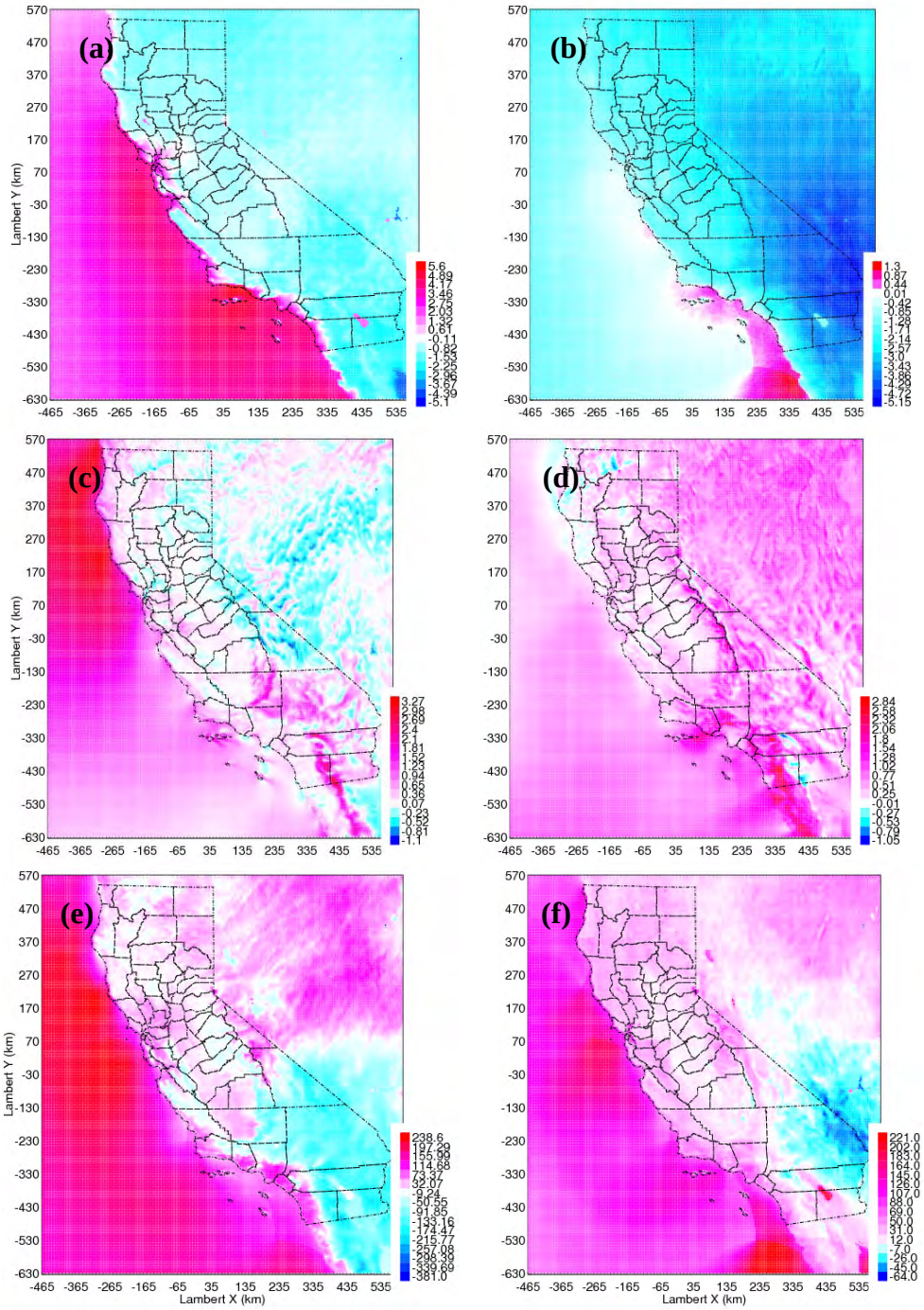

Figure 5-4: Spatial distribution of differences between 7-year averaged WRF results driven by PCM and GFS data (PCM-WRF – GFS-WRF) for T2 (units are in °K) during (a) summer and (b) winter; wsp10 (units are in ms^{-1}) during (c) summer and (d) winter; and PBLH (units are in m) during (e) summer and (f) winter

For downscaled PBLH, the seven-year averaged value from GFS-WRF simulations was around 300-400m in SJV and was even lower in Los Angeles County (LAC) during summer (Figure 5-5a). The former is due to the high pressure system and valley wind (see discussion in Section 5.4.3), while the latter is due to the existence of a marine

atmospheric boundary layer inversion ([123]). The wintertime average PBLH from GFS-WRF simulations was about 200m over SJV and SoCAB (Figure 5-5b). The summertime PBLH bias (Figure 5-4e) from PCM-WRF was within 50m in SJV; while for SoCAB, the bias in the coast (inland) part was around ±100m. The wintertime PCM-WRF PBLH bias (Figure 5-4f) was over 50m for LAC, and relatively small in SJV and other regions of SoCAB. Considering the low PBLH present in these regions, the over predictions in LAC and SJV during both summer and winter were obvious, and it was more substantial in LAC.

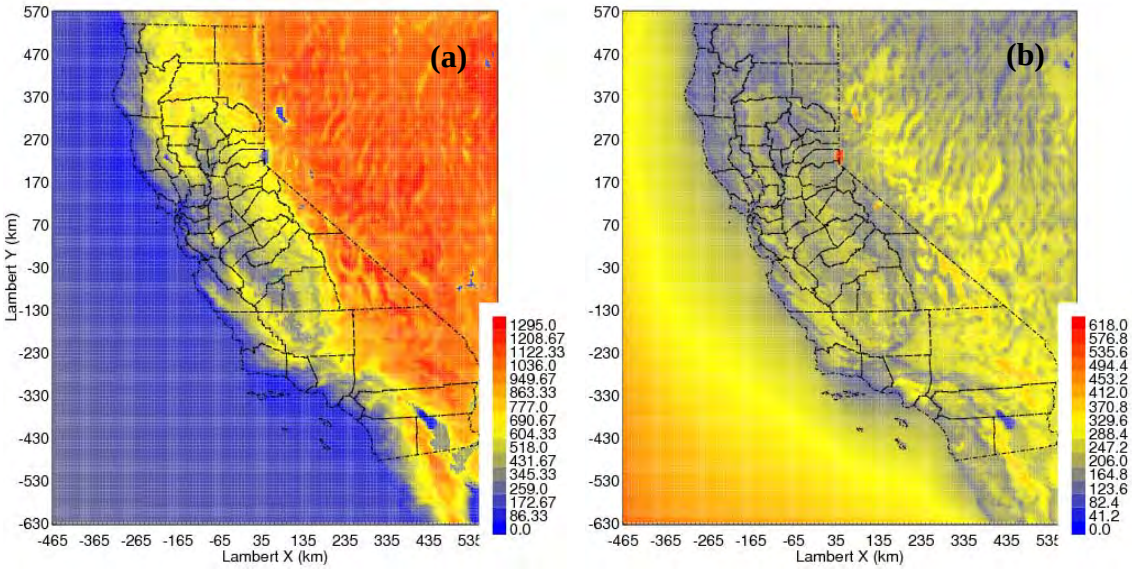

Figure 5-5: Seven-year averaged PBLH from GFS-WRF simulation during (a) summer and (b) winter. Units are in m.

Overall, the downscaling results driven by PCM data underestimated surface temperature and overestimated surface wind and PBLH in SJV and SoCAB (more notably in LAC), which implies that using these downscaling results as input for air quality models would underestimate the air pollution problems in these regions, particularly in LAC.

To investigate the sources of the differences between the GFS-WRF and PCM-WRF simulations, the climatology from the original PCM and GFS data for a much larger region was analyzed. GFS data were averaged to the horizontal resolution of the PCM data to make the comparison easier. Comparing the summertime plots in Figure 5-6 (including color-filled surface temperature, sea level pressure contours, and surface wind vectors), the PSH in PCM (Figure 5-6a) data was stronger and further north. The pressure gradient difference between the two global data (i.e., stronger in PCM due to stronger PSH) could partially explain the higher wsp10 present off the coast of northern CA in the PCM-WRF results (Figure 5-4c). The more northern location of the PSH reduced the ability of cold air in Canada to move south in PCM due to the blocking effect of the coast mountain range in Canada. Therefore, more cold air intruded south and dominated larger areas of inland CA and the adjacent Pacific Ocean in GFS than in PCM data. This explains the positive surface temperature difference between the downscaling results

driven by PCM and GFS data over the Pacific Ocean during summer (Figure 5-4a). In contrast, the under-prediction of inland T2 by PCM-WRF (Figure 5-4a) was not present in the original PCM, thus it was generated by the downscaling process. Another feature shown in Figure 5-6 is that the North American Thermal Low (NATL) was well developed in PCM data during summer but not in GFS (Figure 5-6a vs. 5-6b).

Figure 5-7 shows the averaged 500mb height field from PCM and GFS data in summer. There was a trough located right above the west coast in both models. However, the pressure gradient upstream of the trough was stronger in PCM data. This might explain why the PSH in PCM was stronger and further north (i.e., a stronger wind for a stronger negative vorticity advection). Note that the wind vectors shown in Figure 5-6 around the PSH do not represent the real wind field. The movement of the PSH causes a substantial change of the wind field at a certain point of the domain, and therefore both the wind speed and wind direction are cancelled out considerably when the seasonal averages are calculated.

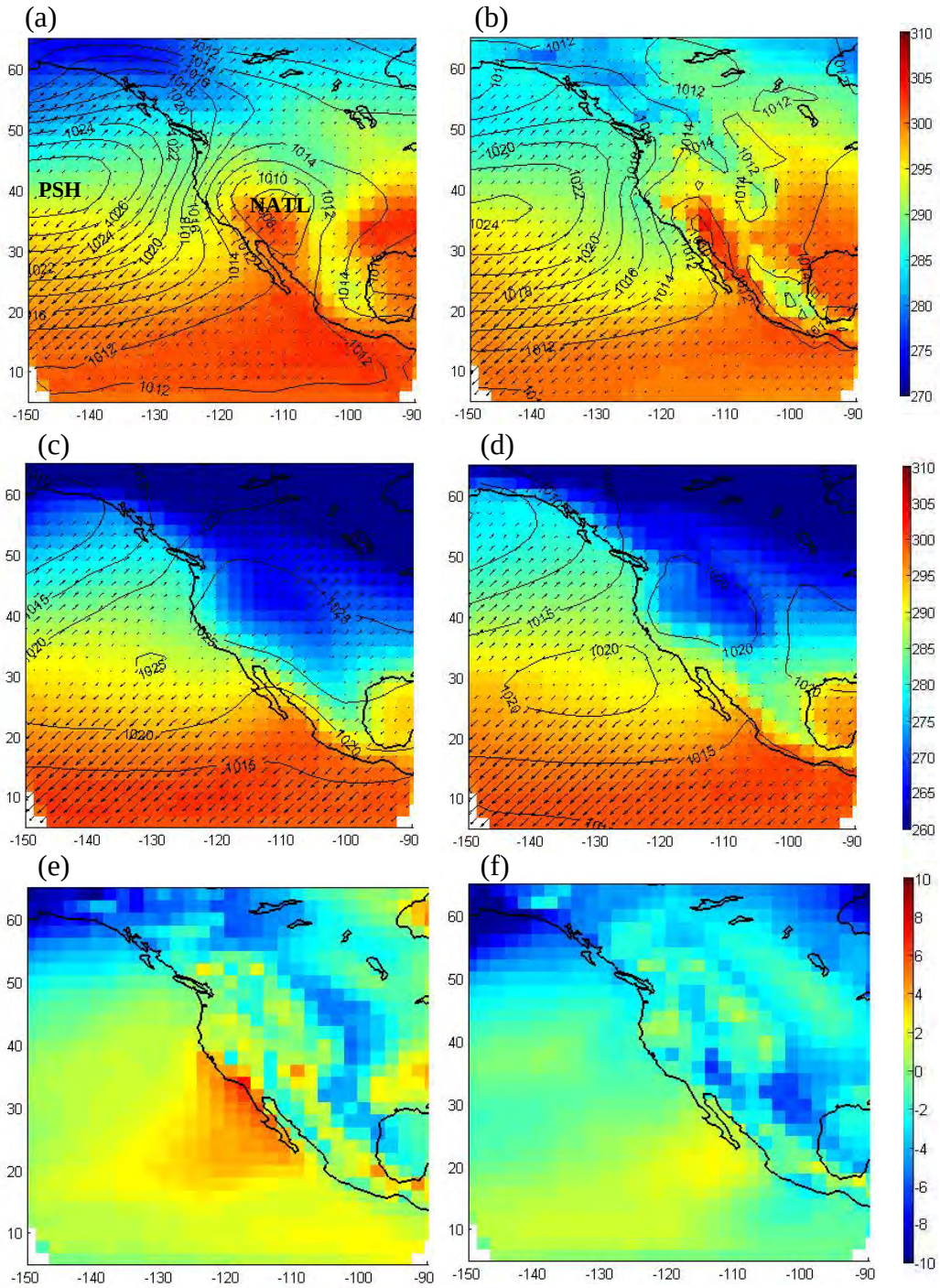

Figure 5-6: Spatial distribution of 7- year averaged T2 (shading, units in °K), sea level pressure (contour lines, units in mb) and wind vectors of (a) PCM data for summer, (b) GFS data for summer, (c) PCM data for winter, (d) GFS data for winter; and T2 difference between PCM data and GFS data (PCM – GFS) for (e) summer and (f) winter.

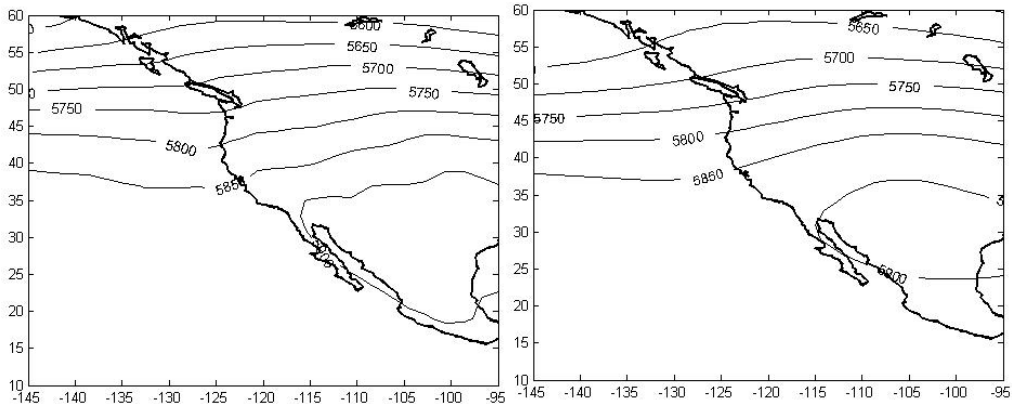

Figure 5-7: Seven year averaged 500mb height field of PCM (left) and GFS (right) data during summer. Units are in m.

Comparing Figures 5-4a and 5-6e, the similarity is obvious over the Pacific Ocean adjacent to CA, where the biases in 2-m temperature from both PCM data and the downscaling results are up to 4-5°. PCM data had a small warm bias (approximately 1-2°) for inland CA, while the downscaling results had small cold bias (approximately -1°). The possible reasons are: 1) the complex topography in CA might introduce extra error when interpolating coarse global data to fine resolution WRF simulations close to the surface; and 2) the summer means were averaged over case 5 (June 18th - July 05) and 6 (July 30th - August 16th) for the downscaling results, but the whole three months (June, July and August) for PCM data, so some discrepancy between the two is expected.

Compared to summertime, the wintertime climatology patterns from PCM (Figure 5-6c) and GFS (Figure 5-6d) data were more similar. This might be due to stronger signals in wintertime (e.g., baroclinic zone). However, it is noted that the high pressure system over the western US was well formed and elongated northwest-southeastward from PCM. This helped transport cold air more efficiently from southern Canada and the northern US southward. As a result, strong cold T2 anomalies between PCM data and GFS occurred in Texas and Arizona (Figure 5-6f), and this was carried over to southeastern CA through downscaling (Figure 5-4b).

Overall, the strength and position of the PSH, which determines the amount and pattern of cold air in Canada intruding south, played an important role in the difference between PCM and GFS data in summer. Thermal lows (highs) in summer (winter) over the western US also contributed to the difference between these two global models to some extent. PCM bias corrections are needed in order to improve the downscaling results.

5.4.2 Surface comparison between simulation results and observation data

In order to evaluate the model performance, the simulation results were compared with METAR surface weather observation data, which are available at 66 stations in the SoCAB and 12 stations in the SJV during the 2000-2006 period. This comparison provides a way to explore the simulation error internal to the WRF model for these

specific areas with this model configuration. Unsurprisingly, the GFS-WRF predictions generally matched the observations better than the PCM-WRF predictions.

Figure 5-8 shows the surface temperature bias of the simulations driven by GFS (dark gray) and PCM (light gray) data averaged over seven years and spatially over all stations in SoCAB (Figure 5-8a) and SJV (Figure 5-8b). Simulations with GFS data overestimated surface temperature for both SoCAB and SJV. WRF performed worse in winter than summer, and the wintertime simulation was worse in the SJV than in the SoCAB. The possible reason for this trend is that winter temperature inversions are typically stronger in the SJV than in the SoCAB. WRF is known to have difficulty simulating the conditions within the shallow boundary layer associated with these temperature inversions. The surface temperature overestimation from PCM-WRF simulations was obvious during fall (cases 7 and 8). The bias comparisons between simulations with the two global datasets are consistent with Figures 5-4a and 5-4b, which show that the simulations with PCM data predicted lower surface temperature overland during summer and winter. The general ± 2° bias for surface temperature from GFS-WRF is generally acceptable considering the complex topography and meso-scale flow patterns in CA. The downscaling results with PCM data had an exceptionally warm bias for case 7, which spans September 9th to 26th, in both regions. Figure 5-9 compares the PCM and GFS difference during this specific time using the same format employed for Figures 5-6a and 5-6b. The overall weather patterns for case 7 were similar to those shown in Figures 5-6a and 5-6b. The PSH weakened in both of the global datasets during fall. The PSH in GFS data helped to bring the cold air from Canada to the western US. In contrast, the PSH in PCM data was elongated to the northeast relative to the one shown in Figure 5-6a, constraining the cold air to latitudes over 45°N. Consequently, the surface temperature differences between the two global data as well as between the simulation results were quite significant in CA for case 7.

(a)

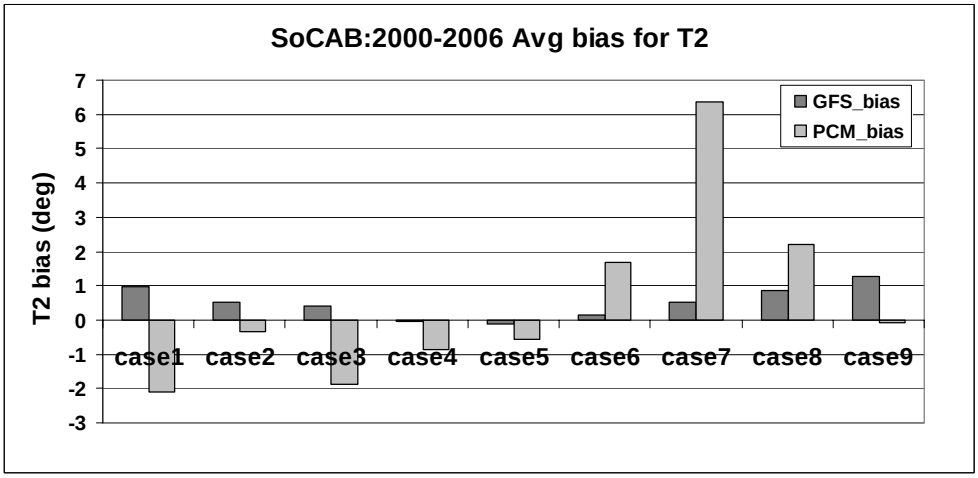

(b)

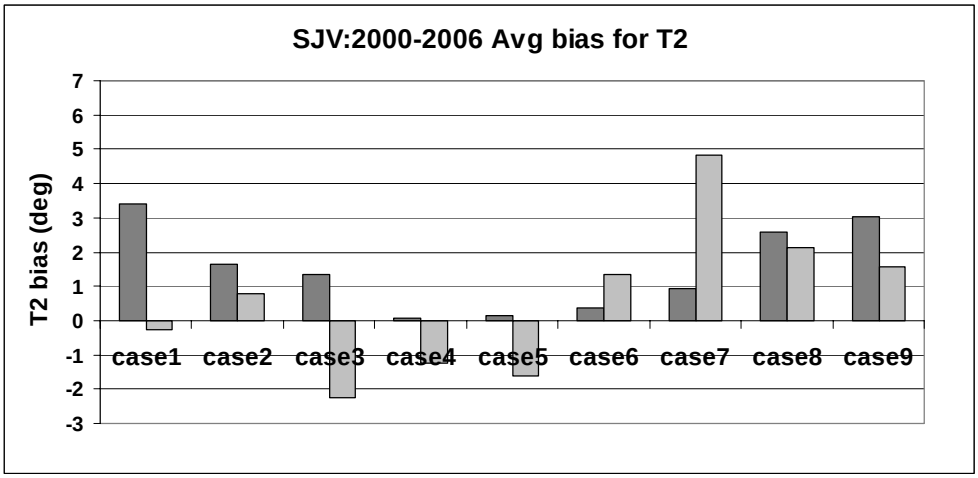

Figure 5-8: Seven-year averaged T2 bias over (a) SoCAB and (b) SJV for each simulation case driven by GFS and PCM data.

(a) (b)

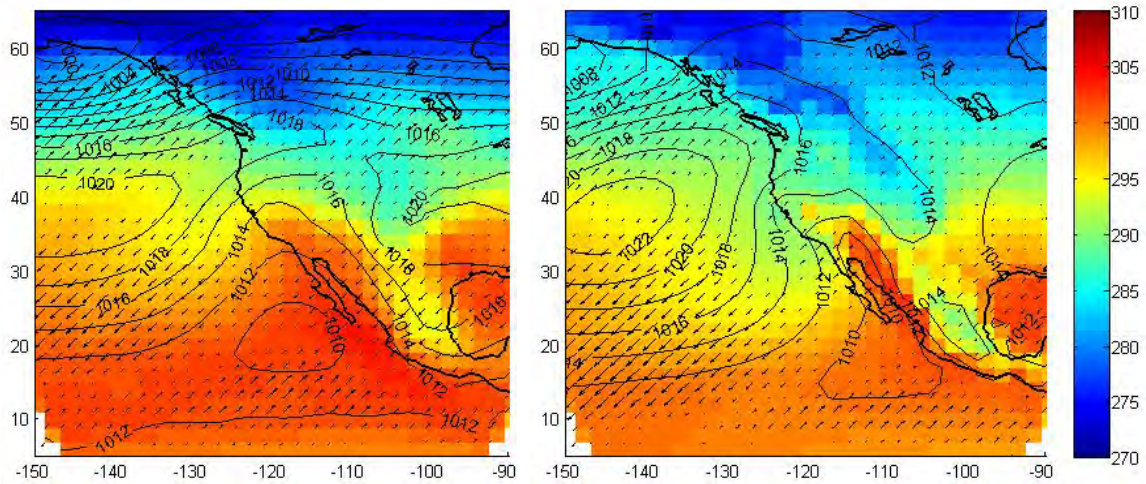

Figure 5-9: (a) and (b) are the same as Figures 5-6a and 5-6b, respectively, but during case 7.

Figure 5-10 shows the wsp10 bias of each simulation case averaged over the seven year study period 2000-06. Both simulations overestimated surface wind for most cases. The much greater overestimation from the simulation with PCM data in the SoCAB during winter (cases 1, 8 and 9) was also shown in Figure 5-4d. The smaller values of bias in SJV could be due to the overall lower wind in the SJV than in the SoCAB. In general, WRF had lower wsp10 bias during summer than winter, though both seasons are known to have relatively calm wind due to the influence of the PSH moving inland. Note that the seasonal trend of model performance for surface wind are opposite in Figure 5-2 and Figure 5-10. The variable shown in Figure 5-2 is RMSE while Figure 5-10 shows bias. Figure 5-2 illustrates results for every day of the year 2000 while Figure 5-10 illustrates results for 1000 days between the years 2000-06. The bigger RMSE but smaller bias during summer can appear if model simulations have a larger uncertainty and the errors are mostly cancelled out due to the opposite signs. Both Figure 5-2 and Figure 5-10 show that WRF surface temperature predictions performed better during summer than winter.

(a)

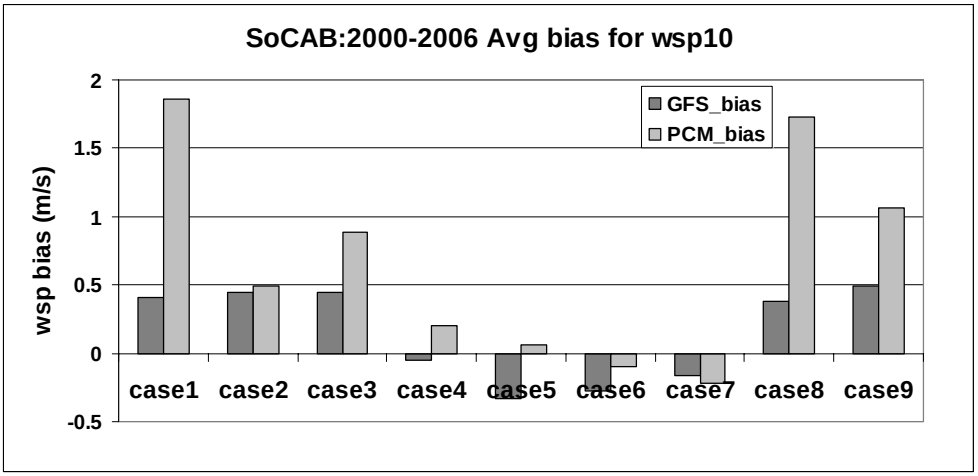

(b)

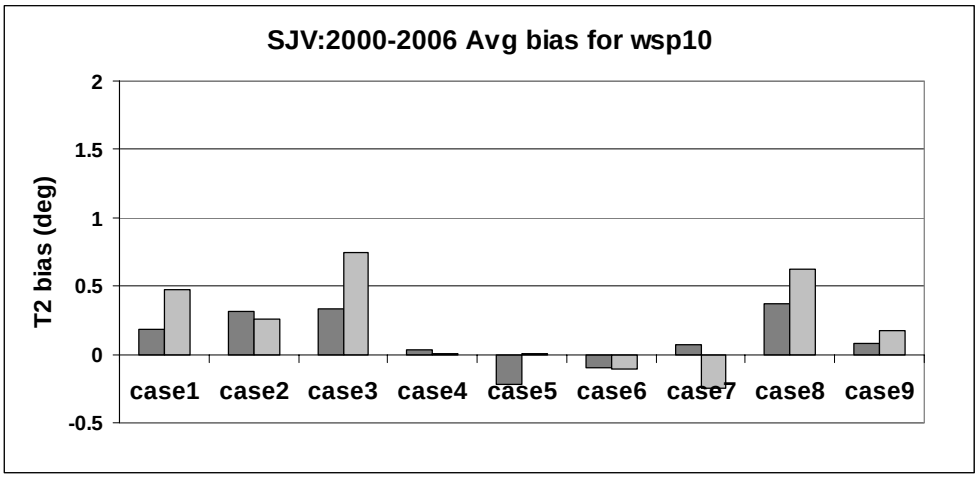

Figure 5-10: Same as Figure 5-8, but for 10-m wind speed.

The magnitudes of the PCM-WRF summertime wsp10 bias were relatively small (less than 0.3m/s) in both the SJV and SoCAB. However, when the WRF results were used as input for the UCD/CIT air quality model, none of the historical high ozone episodes that happened during summer 2000 in SoCAB and SJV were reproduced (figure not shown). The emission inventories and chemical reaction rates employed by the UCD/CIT air quality model have been used to reproduce numerous air quality episodes when diagnostic meteorological fields are used as model input. This strongly suggests that the ozone under-predictions are largely caused by the driving meteorological conditions provided by the WRF simulations. Several air quality model sensitivity tests were conducted by perturbing the temperature and PBLH, which are closely related to ozone concentrations. After eliminating both of these two factors, the surface wind becomes the only possible factor causing under-predictions in simulated ozone concentrations.

Generally, high ozone episodes in the SJV and SoCAB occur during stagnant events, when winds are very calm. Previous studies have shown that WRF has difficulties in capturing the strength of stagnant events and the accompanying low surface wind speed ([124]; [125]). The possible reason might be that the vertical resolution is not high enough within the low boundary layer during the stagnation events to resolve the associated wind accurately. To explore the possibility of this problem in our simulations, the model bias and RMSE were calculated with respect to the observed surface wind speeds. The observed wind speed has discrete values due to the precision of 0.5 ms^{-1} in METAR observation data. Similar results were found both in the SoCAB and SJV, thus only the results for SoCAB are shown in Figure 5-11. Note that over 80% of the observed wsp10 was under 5ms^{-1}, which is the reason why the range of the errors shown in Figure 5-10a are quite different from Figure 5-11a. It is obvious that for very calm wind ($\leq$1.5 ms^{-1}), WRF simulations with both datasets had a relatively large bias and high RMSE. Taking into account the small values of the corresponding wind speed observations, these biases & RMSEs are even more substantial. PCM-WRF results also had relatively large bias (underestimated) and high RMSE during high winds. The linear nature of the trends shown in Figure 5-10a suggests that WRF consistently predicts surface wind speeds of 3-4 ms^{-1} even when actual conditions vary significantly from this value. Ozone events simply do not occur when wind speed is this high, explaining the failure of the modeling system to reproduce summer ozone events.

The difficulty of accurately simulating low surface wind poses a major challenge for the WRF model that must be resolved to provide meteorological inputs for air quality simulations in regions with extreme topography like CA. Potential methods of increasing the vertical resolution within the boundary layer or increasing the surface roughness have been suggested and tested within the WRF community. Each of these approaches is the subject of research beyond the scope of the current project.

(a)

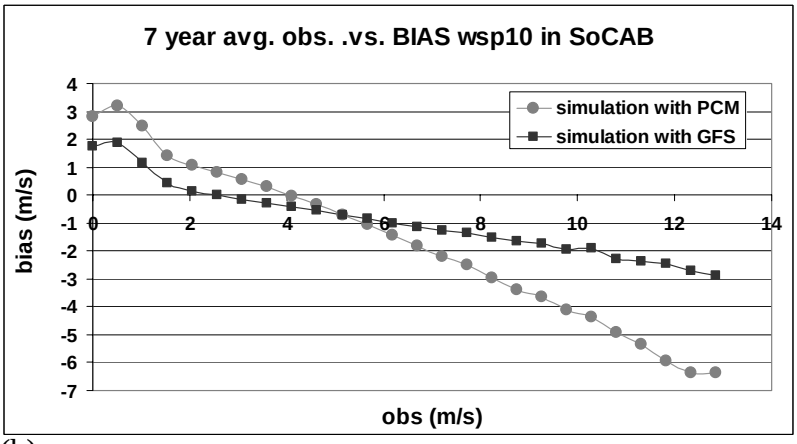

(b)

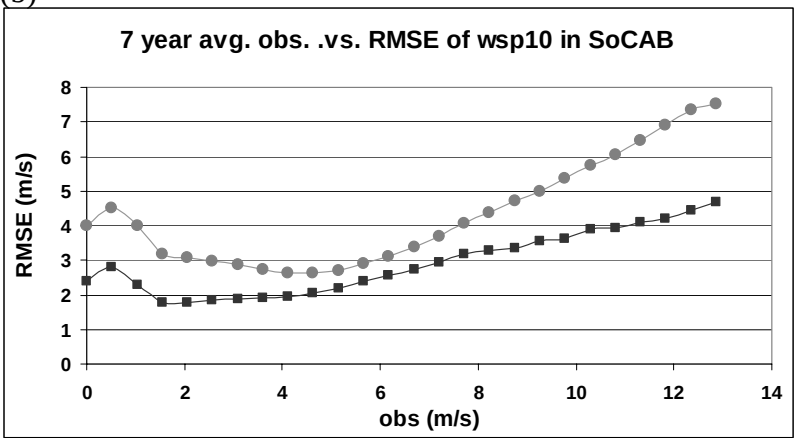

Figure 5-11: 7-year averaged model (a) bias and (b) RMSE with respect to observed wind speed in SoCAB.

The analyses in this section show that GFS-WRF runs overestimated the surface temperature. The surface winds were, in general, substantially overestimated for calm wind conditions and underestimated in high wind conditions. WRF performance was better during summer than other seasons. These patterns very likely represent the WRF systemic error (i.e., bias) in this region.

5.4.3. Low PBLH during summer

As PBLH is one of the most important meteorological inputs to air quality model simulations, more investigation was carried out on this variable. It was mentioned in section 5.4.1 that the 7-year averaged summer PBLH was about 300-400m in the Central Valley, yet at the same latitude in Nevada the PBLH was over 1000m (Figure 5-5a), despite the fact that the surface temperature in the Central Valley is higher (over 3° K) than that in Nevada at the same latitude (figure not shown). In general, the high temperature overland during summer could promote vertical convection, which results in

high summer PBLH. The possible reasons for the low summer PBLH in the Central Valley are explored in this section.

Figure 5-12 shows the three year (2004-2006) averaged daily maximum PBLH from observation data, and PCM-WRF and GFS-WRF simulations at station VIS (the location is shown in Figure 5-1) in the SJV. Observations were only available for three years of the study period. The observed PBLH was derived from a vertical temperature profile obtained from a Radio Acoustic Sounding System (RASS) located at VIS using the dry adiabatic lapse rate for comparison. The observed values of PBLH (pblh_OBS) shown in Figure 5-12 are the seven day averaged daily maximum PBLH; the purpose of calculating the average is to smooth the small variation in the original observation data and better perceive the seasonal pattern. Figure 5-12 illustrates that the PBLH at VIS is shallow during the summertime. The WRF results with both global datasets consistently overestimated PBLH for most of the year. The PBLH from the GFS-WRF simulations was significantly better than that from PCM-WRF during the springtime. Overall, Figure 5-12 shows that both PCM and GFS-WRF simulations captured the seasonal trend of the PBLH over VIS, including the seasonal minimum in summertime PBLH.

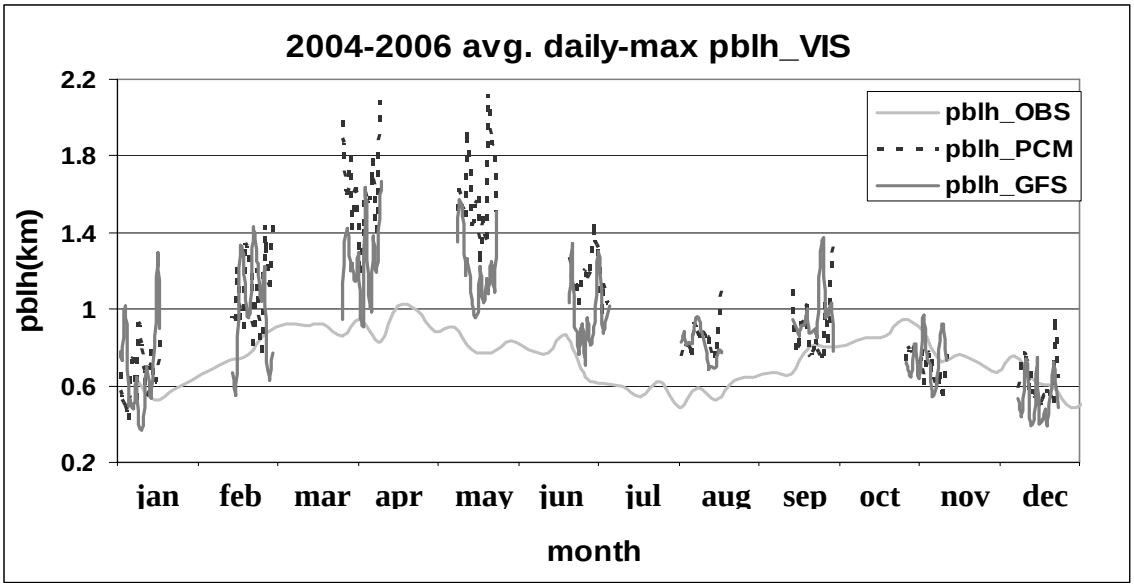

Figure 5-12: Three year (2004-2006) averaged daily maximum PBLH from observations (light gray solid line), PCM-WRF simulations (dark gray dashed line), and GFS-WRF simulations (dark gray solid line) at station VIS.

Analysis of stagnation events over the SJV revealed that the PSH moved inland and dominated the SJV for the majority of the time during case 6 (July 30th to August 16th) during 2004-2006, while it only appeared for six days during 2000. The high pressure system over the SJV always results in stagnation events featuring calm surface wind, low PBLH, etc. in this region. The comparison of the PBLH (from PCM-WRF simulations) averaged over SJV from 2004-2006 and from 2000 is shown in Figure 5-13. It is obvious that without the dominance of a high pressure system, the PBLH for case 6 (circled in Figure 5-13) in 2000 was much higher. Therefore, the high pressure system is one reason for the low summertime PBLH in SJV.

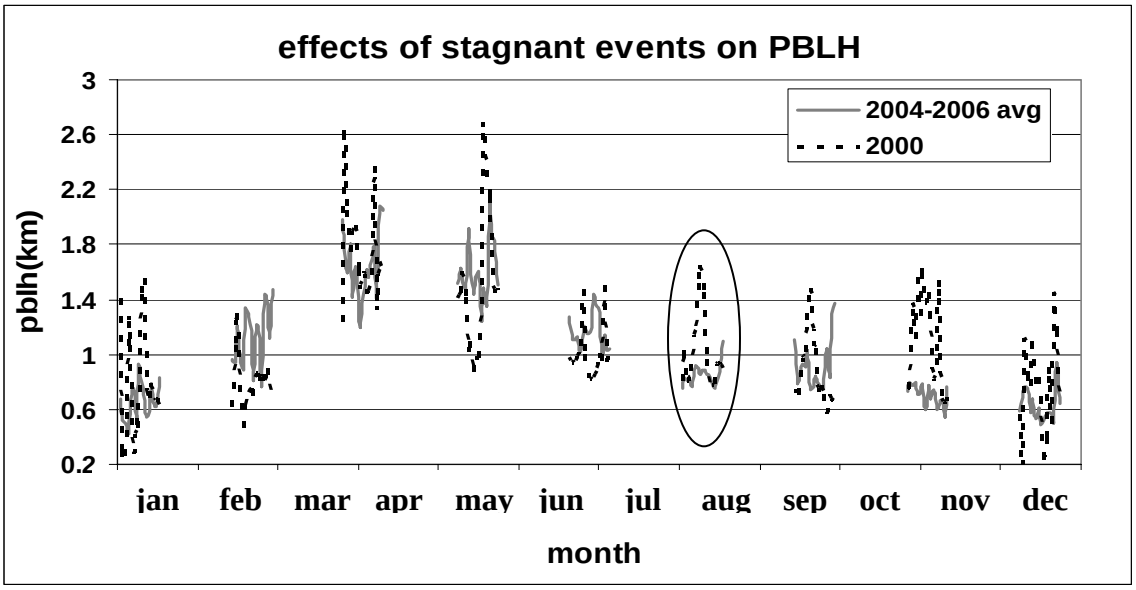

Figure 5-13: Daily maximum PBLH averaged over 2004-2006 (gray solid line) and during 2000 (black dashed line). The encircled part is from case 6 simulation.

Even if the persistent high pressure system in 2000 is removed, the PBLH during summer was still only about half of that in springtime. The seasonal change of the flow patterns in SJV is another factor that affects PBLH. Valleys can have complicated boundary layer structures that vary in with time due to the cross-valley flow. The SJV is a relatively wide valley, with an average valley floor width of 125km and a depth of about 1km on the west and over 3km on the east side; consequently, the flow pattern and the PBL structure in SJV can be very different from the conceptual model of the convective boundary layer in deep valleys ([126]; [127]; [128]). Figure 5-14 shows the vertical cross-sections of vertical wind velocity and potential temperature passing VIS (see Figure 5-1) at 4 PM local time on August 7th, 2000 and March 28th, 2000, which were chosen to represent the flow patterns that normally appear in the afternoon during summer and spring in SJV, when the high pressure system is absent. The time of 4 PM was selected as the WRF outputs used to make these plots were only available four times a day (4 AM, 10 AM, 4 PM and 10 PM Pacific time), among which, 4 PM , when the sun is facing the west side of the mountains, is the time with the highest PBLH. Except for valley wind, there was upward motion around the center of the SJV due to surface heating (Figure 5-14). In summer, the valley wind was strong due to a strong differential heating (Figure 5-14a) and the associated downward flow, which appeared most places between the two mountain ranges, suppressed vertical convection near the surface and led to a very shallow PBLH over the Central Valley. In contrast, during spring, the valley wind signal weakened, and the upward motion was much stronger and present at more places between the two mountain ranges than during summer. Note that VIS (the dots in Figure 5-14) is located almost inside an upward motion area in springtime (Figure 5-14b), and the PBLH might be higher than other places in the valley for this particular case (i.e., case 3 in 2000). Nevertheless, the averaged PBLH in the Central Valley in the summertime was

much shallower than that in the springtime, as indicated in the potential temperature field in Figure 5-14.

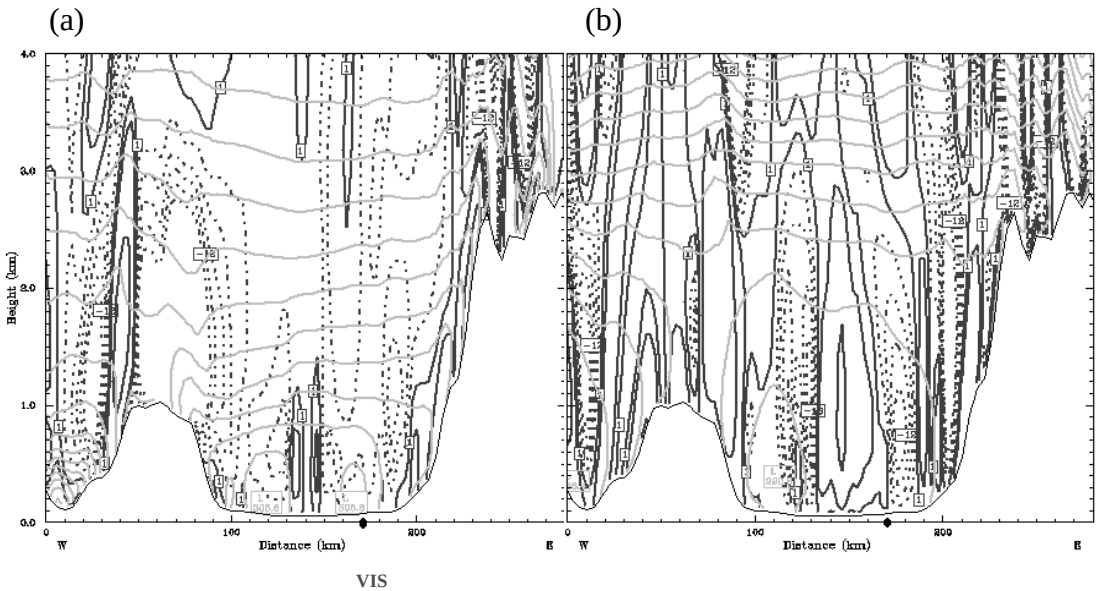

Figure 5-14: Vertical cross sections of positive w (black solid lines), negative w (black dashed lines) and potential temperature (gray solid lines) at 4 PM on (a) August 7, 2000 and (b) March 28, 2000 passing VIS (shown as black dot on x axis). The plotting range is indicated in Figure 5-1. The interval of the potential temperature and negative wind velocity in the plots is 1° K and 0.03ms^{-1}, respectively. A contour interval multiplier of 3 (i.e. 1cms^{-1}, 3cms^{-1}, 9cms^{-1}, etc.) was applied to the positive wind velocity due to the strong upward motion in the mountain region.

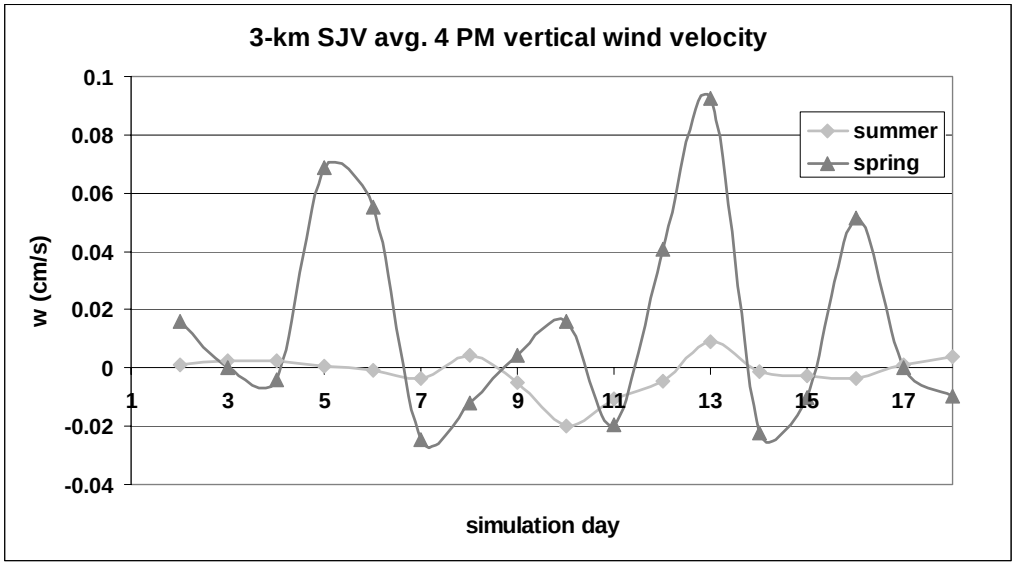

Figure 5-15: SJV averaged 3km vertical velocity at 4 PM during simulation case 6 (summer) and case 3 (spring).

The vertical wind velocity at an elevation of 3 km averaged over the SJV at 4 PM was calculated based on the PCM-WRF simulations for year 2000. Figure 5-15 shows the time evolution of the regional averages during case 6 (summer) and case 3 (spring). The PBLH was lower than 3 km during these simulations (Figure 5-13). The timing of the negative wind speed (w<0) above the PBLH during case 3 matches a time when a high pressure system dominated the Central Valley. Upward vertical wind (w>0) was obvious for other simulation times due to solar heating over the Central Valley during spring. For case 6, weak subsidence occurred in the Central Valley for most of the simulation days because the valley wind dominated the system. Figure 5-15 indicates the overall summertime (springtime) downward or near zero (upward) motion above the SJV boundary layer. Therefore, during the summer, the vertical convection within the boundary layer was suppressed by the valley wind above and resulted in low PBLH.

5.5 Conclusions

This study investigates the climate change impacts on meteorological variables relevant to air quality conditions in CA using the WRF model at a spatial resolution of 4 km. As the first stage of the study, this chapter focuses on the downscaling results for the present climatology (2000-2006) with two different datasets: PCM and GFS data. By comparing these two sets of simulations, the error of the downscaling results due to the PCM bias can be identified. In addition, the GFS-WRF simulation results were also evaluated against observation data to identify biases inherent in the WRF model itself when simulating conditions in California.

The spatial distribution analysis of the climatology from the two simulations focused on PBLH, surface temperature, and wind speed during summer and winter. The PCM-WRF surface temperature was underestimated for almost the whole analysis domain during winter, while the underestimation mainly appeared inland during summer. Similar patterns were apparent in the surface temperature difference between the climatology of the original PCM and GFS data, which indicates that the downscaling biases are inherited from PCM. The sign of bias between the original PCM data and the downscaling results were opposites during summer for inland CA as a result of the downscaling process. The imprecise prediction of the location and strength of the PSH and consequently the pattern and amount of cold air intruding to CA from Canada and the northwestern Pacific Ocean are the main sources of the PCM data bias. Surface wind speed was overestimated by the PCM-WRF simulations in CA and over the neighboring Pacific Ocean. The surface wind overestimation was more obvious in the SoCAB, especially during winter. The PBLH predicted by the PCM-WRF combination was also overestimated for most regions in CA. Surface temperature and wind speed, and PBLH are the three most important meteorological factors affecting regional air quality. The bias of the downscaling results driven by PCM data imply that using these results as inputs for air quality models would underestimate the air pollution problems in CA, particularly in LAC.

The comparison between GFS-WRF downscaling results and surface observations indicate that the WRF model has inherent biases for simulations in CA independent of the PCM boundary conditions. The WRF model bias of T2 and wsp10 were averaged over SJV and SoCAB for each simulation case. In general, WRF simulated surface temperature had a positive bias of less than 2 K. The temperature bias was generally smaller in summer vs. winter, and smaller for the SoCAB than for the SJV. These statistics averaged over the two geographic regions were consistent with the spatial distribution analysis of the two sets of simulations. WRF overestimated surface wind speed both the SJV and the SoCAB. The model bias/RMSE versus observed wsp showed that WRF has difficulty catching low wind events, with average WRF wind speeds hovering around 3 ms^{-1} independent of observed winds. This bias prevents accurate representation of summer ozone episodes and winter PM episodes. It is crucial to solve this problem in order to have accurate air quality predictions using WRF simulation results as the meteorological inputs.

The spatial distribution of simulated PBLH shows that the summertime PBLH is much lower in the SJV compared to other inland regions at the same latitude. Two possible reasons are the dominance of a high pressure system and the strong valley wind in the daytime during summer over SJV; both of which provide downward motion above the boundary layer and suppress vertical mixing in this region.

6.0 THE IMPACT OF CLIMATE CHANGE ON AIR QUALITY RELATED METEOROLOGICAL CONDITIONS IN CALIFORNIA – PART II: PRESENT VERSUS FUTURE TIME SIMULATION ANALYSIS

6.1 Introduction

The IPCC Fourth Assessment Report (2007) states that 'Most of the observed increase in global average temperatures since the mid-20th century is very likely due to the observed increase in anthropogenic greenhouse gas concentrations'. Temperature is a decisive meteorological variable for regional climate and air quality. A temperature change can result in a change in atmospheric and oceanic circulations (Nitta and Yamada 1989, [129]), precipitation ([130]), extreme weather events ([131]), etc. These, in turn, lead to air quality changes.

Previous studies have investigated climate change impacts in the U.S using the dynamical downscaling method. Leung and Gustafson ([62]) explored the potential air quality changes in the U.S. based on the future variations of meteorological variables, such as surface temperature, solar radiation and ventilation using the Penn State/NCAR Mesoscale Model (MM5) to downscale the Goddard Institute of Space Studies (GISS) model. Their results suggest a deterioration of air quality in the western U.S during fall, while the impact on air quality was not clear for other seasons. MM5 has also been applied to downscale PCM simulations ([28]; [132]) to 30-40 km resolutions for current and future climatology, and the results suggest that the downscaling enhances fine-scale features but does not alter the regional mean significantly. Similar conclusions were drawn by Duffy et al. [29]by comparing the simulation results from four different combinations of Regional Climate Model (RCM) and Global Climate Model (GCM). Other studies ([133], [134]) have also suggested that the RCM results are strongly influenced by the driving GCM or reanalysis. The addition of realistic spatiotemporal details to GCM projections through dynamical downscaling is more obvious over regions with strong meso-scale forcing associated with topographic heterogeneity ([28], [135]). The topography in CA is extremely heterogeneous, thus the advantage of dynamical downscaling may be more substantial in this region. However, downscaling at higher spatial resolution than 30-40km is required in order to replicate the orographic effects and comprehensive meso-scale features for the climate studies in CA. [105]used WRF to dynamically downscale Community Climate System Model ver. 3 (CCSM3) data to 12 km resolution to evaluate the downscaling performance in CA. This simulation at 12 km resolution, to the best of our knowledge, represents the highest resolution dynamic downscaling exercise applied to California to date. No studies have performed high-resolution (<10 km) dynamic downscaling over California using climatology that follows the IPCC BAU emissions scenarios.

In this chapter, the WRF model ([111]) is applied to dynamically downscale climatology from the Parallel Climate Model (PCM) to 4 km resolution in CA for both present and future time periods to quantify climate impacts on local meteorology related to air pollution. The chapter is arranged as follows. The methodology and model

configurations are described in section 6.2. The analysis of results, including stagnation events, future change of air-quality related meteorological variables and climate change impacts on land-sea breeze, are presented in section 6.3. The remarks and conclusions are given in section 6.6.

6.2 Model configurations and methodology

The configuration of the WRF model, the domain setup, and the input data used in the present study are identical to those described in chapter 5. The configuration selected in chapter 5 consisted of the Yonsei University (YSU) planetary boundary layer parameterization (PBL) scheme, the Grell-Devenyi cumulus parameterization, WRF single-momentum 6-class (WSM6) microphysics, Rapid Radiation Transfer Model (RRTM) long-wave and Dudhia short-wave radiation. It is demonstrated in chapter 5 that simulations with this configuration reproduce the meteorology in CA for the year 2000 more accurately than five other combinations of microphysics, cumulus parameterization, and PBL schemes when using Global Forecasting System (GFS) reanalysis data from the National Center for Environmental Prediction (NCEP).

The PCM data used in this study is the "business as usual" (BAU) scenario simulation B06.44, in which the greenhouse gas emissions increase by one percent per year. The simulation spans a period of approximately one century (1995-2099). The years 2000-06 and 2047-53 were chosen for downscaling to represent the current and future climatology, respectively. An interval of approximately fifty years between present and future climate was selected because PCM is known to have lower climate sensitivity than other GCMs ([136], [109]) and the climate change effects on regional meteorology and air quality in CA may not be evident over shorter time intervals. Simulations for two out of every six weeks were conducted, as described in chapter 5, in order to span a climatologically relevant period with a reasonable amount of computational resources.

The analysis conducted in chapter 5 shows that PCM-WRF predictions averaged over the current climate period (2000-06) have considerable bias compared to GFS-WRF predictions that are presumably more accurate because they are driven by observed meteorological trends. The comparison of the PCM-WRF results and the GFS-WRF results with observations indicated that the PCM bias was partially passed to the downscaled WRF results via initial and boundary conditions, causing a systematic warm bias over California. The model predictions match the surface observations better during summer than the other seasons. In this chapter, it is assumed that the PCM bias does not increase with time during the PCM simulation period (1995-2099). Therefore, the difference between the present and future downscaled results will ideally eliminate the bias inherited from PCM data, yielding a reasonable estimate for the climate change impact on the regional meteorology and air pollution in CA.

The analysis conducted in chapter 5 shows that the WRF model has inherent bias relative to observations even when driven by the GFS dataset. WRF generally does not predict regional wind-speeds lower than 3 ms^{-1} even though observed wind-speeds commonly

fall below this threshold during pollution events. Once again, it is hoped that the bias introduced by the WRF simulations are consistent during both present and future years so that the comparison yields a reasonable estimate for climate change impacts on meteorology relevant to air pollution events.

6.3 Results

6.3.1. Stagnation Event Analysis

Air pollution episodes in CA normally occur during stagnation events mainly characterized by slow winds and low atmospheric boundary layer mixing depths. Future changes to the duration and strength of stagnation periods will directly influence future pollutant concentrations. Stagnation events are often associated with dominant high pressure systems. Sea level pressure plots are particularly useful indicators of atmospheric stagnation. However, the coherence between the sea level pressure field and the stagnation events in the SoCAB is unclear, and the appropriate synoptic meteorological features to identify stagnation events over this region are not yet established. Therefore, in this section the stagnation analysis and comparison between present and future climatology focuses on the SJV only. The future changes of meteorology and consequent air pollution conditions in the SoCAB are studied based on seasonal averages, which are discussed in section 6.3.2.

The four criteria to define a stagnation event in the SJV are: 1) a high pressure system, WPSH for most cases, intrudes inland and stalls over the region for more than three days; 2) a large magnitude of the sea level pressure gradient (>5 pa/km) between the center to the outer edge of the high pressure system; 3) surface wind speeds below 3.5 m/s in the valley; and 4) low PBLH (threshold differs by season). Pollutant emissions are trapped below the low boundary layer during stagnation events and low wind speed provides very little ventilation, resulting in the steady accumulation of pollutants over time.

As described in chapter 5, GFS reanalysis data was employed to drive WRF simulations between 2000-06 as a benchmark to evaluate the PCM-WRF downscaling. Figure 6-1 shows the normalized number of stagnation days in the SJV for each season predicted by the GFS-WRF simulations for the present climate period and the PCM-WRF simulations in the present and future climate periods. The normalized number of stagnation days was calculated for each season by dividing the number of stagnation days by the total number of simulated days and then multiplying by the total number of days within that season. This treatment assumes that stagnation days fall randomly throughout each year and that the intermittent simulation pattern captures an unbiased sampling of those stagnation events. Seasons were defined as spring (=simulation cases3 & 4, see chapter 3), summer (=simulation cases 5 & 6), fall (=simulation cases7 & 8), and winter (=simulation cases1, 2 & 9). The results illustrated in Figure 6-1 reveal that the PCM-WRF underestimated the frequency of stagnation events (relative to GFS-WRF) for current climate simulations for all seasons except for spring. The under estimations from PCM-WRF were 3% and 17% for summer and winter, respectively. PCM-WRF performed better during spring and summer than fall and winter. The future change of the stagnation event frequency was

more significant during summer and fall than spring and winter (Figure 6-1). This trend is consistent with the study by Leung and Gustafson ([62]), which employed MM5 to dynamically downscale GISS data to the whole continental U.S. for both present (1995-2005) and future (2045-2055). However, this previous study predicted an increase of stagnation occurrence in the future during both summer and fall in most parts of CA, whereas the results from the current study predict a decrease of 28% in the future during fall.

The two main air pollution seasons in the SJV are summer (ozone) and winter (PM). The PCM-WRF results suggest a ~15% and ~8% future increase in the number of stagnation days for summer and winter, respectively. Conversely, the number of spring stagnation days was predicted to decrease by 7%. These trends indicate that stagnant conditions will encourage air pollution formation in future in the SJV during traditional pollution seasons (summer and winter), with reduced air pollution events in the spring and fall. It is noteworthy that the annual total numbers of stagnation days between present and future climate are similar (only one day difference), but shifted to different seasons, as discussed above.

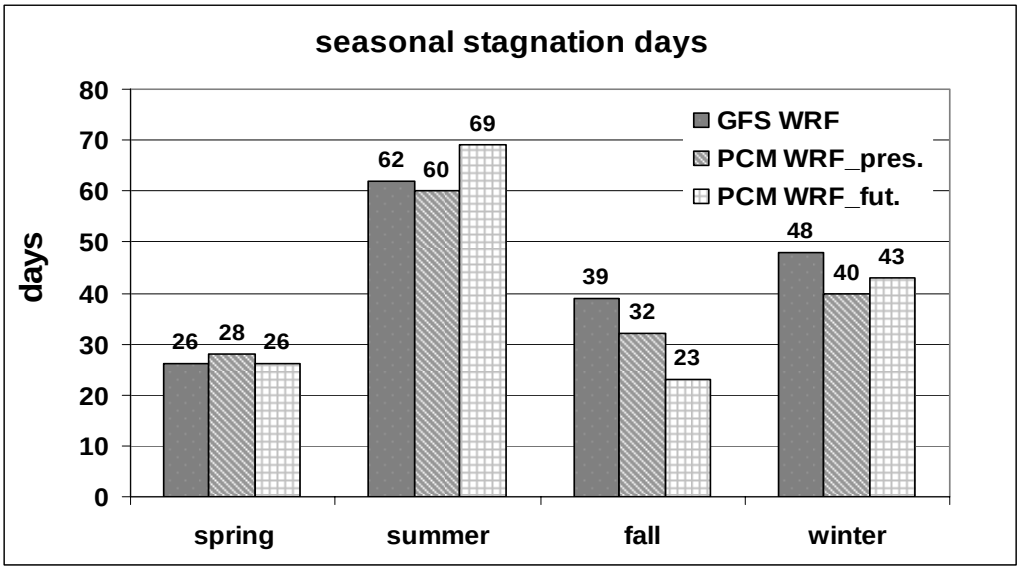

Figure.6-1: Normalized seasonal stagnation days from different WRF simulations: GFS-WRF, PCM_WRF_pres. (PCM-WRF runs for 2000 to 2006) and PCM_WRF_fut. (PCM-WRF runs for 2047 to 2053).

The "strength" of a stagnation event can be calculated as the product of the surface wind speed and PBLH (= total ventilation rate). Ventilation is the dominant index that determines pollutant concentrations during stagnation events. Figure 6-2 shows the regional (SJV-wide) averaged total ventilation rate that was calculated based on all of the stagnation events occurring in each season during the present (2000-06) and future (2047-53) WRF simulations. The comparison between 'GFS WRF' and 'PCM WRF_pres.' for current climate simulations indicates weaker stagnations (i.e. larger ventilation rate) from PCM-WRF runs, except during the fall. The PCM-WRF simulations overestimated the

ventilation rates (relative to GFS-PCM) by 5% and 11% for summer and winter, respectively. In combination with the stagnation duration analysis, this suggests a significant under-estimation of the stagnation events from PCM-WRF simulations during the two main air pollution seasons, especially in winter.

The comparison between PCM WRF_future and PCM WRF_present illustrated in Figure 6-2 indicates that the total ventilation rate in the SJV was predicted to decrease for all seasons except spring. The most significant change of the total ventilation rate (-12%) took place during winter. The future decrease of the ventilation rates in summer and winter suggests that the future stagnation events will be more severe in the SJV. Furthermore, the frequency of these events during summer and winter will also increase in the future (Figure 6-1), indicating the potential for negative impacts on future air quality in this region during the two main air pollution seasons. Chapters 7 and 8 will quantify these changes for average and extreme air pollution events.

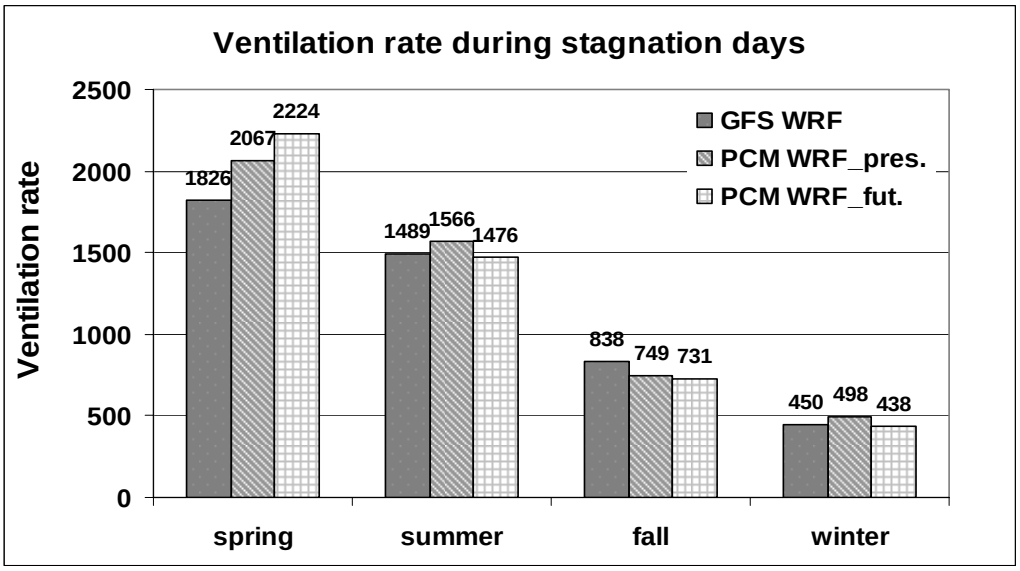

Figure 6-2: Same as Figure 6-1, but for SJV wide averaged ventilation rate during the stagnation events. Units are $m^2 s^{-1}$.

Compared to GFS-WRF runs, both the duration and strength of the stagnations were underestimated from PCM-WRF during summer and winter. Furthermore, it was shown in chapter 5 that WRF inherently has difficulty capturing the low winds associated with the stagnation events. Both of these biases will lead to over-ventilation of pollutants in air quality simulations driven by the PCM-WRF meteorological fields. The biases in predicted PM concentration during the period 2000-06 will be discussed in chapter 7.

6.3.2. Future changes of air quality related meteorological fields

The climate-induced changes to meteorological variables that affect air quality were explored by comparing the future and present seven-year averages during the summer

and winter seasons. The seven-year averages for the seasons of interest were calculated for each grid point using the hourly averaged values (chapter 5) in the analysis domain. The spatial distributions of the difference between the future and present averages emphasize how climate change will affect sub-regions of CA differently.

6.3.2.a. Surface wind analysis

Figures 6-3a and 6-3b illustrate the spatial distribution of the changes in 10 meter wind speed (10-m wsp) (future – present) during summer and winter, respectively. Overall, the changes to 10-m wsp over most inland regions of CA had opposite signs during the two seasons (i.e. decrease during summer and increase during winter). The regional averaged wsp change was approximately -3% and 2% during summer and winter, respectively in the SJV. Future 10-m wsp was predicted to decrease by less than 1% during summer and increase by ~3% during winter in the SoCAB. Los Angeles County (LAC) is one of the most polluted regions in CA. The average wintertime 10-m wsp over LAC will increase by approximately 0.5 m s^{-1} in the future (Figure 6-3b), which is significant taking into account that the present seven-year averaged wintertime 10-m wsp is ~3-4 m s^{-1} in this region (figure not shown). Conversely, future summertime 10-m wsp was predicted to decrease by about 0.5 m sec^{-1} over most of northern CA (including the SJV) (Figure 6-3a), whereas, the present summertime averages for these regions are below 3 m s^{-1}.

The analysis in chapter 5 showed that the location and strength of the WPSH is the decisive large scale factor that drives the climatology over CA and the adjacent Pacific Ocean. The influence of high pressure systems is more obvious during the summer when the strength of the WPSH reaches an annual maximum. The present and future seven-year averaged summertime sea level pressure plots of the original PCM data (Figure 6-4) indicate a slightly weaker circulation associated with WPSH in the future, resulting in weaker northwesterly winds on the right side of the WPSH. This could at least partially account for the decrease of the surface wind speed over most of the Pacific Ocean within the analysis domain during summer (Figure 6-3a). The future change of the wintertime WPSH is not as clear. The most obvious summertime surface wind decrease is along the coastline of northern and central CA (dark blue shown in Figure 6-3a), which may contribute to changes in the land-sea breeze pattern in this region. More details about the summertime land-sea breeze are explored in section 6.3.3.

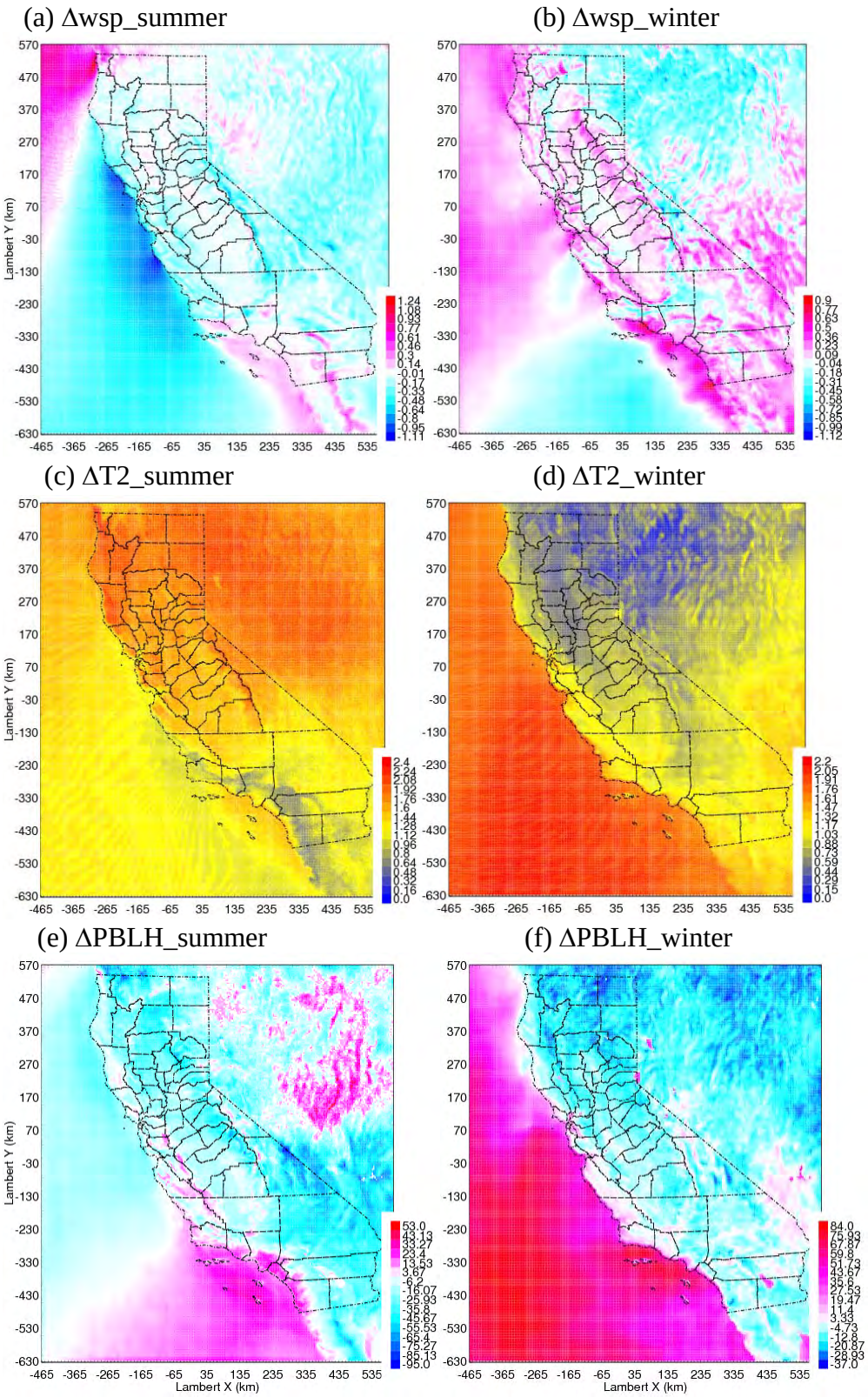

Figure 6-3: Predicted change (future-present) in annual average surface wind speed (units in m s^{-1}), 2-m temperature (units in °K) and PBLH (units in m) during summer and winter.

(a) (b)

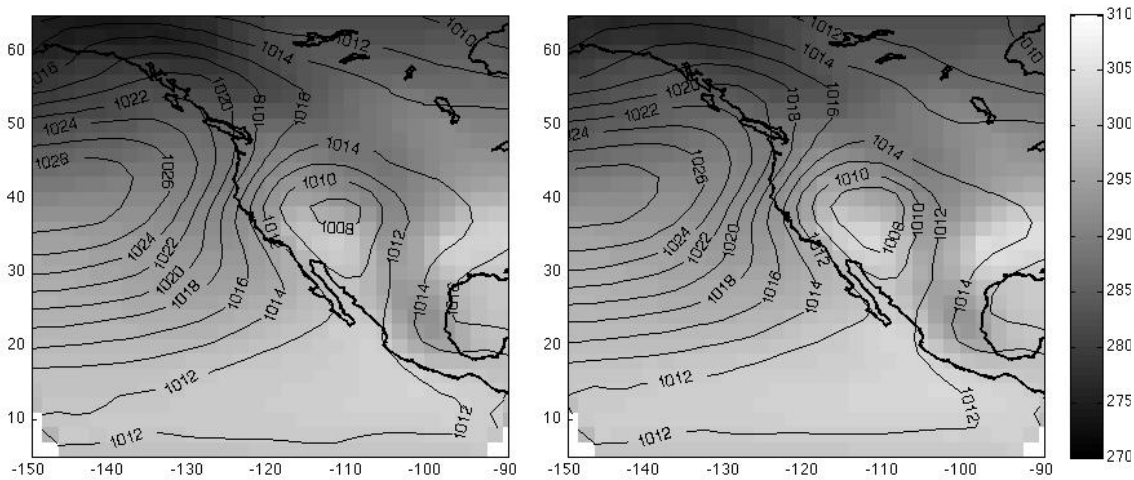

Figure 6-4: (a) Present and (b) future seven year averaged summertime surface temperature (shading) and sea level pressure (contours). Units are ^{o}K for temperature and hPa for sea level pressure.

6.3.2.b. Surface temperature analysis

The predicted future 2-m air temperature change (future - present) was positive for the whole domain during both summer and winter seasons (Figures 6-3c and 6-3d), and the largest temperature increase of 1.5-2 K occurred over CA's Central Valley (CV) during summertime. A belt with relatively small temperature increase (<0.8 K) was apparent for the coastal regions of southern CA, including the western part of SoCAB and Mexico. The magnitude of the future surface temperature rise gradually decreases from the northern boundary (over 2°K) to the southern boundary (less than 1°K) for the inland part of the domain during summer (Figure 6-3c), while an opposite trend is noticed during winter (less than 0.5 K in the north and above 1.3 K in the south; Figure 6-3d). On a synoptic scale, the two areas predicted to experience the greatest future surface temperature increase during summer (Figure 6-5a), are in northwest Canada and the western U.S. centered in Nevada. The latter region likely contributes to the aforementioned inland summertime north-south trend in temperature change. In contrast, in the winter the region with maximum future temperature increase in the western U.S. moves northeast (away from CA) and another region with a relatively large temperature increase appears centered at the Pacific Ocean, adjacent to Mexico (Figure 6-5b), which drives the wintertime CA regional temperature change trend (Figure 6-3d). The much more complex pattern in the downscaled results (Figures 6-3c and 6-3d) compared to the driving PCM data (Figure 6-5) underlines the need for detailed downscaling exercises when evaluating how climate change will influence future meteorology and air quality on regional scale.

The pattern of temperature change in the winter season (Figure 6-3d) is somewhat unexpected. Water has a greater heat capacity than land and the anthropogenic greenhouse gas emissions that drive global warming are mainly released over land, therefore, it is anticipated that future temperature increase will be greater over land than over the adjacent ocean. Nevertheless, the opposite trend was observed here during winter (Figure 6-3d), with future temperature predicted to increase by approximately 2° K over the ocean but only less than 1° K over land. A similar pattern was also noticed in the original PCM data (Figure 6-5b), but to a lesser extent. The further temperature change contrast over ocean versus land in PCM-WRF simulations is created during the downscaling process, as the large-scale temperature features can cause greater wintertime cloud cover, humidity, and precipitation over land. The PCM model projected summertime temperature increase was around 1.5° K over inland region of CA, and slightly lower over the neighboring Pacific Ocean (Figure 6-5a). The large-scale spatial pattern and absolute magnitude of the summertime temperature future variation from WRF simulations (Figure 6-3c) match the original low-resolution PCM data (Figure 6-5a). Due to the much finer resolution of the analysis domain and the well-resolved topography in WRF, the climate signal from the downscaling results can be significantly different from the driving GCMs (PCM in this study), particularly in regions with heterogeneous land surface ([135], [137]). The surface temperature signals in the WRF downscaling results have much finer features associated with topography and the coastline compared to the original PCM data, especially during winter (Figure 6-3d vs. Figure 6-5b).

Both the WRF results (Figures 6-3c and 6-3d) and PCM data (Figure 6-5) imply that the temperature contrast between summer and winter seasons in CA will intensify in the future due to the greater temperature increase over land during summer than during winter. Similar patterns were found in CCM3 data, caused by consistent intraseasonal fluctuations of surface temperature and the variations in atmospheric water vapor content ([107]).

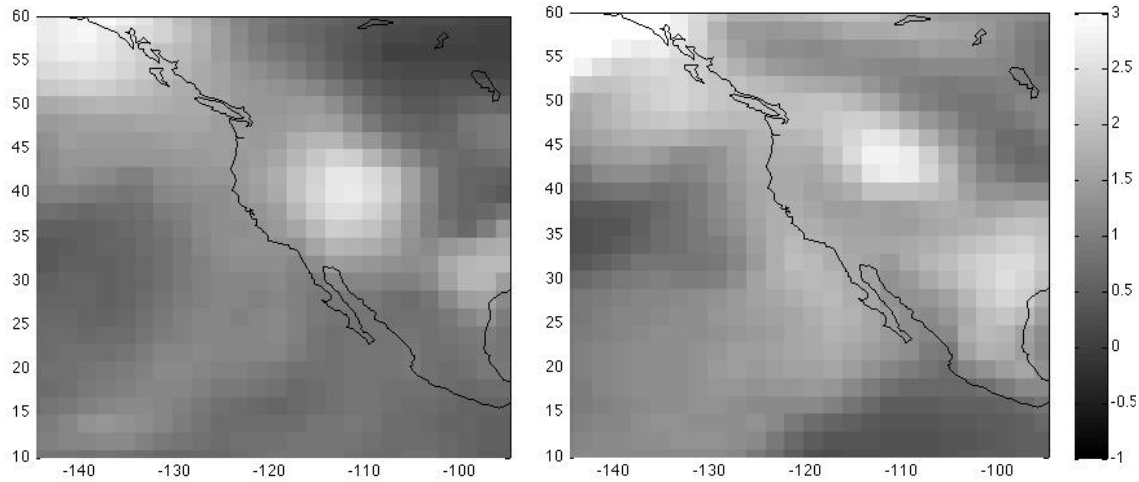

Figure 6-5: Predicted change (future-present) in 2-m surface temperature during (a) summer and (b) winter by the Parallel Climate Model (PCM). Units are ^{o}K.

6.3.2.c. PBLH analysis

Figures 6-3e and 6-3f give the spatial distribution of the temporally averaged PBLH difference (future - present) during summer and winter. PBLH is a diagnostic variable in WRF that is calculated based on the instability and wind shear of the atmosphere ([114]). PBLH was predicted to decrease during both summer and winter seasons for most inland CA regions, except for some coastal regions. The decrease of seven-year averaged PBLH across the entire SJV was 10-30m during summer and around 10m during winter. The present averaged PBLH over the SJV was predicted to be approximately 400 m (200 m) during summer (winter) (Figure 6-6), thus the future PBLH decreases are approximately 5% for both seasons. Future PBLH was predicted to increase across the Pacific Ocean within the study domain during winter (Figure 6-3f) and across the portion of the Pacific Ocean adjacent to southern CA during summer (Figure 6-3e). Similar changes also appeared over coastal regions influenced by the marine boundary layer, especially along the coastal regions of the SoCAB where the future summertime PBLH was predicted to increase by 20-30m (Figure 6-3e).

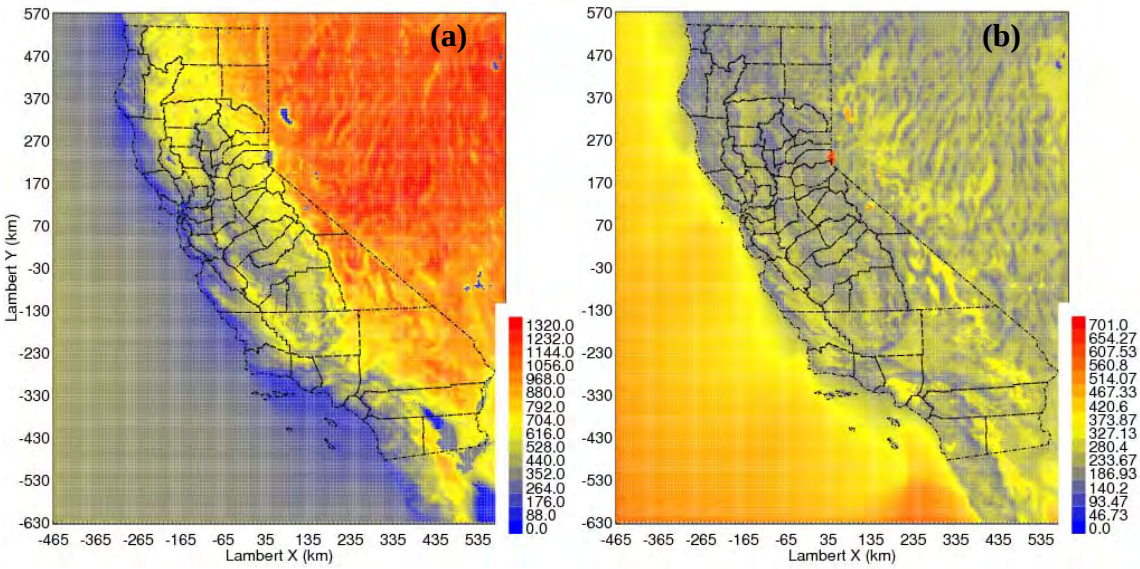

Figure 6-6: Present-day seven year averaged (2000-06) PBLH during (a) summer and (b) winter. Units are m.

The PBLH for most of LAC was within the marine atmospheric boundary layer inversion zone where the average summertime PBLH only reaches ~400m (Figure 6-6a). Therefore, the predicted 20~30m PBLH increase in the coastal part of LAC represents a change of 7.5%. Sub-regions of the SoCAB further inland were predicted to experience a decrease in PBLH similar to trends predicted for the SJV. As mentioned previously in section 6.3.1, stagnation events happen frequently in SJV during summer. Unsurprisingly, the summertime averaged PBLH over inland regions of SoCAB, such as San Bernardino County and the eastern part of Riverside County, was about twice that of the values in SJV (Figure 6-6a). Meanwhile, the future PBLH decrease for these inland regions of the SoCAB was roughly double the decrease predicted in the SJV during summer, yielding a similar percentage change in both regions. The current seven-year averaged PBLH over the SJV during the winter season was slightly lower than values in the inland SoCAB (Fig 6b), whereas, the predicted future decrease of PBLH was greater over SJV than over inland SoCAB. Therefore, the wintertime PBLH decrease was more significant in SJV. There was an obvious future wintertime PBLH increase over water, including the Pacific Ocean and inland lakes (such as the Salton Sea and Lake Tahoe, etc) (Figure 6-3f), while this trend was not clear during the summertime. The present seven-year averaged PBLH over the ocean was around 400m during both summer and winter (Figure 6-6), so the future PBLH was predicted to increase by roughly 20% over the Pacific Ocean during winter (Figure 6-3f). These changes could potentially affect concentrations of pollutants emitted by off-shore shipping activities in addition to dimethyl sulfide (DMS) and other precursor species emitted from the coastal ocean waters.

6.3.2.d Integrated analysis of wind, temperature, and PBLH

Surface wind, temperature, and PBLH are the three most important meteorological variables directly related to regional air quality. These variables influence air pollutant concentrations simultaneously and so it is necessary to perform an integrated assessment to predict their effects on future air quality. During the summer, the surface wind speed was predicted to increase slightly and the PBLH was predicted to increase by ~8% in the coastal region of LAC, providing greater ventilation for the summertime pollutants. In contrast, both surface wind and PBLH were predicted to decease, and surface temperature was predicted to increase significantly in the SJV and inland portions of the SoCAB. These future atmospheric conditions are less conducive to the accumulation of pollutants at coastal locations and more conducive to the accumulation of pollutants at inland locations during the summer.

Predicted changes to wind speed were modest in the SJV during winter with some sub-regions predicted to experience slight increases while others experience slight decreases. PBLH was predicted to decrease slightly in the SJV. These combined trends will lead to a slight increase in wintertime PM concentrations in some regions of the SJV and a slight decrease in others. Wind speed was predicted to increase strongly over most of the SoCAB, especially in LAC, together with a slight decrease of PBLH, leading to an overall increase in ventilation for this region during the winter.

Note that the discussion of the potential air quality change for the SJV region is based on an analysis of all simulation days. The conclusions are therefore different from those in the previous section, which are based on an analysis of stagnation events only. The net effect of PCM-WRF meteorology on predicted air quality will be quantified in chapters 7-8 of this report.

6.3.3 Climate change impacts on land-sea breeze

Daytime surface temperature typically increases more over land than over the adjacent ocean due to the fact that water has a higher heat capacity than soil, and water can therefore absorb a greater amount of incoming solar radiation with less of an associated increase in temperature. The higher temperatures over coastal inland regions induce vertical air movement via buoyancy forces resulting in lower sea level pressure compared to the adjacent region over the ocean. This forcing induces onshore air mass movement at the surface level (cooler ocean air moves inland) and a compensating offshore movement aloft. The flow pattern is reversed during the night when the air over land is cooler than the air over the ocean, but the nighttime land breeze is typically much weaker than the daytime sea breeze. Land-sea breeze [138] is apparent around the coastal regions of CA during periods when the meteorology is not dominated by other strong weather systems. Although the WPSH is persistent, the associated synoptic scale flows are normally

weaker than the flows due to surface forcing (i.e., sea breeze and mountain valley wind) [139]. The land-sea breeze signal is normally more evident during summer than winter due to stronger solar heating effects.

The sea breeze in southern CA follows a classical pattern similar to that described by [140], [141], and [142]. The cool marine surface air moves inland with a penetration distance that depends on the land-sea temperature contrast. This influx of cool marine air reduces the daytime temperature near the ground, leading to the establishment of a temperature inversion (cold air trapped beneath warmer air aloft) that inhibits vertical mixing in the atmosphere. The pollutant emissions are trapped within the shallow mixing layer associated with the temperature inversion. In contrast, the nighttime land breeze may transport these pollutants back out over the ocean in an elevated layer of warmer air that stays aloft in the land breeze front (a convergence zone). This recycled plume may return onshore during the afternoon of the next day, affecting the pollutant concentrations near the surface. In general, the land-sea breeze potentially reduces the net ventilation by trapping pollutants close to the surface within the coastal zone of Southern CA.

The effect of the sea breeze around the San Francisco Bay Area is quite different than the pattern established in southern CA. The analysis in Section 6.3.1 showed that stagnation events occur frequently during the summer in the CV, and pollutants accumulate close to the emissions' source due to lack of ventilation. The sea breeze in the Bay Area transports the marine air and emissions from San Francisco into the CV through the Carquinez Strait. The sea breeze flow separates into a northward flow towards the Sacramento Valley and a southward flow towards the SJV as it impinges against the Sierra Nevada Mountains located on the eastern side of the CV ([143]). These marine air flows transport pollutant emissions between regions within the valley and they reduce the temperature and increase the humidity of the air in the valley at the same time. Cooler surface temperatures result in greater atmospheric stability which further traps local emissions. The nighttime return flow back towards the ocean is very weak in the CV due to the complex topography and flow patterns in this region. The future change of the summertime land-sea breeze system will potentially influence the climate and air quality in both the CV and the coastal part of the SoCAB.

The strength of the land-sea breeze is directly proportional to the land-sea temperature contrast, which reaches its peak around 2-3pm before the net warming effect becomes negative. Figures 6-7a and 6-7b show the predicted future change of the summertime surface temperature at 2 pm and 2 am over CA. The 2 pm surface temperature increase in the Sacramento Valley (SV), which is northern part of the CV, was greater than the temperature increase over the neighboring Pacific Ocean at the same latitude by approximately 0.5^{o}K. The increased land-sea temperature contrast will produce a stronger sea breeze in this region. In Southern CA, the 2 pm temperature increase is only ~0.7 K in the coastal region, while the temperature increase over the adjacent ocean is ~1.5 K. Hence, there will be a future decrease of land-sea temperature contrast, leading to a reduced sea breeze. The future change of land-sea temperature contrast was more significant in southern CA than in the Bay Area, therefore the changes to the sea breeze system were predicted to be more evident in Southern CA.

The pattern of predicted temperature change at 2 am (Figure 6-7b) was quite similar to the pattern predicted at 2 pm (Figure 6-7a) in northern CA, but the effect on the land breeze will be reversed. Hotter nighttime temperatures over land weaken the land-breeze rather than strengthen it. The predicted change between air temperatures over inland and ocean regions at 2 am in Southern CA suggests a slight strengthening of the predicted land breeze in this region. The weaker daytime sea breeze and stronger nighttime land breeze in Southern CA implies that more polluted inland air will be brought over ocean at night, while fewer residual plumes over the ocean will move inland during daytime.

The direction of the land-sea breeze is perpendicular to the coastline: the daytime sea breeze blows onshore and the nighttime land breeze blows offshore. The coastlines around both the Bay Area (gateway to the CV) and Southern CA are approximately aligned in the northwest-to-southeast direction (45°). The sea breeze therefore flows approximately from the southwest direction (i.e., southwesterly wind), while the land breeze flows approximately from the northeast direction (i.e., northeasterly wind) in both regions. The seven-year averaged southwesterly component of the wind at 2 pm (2 am) was calculated for each grid point during the summer season. Positive (negative) values of the southwesterly component correspond to sea (land) breeze. The formula used to calculate the southwesterly wind component was $U \times \sin(45^o) + V \times \cos(45^o)$, where U is the x-component of the 10-m wind and V is the y-component of the 10-m wind. Figures 6-7c and 6-7d illustrate the future change of the southwesterly wind at 2 pm and 2 am for the summer season. The southwesterly flow is shown to increase in the CV (Figure 6-7c), which is likely due to the marine flows with southwesterly momentum entering the valley through the Carquinez Strait. In contrast, Figure 6-7c suggests a future sea breeze decrease in the coastal region of Southern CA The predicted sea breeze behaved exactly as expected based on the predicted land-sea temperature contrast in these two regions. The predicted nighttime southwesterly flows (Figure 6-8d) slightly increased for the coastal part of Southern CA. The nighttime coastal wind should be offshore (northeasterly signified by a negative value), therefore the land breeze was predicted to slightly decrease in the coastal part of SoCAB. The opposite was predicted for the Bay Area and the CV. The predicted future changes to the sea breeze were larger than to the land breeze (Figure 6-8c vs. 6-8d), due to the fact that the daytime sea breeze is normally stronger than the nighttime land breeze.

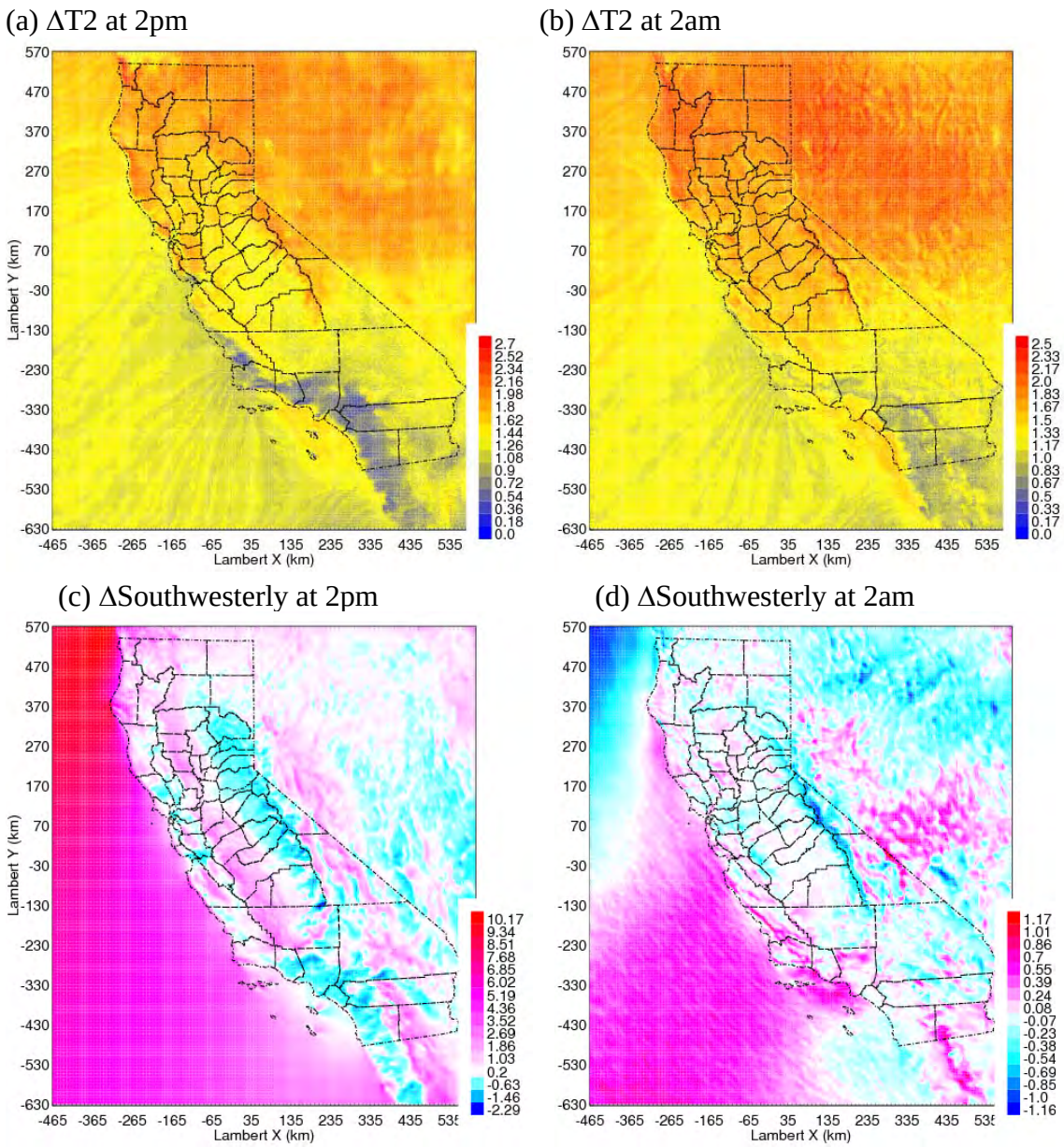

Figure 6-7: Spatial distribution of future change for surface temperature and southwesterly wind component at 2pm and 2am during summer. Units are ^{o}K.

6.3.4 Significance Test

The comparison between meteorology in the future and present climate periods is complicated by the natural variation within each seven year interval. Large amounts of inter-annual variability can make it impossible to discern the effects of climate change with reasonable confidence. In the present study, the hypothesis that climate change had no effect on meteorological variables was tested by quantifying the probability that the simulation results yielded no actual change as a p-value (Figure 6-8). The p-value was calculated based on the annual mean and variance of meteorological data from each seven-year interval in both present (2000-2006) and future (2047-2053) time periods using the student t-distribution with 12 degrees of freedom. A small p-value indicates that the climate change signals are stronger than the inter-annual variability ([144]), while a large p-value indicates that we can't reject the hypothesis that climate change has no impact on the variable of interest. Normal thresholds for statistical significance require p-values smaller than 0.1 (90% confidence) or 0.05 (95% confidence). The highest confidence results (lowest p-values) apparent in Figure 6-8 are those associated with temperature, suggesting that the predicted increases in surface temperature are statistically significant at the 95% confidence level relative to inter-annual variability. This pattern is expected due to the fact that the green house gas concentrations increase 1% per year in the driving PCM data. The p-values calculated for wind speed and PBLH are higher, with no broad region experiencing future changes that were statistically significant at the 95% confidence level. Changes to wind speed were significant in the southern portion of the SJV (summer only) and in the coastal portion of the SoCAB (summer and winter). Overall, the p-values for temperature, wind speed, and PBLH are smaller during summer than winter in CA, suggesting the climate change is likely to be more statistically significant during summer.

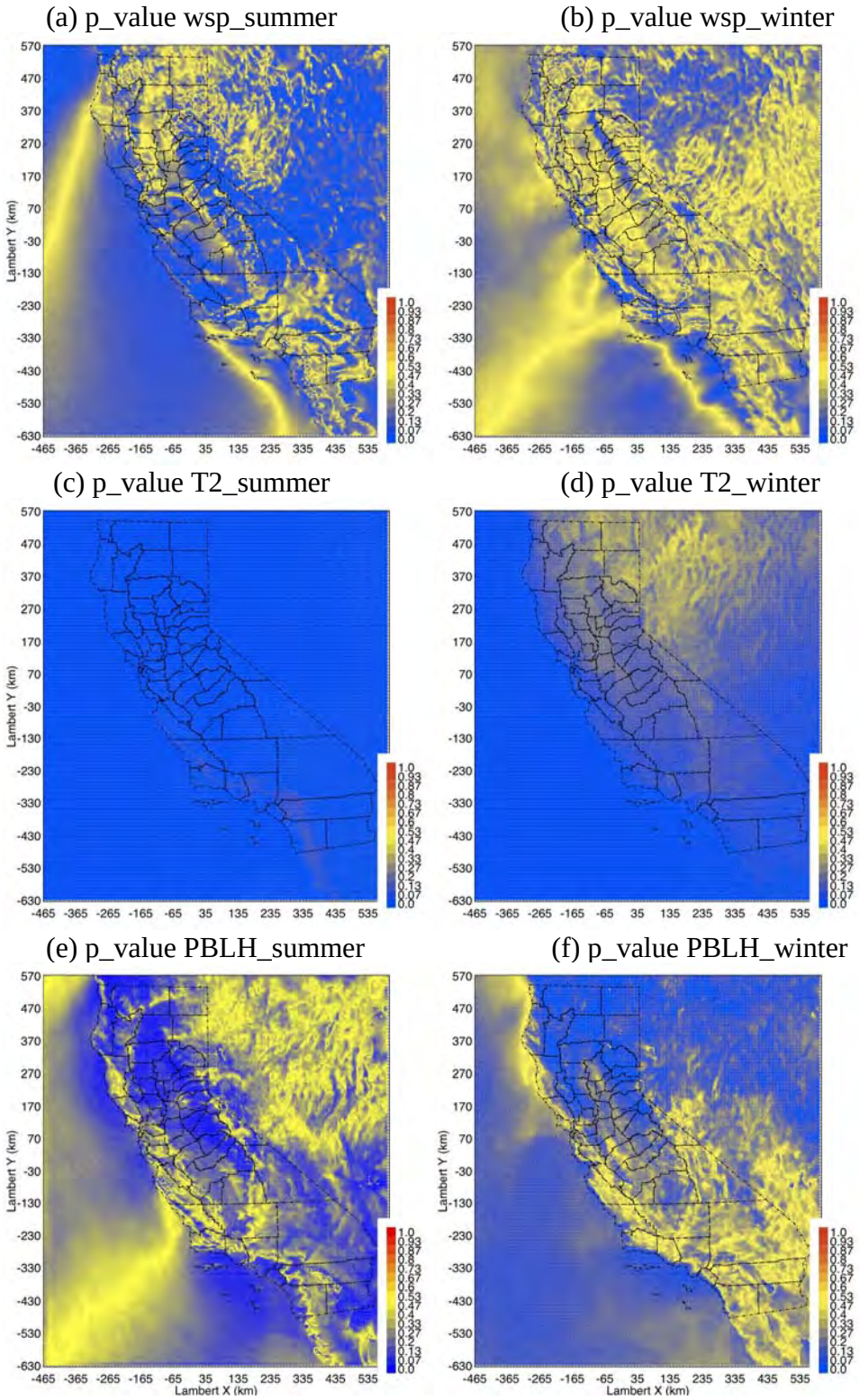

Figure 6-8: Corresponding p-values of the plots in Figure 6-3. The p-value quantifies the likelihood that average meteorological conditions are identical in the present (2000-2006) and future (2047-2053). Note that smaller p-values represent bigger climate change signals.

6.4 Conclusions

In this chapter, the present and future climatology in CA was simulated by dynamically downscaling global PCM predictions generated under a BAU scenario to a spatial resolution of 4 km over a span of 14 years (2000-2006 in the present and 2047-3053 in the future) to characterize the intricate meso-scale features in CA induced from complex topography. The spatial resolution used in this study was much finer than previous CA climate studies carried out over a comparable time window. The changes in the predicted future meteorology have direct implications for air pollution in two of the most polluted air basins in the U. S. - the SJV and the SoCAB.

The frequency of stagnation events in the SJV was predicted to increase during both summer (~15%) and winter (~8%) in 2047-53 vs. 2000-06. The strength of the stagnation events (inversely proportional to the regional ventilation rate) was predicted to increase during all seasons except for spring. The combination of these changes suggests that air pollutant concentrations may increase during extreme pollution events in the future because of climate change.

Future changes to average surface wind speed, temperature, and PBLH were calculated for the two main air pollution seasons (i.e. summer and winter) between 2047-53 vs. 2000-06. In the coastal areas of LAC, both the wind speed and PBLH were predicted to increase, while the temperature was predicted to remain relatively unchanged during the summertime. These changes will provide more ventilation for the summertime pollutants in this region. The situation is reversed in both the inland portions of the SoCAB and the SJV, providing more favorable meteorological conditions for the buildup of pollutants during summer. The change to wind speed, temperature, and PBLH during the wintertime was less obvious and somewhat uncertain. The analysis of the surface wind and PBLH indicated a slightly stronger ventilation rate in the SoCAB in the future, with no clear trend for the SJV.

The summertime land-sea temperature contrast was shown to increase in northern CA (decrease in southern CA) at 2pm, which implies a stronger (weaker) sea breeze intruding into the CV (SoCAB). The situation was reversed at 2am, so that the nighttime land breeze was predicted to be weaker (stronger) around the Bay Area (SoCAB) in the future. The analysis of the land-sea breeze speed (southwesterly component of the 10-m wind around the coastal regions) confirms that the sea breeze will increase (decrease) around the Bay Area (coastal region of SoCAB) during the summer.

Confidence intervals calculated for the change to meteorological variables between 2000-06 and 2047-53 indicate that increased temperature is statistically significant ($p<0.05$) but changes to wind speed and PBLH are not generally significant ($p>0.01$) across broad geographical regions of California. The inter-annual variability within the time periods 2000-06 and 2047-53 appears to be larger than the changes that occur between these periods for wind speed and PBLH.

7.0 CLIMATE IMPACT ON AIRBORNE PARTICULATE MATTER CONCENTRATIONS IN CALIFORNIA USING SEVEN YEAR ANALYSIS PERIODS

7.1 Introduction

Exposure to elevated concentrations of airborne particles with aerodynamic diameters less than 2.5 µm ($PM_{2.5}$) has serious health consequences (see for example [145]). The National Ambient Air Quality Standard for annual average $PM_{2.5}$ is currently 15 µg m^{-3} and the more stringent California State Air Quality Standard for $PM_{2.5}$ is currently 12 µg m^{-3}. Despite the adoption of a more stringent state standard, annual average $PM_{2.5}$ concentrations measured in California's San Joaquin Valley (SJV) (21.5 µg m^{-3}) and South Coast Air Basin (SoCAB) (19.7 µg m^{-3}) were the highest in the nation during the years 2007-2008. Some estimates predict that more than 18,000 California residents die prematurely each year due to air pollution [146]. Meteorological parameters including temperature, precipitation, clouds, atmospheric water vapor, boundary layer height, wind speed, and wind direction influence the atmospheric chemistry and transport processes that determine $PM_{2.5}$ concentrations (see for example Kleeman, 2008; Aw and Kleeman, 2003; Sillman and Samson, 1995). Climate change will modify weather patterns in California with unknown consequences for $PM_{2.5}$ concentrations.

The effect of global climate on regional $PM_{2.5}$ concentrations can be studied using a dynamic downscaling approach where Global Climate Models (GCMs) provide initial and boundary conditions for Regional Climate Models (RCMs) with subsequent analysis using regional chemical transport models. California has several unique features that make this type of detailed analysis challenging. California's topographic features transition abruptly between mountains, valleys, deserts, lakes and oceans over distances of 10's of km. Emissions patterns in California also change quickly over small spatial scales due to the complex arrangement of residential, commercial, industrial, agricultural, and natural land use types. Intricate meteorological features that strongly influence air pollution concentrations such as the land-sea breeze system and mountain-valley flows must also be modeled using high spatial resolution. Regional air quality studies in California are usually carried out at spatial scales finer than 10 km to resolve these features. Long time periods must also be considered when studying climate-air quality interactions in California. Natural annual variation in meteorology such as the El-Nino Southern Oscillation (ENSO) has a strong effect on air quality. The period of the ENSO cycle in recent decades has been 3-8 years suggesting that air quality analysis must be carried out over a similar time scale in order to be climatologically relevant. The combined need for fine spatial scales and long simulation times results in a computationally challenging analysis for climate-air quality interactions in California.

Several recent studies have examined the effects of global climate change on regional air quality across the entire United States including California (see for example [18, 19, 21, 26, 147-150]). The GCMs employed in the studies to date include the Goddard Institute for Space Studies (GISS) GCM ([151]), the NCAR/DOE Parallel Climate Model (PCM) [108], and the Stanford GATOR-GCMOM model [19]. Most of the regional climate

analysis was conducted using the fifth generation Penn State/NCAR Mesoscale Model (MM5) [152] although the GATOR-GCMOM model provides a unified framework from global to regional scales. Of those studies that compared $PM_{2.5}$ concentrations in present and future climates, [18]simulated air quality for the entire United States using 36 km resolution for the years 2001 and 2050. The results of their study indicate that that the annual average $PM_{2.5}$ concentration in some parts of California is likely to decrease by ~1.5 μg m^{-3} in the future due to the effects of climate change alone under the A1B emissions scenario. Avise et al., ([21]) also conducted a climate – air quality study for the entire United States using 36 km resolution but they focused their analysis on a single month (July) in the years 1990-1999 and 2045-2054. Results were averaged within the administrative regions defined by the United States Environmental Protection Agency (USEPA). Avise et al. ([21]) predicted that 24-hr average concentrations of $PM_{2.5}$ mass, $PM_{2.5}$ sulfate, $PM_{2.5}$ nitrate, and $PM_{2.5}$ ammonium for EPA's Region 9 (containing California) would decrease by ~0.4 μg m^{-3}, ~0.1 μg m^{-3}, ~0.1 μg m^{-3}, ~0.1 μg m^{-3}, respectively, due to the effects of climate change alone. Dawson et al. ([149]) modeled the climate effects on 24-hr average total mass and speciated $PM_{2.5}$ concentrations for the eastern United States under the A2 emissions scenario. In this study, the authors used 36-km resolution and modeled January and July in 5 present years (1990s) and 5 future years (2050s)) to report that on average the total mass and speciated $PM_{2.5}$ concentrations are likely to decrease in January due to increased precipitation and increase in July due to decreased ventilation in the future.

None of the previous studies for the entire United States have simultaneously used spatial resolution finer than 10 km and analysis times longer than 3 years to determine how climate change will influence the annual average $PM_{2.5}$ concentration in California. The current study applies a dynamic downscaling approach with 8-km spatial resolution during 7 years of current climate and 7 years of future climate to address this question. The 7-year analysis period during the current climate is long enough to allow for a meaningful comparison between simulated vs. measured $PM_{2.5}$ concentrations. To the best of our knowledge, this comparison is the most rigorous evaluation of a climate – air quality modeling system ever conducted. The 7-year analysis windows also contain enough data to support a statistical analysis of annual variability so that confidence intervals can be calculated for the differences between present vs. future conditions. The results of the current study reduce the uncertainty of likely climate impacts on annual-average $PM_{2.5}$ concentrations in California at the regional scale.

7.2 Methods

Figure 7-1 shows a schematic diagram of the regional climate – air quality modeling system employed in this study. The regional climate is simulated by dynamically downscaling output from the Parallel Climate Model (PCM) using the Weather Research and Forecasting (WRF) model, and the air quality is simulated using the latest generation of the UCD/CIT air quality model for the entire state of California. A detailed description of the modeling system is provided below.

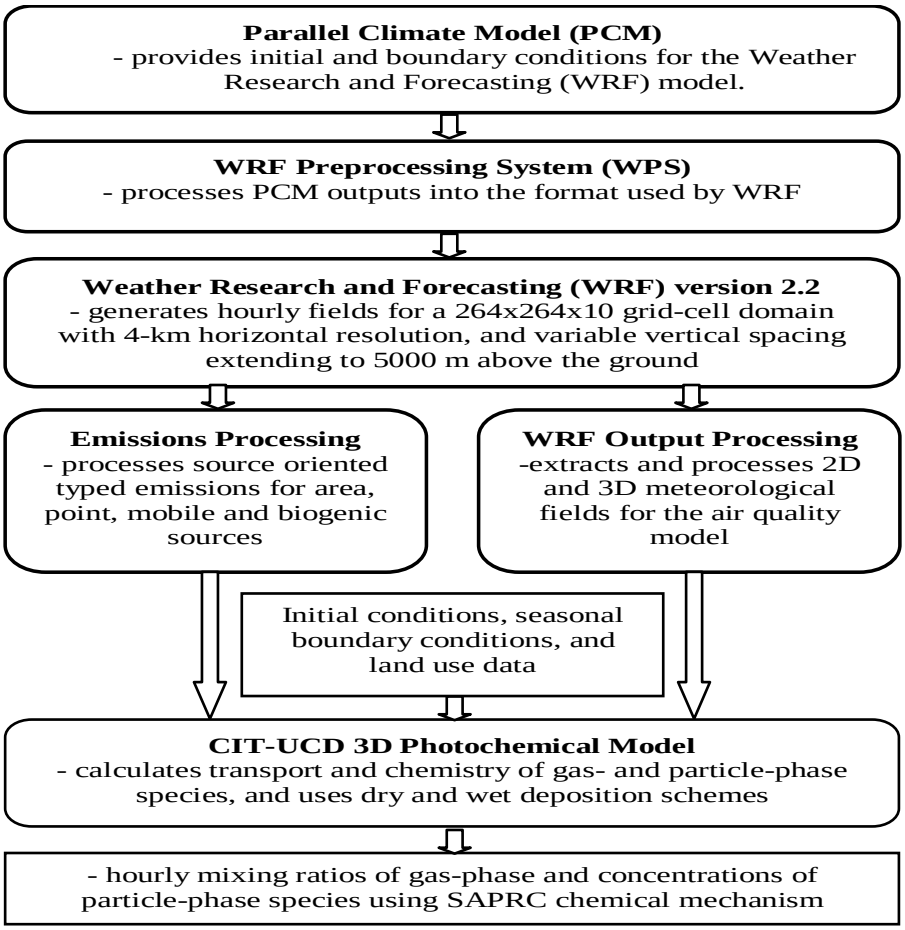

Figure 7-1: Flow Chart of the climate downscaling and air quality modeling systems.

PCM is a Global Climate Model (GCM) that was developed at the National Center for Atmospheric Research (NCAR) [108]. The parent PCM dataset utilized in this study was available in 2.8°(~240-km) x 2.8°(~310-km) horizontal resolution with 18 hybrid vertical layers from ground to ~4 hPa. PCM output was obtained for a 7-year period in the present-day climate (2000-06) and a 7-year period in the future climate (2047-53) under the "business as usual" (B06.44) global emissions scenario. Seven year windows were selected to account for the effects of El Nino Southern Oscillation (ENSO) events and the intra-annual variability in the climate data that would have different implications in the final air quality results (see for example, [33]). The PCM output was processed through the WRF Preprocessing System (WPS) in preparation for regional downscaling.

Version 2.2 of the WRF model [153] was utilized to generate the regional climate data in this study. All of the WRF simulations were carried out using an optimized configuration of the modeling system for California ([154], manuscript in preparation). The optimization process tested six different configurations of WRF for conditions in central California. The best agreement with measured meteorological parameters was produced by the Yonsei University (YSU) planetary boundary layer (PBL) scheme [114], Grell-Devenyi cumulus parameterization scheme [118], WRF single-momentum 6-class

(WSM6) microphysics scheme [120], Rapid Radiation Transfer Model (RRTM) long-wave scheme [121], and Dudhia short-wave radiation scheme [122]. The WRF simulations used a three-domain 1-way nesting technique, where the coarse grid output provided initial and lateral boundary conditions for the fine grid simulations with horizontal resolutions of 36-km, 12-km, and 4-km, respectively. Meteorological fields with 4-km resolution were generated for a domain with 264x264 grid cells in the horizontal plane and 10-vertical layers extending to a height of 5000 meter above the ground. The heights of the vertical layers in WRF were matched with those of the air-quality model such that the model used finer vertical resolutions near the surface. All of the variables were saved on the A-grid (i.e. in the center of a grid-cell) except for the u- and v-components of wind speed, which were staggered using the Arakawa C-grid (i.e. on the face center of each grid-cell). The native C-grid output was retained for the wind field in order to achieve better accuracy in the air quality transport calculations. The gridded WRF output was averaged over each 60-minute simulation period for every simulated day. A total of nine periods were simulated for each year such that each consisted of 17 days followed by 25 days that were not simulated. The first simulation day of each year was set to be Jan 1. This approach captures an unbiased sample of predicted meteorology and air quality across the full seven year period that reflects both seasonal variation and annual variability while still keeping the analysis time to a reasonable level.

Finer grid resolution provides a better description of small-scale meteorological dynamics such as sea-land breezes and orographic winds during regional meteorological modeling, but this resolution does not necessarily need to be retained in subsequent regional air quality modeling exercises. In the present study, the 4-km WRF meteorological fields were extracted and averaged to 8-km resolution to generate inputs for the air quality modeling. The coarser resolution of the air quality model reflects a balance between accuracy and speed. Each 7-year study period involved 1,008 simulation days over a domain composed of 131x128x10 grid cells requiring approximately 45 days of real time to complete. Ying et al. ([155]) showed that increasing the resolution of simulations in the Central Valley of California from 8-km to 4-km does not significantly improve accuracy but it increases the computational effort by a factor of 4. A previous study carried out in Marseilles-Fos-Berre in the south of France has also found that beyond a certain point finer grid resolution does not necessarily yield better air quality predictions [156]. The South Coast Air Quality Management District (SCAQMD) provides emissions inventories with 5-km spatial resolution for the SoCAB and numerous previous air quality studies have been carried out at this scale [34, 41, 157] without the perceived need to improve resolution to 4-km. The requirement for uniform grid spacing across the entire state of California combined with the balance between efficiency vs. accuracy produced the compromise of 8-km grid resolution during the air quality modeling carried out in this study.

The initial conditions (ICs) of gas-phase and particle-phase species were generated following the work of [155] and [158]. Table 1 summarizes the domain average IC concentrations of major model species used in the current study as a function of season. The IC concentrations can be quantified within the UCD/CIT framework through the use

of internal tracers. It was found that the influence of IC concentrations on air quality chemistry diminishes by the end of first 3-4 days in the current study. As a result, predicted concentrations from the first 4-days of each simulation period were disregarded in the calculations of periodic/annual average particulate matter (PM) concentrations.

Table 7-1: Domain-averaged initial concentrations of major model gas and particle species at the surface.

		Domain Average Concentration			
Species	Unit	Winter (DJF)	Spring (MAM)	Summer (JJA)	Fall (SON)
Carbon monoxide (CO)	ppm	0.2823	0.2823	0.2823	0.2823
Carbon dioxide (CO_2)	ppm	332.00	332.00	332.00	332.00
Sulfur dioxide (SO_2)	ppm	0.0020	0.0020	0.0020	0.0020
Nitrogen dioxide (NO_2)	ppm	0.0046	0.0046	0.0046	0.0046
Nitric oxide (NO)	ppm	0.0033	0.0033	0.0033	0.0033
Reactive hydro carbon (RHC)	ppm	0.0513	0.0513	0.0513	0.0513
Ozone (O_3)	ppm	0.0401	0.0401	0.0401	0.0401
Nitric acid (HNO_3)	ppm	0.0010	0.0010	0.0010	0.0010
Ammonia (NH_3)	ppm	0.0029	0.0029	0.0029	0.0029
Hydrochloric acid (HCl)	ppm	0.0010	0.0010	0.0010	0.0010
Formaldehyde (HCHO)	ppm	0.0000	0.0000	0.0000	0.0000
Acetaldehyde (CH_3CHO)	ppm	0.0000	0.0000	0.0000	0.0000
Aldehydes (RCHO)	ppm	0.0000	0.0000	0.0000	0.0000
Acetone (ACET)	ppm	0.0006	0.0006	0.0006	0.0006
Methyl ethyl ketone (MEK)	ppm	0.0000	0.0000	0.0000	0.0000
Methyl glyoxal (MGLY)	ppm	0.0000	0.0000	0.0000	0.0000
Glyoxa (GLY)	ppm	0.0000	0.0000	0.0000	0.0000
Peroxy acetyl nitrate (PAN)	ppm	0.0003	0.0008	0.0008	0.0005
Hydrogen peroxide (H_2O_2)	ppm	0.005	0.005	0.005	0.005
Isoprene (ISO)	ppm	0.0003	0.0003	0.0003	0.0003
Elemental carbon (EC)	$\mu g\ m^{-3}$	0.18	0.18	0.18	0.18
Organic carbon (OC)	$\mu g\ m^{-3}$	0.66	0.66	0.66	0.66
Nitrate (N(V))	$\mu g\ m^{-3}$	0.36	0.36	0.36	0.36
Sulfate (S(VI))	$\mu g\ m^{-3}$	0.45	0.45	0.45	0.45
Chloride (Cl(-1))	$\mu g\ m^{-3}$	0.19	0.19	0.19	0.19
Sodium (NA(1))	$\mu g\ m^{-3}$	0.21	0.21	0.21	0.21
Ammonium (N(-III))	$\mu g\ m^{-3}$	0.24	0.24	0.24	0.24
OTHER	$\mu g\ m^{-3}$	1.62	1.6	1.6	1.60
H2OPART	$\mu g\ m^{-3}$	0.891	0.89	0.89	0.89

The boundary conditions (BCs) of various gas-phase and particle-phase species were adjusted for seasonal variability [159, 160]. The scaling for vertical boundary conditions was obtained from Ying et al. ([155]), and boundary conditions at the top of the model domain were interpolated from the lateral boundary conditions in the top model layer.

Table 2 summarizes the average BC concentrations of selected model species along the West Coast as used in the current study as a function of season.

Table 7-2: Average boundary concentrations of various model gas and particle species concentrations along the western boundary of the modeling domain.

		Domain Average Concentration			
Species	Unit	Winter (DJF)	Spring (MAM)	Summer (JJA)	Fall (SON)
Carbon monoxide (CO)	ppm	0.4000	0.4000	0.4000	0.4000
Carbon dioxide (CO_2)	ppm	332.0000	332.0000	332.0000	332.0000
Sulfur dioxide (SO_2)	ppm	0.0010	0.0010	0.0010	0.0010
Nitrogen dioxide (NO_2)	ppm	0.0010	0.0004	0.0003	0.0004
Nitric oxide (NO)	ppm	0.0010	0.0004	0.0003	0.0004
Reactive hydro carbon (RHC)	ppm	0.0069	0.0069	0.0069	0.0069
Ozone (O_3)	ppm	0.0350	0.0400	0.0400	0.0350
Nitric acid (HNO_3)	ppm	0.0007	0.0007	0.0007	0.0004
Ammonia (NH_3)	ppm	0.0025	0.0025	0.0025	0.0025
Formaldehyde (HCHO)	ppm	0.0015	0.0015	0.0015	0.0015
Acetaldehyde (CH_3CHO)	ppm	0.0020	0.0020	0.0020	0.0020
Aldehydes (RCHO)	ppm	0.0014	0.0014	0.0014	0.0014
Acetone (ACET)	ppm	0.0015	0.0015	0.0015	0.0015
Glyoxal (GLY)	ppm	0.0002	0.0002	0.0002	0.0002
Peroxi acetyl nitrate (PAN)	ppm	0.0005	0.0005	0.0005	0.0003
Isoprene (ISO)	ppm	0.0000	0.0000	0.0000	0.000
Elemental carbon (EC)	$\mu g\ m^{-3}$	0.01	0.01	0.01	0.01
Organic carbon (OC)	$\mu g\ m^{-3}$	0.02	0.02	0.02	0.02
Nitrate (N(V))	$\mu g\ m^{-3}$	0.04	0.03	0.03	0.03
Sulfate (S(VI))	$\mu g\ m^{-3}$	0.05	0.05	0.05	0.05
Chloride (Cl(-1))	$\mu g\ m^{-3}$	0.06	0.06	0.06	0.06
Sodium (NA(1))	$\mu g\ m^{-3}$	0.06	0.06	0.06	0.06
Ammonium (N(-III))	$\mu g\ m^{-3}$	0.01	0.01	0.01	0.01
OTHER	$\mu g\ m^{-3}$	0.03	0.03	0.03	0.03
H2OPART	$\mu g\ m^{-3}$	1.47	0.35	1.09	0.65

The base-case raw emissions inventories for the year 2000 were obtained from the California Air Resources Board (CARB) and the SCAQMD. Area source and point source emissions were used without modification in all simulations. On-road mobile source emissions were adjusted for the variation of meteorological conditions experienced during each simulation using CARB's Emissions Factors (EMFAC) model. EMFAC produces mobile emissions summaries for different pollutants and technology classes in 69 geographical locations spanning the entire state of California. EMFAC is also able to predict how temperature and humidity influence mobile source emissions of nitrogen oxides (NOx) and reactive hydrocarbons (RHCs). EMFAC results were generated for the base-case year 2000 emissions inventory and for the conditions predicted to occur within each of the 69 geographical regions at each simulated hour.

The base-case year 2000 mobile source emissions were then scaled by the ratio of $EMFAC^{actual}/EMFAC^{base\text{-}case}$ for each pollutant of interest in each grid cell of the model domain. WRF predictions for hourly-averaged temperature and surface shortwave radiation in each grid cell were also combined with the MODIS satellite data and fed into CARB's BEIGIS model to predict episode-specific biogenic volatile organic compound emissions. The adjusted mobile source emissions and the newly generated biogenic emissions were then processed with the remaining area and point sources to provide a source oriented model-ready gridded hourly emissions inventory.

The UCD/CIT air quality model employed in this study is based on the original CIT 3-D photochemical model [99, 161] with updates to provide a source-oriented framework (see for example, [34-37, 46, 155, 162]). Only those aspects of the UCD/CIT model that were updated during the current study are discussed here.

Previous studies [163-167] have found mass consistency errors when the meteorological model and the chemistry-transport model do not use the same grid system, the same interpolation strategies and/or the same transport algorithms. [164] proved the existence of the mass consistency errors while using the MM5/CMAQ modeling system and recommended an effective way to overcome the problem by re-calculating the vertical wind velocity using the horizontal wind components and atmospheric density generated by the meteorology model. Calculation of vertical winds was therefore incorporated into the UCD/CIT modeling framework in the current study. The UCD/CIT model was also updated so that it could work with either prognostic wind fields (C-grid) or diagnostic wind fields (A-grid).

The computational burden of simulating air quality in a large domain over 2016 days motivated revisions to the approach for gas-particle transfer of inorganic species in the UCD/CIT model. The original approach for gas-particle conversion involved fully dynamic transfer of both acidic and basic species between the gas and particle phase, requiring many thousands of calls to the thermodynamics routines during each integration time step within each grid cell. The fully dynamic approach for gas-particle conversion was replaced by the approach proposed by [168] whereby acid gases are treated as fully dynamic species while ammonia is considered to be in equilibrium between the gas and particle phases. The original thermodynamic routines were based on the Aerosol Inorganic Module (AIM) developed by [169] with updates to correct coding errors and impose minimum water constraints to keep the solution in the continuum region [170]. The modified approach used in the present study replaces the AIM thermodynamics module with ISORROPIA II [171, 172] to calculate the vapor pressure of semi-volatile inorganic species above each particle surface. The combination of these changes increased the speed of the model calculations by roughly a factor of two with less than 10% difference in the final predicted concentrations of gas-phase and particle-phase species.

Wet deposition calculations were added to the UCD/CIT model so that it could correctly predict removal rates for gases and particles during rain events. The rain drop size

distribution was calculated as a function of total precipitation rate [173] followed by a calculation of the pollutant washout rate [174].

The original version of the UCD/CIT model relied on independently generated emissions inventories for sea salt over ocean grid cells. The input data and correlations used to calculate sea salt emissions are relatively simple, and so the sea salt emissions algorithm was embedded directly within the UCD/CIT model in the present study. Sea salt emissions over the open ocean [175] and sea salt emissions in the surf zone [176] were both predicted by this new module based on the surface wind speed.

7.3 Results

Airborne particulate matter concentrations in California are strongly influenced by temperature, relative humidity, UV radiation, wind speed, and mixing height [33, 61]. It is instructive to examine the climate-induced changes to these meteorological variables over 7 year windows to gain greater insight into the processes that influence $PM_{2.5}$ concentrations. Figure 7-2 shows the differences between the future (2047-53) and present-day (2000-06) averages for ground-level temperature, humidity, wind speed, precipitation, mixing height, and UV radiation. Figure 7-2a shows that the surface air temperature is predicted to increase by 1.0-1.7 °C over the Pacific Ocean west of California and increase by 0.2 to 1.2 °C over California inland regions in the future years compared to the present-day. The predicted increase is slightly greater (~1.0 °C) in large urban areas such as Los Angeles, Bakersfield, Fresno, San Francisco and Sacramento compared to rural and mountainous areas (~0.2-0.8 °C).

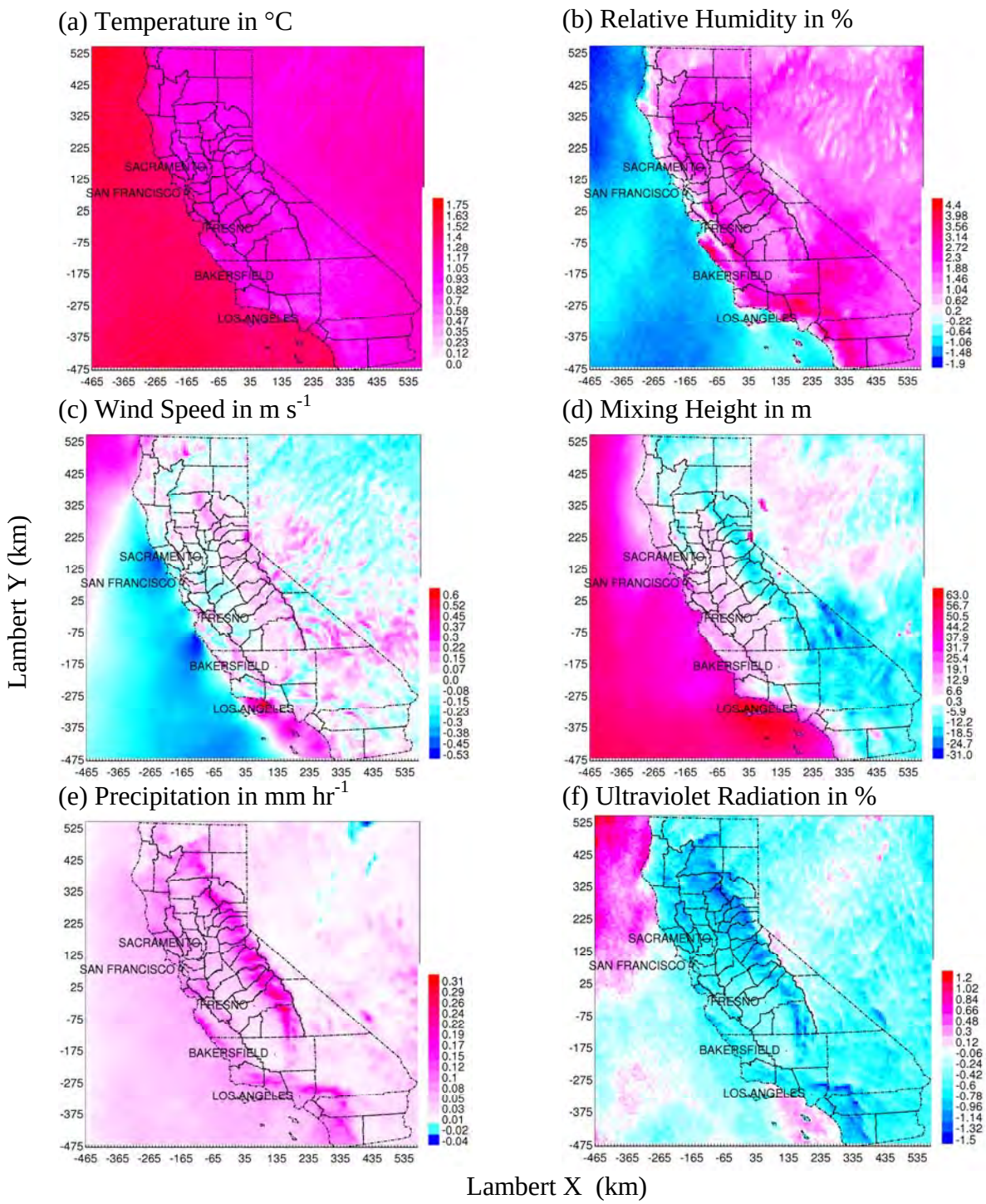

Figure 7-2: Panels (a)-(f) show changes in annual average values in meteorological parameters likely to occur due to climate change in the future (2047-53) from the present-day (2000-06).

The prediction of larger temperature increases over the ocean than over land is caused by large scale features of the PCM simulation that drive the WRF model during the downscaling exercise. Future PCM predictions for air temperature 2 m above the surface increase more over the Pacific Ocean than over the California land mass during the months of December, January, and February. Much of this change is driven by the sea-surface temperature inherited from the PCM simulations and by an increased frequency of precipitation events over land during the winter months. These PCM temperature and precipitation patterns are consistent with the results produced by the Community Climate System Model (CCSM) operated under the SRES A2 emissions scenario. Although some GCMs may predict greater future temperature increase over land than over the ocean during winter months, the results of the PCM simulations used in the current study are a legitimate example of a relatively modern simulation of climate that contributes to the ensemble of results that have been produced by the scientific community to date. In contrast to the winter trends, both PCM and CCSM predict that air temperatures over land increase more than air temperatures over water during the summer months (see chapter 6). Hotter temperatures generally encourage lower $PM_{2.5}$ concentrations in California through the evaporation of ammonium nitrate aerosol [61]. A downward bias in future surface temperature over land would produce an upward bias in predicted future $PM_{2.5}$ concentrations.

The predicted change in future (2047-53 vs 2000-06) relative humidity (RH) at the surface is shown in Figure 7-2b. RH is predicted to decrease by ~0.20-1.9 % over the ocean as the air temperature warms because the amount of additional water vapor evaporated from the ocean surface does not keep pace with the additional capacity of the warmer atmosphere to hold water vapor. RH is predicted to increase by ~ 0.20-4.4% over land as the moist air cools by 0.5-0.8^{o}C reducing its capacity to hold water vapor. The SoCAB is predicted to experience the greatest increase in RH by as much as 4% compared to only ~0.2-0.7% in the SJV in the future. Increasing RH encourages the partitioning of ammonium nitrate to the particle phase (Kleeman, 2008). Any upward bias in predicted RH would once again bias $PM_{2.5}$ concentrations upwards.

Wind speed and mixing height are two of the most critical meteorological parameters for air pollution calculations since they determine the ventilation of fresh emissions away from the surface. Air pollution episodes in California are generally characterized by a stagnation period (low ventilation) lasting more than 2-days. Figure 7-2c shows that the future wind speed (2047-53) is predicted to increase by as much as ~0.3 ms^{-1} relative to current years (2000-06) around Los Angeles, and in some parts of the SJV + Sacramento Valley air basins. These changes are important since average wind speed in these air basins are approximately 2.7 ms^{-1}. The mixing height (planetary boundary layer) shown in Figure 7-2d is predicted to increase by ~25-30 m in the coastal areas but decrease by ~25-30 m in the Sierra Nevada mountain range. The average future mixing height is predicted to increase by ~6 m in the SJV and by ~20 m in the lower part of the SoCAB. All of these changes are small compared to the base-case average mixing height of ~600 m and so they have little effect on pollutant concentrations. The major driver for changes to future air pollution concentrations associated with ventilation is the changes to wind speed illustrated in Figure 7-2c.

Figure 7-2e shows that the average future (2047-53) precipitation rate is predicted to increase by ~0.3 mm hr^{-1} in the Sierra and some areas in the SoCAB relative to current years (2000-06). Precipitation in the SJV is predicted to increase by ~0.01-0.04 mm hr^{-1} in the future (~80% increase over current levels). The increased rate reflects the increased humidity in the atmosphere resulting in greater precipitation rates during rain events and a general lengthening of the rainy season. Future SJV precipitation rates increased by ~40% in the current rainy season (DJF) but increased by ~240% in the months before and after the traditional rainy season (Sept, Oct, Mar, May). Increased precipitation enhances the wet deposition of pollutants leading to reduced atmospheric concentrations.

Figure 7-2f illustrates that future (2047-53) UV radiation is predicted to decrease by ~1.0-1.3 % in the Sierras, and by ~0.4-0.5 % in the SJV and SoCAB. UV flux decreases as cloud cover increases and so the trend in UV radiation is consistent with the pattern of precipitation rates in the future, i.e., the UV radiation is likely to decrease as precipitation rates increase. UV radiation drives photochemical chemical reactions in the atmosphere, thus reduced UV will reduce the production of secondary PM. Further details of the effects of climate on air pollution meteorology in California are discussed by Zhao *et al*. ([154])

Figure 7-3a shows the present-day (2000-06) annual average concentrations of $PM_{2.5}$ mass for the entire state of California. Higher $PM_{2.5}$ concentrations (>15 μg m^{-3}) are predicted around the urban centers such as Los Angeles, Bakersfield, Fresno, San Francisco and Sacramento because primary particulate emissions sources are concentrated in these regions. Elevated total $PM_{2.5}$ concentrations (>~10 μg m^{-3}) are also predicted along the major transportation routes in the SJV and SoCAB. The highest $PM_{2.5}$ total mass concentrations are predicted in the vicinity of El Centro in the southeast portion of the domain due to the influence of windblown dust.

Figures 7-3(b-f) show the contribution to present-day $PM_{2.5}$ total mass from elemental carbon (EC), organic carbon (OC), nitrate (N(V)), ammonium (N(-III)) and sulfate (S(VI)) concentrations, respectively. Primary particulate matter components such as EC and OC account for approximately ~50% of the total $PM_{2.5}$ mass concentrations in California during the present-day (2000-06) simulations. Maximum annual average EC concentrations of ~0.5-1.0 μg m^{-3} are found in the major urban areas and along the major transportation routes as shown in Figure 7-3b. The highest EC concentration of ~1.8 μg m^{-3} was predicted around the port of Oakland in the San Francisco Bay Area under the present-day climate.

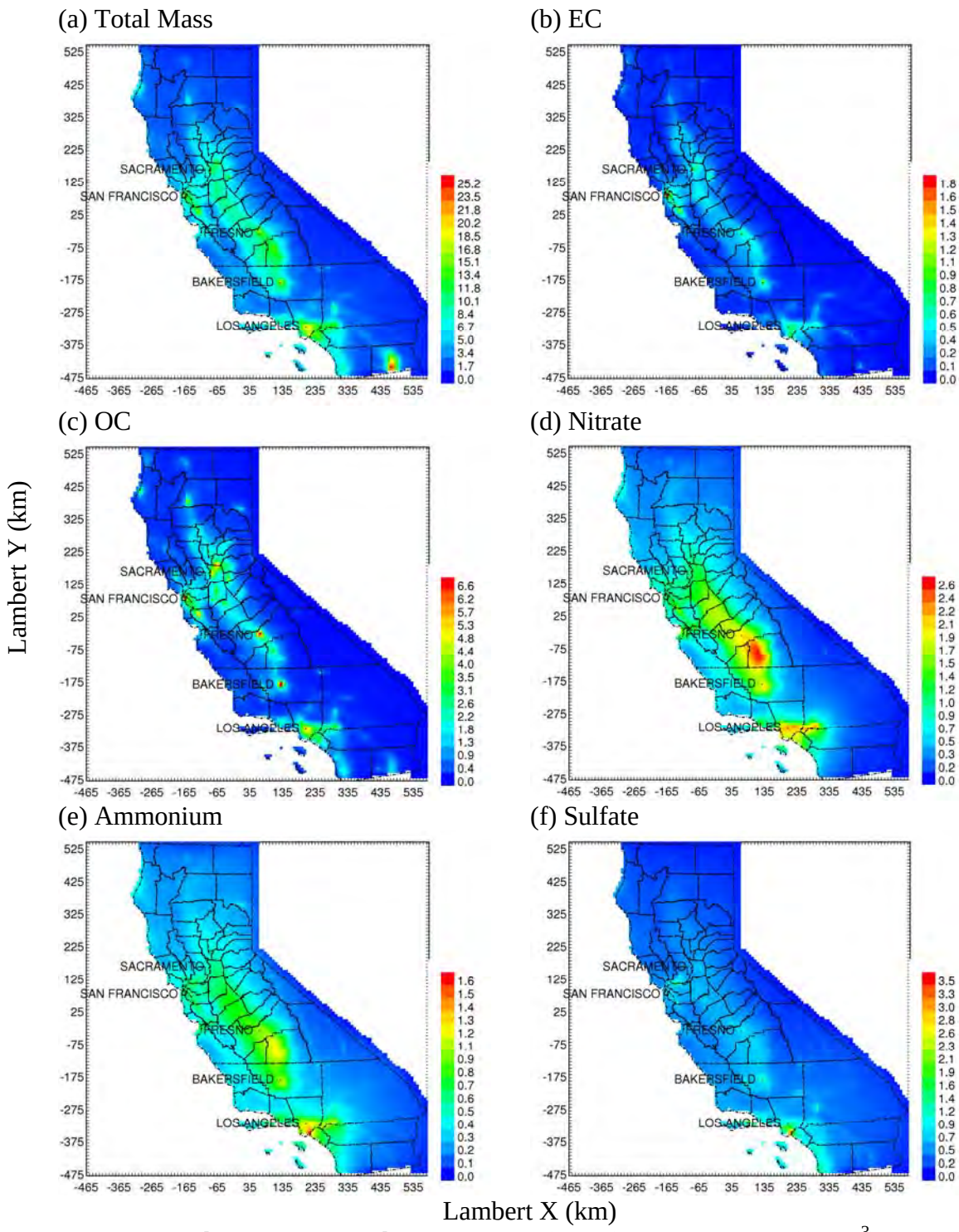

Figure 7-3: Annual average Particulate Matter 2.5 ($PM_{2.5}$) concentrations (μg m^{-3}) in CA for the present day (2000-06) (a) total mass, (b) elemental carbon, (c) organic carbon, (d) nitrate, (e) ammonium, and (f) sulfate.

Predicted annual average OC concentrations are also higher around the major sources of primary emissions in the domain (Figure 7-3c). Maximum annual average OC concentrations in the range of ~5.0-6.6 μg m^{-3} are predicted in the San Joaquin and Sacramento Valleys near major urban areas, while predicted OC concentrations in the SoCAB are in the range of ~3.0-5.0 μg m^{-3}.

Figure 7-3d shows the predicted annual average concentrations of $PM_{2.5}$ nitrate in California. Nitrate accounts for ~12% of the annual average $PM_{2.5}$ mass over broad segments of the state. Predicted nitrate concentrations range from ~1.2-2.6 μg m^{-3} in the SJV to ~1.2-2.0 μg m^{-3} in the SoCAB. The majority of the particulate nitrate is neutralized by ammonium ion and so it is not surprising that the pattern of annual-average ammonium ion concentration (Figure 7-3e) appears similar to the pattern of nitrate concentration. The highest annual average nitrate concentrations are generally found where gas-phase ammonia emissions from agricultural sources are highest (including large dairy farms in the eastern portion of the SoCAB). Predicted ammonium nitrate concentrations had a strong seasonal dependence with concentrations in the winter season (DJF) ~3 times larger than the summer (JJA).

Predicted annual average concentrations of sulfate (S(VI)) were ~<1.0 μg m^{-3} in the SJV but as high as ~1.0-3.5 μg m^{-3} in the SoCAB. Higher annual average concentrations of sulfate (~2.0 μg m^{-3}) were also found along the coastal areas of the SoCAB. This spatial pattern gives strong clues that shipping emissions are the dominant source of sulfate aerosol in the present day simulations.

Climate – air quality predictions are often presented with little verification that the base-case modeling system is able to reproduce present-day air quality concentrations over multi-year periods. Climate- air quality modeling systems that use GCM inputs downscaled to regional scales cannot resolve individual air pollution events but the multi-year average concentrations predicted by these systems should ideally match the multi-year average measurements in each region of interest. Previous studies have evaluated the performance of the UCD/CIT 3D photochemical airshed model driven by observed meteorological fields [155]. The present study is the first to evaluate model performance over a climatologically relevant time-frame (7-year averages) using prognostic meteorology produced by a GCM.

Figure 7-4 shows comparisons between the predicted and observed concentrations of primary and secondary $PM_{2.5}$ components averaged between the years 2000-06 at representative locations in California's most heavily populated air basins. The Central Los Angeles (CELA) site is located in the SoCAB. The Modesto (M14), Visalia (VCS), Fresno (FSF) and San Jose (SJ4) sites are situated in the greater SJV, and the Sacramento (S13) site is in the Sacramento Valley air basin. For each site, 24-hr average measured concentrations of the $PM_{2.5}$ total mass and the major chemical components that contribute to $PM_{2.5}$ mass were obtained from CARB. The corresponding predicted concentrations were then extracted for the present-day (2000-06) air quality simulations. Daily average concentrations were used to calculate mean values and standard deviations over the 7-year period.

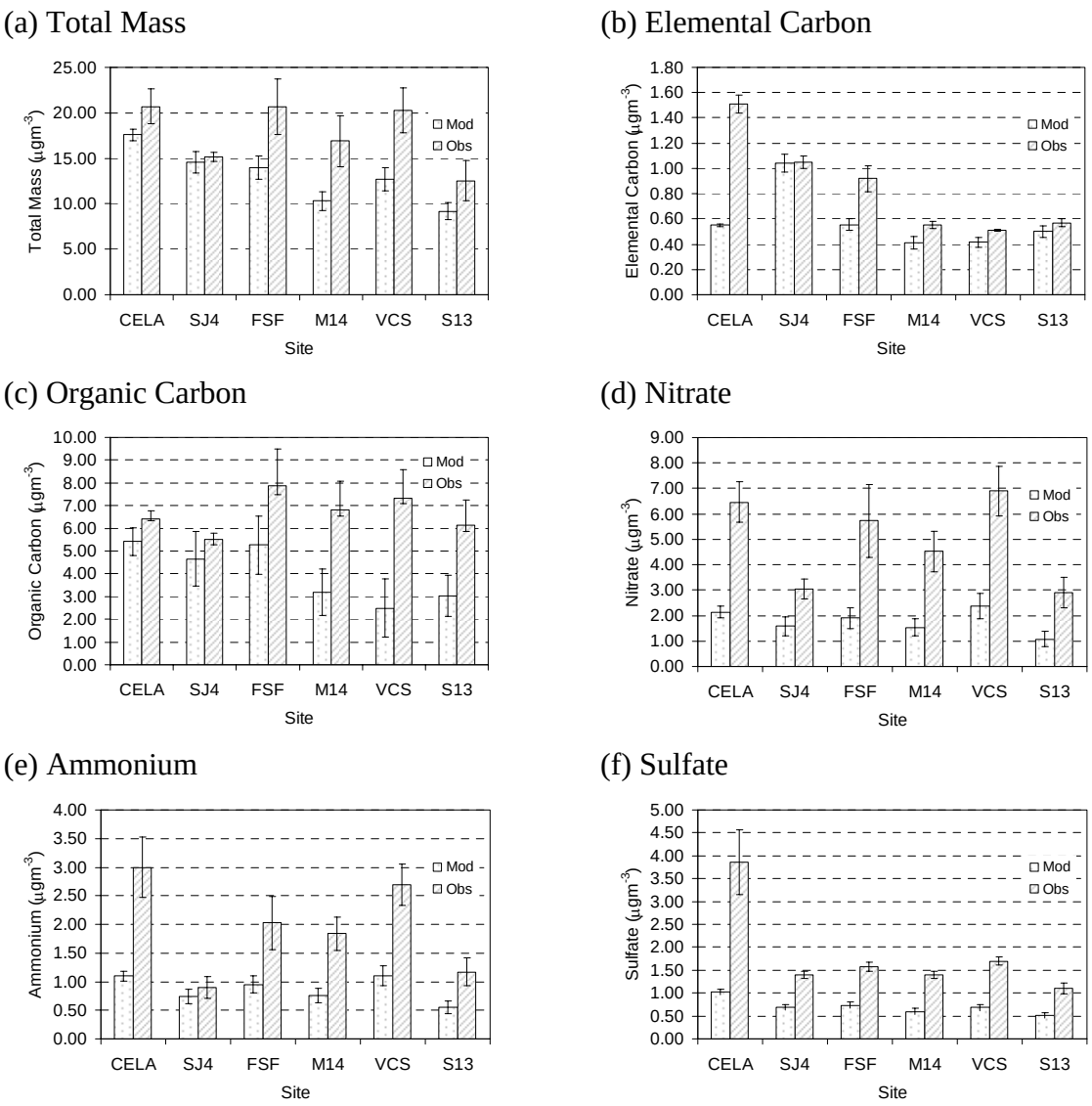

Figure 7-4: Comparison between modeled and observed 7-year average $PM_{2.5}$ (a) total mass, (b) elemental carbon, (c) organic carbon, (d) nitrate, (e) ammonium, and (f) sulfate concentrations at different sites in California: (1) CELA-central Los Angeles North Main St, (2) SJ4-San Jose 4th St, (3) FSF-Fresno 1st St, (4) M14-Modesto 14th St, (5) VCS-Visalia Church St, and (6) S13-Sacramento T St.

Panels (a–c) in Figure 7-4 show the comparisons between the predicted and observed concentrations of $PM_{2.5}$ total mass, $PM_{2.5}$ elemental carbon (EC), and $PM_{2.5}$ organic carbon (OC). Annual average $PM_{2.5}$ total mass concentrations above 20.0±2.0 μg m^{-3} were measured in both the SoCAB and the SJV. Predicted maximum $PM_{2.5}$ total mass concentrations (~13-18 μg m^{-3}) were 4-39% lower than measured values, with consistent under-predictions at all sites. Model performance was relatively better at Central Los

Angeles (CELA), San Jose (SJ4) and Sacramento (S13) compared to other sites. In general, the variation between measured $PM_{2.5}$ concentrations at different sites is greater than the variation between predicted $PM_{2.5}$ concentrations at those same locations (compare the height of the average bars between locations in Figure 7-4a). In contrast, the time variation of the predicted $PM_{2.5}$ concentrations at the same site can be greater than, equivalent to, or less than the time variation of measured $PM_{2.5}$ concentrations at that same site (compare the size of the uncertainty bars at each location in Figure 7-4a).

Figure 7-4b illustrates that present-day (2000-06) predictions for EC concentrations are 64% lower than measured values at central Los Angeles and 12%-39% lower than measured values at all other sites except San Jose where they agree well with measurements. EC is a primary pollutant and so wide-spread under-predictions suggest a systematic bias in emission rates, removal rates, and/or ventilation (i.e., wind speed × mixing height). The fundamental equations and input data files used to represent emissions and removal rates have been validated during numerous retrospective modeling studies that used diagnostic wind fields [50, 155]) and so it seems likely that the ventilation rates generated by the prognostic PCM-WRF meteorological fields are slightly over-predicted. Recent studies confirm that prognostic meteorological fields provide greater ventilation than diagnostic meteorological fields in central California [177]. A zero-order approximation of the air pollution system would predict that concentration (C) ($\mu g\ m^{-3}$) = emissions rate (E) ($\mu g\ hr^{-1}$) / ventilation rate (V) ($m^3\ hr^{-1}$). From this simplified relationship we can derive that the relative change in concentration is inversely proportional to the relative change in ventilation ($\Delta C/C = -\Delta V/V$). The concentration under-prediction at each location could therefore be corrected with a change in average surface wind speed of ~0.15 m sec^{-1} at the Sacramento (S13) site to ~1.98 m sec^{-1} at the Modesto (M13) site. The analysis of PCM-WRF wind speed bias illustrated in chapters 5-6 indicates that it is possible and even likely that wind speeds are over-predicted by at least this amount in the current study.

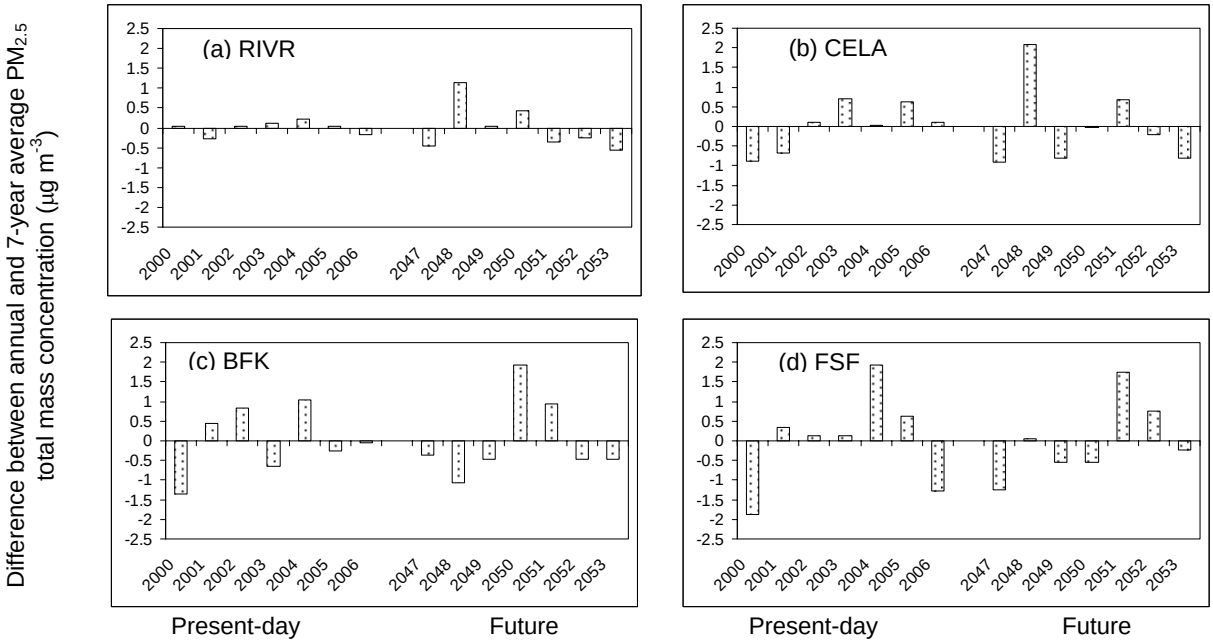

Figure 7-5: Predicted variations around the 7-year average $PM_{2.5}$ total mass concentration at four sites in California: (a) Riverside-Rubidoux (RIVR), (b) Central Los Angeles (CELA), (c) Bakersfield (BFK), and (d) Fresno (FSF)

Panel (c) shows the measured and predicted annual average concentrations of OC at the six representative sites chosen for model evaluation. Measured annual average OC concentrations ranged from 5.5-8 µg m^{-3} while predicted OC concentrations range from 2.5-5.4 µg m^{-3}. In short, OC concentrations were under-estimated by ~33-60% at all sites except for central Los Angeles (CELA) and San Jose (SJ4) where predictions match observations reasonably well. OC can either be emitted directly from sources (primary) or it can be produced in the atmosphere through precursor reactions that form products with low saturation vapor pressure (SOA). In the present study, ~99% of the annual average OC concentrations was attributed to primary organic compounds with the remaining ~1% attributed to SOA formation. Recent studies suggest that primary organic aerosol is semi-volatile [178] implying that SOA formation dominates total OC formation but major questions remain unanswered concerning the exact composition and formation mechanism of this material. Mechanisms that depend on high concentrations of intermediate-volatility precursor compounds have been proposed [179], and even implemented in regional calculations [180], but the intermediate volatility framework characterizes all compounds solely by their saturation vapor pressure. It therefore requires numerous parameterizations for critical elements (rate at which compounds transition between volatility bins, temperature dependence of partitioning, etc.) that (to date) are based on simplistic laboratory experiments. Much work remains to be done using additional laboratory experiments and retrospective field studies supported by comprehensive measurements to constrain these critical parameters before the intermediate volatility framework can be used confidently for climate – air quality

predictions. More chemically complete models for SOA formation that include calculations for activity coefficients in aqueous and organic phases [158] have been shown to form roughly the same amount of SOA as more simplistic two product absorption models [98]. The more computationally efficient two-product model was used in the current study, with the caveat that it does not completely describe all aspects of SOA formation.

Panels (d-f) show the measured and predicted annual average concentrations of $PM_{2.5}$ nitrate, ammonium, and sulfate, respectively. The plots show that the model under-predicts the concentrations of secondary species at all the chosen monitoring sites by ~18-73%. The majority of this under-prediction is likely caused by the excess ventilation produced by the PCM-WRF meteorological predictions (see discussion for Figure 7-4b) exacerbated by the non-linear chemical system for the formation of secondary PM [33]. The pattern of variation between sites appears to be similar for the measured and predicted concentrations of secondary PM since model predictions are able to identify the sites with the highest and lowest concentrations of each secondary pollutant.

Natural annual and intra-annual variability makes it extremely difficult to quantify climate impacts on airborne particulate matter concentrations in California. Panels in Figure 7-5 show the differences between predicted annual average $PM_{2.5}$ concentrations and their 7-year averages at Riverside, central Los Angeles, Bakersfield, and Fresno over the periods 2000-06 and 2047-53. The relative standard deviations (standard deviation divided by the mean) are 2%, 3%, 6% and 9% for the present (2000-06), and 5%, 6%, 8% and 7% for the future (2047-53) periods at Riverside, central Los Angeles, Bakersfield, and Fresno, respectively. This annual variability in $PM_{2.5}$ mass concentrations is mainly caused by normal variation in yearly meteorology combined with ENSO effects operating on a ~3-8 year cycle. One of the key objectives in this study was to capture this annual variability both in the present (2000-06) and future (2047-53) air quality simulations so that the effects of global change can be understood over a climatologically relevant period.

The differences between the future (2047-53) and present-day (2000-06) annual average concentrations of $PM_{2.5}$ total mass, EC and OC are illustrated in Figure 7-6. Panels (a, c, e) display the difference between the 7-year averages while panels (b, d, f) display the significance of this result expressed as the p-value. The p-value quantifies the likelihood that present day (2000-06) concentrations and future (2047-53) concentrations are equal. The p-value is calculated using information about the mean and variance within each 7-year window. Small p-values are produced when large differences exist between present and future concentrations while the annual variability of concentrations within the present and future analysis windows is small. The 7-year analysis windows used in the current study are long by atmospheric chemical modeling standards but relatively short by statistical standards and so p-values were calculated using the student T distribution with 12 degrees of freedom rather than the Normal distribution.

Figure 7-6a shows that the future annual average $PM_{2.5}$ mass concentration is predicted to increase by ~0.2-0.5 $\mu g\ m^{-3}$ in the Sacramento Valley and northern portions of the SJV.

The corresponding p-values shown in panel (b) are ≥0.4 indicating that the differences between 2047-53 and 2000-06 are small relative to the annual variability in the predicted signal. $PM_{2.5}$ concentrations are predicted to decrease by ~0.3-0.7 μg m^{-3} in the southern portion of the SJV and decrease by ~0.3-1.1 μg m^{-3} along coastal regions of California including the heavily populated San Francisco Bay Area and the SoCAB surrounding Los Angeles. The corresponding p-value analysis shows that the majority of these changes are statistically significant ($p<0.05$). As discussed previously, the majority of this decreased concentration stems from increased wind speeds and warmer temperatures providing greater ventilation of primary emissions and increased volatilization of secondary components. The increased wind speed is predicted largely because of the synoptic features of the GCM inputs that were used in the analysis. GCM calculations have a certain degree of inherent uncertainty and so ensembles of GCM calculations are usually employed to build confidence in the results of climate calculations. The present study provides a first data-point for a GCM-WRF-air quality model calculation of climate impacts on air quality that should be followed up with a full ensemble of downscaling runs using multiple GCMs as their starting point.

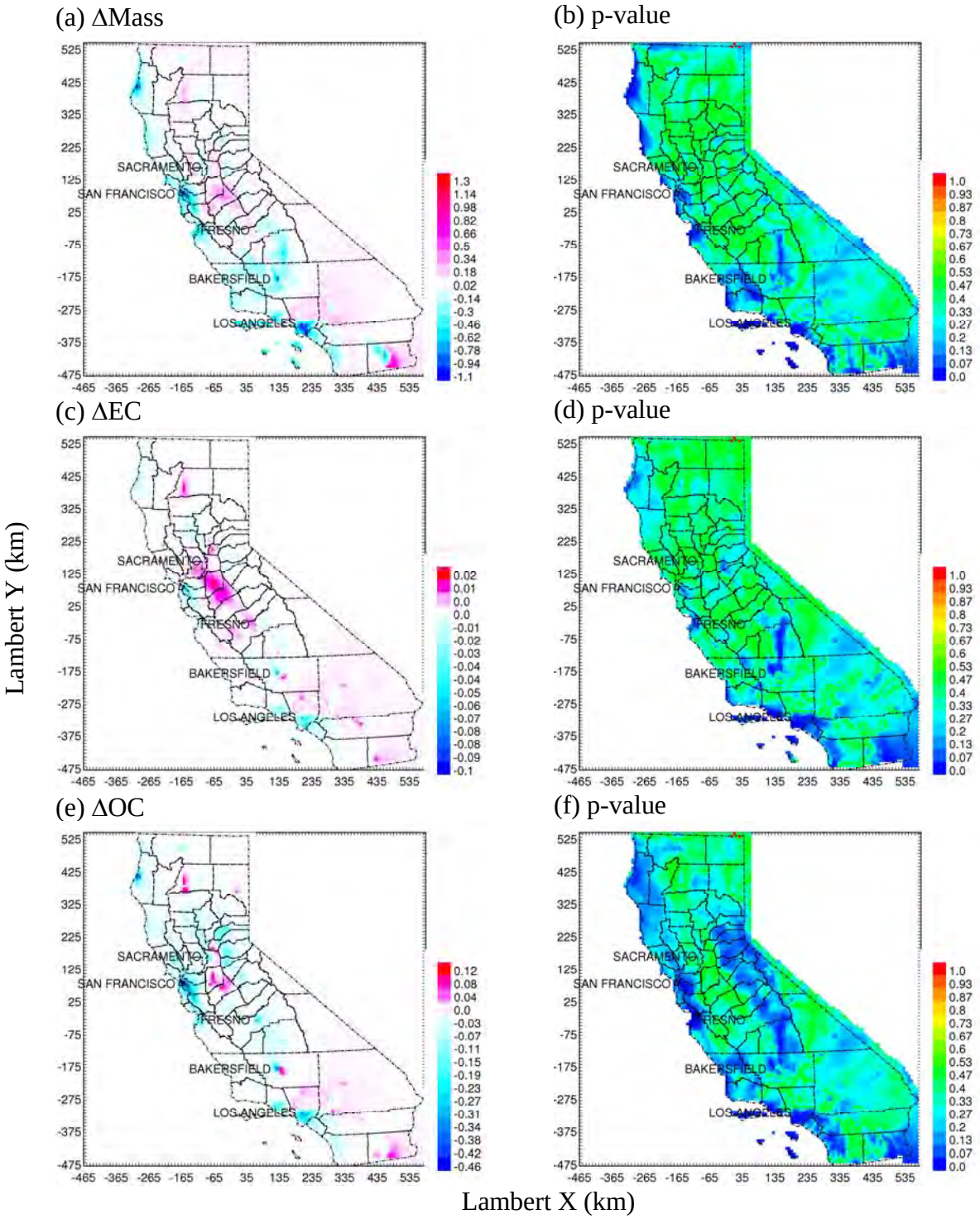

Figure 7-6: Changes in annual average total mass and primary $PM_{2.5}$ concentrations (μg m^{-3}), and their corresponding p-values in CA likely to occur in the future (2047-53) due to climate change from the present-day (2000-06). The p-value quantifies the likelihood that average future concentrations are equal to present day concentrations.

In general, the major features of the $PM_{2.5}$ mass analysis illustrated in Figure 7-6(a,b) are echoed for $PM_{2.5}$ EC in Figure 7-6(c,d) and for $PM_{2.5}$ OC in Figure 7-6(e,f). The only significant trends at the 95% confidence level are localized along the California coast where concentrations generally decrease due to the effects of increased ventilation. Future (2047-53) annual average EC concentrations are predicted to decrease by ~0.02-0.1 μg m^{-3} while future annual average OC concentrations are predicted to decrease by ~0.2-0.46 μg m^{-3} in coastal regions relative to current conditions (2000-06) due to climate change alone.

Figure 7-7 shows the predicted change in annual average concentrations for the secondary $PM_{2.5}$ species and their corresponding p-values using the same format as Figure 7-6. Patterns for nitrate and ammonium ion (panels (a-d)) are similar with 95% confidence achieved for reductions in the SoCAB, in the southern portion of the SJV and extending along the Pacific coast between LA and San Francisco. $PM_{2.5}$ nitrate concentrations are predicted to decrease in both of these regions by up to 0.26 μg m^{-3} with a corresponding decrease of 0.13 μg m^{-3} in ammonium ion concentrations. $PM_{2.5}$ nitrate concentrations are predicted to increase in the northern SJV and southern SV by up to 0.2 μg m^{-3} and in the eastern portion of the SoCAB by up to 0.15 μg m^{-3} with corresponding p-values < 0.1 in portions of these regions. The majority of this increased nitrate concentration stems from the impact of higher background ozone concentrations in future years, which increases the rate of nitric acid production (see Chapter 2).

$PM_{2.5}$ sulfate concentrations are predicted to decrease very slightly in northern CA and around central Los Angeles but increase slightly in the eastern portions of southern California. Each of these trends is significant at the 95% confidence level in portions of the domain. Sulfate increases result from increased temperatures that speed up oxidation of S(IV). .

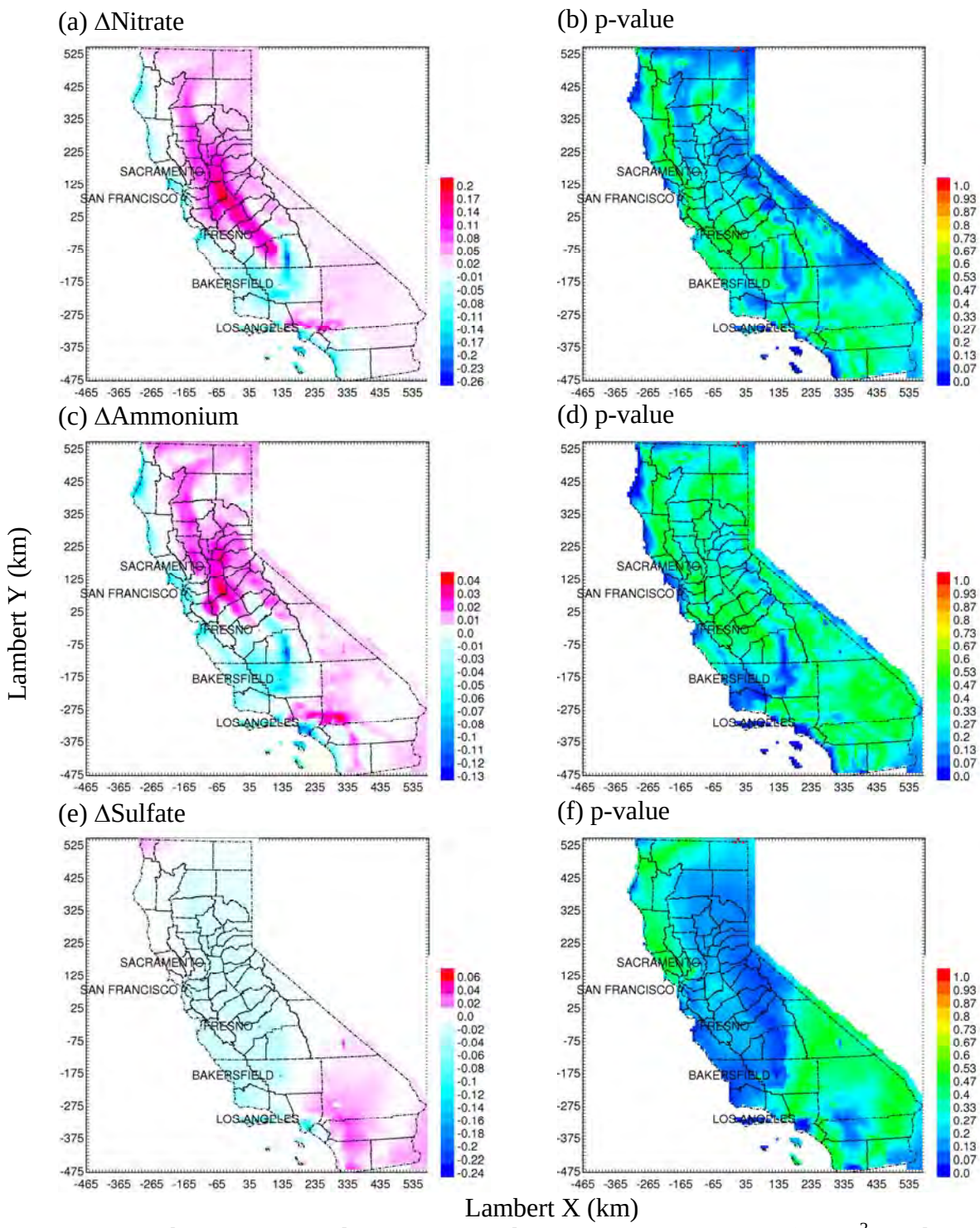

Figure 7-7: Changes in annual average secondary $PM_{2.5}$ concentrations (μg m^{-3}), and their corresponding p-values likely to occur in the future (2047-53) due to climate change from the present-day (2000-06). The p-value quantifies the likelihood that average future concentrations are equal to present day concentrations.

7.4 Summary and Conclusions

The effect of global climate change on annual average $PM_{2.5}$ mass concentrations in California has been studied using seven-year analysis periods that allowed for meaningful statistical analysis of the results. A regional climate – air quality modeling system was employed that downscaled PCM output using the WRF model followed by emissions generation and air quality simulations using the UCD/CIT photochemical model to predict $PM_{2.5}$ concentrations. Simulations were carried out for the present-day climate (2000-06) and for future climate (2047-53) predicted under the "business as usual" global emissions scenario. Air pollutant emissions in California were held at their nominal year 2000 levels to directly examine the effect of climate on regional air quality.

The present-day results from the climate-air quality modeling system successfully predicted the spatial pattern of high $PM_{2.5}$ concentrations in California but the absolute magnitude of the annual average $PM_{2.5}$ concentrations were under-predicted by ~10-35% at different sites in the major air basins. Of the total $PM_{2.5}$ mass, primary PM concentrations were only under-estimated by 4-39% while secondary PM concentrations were under-estimated by ~18-73%. The majority of this under-prediction is likely caused by the excess ventilation produced by the PCM-WRF meteorological predictions; this bias should be consistent in both present and future climate scenarios so that a minimum amount of net bias is introduced into the comparison. The present study is the first to evaluate climate – air quality model performance over a climatologically relevant time-frame (7-year averages) using prognostic meteorology produced by a GCM. It is likely that other modeling systems would have similar performance features if they were checked against observations.

Future predictions indicate that changes to global climate lead to changes in key regional meteorological parameters that affect airborne particulate matter concentrations in California. An analysis of the major meteorological variables shows that the future surface temperature, relative humidity (RH), rain rate, and wind speed are predicted to increase while the UV radiation is predicted to decrease in major urban areas in the SJV and SoCAB. These changes lead to a predicted decrease in $PM_{2.5}$ mass concentrations of ~0.3-0.7 $\mu g\ m^{-3}$ in the southern portion of the SJV and ~0.3-1.1 $\mu g\ m^{-3}$ along coastal regions of California including the heavily populated San Francisco Bay Area and the SoCAB surrounding Los Angeles. The 95 % confidence interval spans zero for $PM_{2.5}$ concentration changes in other parts of California. The natural annual variability in the $PM_{2.5}$ predictions was generally larger than the changes induced by climate. Secondary PM concentrations were predicted to increase in portions of California while primary PM concentrations were predicted to decrease in other regions. These results somewhat contradict previous studies that have predicted decreased $PM_{2.5}$ concentrations throughout California in response to climate change. Those previous studies used coarser spatial resolution and shorter averaging times that made it difficult to fully analyze geographical variation and annual variability in California. The 8 km spatial resolution combined with the seven-year analysis periods used in the current study provide the most comprehensive picture to date about climate effects on $PM_{2.5}$ concentrations in California.

GCM calculations have a certain degree of inherent uncertainty and so ensembles of GCM calculations are usually employed to build confidence in the results of climate calculations. The present study provides a first data-point for a GCM-WRF-air quality model calculation of climate impacts on air quality in California that should be followed up with a full ensemble of downscaling runs using multiple GCMs as their starting point.

8.0 CLIMATE IMPACT ON POPULATION-WEIGHTED AIRBORNE PARTICULATE MATTER CONCENTRATIONS IN CALIFORNIA DURING SHORT AND LONG TIME PERIODS

8.1 Introduction

Air pollution is a persistent public health problem in the United States with approximately 126 million people living in regions that violate the National Ambient Air Quality Standards (NAAQS). The pollutant of greatest current concern is airborne particulate matter with aerodynamic diameter smaller than 2.5 µm ($PM_{2.5}$). Epidemiological studies have estimated rates of mortality and morbidity associated with $PM_{2.5}$ (see for example, [11]; [10]; [9]) yielding predictions that an average of 24000 people die from exposure to particulate matter each year in the United States ([181]). California experiences a disproportionately high fraction of these deaths ([146]) because it is home to two of the air basins that experience some of the highest $PM_{2.5}$ concentrations each year. The South Coast Air Basin (SoCAB) is home to ~15M residents with an annual-average $PM_{2.5}$ concentration that is ~1.5 times higher than the NAAQS and a 24-hr average $PM_{2.5}$ concentration that is ~2.3 times higher than the NAAQS. The San Joaquin Valley (SJV) is home to ~3M residents with $PM_{2.5}$ concentrations that exceed the NAAQS by factors of ~1.4 (annual-average) and ~2.3 (24-hr average).

Meteorology plays an important role in California's air pollution problems. Persistent stagnation events develop when high pressure systems stall over the air basins trapping warm air over cooler air at the surface leading to reduced ventilation of emissions. Temperature, wind speed and direction, and mixing height in the atmosphere play critical roles in determining patterns of air quality over multiple scales of time and space by affecting emissions, atmospheric transformation, and deposition of particles ([182]). Global climate change is likely to change these meteorological parameters affecting air quality (see for example, [61];[33];[55]) with unknown consequences to human health.

California has a complex terrain that includes mountains, valleys, desserts and ocean, which makes the climate-air-quality study even more challenging compared to other parts of the United States. Recently Tagaris *et al*. ([18]) investigated the potential impact of climate change on $PM_{2.5}$ related health effects for the United Stated using the Environmental Protection Agency (EPA's) Environmental Benefits Mapping and Analysis Program (BenMAP). The authors showed that the national average premature mortality is likely to increase by 4000 cases in 2050 compared to 2001 along with both increasing and decreasing mortality cases in different states due to climate change alone. According to their analysis, California is likely to experience an average decrease of 186 cases of premature death with decreasing trends also in other $PM_{2.5}$-related health issues including chronic and acute bronchitis, asthma, hospital admissions, and respiratory diseases in the future. This health effects analysis was based on a limited air quality simulation [18] that did not fully address the spatial scales and time scales of the climate - air quality interactions that are critical in California. Subsequent analysis performed using longer simulation periods with higher spatial resolution [144] have helped provide

more accurate estimates not only of the mean predicted response in $PM_{2.5}$ concentrations caused by climate change, but also the uncertainty of that response relative to inter-annual variability.

The objective of the current study is to quantify the impact of climate change on population-weighted concentrations of $PM_{0.1}$, $PM_{2.5}$, and PM_{10} mass, component species, trace metals, and sources in California. The analysis is based on more than 1000 simulated days of present climate and 1000 simulated days of future climate that span enough years to capture inter-annual variability associated with large scale patterns such as El Nino Southern Oscillation (ENSO) cycles. The large number of simulation days allow for an analysis of extreme events in addition to the analysis of average concentrations. The results are put into proper context by rigorously quantifying the magnitude of the climate effect relative to inter-annual variability.

8.2 Methods

The impact of climate change on regional air quality over the entire state of California was studied using the Parallel Climate Model (PCM), the Weather Research and Forecasting (WRF) model, and the latest generation of the UCD/CIT air quality model. A schematic diagram and detailed description of the modeling system is presented elsewhere ([144]). An overview of the modeling system is presented below.

PCM ([108]) data generated under the "business as usual" climate emissions scenario was dynamically downscaled to 4-km resolution using the WRF model version 2.2 [153] for present-day (2000-06) and future (2047-53) time periods. The WRF model was optimized for California simulations with the physics schemes described by Mahmud *et al*. [144]. A total of 153 days equally divided into nine periods of 17 days each were simulated for each year. Gaps of 25 days were left between simulation periods to evenly distribute the active days starting on Jan 1 throughout the year. This pattern captures an unbiased sample of 1008 days over each of the seven-year periods. The WRF 4-km fields were averaged to 8-km for the air quality simulations to increase the speed of the calculation without sacrificing significant accuracy in the final results (see for example [155]). The final air quality modeling domain was composed of 131x128x10 grid cells (x-y-z) spanning the entire state of California with a first vertical height of 30 m and a total vertical depth of 5km above ground.

The base-case raw emissions inventories for the year 2000 were obtained from the California Air Resources Board (CARB) and the South-Coast Air Quality Management District (SCAQMD). On-road mobile source emissions and biogenic volatile organic emissions were adjusted for the variation of meteorological conditions experienced during each simulation using CARB's Emissions Factors (EMFAC) model, and biogenic processing model (BEIGIS) model, respectively. The techniques to adjust these emissions are summarized by Mahmud *et al*. [144]. Source-oriented and gridded hourly emissions were generated by merging the adjusted on-road mobile and biogenic sources with the original area and point source emissions. Seasonally variable initial conditions (ICs) and boundary conditions (BCs) of gas-phase and particle-phase species were

specified for the air quality model calculations. A summary of the ICs and BCs is provided by Mahmud *et al*. [144]).

The source oriented UCD/CIT 3-D photochemical model (see for example, [34-37, 46, 155, 162]) was updated in the current study [144] with a scheme to re-calculate vertical wind to enforce mass conservation. The fully dynamic treatment of gas-particle conversion using the Aerosol Inorganic Module (AIM) thermodynamic code [169] was replaced by the approach proposed by [168] using the ISORROPIA II thermodynamics package [171, 172] to calculate the vapor pressure of semi-volatile inorganic species above each particle surface. The revised model also includes a new wet deposition scheme and a sea salt emissions scheme.

Figure 8-1 shows the air quality modeling domain and three air basins of interest: the Sacramento Valley air basin (SV), the San Joaquin Valley air basin (SJV) and the South Coast Air Basin (SoCAB). Population-weighted concentrations of particles were calculated for these air basins and for the entire state of California so that the impacts of climate change on public health via changes to air quality could be viewed more directly. According to the 2000 census California has a total population of 33.9 millions, with a total land area of 4.24×10^5 km^2. The population of the SV was 2.4 million with an area of 0.38×10^5 km^2, the population of SJV was 3.2 million with an area of 0.60×10^5 km^2, and the population of the SoCAB was 14.6 million with an area of 0.18×10^5 km^2. In order to understand the climate change effects independent of future changes in population dynamics, the year 2000 population densities and distributions were assumed to be the same in future years in this study. The population-weighted concentration is calculated as $\sum_{i=1}^{n} \frac{p_i \times C_i}{p_{tot}}$, where i designates each computational cell in the domain, p_i is the population at a given cell location, C_i is the particulate concentration in the same cell location, and p_{tot} is the total population in the domain of interest (i.e. air basin wide total population).

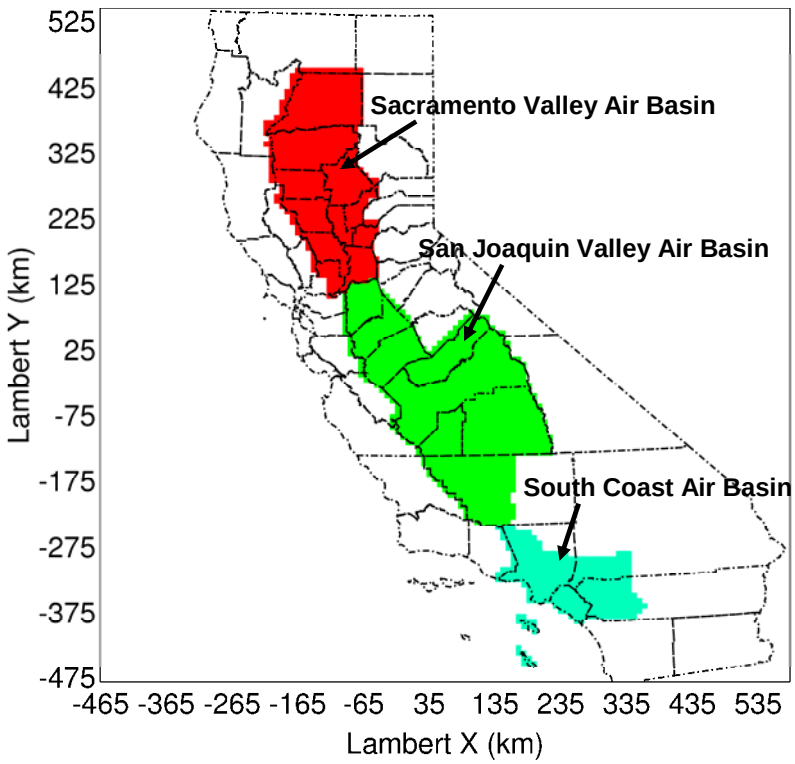

Figure 8-1: Three major air basins in California: (1) Sacramento Valley Air Basin (SV), (2) San Joaquin Valley Air Basin (SJV), and (3) South Coast Air Basin (SoCAB)

8.3 Results and discussion

8.3.1 Annual Average PM Concentrations

The difference between future (2047-53) and present-day (2000-06) population-weighted annual average concentrations of $PM_{2.5}$ are displayed in Figure 8-2 for the entire state of California, and the three major air basins highlighted in Figure 8-1. It should be noted here that the emissions for both the future and present day simulations were kept at 2000 levels. Only the meteorology was varied between the future and present-day simulations to quantify the effect of climate change and increased ozone boundary conditions. Concentrations of total mass, major components, trace metals and source categories contributing to the total mass of primary particles were calculated. The error bars in these figures represent 95% confidence intervals for the mean difference based on the inter-annual variability within each analysis period.

Population-weighted annual average concentrations of $PM_{2.5}$ total mass were predicted to decrease by ~2% in the SoCAB with little change predicted for the SV and SJV. Concentrations of all major $PM_{2.5}$ components such as elemental carbon (EC), organic carbon (OC), sulfate (S(VI)), and ammonium ion (N(-III)) followed this downward trend. In contrast, statewide population-weighted concentrations of $PM_{2.5}$ nitrate (N(V)) increased by ~2%. Population-weighted primary $PM_{2.5}$ concentrations from all sources including dust, shipping, wood smoke, diesel combustion, gasoline combustion, meat

cooking, high sulfur content fuels, and miscellaneous were predicted to decrease by between ~2-6% in California in the future.

Figures 8-3 and 8-4 present the same analysis for the $PM_{0.1}$ and PM_{10} size fractions with largely the same conclusion that future analysis period tends to have lower annual-average population-weighted concentrations than present-day analysis period. The population-weighted annual average concentration of $PM_{0.1}$ total mass was predicted to decrease by ~9% in California during future years (2047-53) relative to present years (2000-06) with the majority of this change occurring in the SoCAB (Figure 8-3). Primary $PM_{0.1}$ source contributions to EC and OC concentrations decreased in the SV but increased in the SJV and SoCAB. Secondary $PM_{0.1}$ component concentrations decreased in the SoCAB with mixed results in the SV and SJV.

Figure 8-4 shows the future change (%) in population-weighted annual average concentrations of PM_{10} in the future (2047-53) compared to the present-day (2000-06) for California and the three air basins of interest. Patterns for PM_{10} total mass, component species, trace metals, and contributions from different sources were similar to $PM_{2.5}$ patterns. PM_{10} total mass was predicted to decrease by ~3% in California in the future. Concentrations of EC, OC, S(VI), and N(-III) were predicted to decrease in the range between ~1-4%. Population-weighted concentrations of trace metals, and contributions from different sources were also predicted to decrease in the future by as much as ~3-6%.

Uncertainty analysis must be considered to put the results illustrated in Figures 8-2 to 8-4 into proper context. The error bars in these figures represent the 95% confidence interval based on the inter-annual variability within each analysis period. The most significant feature displayed in these figures is the size of the uncertainty bars induced by inter-annual variability vs. the size of the average change between future and present years. In almost all cases, the magnitude of the inter-annual variability is greater than the average change between future and present years. The only exceptions to this trend are slightly reduced concentrations of OC associated with reduced contributions from shipping and combustion of fuels with high sulfur content.

The fact that 95% confidence intervals displayed in Figures 8-2 to 8-4 overlap zero implies that a random selection of different years within each climate period could lead to either positive or negative effects on concentrations. The Intergovernmental Panel on Climate Change (IPCC) Third Assessment Report (AR3) (2001) and the Fourth Assessment Report (AR4) (2007) projected future global changes relative to the present-day based on 30-year (1960-1989) and 20-year (1980-1999) averages, respectively. In the current study, only ~40% of the days within seven-year periods in the present-day (2000-06) and future (2047-2053) were simulated. The reduced analysis window greatly lowers the computational burden of the problem while still capturing the inter-annual variability associated with the ENSO cycle. Unfortunately, the limited number of sample points also increase the uncertainty of the comparison between present-day vs. future climate since the uncertainty range in the comparison is inversely proportional to the square root of n (=number of simulated days). The current results provide a best estimate for the effect of climate on annual-average population-weighted PM concentrations in

California, but the length of the analysis periods must be expanded to calculate a full set of statistically significant changes.

It must also be recognized that the inter-annual variability is only one source of uncertainty in the climate-air quality calculation. Most notably, the uncertainties introduced by the choice and configuration of the GCM, RCM, and air quality models are not included in the current analysis. Running a complete ensemble of calculations over a full 20-year analysis period would fully characterize this uncertainty but this effort was beyond the scope of the current study.

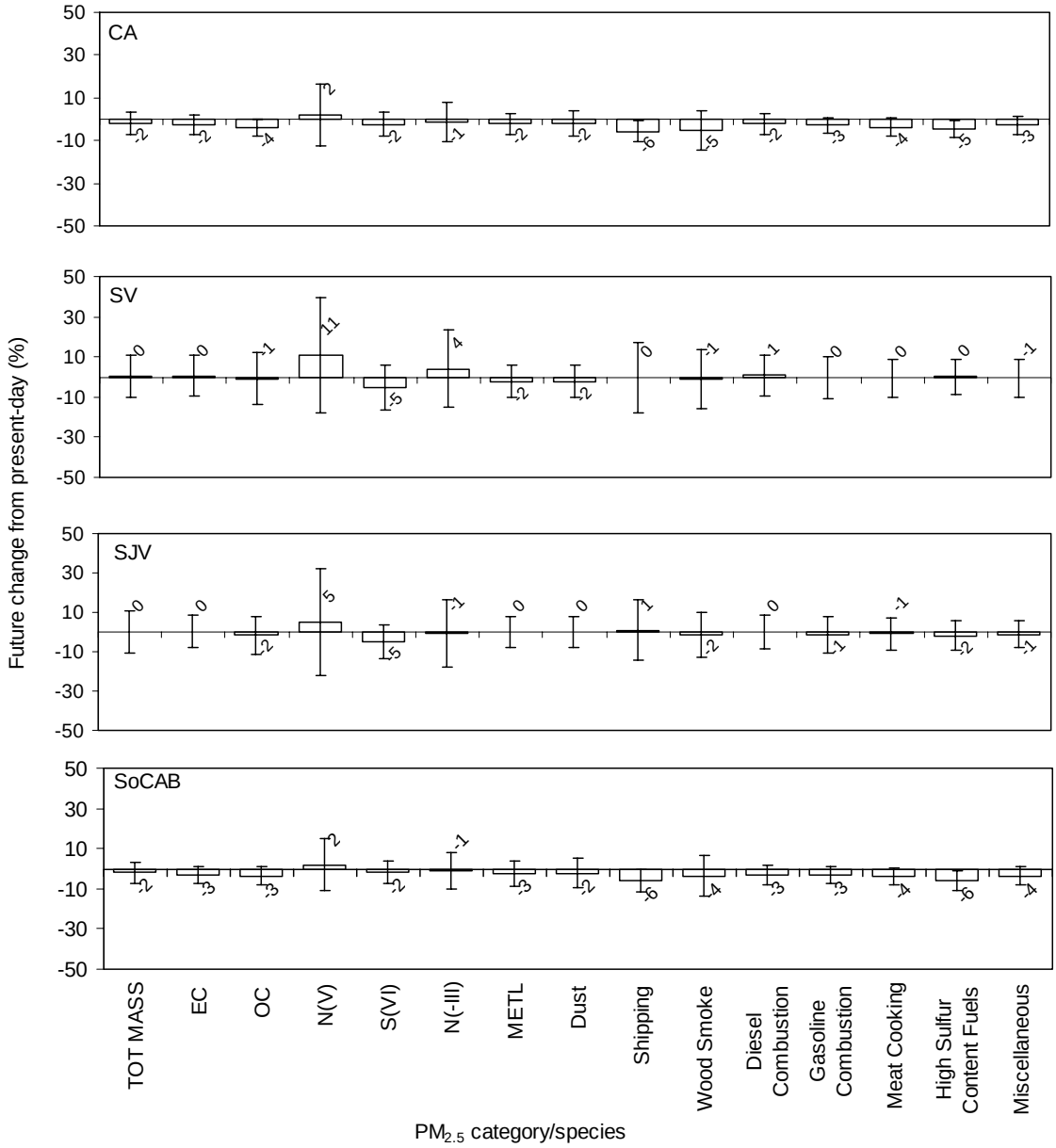

Figure 8-2: Future (2047-53) change in population-weighted concentrations of $PM_{2.5}$ total mass, primary and secondary components, trace metal and source categories contributing to the total mass from present-day (2000-06). Panels (top-down) show California state-wide average, Sacramento Valley (SV) air basin average, San Joaquin Valley (SJV) air basin average, and South Coast Air Basin (SoCAB) average results. The error bars represent the 95% CI.

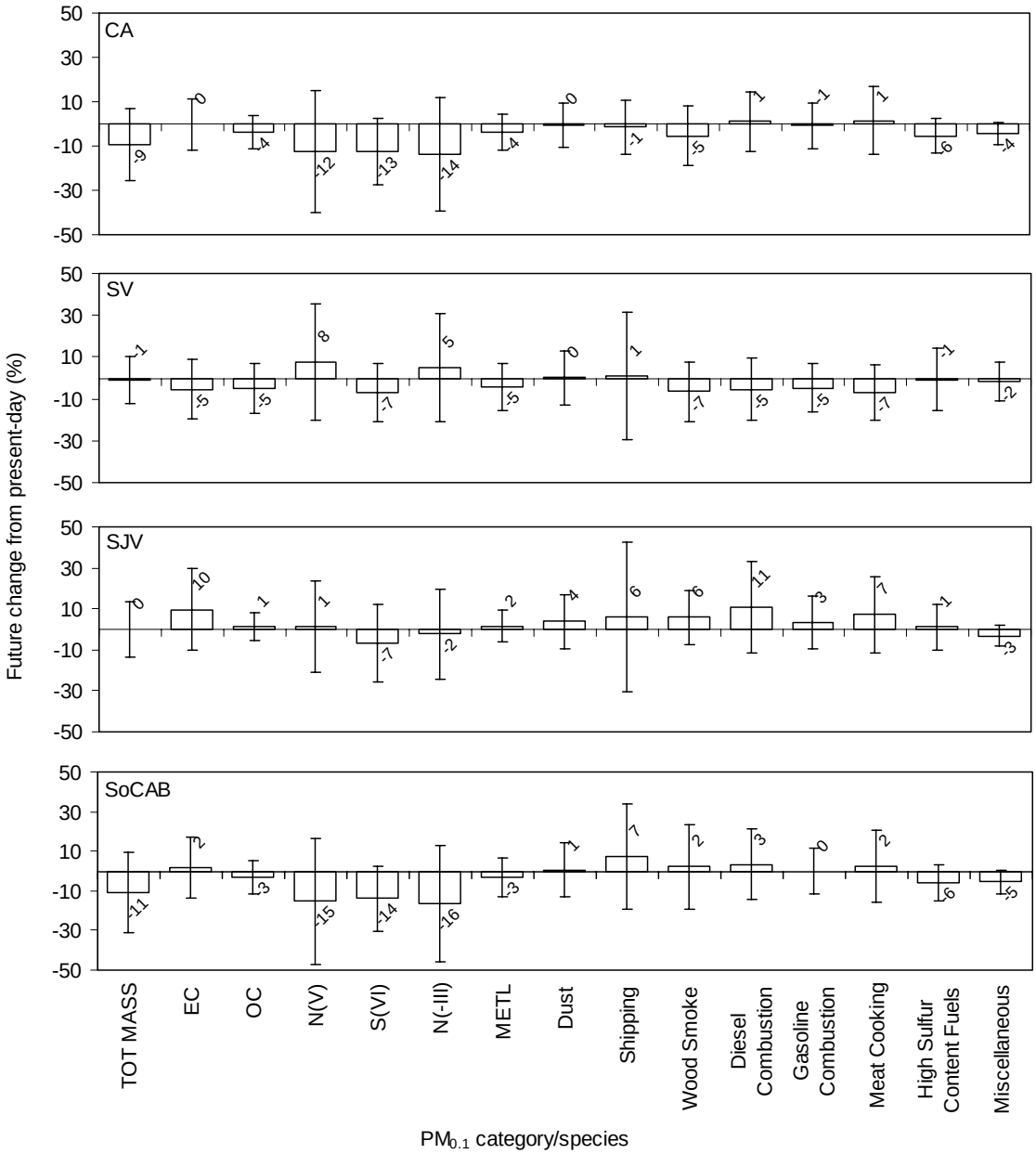

Figure 8-3: Future (2047-53) change in population-weighted concentrations of $PM_{0.1}$ total mass, primary and secondary components, trace metal and source categories contributing to the total mass from present-day (2000-06). Panels (top-down) show California state-wide, Sacramento Valley (SV) air basin, San Joaquin Valley (SJV) air basin, and South Coast Air Basin (SoCAB) average results. The error bars represent the 95% CI.

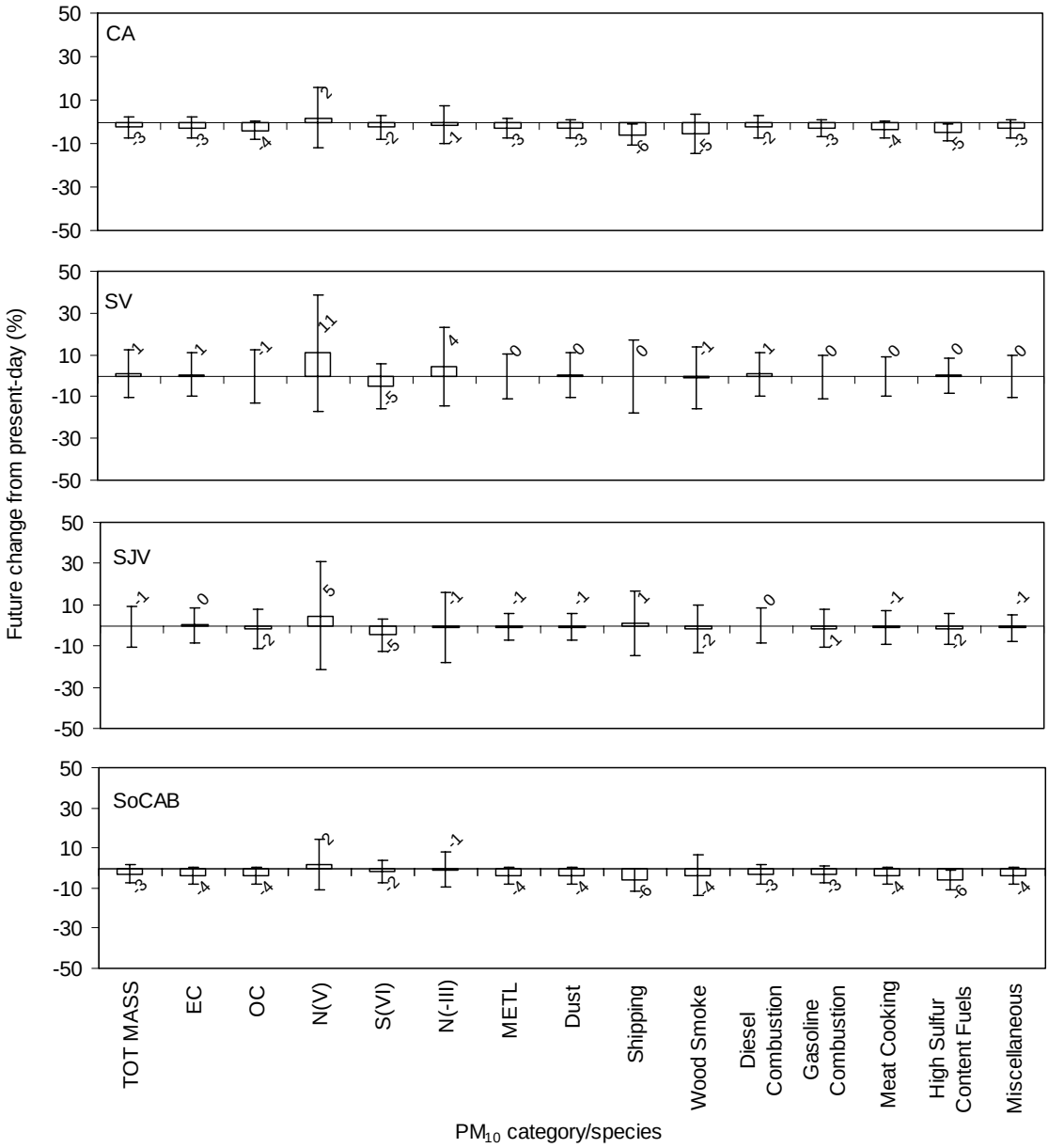

Figure 8-4: Future (2047-53) change in population-weighted concentrations of PM_{10} total mass, primary and secondary components, trace metal and source categories contributing to the total mass from present-day (2000-06). Panels (top-down) show California state-wide average, Sacramento Valley (SV) air basin average, San Joaquin Valley (SJV) air basin average, and South Coast Air Basin (SoCAB) average results. The error bars represent the 95% CI.

8.3.2 Extreme Events

Short-term exposures to high concentrations of airborne particulate matter could lead to serious health effects for susceptible populations. The impact of climate change on extreme air pollution events was examined in detail during the current study. Figure 8-5 shows the distribution of population-weighted daily average $PM_{2.5}$ total mass concentrations for 1008 days of present climate (panel a) and 1008 days of future climate (panel b). The 24-hr average concentrations in both analysis periods are approximately normally distributed with a slightly lower mean value in the future compared to present-day. In contrast, the extreme concentration events defined to be the highest 1% of the predicted concentrations are higher in the future than in the present time period. The shaded regions in panels (a) and (b) show that the extreme values in the present climate range from 16.5-19.2 μgm^{-3} while the extreme values in the future climate range from 16.6-24.7 μgm^{-3}. Further analysis was carried out to understand the effects of climate change on these extreme concentrations.

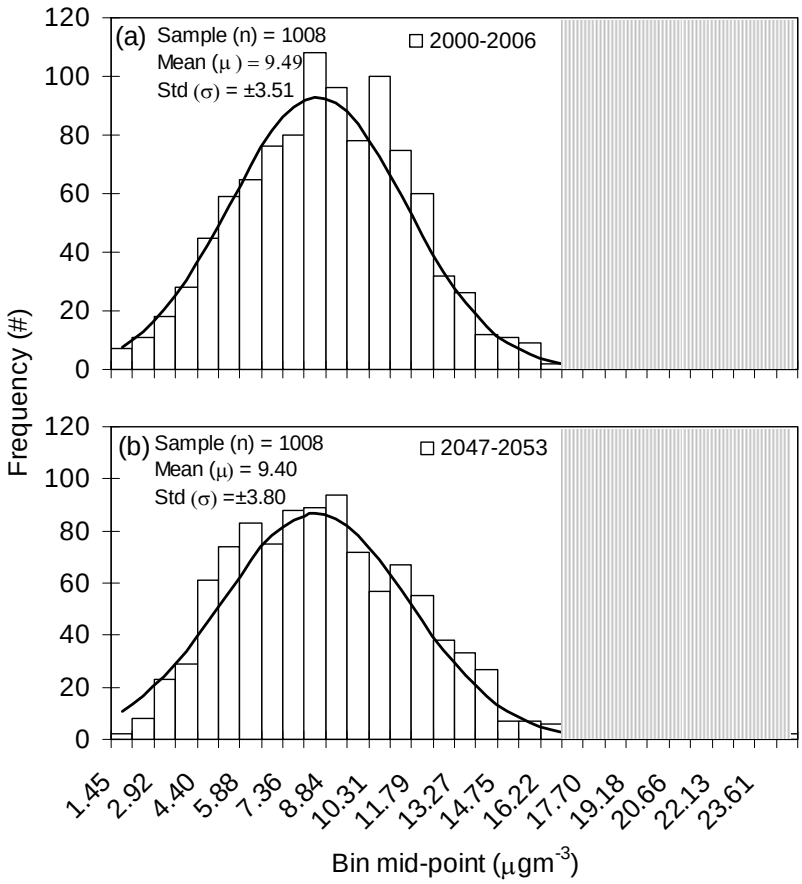

Figure 8-5: Frequency distribution of 24-hr average population-weighted $PM_{2.5}$ total mass concentrations for California under the (a) present-day (2000-2006) and (b) future (2047-2053) climate conditions. The shaded regions encompass values higher than the 99th percentile value of each distribution.

Figure 8-6 shows the average $PM_{2.5}$ total mass concentrations corresponding to the 10 days with the highest population-weighted PM2.5 concentrations in California (99th percentile extreme concentrations). Panel (a) shows the 10-day average concentrations for the future extreme events (2047-53), panel (b) shows the 10-day average concentrations for the present-day extreme events (2000-06), and panel (c) shows the difference between the future and present-day extreme events.

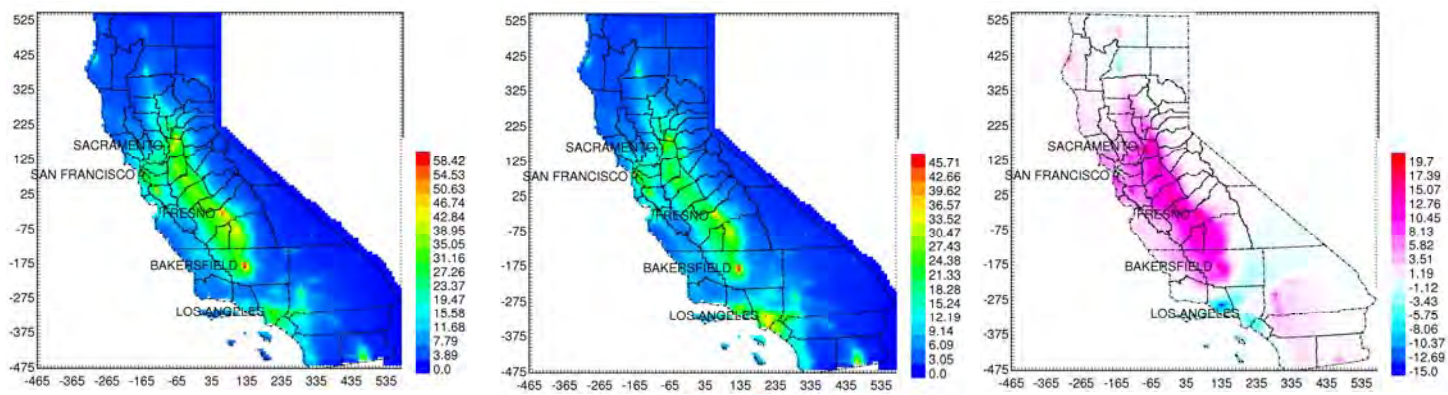

Figure 8-6: Average of worst 24-hr average $PM_{2.5}$ total mass concentrations ($\mu g\ m^{-3}$) corresponding to days with population-weighted concentrations above the 99th percentile values as illustrated in Figure 8-3 for California under the (a) future (2047-2053), and (b) present-day climate (2000-2006) conditions. Panel (c) shows the difference between the future (a) and present-day (b).

Extreme events in the future climate are characterized by PM2.5 concentrations of ~45-55 μgm^{-3} in and around cities including Bakersfield, Fresno, and Sacramento (panel (a)). In comparison, extreme events in the present climate exhibit PM2.5 concentrations in the range between ~35-45 μgm^{-3} in and around major cities (panel b). The extreme concentrations exceed both the California Ambient Air Quality Standard (CAAQS) of 20 $\mu g\ m^{-3}$ and the National Ambient Air Quality Standard (NAAQS) of 35 $\mu g\ m^{-3}$ for 24-hr average $PM_{2.5}$ total mass concentration. Panel (c) shows that the extreme concentrations are predicted to increase by ~15-19 $\mu g\ m^{-3}$ in and around Bakersfield, Fresno, Sacramento, and San Francisco in the future compared to present-day. The maximum future increase of ~18-20 $\mu g\ m^{-3}$ is predicted to occur in areas between Fresno and Bakersfield in the SJV. Extreme $PM_{2.5}$ concentrations in Los Angeles are predicted to decrease by ~2 $\mu g\ m^{-3}$ in the future with larger decreases of ~15 $\mu g\ m^{-3}$ predicted in Ventura county west of Los Angeles.

Further analysis using the population-weighted 10-day average extreme concentrations for $PM_{0.1}$, $PM_{2.5}$ and PM_{10} was carried out to understand the climate effects on total mass, component species, and sources contributing to the total primary mass concentration of PM. The results are shown in Figures 8-7 through 8-9. Error bars were calculated by sequentially withholding data from each year of the analysis to generate 7 different estimates of extreme concentrations during current and future climate. The variance of

those estimates in each time period was then combined to generate 95% confidence intervals. The results show that even though PM concentrations increase strongly during future extreme events (see Figure 8-6), the uncertainty caused by intra-annual variability is larger than the net change between present and future climate in many cases.

Figure 8-7 displays the population-weighted average $PM_{0.1}$ concentrations during extreme events. No statistically significant climate-induced changes in $PM_{0.1}$ concentrations were detected for any species or source contribution (as the 95% confidence interval spans zero).

Figure 8-8 displays the population-weighted average $PM_{2.5}$ concentrations during extreme events. Total mass, EC, OC, NO_3^- and NH_4^+ concentrations were predicted to increase in the future for the SV and SJV although these changes do not reach 95% significance. Increases in the population-weighted concentrations of trace metals (METL) and primary source contributions from diesel engines (Statewide) and dust (SJV) are statistically significant. The $PM_{2.5}$ SO_4^{2-} concentration was predicted to decrease in all three air basins, as were primary source contributions from shipping and high sulfur content fuel combustion. These results reflect the effects of stagnant wind conditions during extreme events that trap local emissions close to populations but failed to transport off-shore shipping emissions to inland locations.

Figure 8-9 displays the climate effects on population-weighted PM_{10} concentrations during extreme events. Population-weighted concentrations of PM_{10} total mass, chemical species, trace metals and primary source contributions are predicted to increase in the future for the SV and SJV, with smaller changes in the SoCAB. The total mass concentration of PM_{10} was predicted to increase by 9% in California, 39% in the SV, 47% in the SJV and only -7% in the SoCAB. Once again, the 95% confidence interval spans zero for the majority of these results relative to the inter-annual variability. The only statistically significant trends displayed in Figure 8-9 are an increase in population-weighted concentrations of primary diesel PM (SJV) and a decrease in primary shipping PM (statewide).

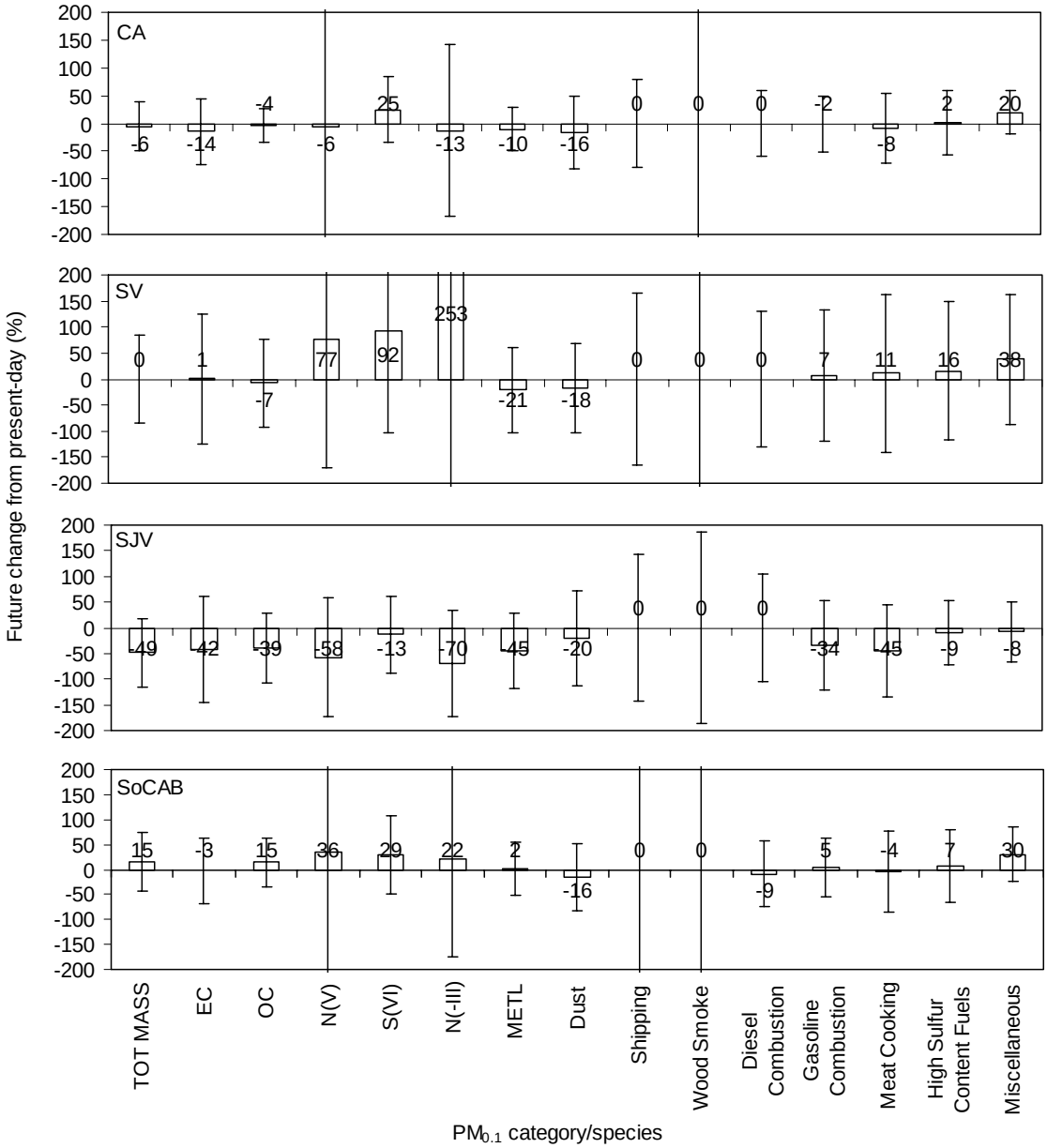

Figure 8-7: Climate change effects on 24-hr average population-weighted concentrations of $PM_{0.1}$ total mass and component species, and contributions from various sources to the total mass using average data above the 99th percentile value in the 7-year data distribution in the present-day and future periods.

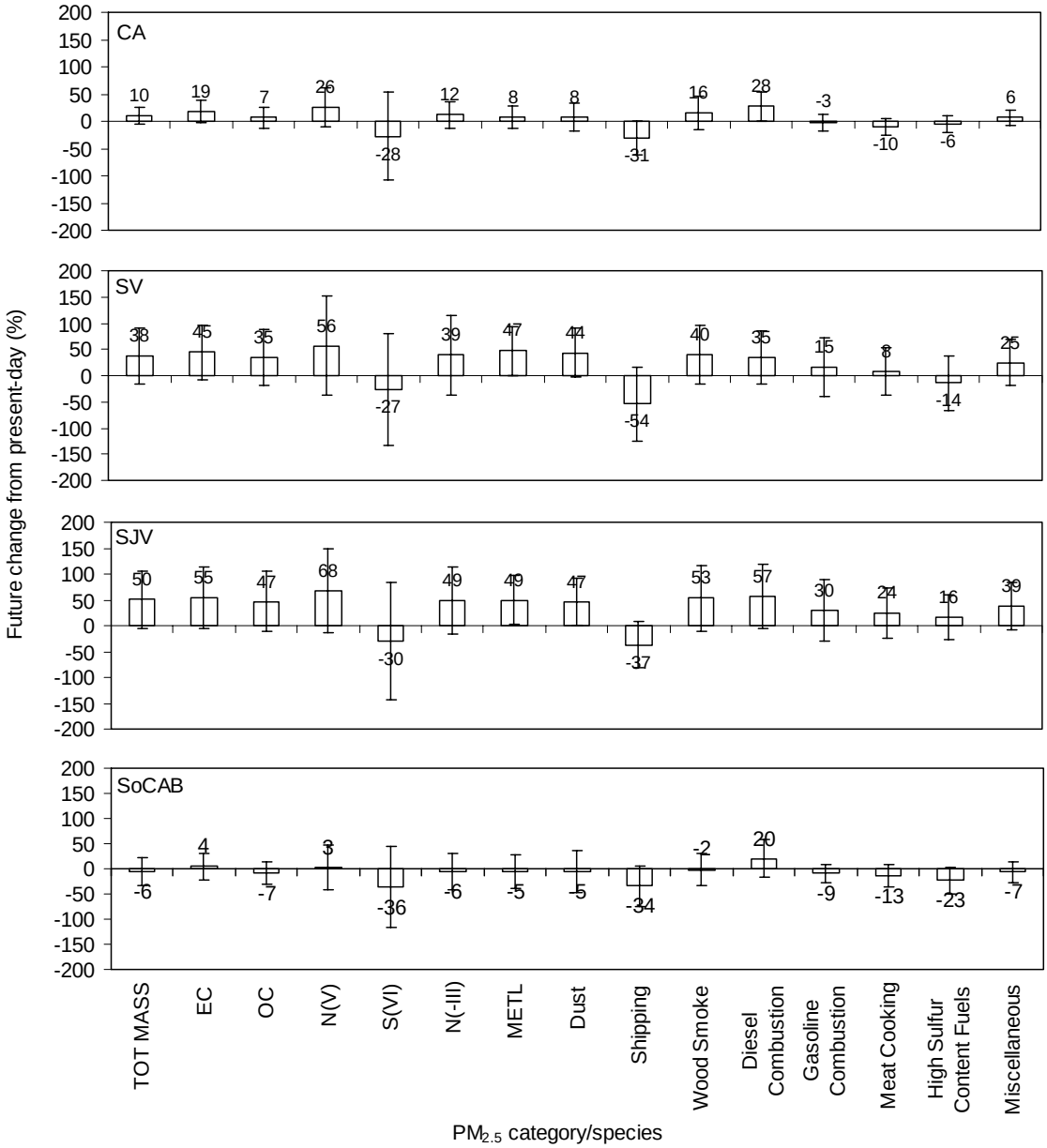

Figure 8-8: Climate change effects on 24-hr average population-weighted concentrations of $PM_{2.5}$ total mass and component species, and contributions from various sources to the total mass using average data under the shaded regions illustrated in Figure 8-6.

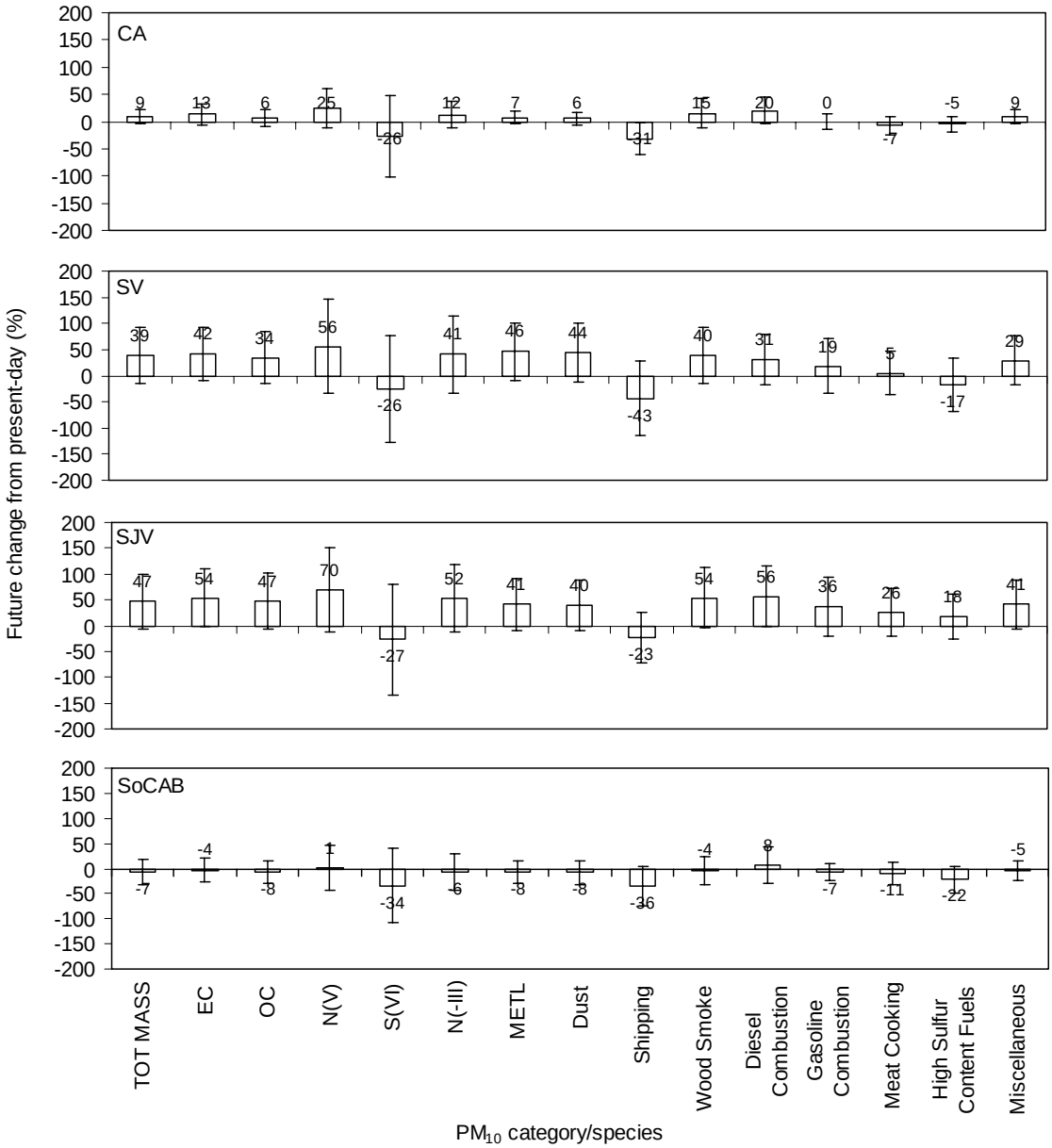

Figure 8-9: Climate change effects on 24-hr average population-weighted concentrations of PM_{10} total mass and component species, and contributions from various sources to the total mass using average data above the 99th percentile values in the 7-year data distribution in the present-day and future periods.

8.4 Conclusions

The effects of climate change on airborne PM mass concentrations in California between the years 2000-06 and 2047-53 are generally smaller than the natural inter-annual variability within either of these periods. Population-weighted concentrations of $PM_{0.1}/PM_{2.5}/PM_{10}$ mass in the SoCAB, SJV, SV, and across the entire state were not statistically different in the future climate vs. the present climate even though 1008 representative days were simulated in each climate period. Likewise, concentrations of PM chemical components and primary source contributions generally did not respond to climate change in a statistically significant fashion other than a few notable exceptions discussed below. The results of these tests are unable to reject the hypothesis that climate change has only a small effect on population-weighted airborne PM mass in California's major air basins. This implies that any calculation that combines the population-weighted concentrations from <1000 sample days with mortality or morbidity coefficients derived from epidemiological studies would likewise be unable to find statistically significant effects of climate change on human health due to changes in airborne PM mass. This finding contradicts the results from recent studies that show projected health impacts of climate change via changes to airborne PM in California [18].

Even though the majority of the 95% confidence intervals for climate effects on airborne PM mass overlapped zero, a few PM sub-categories did experience statistically significant changes in response to climate. Statewide population-weighted annual-average concentrations of $PM_{2.5}$ organic carbon (OC) are predicted to decrease by ~4% in the future and statewide population-weighted annual-average $PM_{2.5}/PM_{10}$ concentrations from shipping and combustion of high sulfur fuel are predicted to decrease by ~5-6%. These trends reflect the increase in annual-average wind speed over coastal portions of California.

An analysis of extreme pollution events suggests that future climate will lead to increased concentrations of 99th percentile population-weighed concentrations of primary PM. Statewide population-weighted $PM_{2.5}$ primary diesel concentrations are predicted to increase by ~28% during future extreme pollution events. Likewise, population-weighted concentrations of $PM_{2.5}$ road dust are predicted to increase by ~47% in the SJV during future extreme pollution events. Population-weighted concentrations of offshore shipping primary PM are predicted to decrease by ~31% in future extreme pollution events. These trends are consistent with the increased strength of future stagnation events which trap pollutants close to the emissions source. Stronger stagnation events increase population-weighted concentrations of emissions released close to major cities and decrease the effects of more remote sources.

Longer averaging times are needed to reduce the uncertainty associated with inter-annual variability discussed above. Ensembles of models are needed to capture the full uncertainty inherent in the analysis.

9.0 CLIMATE IMPACT ON PARTICULATE MATTER (PM) IN CALIFORNIA FOR EMISSIONS PROJECTED IN 2050

9.1 Introduction

The atmospheric chemistry involved in the production of secondary PM is non-linear, meaning that changes to emissions inventories are not necessarily proportional to changes in ambient PM concentrations. Meteorological conditions influence this non-linear behavior through differential effects on individual chemical reaction rates and partitioning behavior (see chapters 2 and 3). Climate change may therefore have a different effect on PM concentrations under 2050 emissions conditions vs. 2000 emissions conditions. The purpose of the present chapter is to describe the methodology used to estimate 2050 emissions and then to repeat the analysis conducted in Chapters 7 and 8 to determine if any of the conclusions would change because the differences between the 2000 vs. 2050 emissions expose some non-linear feature of the atmospheric chemistry. Results are summarized as regional plots and population-weighted concentrations to facilitate a direct comparison with the previous chapters.

9.2 Emissions Projections

The starting point for the 2050 emissions inventory used in the current study was a base-case statewide raw emissions inventory for the year 2029 obtained from CARB and a base-case SoCAB raw emissions inventory for the year 2030 provided by SCAQMD. Both of these starting inventories were developed to demonstrate compliance with State Implementation Plans to meet the requirements of the $PM_{2.5}$ NAAQS.

Base-case emissions were projected to the year 2050 by estimating the effects of additional population growth on source activity. The standard methodology to predict future emissions based on a known reference year is to multiply the reference emissions by a growth factor associated with increased population or economic expansion and by a control factor representing improved emissions control technology. The equation describing this simple approach in the current study is:

$$\text{Emissions}^{2050} = \text{Emissions}^{\text{base year}} * \text{Fgrowth} * \text{Fcontrol} \qquad (1)$$

In all cases, growth factors between 2029/2030 and 2050 were calculated using population projections published by the California Department of Finance [183]. Control factors between 2029/2030 and 2050 were generally set to 1.0 since all existing official controls are included in the 2029/2030 inventories and development of additional emissions controls to ensure compliance with the NAAQS in the presence of upward population pressure between 2030-2050 was beyond the scope of the current project. Exceptions to this rule included a complete ban on wood combustion for residential heating during winter months, and the incorporation of diesel particulate filters (DPFs) with 90% efficiency on all diesel engines. The ratio of NO_2/NO emissions was doubled for diesel engines to account for the effects of the DPFs.

The general assumption behind the use of population growth as a surrogate for changes to emissions is that most mobile, residential, commercial, and industrial activity scales either directly or indirectly with population. The direct effects of population on mobile and residential emissions are obvious since increased population leads to increased vehicle miles traveled and increased numbers of households that all have associated emissions. Increased population also leads to secondary effects such as increased demand for consumer products which spurs commercial and industrial activities.

Factors such as the capacity of transportation facilities and land-use policies that govern the growth of cities will result in non-uniform emissions growth in the future [184]. A rigorous analysis of these factors for the year 2050 was beyond the scope of the current project. The spatial pattern of emissions growth was considered with county-level resolution. County-specific growth factors were calculated for all mobile and residential emissions categories based on population growth projections within each county. County-specific growth factors were also applied to commercial and industrial sources with the exception of boats/ships and locomotives that were scaled based on statewide population growth factors. Table 9-1 summarizes the county-specific growth factors obtained from the DOF that were used in the current study between the years 2029/2030 and 2050.

A number of emissions categories were judged to be relatively constant and were not scaled to account for population growth between 2029/2030 and 2050. These constant sources included military activities, fugitive/windblown dust, agricultural dust, and unplanned/wildfires. Recent studies have indicated that climate change may influence the frequency and severity of wildfires [185-188], but a rigorous analysis of this issue was beyond the scope of the current study.

Once the 2050 emissions inventories were prepared, processing for model use was identical that that described in Chapter 7. Area source and point source emissions were used without further modification in all simulations. On-road mobile source emissions were adjusted for the variation of meteorological conditions experienced during each simulation using CARB's Emissions Factors (EMFAC) model. WRF predictions for hourly-averaged temperature and surface shortwave radiation in each grid cell were also combined with the MODIS satellite data and fed into CARB's BEIGIS model to predict episode-specific biogenic volatile organic compound emissions. No changes to vegetation patterns were incorporated in the current study. The adjusted mobile source emissions and the newly generated biogenic emissions were then processed with the remaining area and point sources to provide a source oriented model-ready gridded hourly emissions inventory.

Table 9-1: County-specific growth factors between 2029/2030 and 2050 based on Department of Finance population projections.

County	Population GF (DoF) 2030-2050	County	Population GF (DoF) 2030-2050
Alameda	1.41	Orange	1.39
Alpine	1.09	Placer	2.98
Amador	1.94	Plumas	1.36
Butte	2.16	Riverside	3.03
Calaveras	1.97	Sacramento	1.76
Colusa	2.19	SanBenito	2.70
ContraCosta	1.89	SanBernardino	2.13
DelNorte	2.03	SanDiego	1.59
ElDorado	1.98	SanFrancisco	1.09
Fresno	2.40	SanJoaquin	3.13
Glenn	2.38	SanLuisObispo	1.47
Humboldt	1.20	SanMateo	1.15
Imperial	2.70	SantaBarbara	1.33
Inyo	1.38	SantaClara	1.55
Kern	3.16	SantaCruz	1.30
Kings	2.71	Shasta	2.01
Lake	1.82	Sierra	0.96
Lassen	1.64	Siskiyou	1.49
LosAngeles	1.36	Solano	2.05
Madera	3.32	Sonoma	1.65
Marin	1.24	Stanislaus	2.64
Mariposa	1.64	Sutter	3.55
Mendocino	1.55	Tehama	2.22
Merced	3.08	Trinity	2.30
Modoc	2.50	Tulare	2.78
Mono	2.77	Tuolumne	1.34
Monterey	1.60	Ventura	1.62
Napa	2.01	Yolo	1.93
Nevada	1.47	Yuba	3.32
		STATE	1.74

9.3 Results

Figure 9-1 illustrates the predicted airborne fine particulate matter concentrations in California averaged between the years 2000-06 using the emissions estimated for 2050. The results are noticeably different from those calculated using the year 2000 emissions (see Figure 7-3). The maximum $PM_{2.5}$ concentration of 30 µg m^{-3} occurs near the city of El Centro south of the Salton Sea. The majority of this material is composed of dust that is primarily composed of crustal material. The major population centers of San Francisco and Los Angeles are predicted to experience slightly lower concentrations between 14-20 µg m^{-3}, while the San Joaquin Valley is predicted to experience concentrations between

10-16 μg m^{-3} under the 2050 emissions predictions. Significant contributions from EC, OC, nitrate, ammonium ion, and sulfate are evident in each of these locations.

It should be noted that the $PM_{2.5}$ concentrations predicted using the meteorology from 2000-06 and the emissions estimated for 2050 violate the annual-average National Ambient Air Quality Standards (NAAQS) (15 μg m^{-3}) and the California Ambient Air Quality Standards (12 μg m^{-3}). This study should not be interpreted as a comment on the current State Implementation Plans to achieve attainment for $PM_{2.5}$ since the emissions estimates for 2050 generated during the current project are not official estimates from the California Air Resources Board. Rather, the emissions estimates prepared for 2050 reflect a projected growth of the official 2030 emissions using the best available methods within the time and scope allowed by the current project. No effort was made to formulate additional regulations to control increased emissions associated with population growth between the years 2030 and 2050.

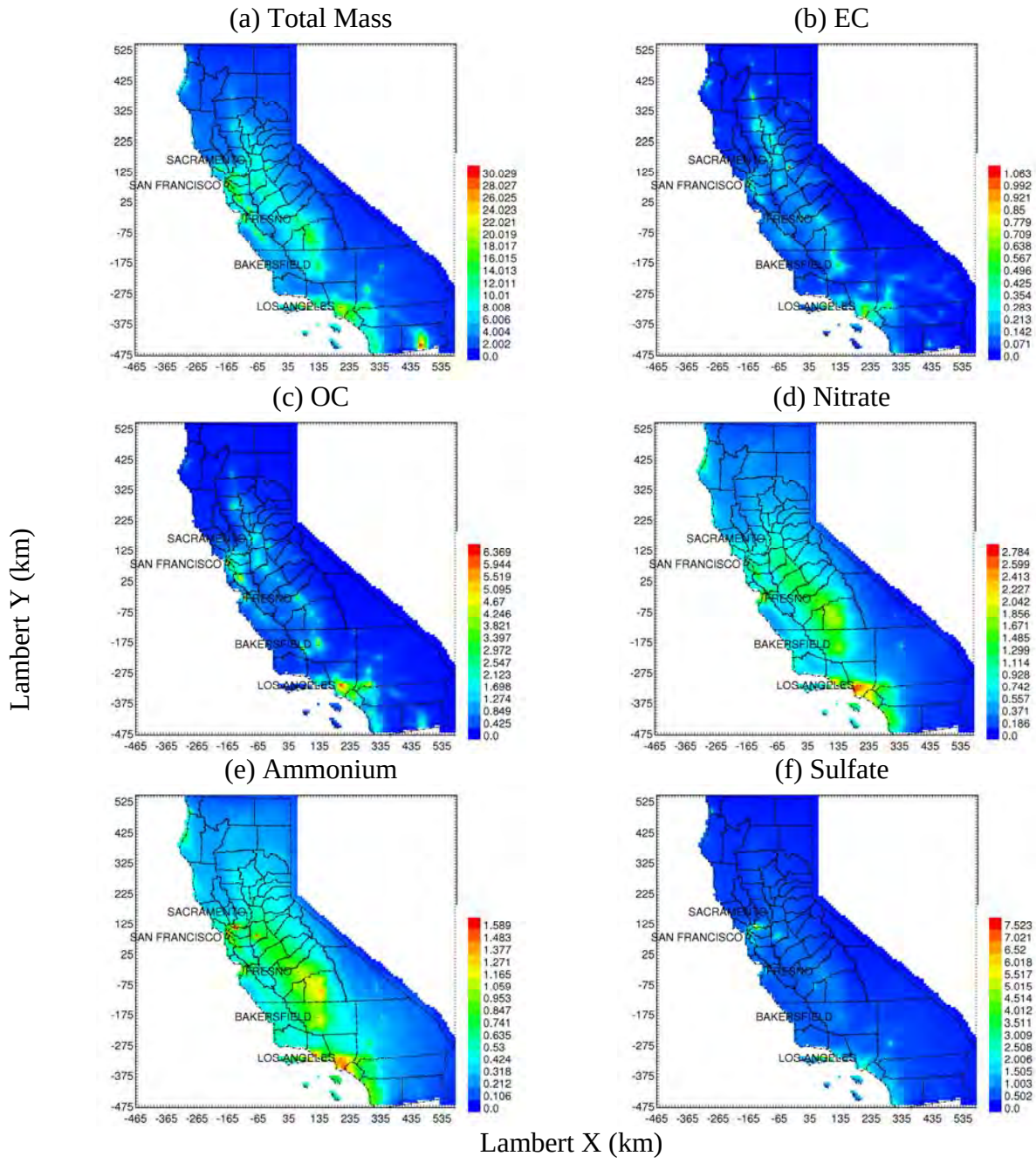

Figure 9-1: Annual average fine particulate matter ($PM_{2.5}$) concentrations in CA for the present day (2000-06) utilizing the emissions control projected for 2050: (a) total mass, (b) elemental carbon, (c) organic carbon, (d) nitrate, (e) ammonium, and (f) sulfate.

Figure 9-2 illustrates the difference between predicted $PM_{2.5}$ concentrations in 2047-53 vs. 2000-06 using the emissions predicted for the year 2050. The results are organized to show the difference for total mass and various components of total mass in the first column, and the p-value in the second column. The p-value quantifies the probability that climate change causes no difference between future years and present years. The p-value largely depends on the variability within the period 2000-06 and 2047-53 caused by inter-annual differences associated with El Nino events and other large scale weather patterns.

The results illustrated in Figure 9-2 are similar to those illustrated in Chapter 7. Slightly increasing concentrations and slightly decreasing concentrations are evident in different regions of California, but only limited areas experience changes that approach statistical significance at the 95% confidence level. $PM_{2.5}$ concentrations in the coastal region of Los Angeles and southern California are predicted to decrease by ~1 μg m^{-3} due to reduced concentrations of primary components such as OC and EC. The meteorological drivers for this change are identical to those discussed in Chapter 5: higher wind speeds on average in coastal Los Angeles provide greater dilution of primary emissions reducing overall $PM_{2.5}$ concentrations. Reduced concentrations of ammonium nitrate are also evident in the coastal regions of southern California. Increased wind speed likely also plays a role in those changes by providing extra dilution that prevents the buildup of ammonium nitrate precursors.

$PM_{2.5}$ mass concentrations in the southern portion of the SJV are also predicted to decrease by ~1 μg m^{-3} due to the effects of climate change. The majority of this change is driven by decreased ammonium nitrate concentrations. The reduction of agricultural ammonia emissions predicted in 2050 in the SJV leads to more balanced concentrations of gas-phase nitric acid and ammonia which makes the particulate ammonium nitrate formation more sensitive to temperature fluctuations [33]. Increased temperatures in the future SJV therefore have a larger impact on ammonium nitrate formation when considering the 2050 emissions (Figure 9-2) than the 2000 emissions (Figure 7-7).

The final noteworthy trend illustrated in Figure 9-2 is the predicted increase in $PM_{2.5}$ sulfate concentrations across much of the inland portion of Southern California in response to climate change. This trend results because warmer future temperatures and increased relative humidity lead to increased hydroxide radical (OH) concentrations that convert gaseous SO_2 emissions to sulfuric acid more quickly in the future. Sulfuric acid is non-volatile over all relevant atmospheric temperatures (with or without climate change) and rapidly condenses to form particulate sulfate.

The trends for particulate ammonium nitrate and particulate sulfate that are evident in Figure 9-2 are consistent with predictions made during previous studies that performed perturbation analysis of the atmospheric chemistry during historical air pollution episodes [33], [61].

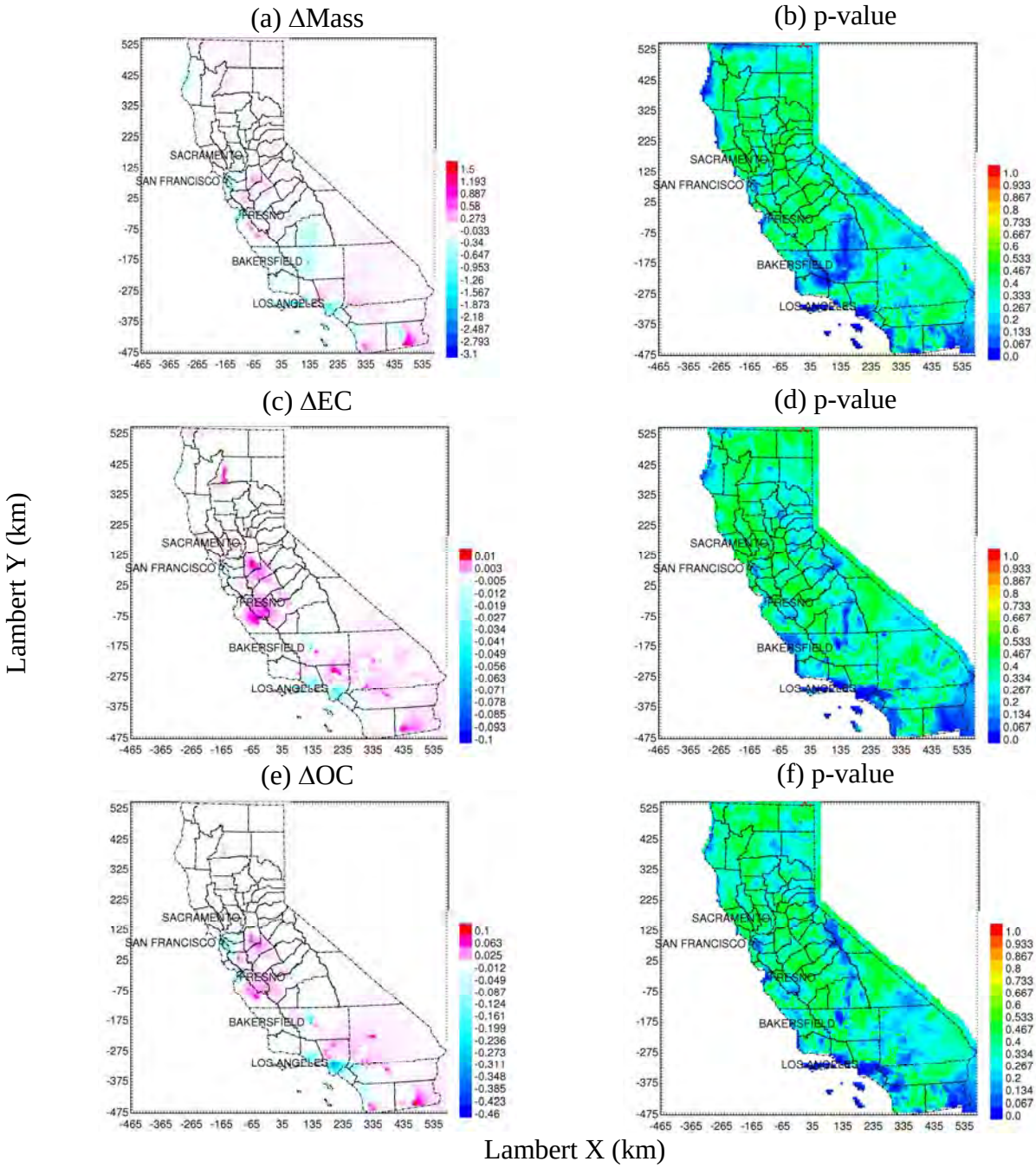

Figure 9-2: Changes in annual average total mass and primary $PM_{2.5}$ concentrations (μg m^{-3}), and their corresponding p-values in CA likely to occur in the future (2047-53) due to climate change and projected emissions control for 2050 from the present-day (2000-06). The p-values were calculated for a one-tailed student t-distribution from annual average concentrations at 95% confidence interval.

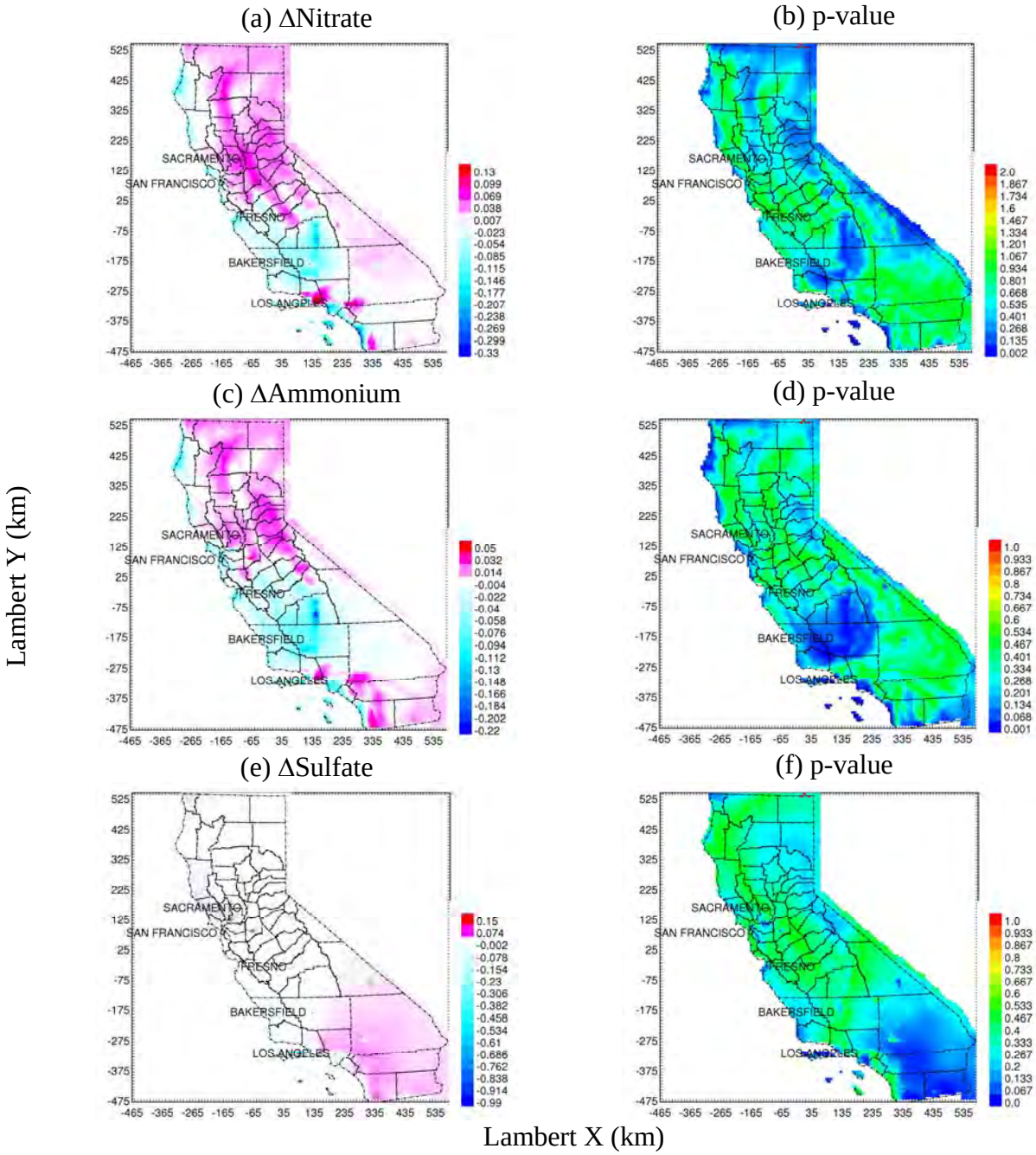

Figure 9-2 continued: Changes in annual average secondary $PM_{2.5}$ concentrations (μg m^{-3}), and their corresponding p-values in CA likely to occur in the future (2047-53) due to climate change and projected emissions control for 2050 from the present-day (2000-06). The p-values were calculated for a one-tailed student t-distribution from annual average concentrations at 95% confidence interval.

Figure 9-3 illustrates the population-weighted annual-average $PM_{2.5}$ concentrations of total mass, individual chemical components, and primary source contributions calculated for the state of California (CA), and Sacramento Valley (SV), and San Joaquin Valley (SJV), and the South Coast Air Basin (SoCAB). The population distribution used in the concentration weighting calculations was consistent with the population distribution assumed during the generation and spatial disaggregation of emissions. The uncertainty bars shown in Figure 9-3 quantify the 95% confidence interval of the difference between the seven future years (2047-53) and the seven present years (2000-06).

The 95% confidence intervals for annual-average population-weighted $PM_{2.5}$ mass and almost all components / sources that contribute to that mass shown in Figure 9-3 overlap zero. This pattern indicates that climate impacts induce small changes in the $PM_{2.5}$ concentrations associated with 2050 emissions relative to the inter-annual variability present in any given seven year period. Some sub-categories of annual-average population-weighted primary source contributions do have statistically significant responses to climate change. Annual-average population-weighted primary $PM_{2.5}$ from meat cooking and high sulfur fuel combustion averaged across the entire state were reduced by 3-4%, and primary $PM_{2.5}$ from shipping and diesel combustion in the SoCAB was reduced by 5-6%. These trends largely reflect the impact of increased wind speed over coastal areas of California.

Figures 9-4 and 9-5 examine the impact of climate change on annual-average PM_{10} and $PM_{0.1}$ concentrations of total mass, chemical components, and primary source contributions using the 2050 emissions as the reference point. The format of Figures 9-4 and 9-5 is identical to Figure 9-3. As was the case for $PM_{2.5}$, the major trends for annual-average population-weighted PM_{10} and $PM_{0.1}$ produced using 2050 emissions are consistent with the results produced using the 2000 emissions. The differences in future vs. present PM mass concentrations are generally not significant (95% confidence) relative to inter-annual variability. Annual-average population-weighted PM_{10} primary source contributions from shipping, diesel combustion, meat cooking, and high sulfur fuel combustion decrease in the SoCAB due to the effects of increased wind speed. These same trends are apparent in the statewide averages although 95% confidence is only reached for meat cooking.

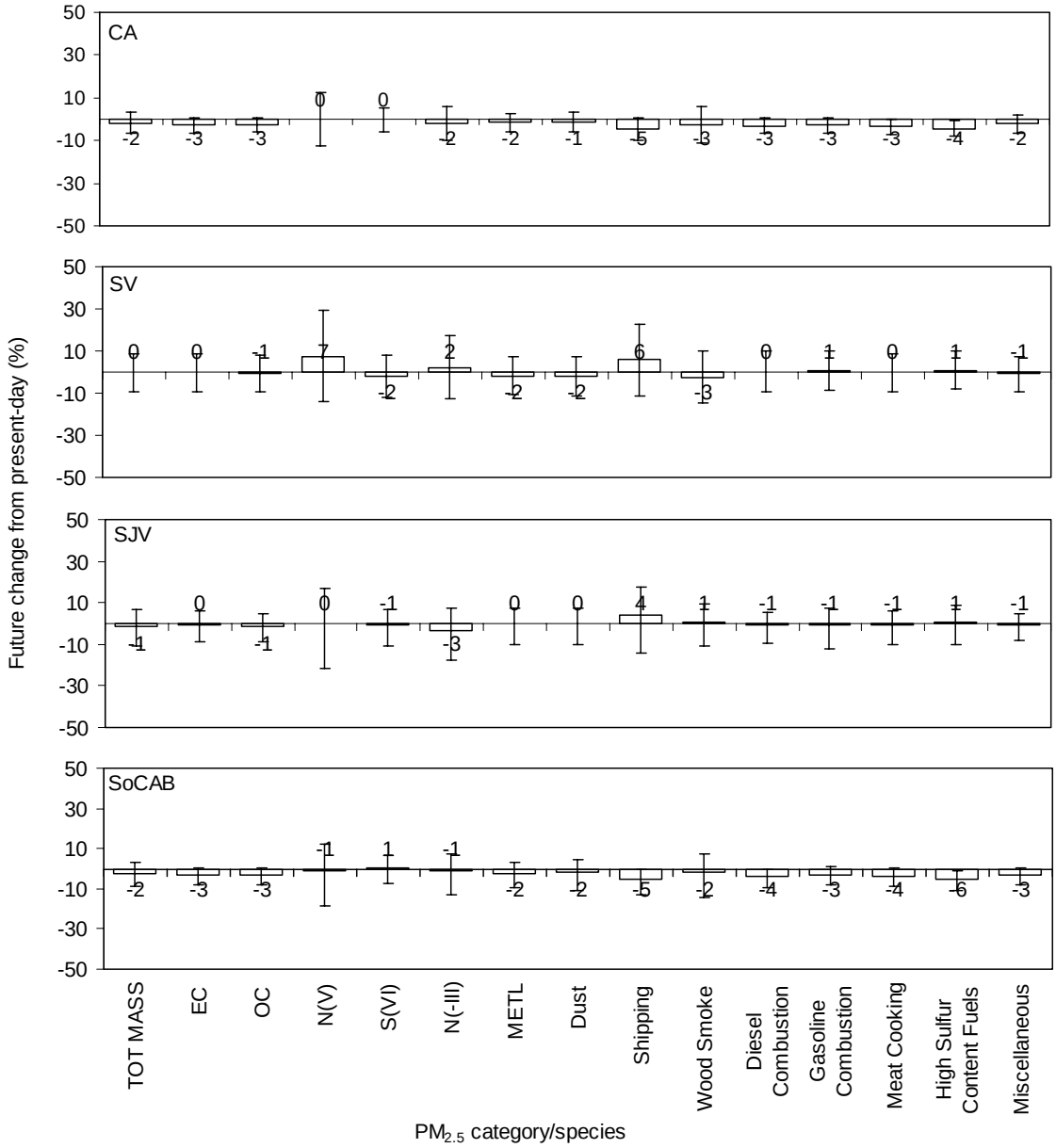

Figure 9-3: Future change (2047-53 vs. 2000-06) in population-weighted concentrations of $PM_{2.5}$ total mass / components / primary source contributions. Panels (top-down) show California state-wide average, Sacramento Valley (SV) air basin average, San Joaquin Valley (SJV) air basin average, and South Coast Air Basin (SoCAB) average results.

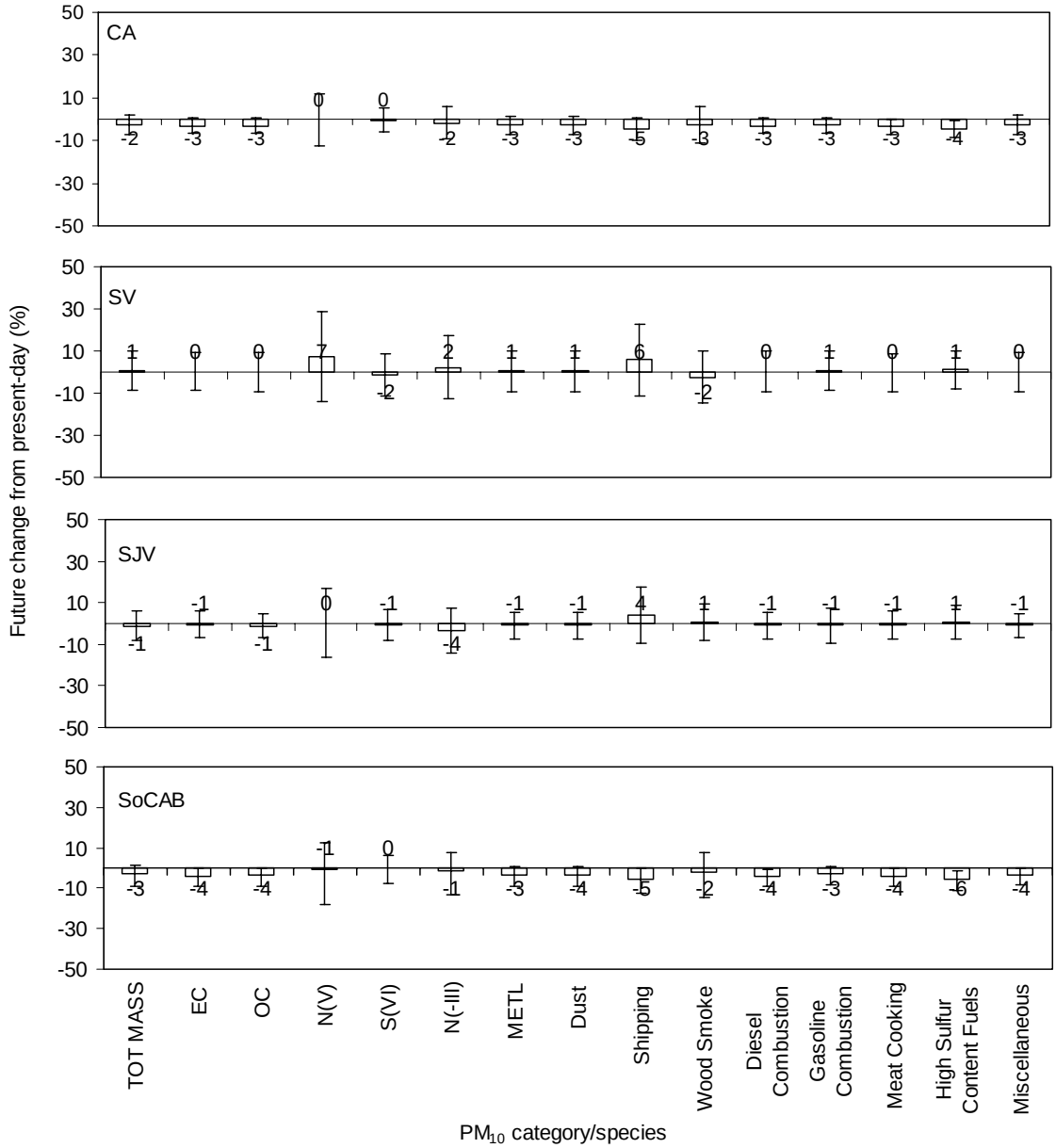

Figure 9-4: Future change (2047-53 vs. 2000-06) in population-weighted concentrations of PM_{10} total mass / components / primary source contributions. Panels (top-down) show California state-wide average, Sacramento Valley (SV) air basin average, San Joaquin Valley (SJV) air basin average, and South Coast Air Basin (SoCAB) average results.

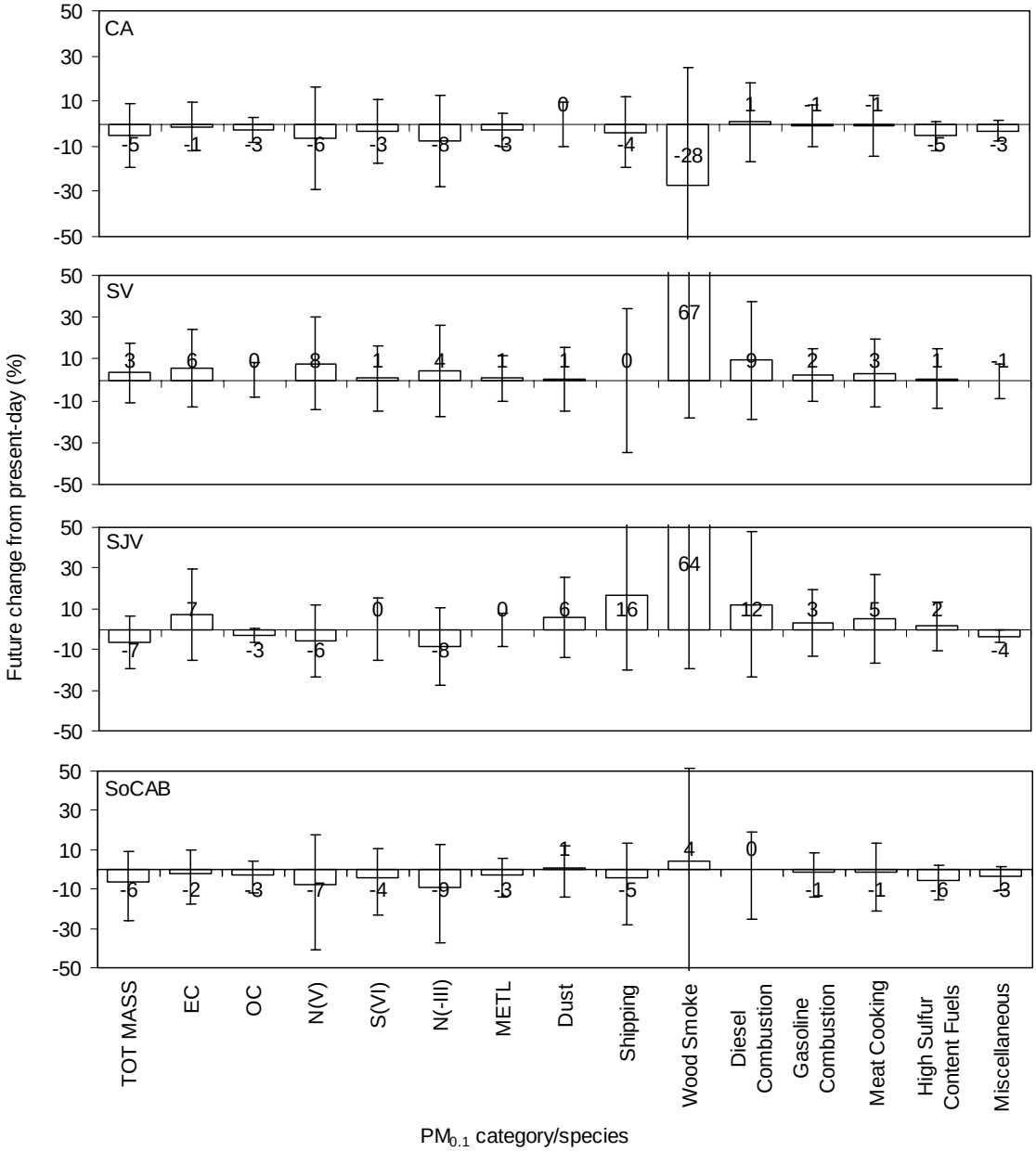

Figure 9-5: Future change (2047-53 vs. 2000-06) in population-weighted concentrations of $PM_{0.1}$ total mass / components / primary source contributions. Panels (top-down) show California state-wide average, Sacramento Valley (SV) air basin average, San Joaquin Valley (SJV) air basin average, and South Coast Air Basin (SoCAB) average results.

Figure 9-6 summarizes the distribution of statewide population-weighted 24-hr average $PM_{2.5}$ concentrations generated for current climate conditions (top panel) and future climate conditions (bottom panel) using 2050 emissions. The shaded region at the right of each plot illustrates the top 1% of predicted values during each period. The behavior of these extreme 99th percentile events in the presence of climate change is of interest because of the potential risk to all exposed segments of the population. A comparison of Figure 9-6 to Figure 8-5 indicates that the emissions inventory for 2050 produces a different distribution of extreme PM concentrations than the emissions inventory for the year 2000.

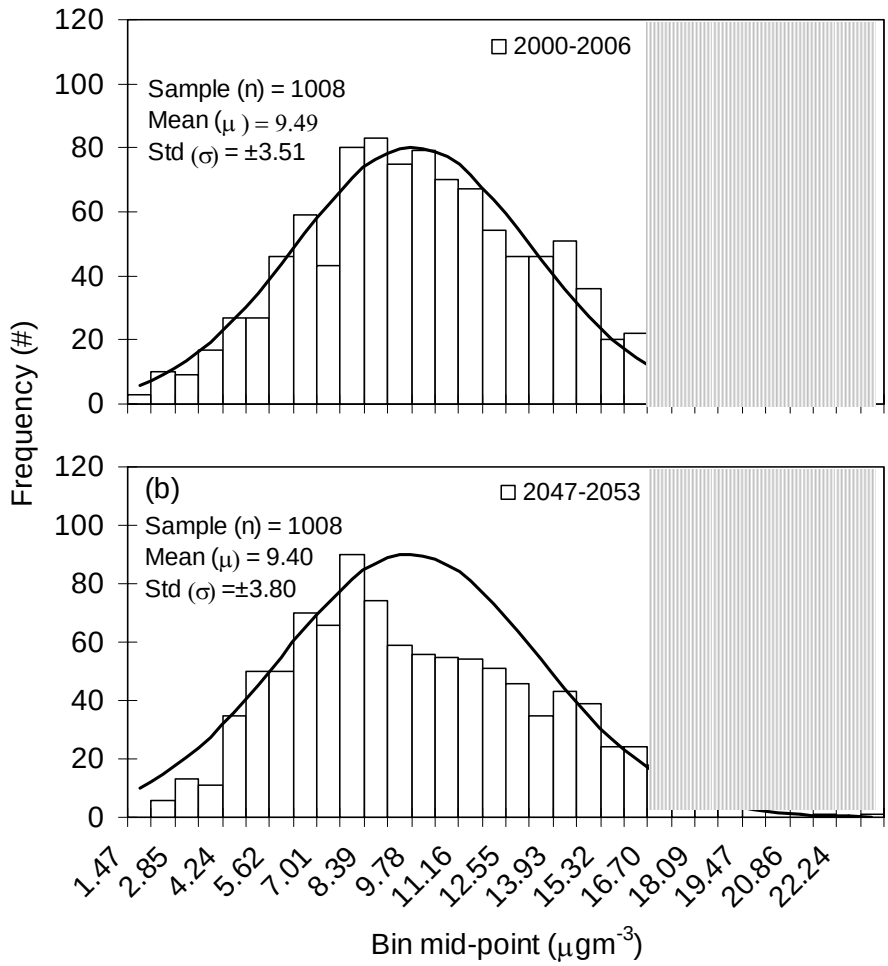

Figure 9-6: Frequency distribution of 24-hr average population-weighted $PM_{2.5}$ total mass concentrations for California under the (a) present-day (2000-2006) and (b) future (2047-2053) climate conditions. The shaded regions encompass values higher than the 99th percentile value of each distribution.

Figure 9-7 illustrates the regional $PM_{2.5}$ concentrations predicted over California on the 1% of days with the highest population weighted concentrations during the future (2047-53) and present (2000-06) time periods using the 2050 emissions as a fixed reference point. Figure 9-7c illustrates the difference between future and present extreme 99th percentile events. Future concentrations of $PM_{2.5}$ are predicted to increase by ~7 µg m^{-3} across central California and inland portions of southern California during extreme events. Extreme $PM_{2.5}$ concentrations along coastal portions of southern California are not predicted to change in the future. This response is distinctly different than the results shown in Figure 8-6 where future extreme events had $PM_{2.5}$ concentrations that were ~18-20 µg m^{-3} greater in the SJV and 2-4 µg m^{-3} greater in the SJV. The apparent reduction in the climate sensitivity of the PM concentrations caused by the changes in the emissions inventory between 2000 and 2050 is qualitatively consistent with the reduced climate sensitivity of the ozone system caused by changes in the emissions between 1980 and 2000 (see chapter 4; [103]).

As was the case with the analysis of extreme events using the 2000 emissions, the results shown in Figure 9-7 need to be viewed in the context of inter-annual variability. It is not appropriate to describe the behavior of the upper tail of the distribution shown in Figure 9-6 using the standard error from the overall distribution. The variation of the extreme events was therefore calculated by withholding individual years out of the analysis producing an ensemble of extreme 99th percentile events that were then analyzed to determine the mean and the 95% confidence interval.

(a) Future (2047-53) **(b) Present-day (2000-06)** **(c) Δ (future, present-day)**

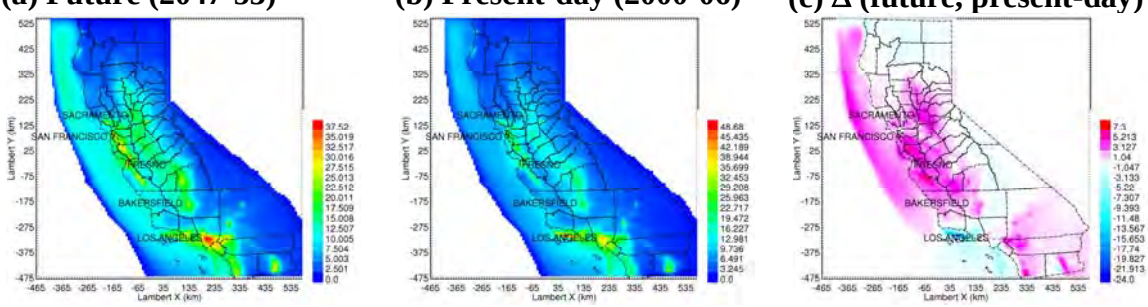

Figure 9-7: Average of the highest 24-hr average $PM_{2.5}$ total mass concentrations (µg m^{-3}) corresponding to days with population-weighted concentrations above the 99th percentile values as illustrated in Figure 9-3 for California under the (a) future (2047-2053), and (b) present-day climate (2000-2006) conditions. Panel (c) shows the difference between the future (a) and present-day (b).

Figure 9-8 illustrates the difference between future and present population-weighted average concentrations of $PM_{0.1}$ during extreme 99th percentile concentration events using the 2050 emissions as a fixed reference point. Uncertainty bars illustrate the 95% confidence interval for the concentration change during extreme events. The 95% confidence intervals span zero (no change) for all population-weighted $PM_{0.1}$ changes except for a ~34% decrease in sulfate (S(VI)) accompanied by a ~21% decrease in population-weighted PM from combustion of high sulfur fuel.

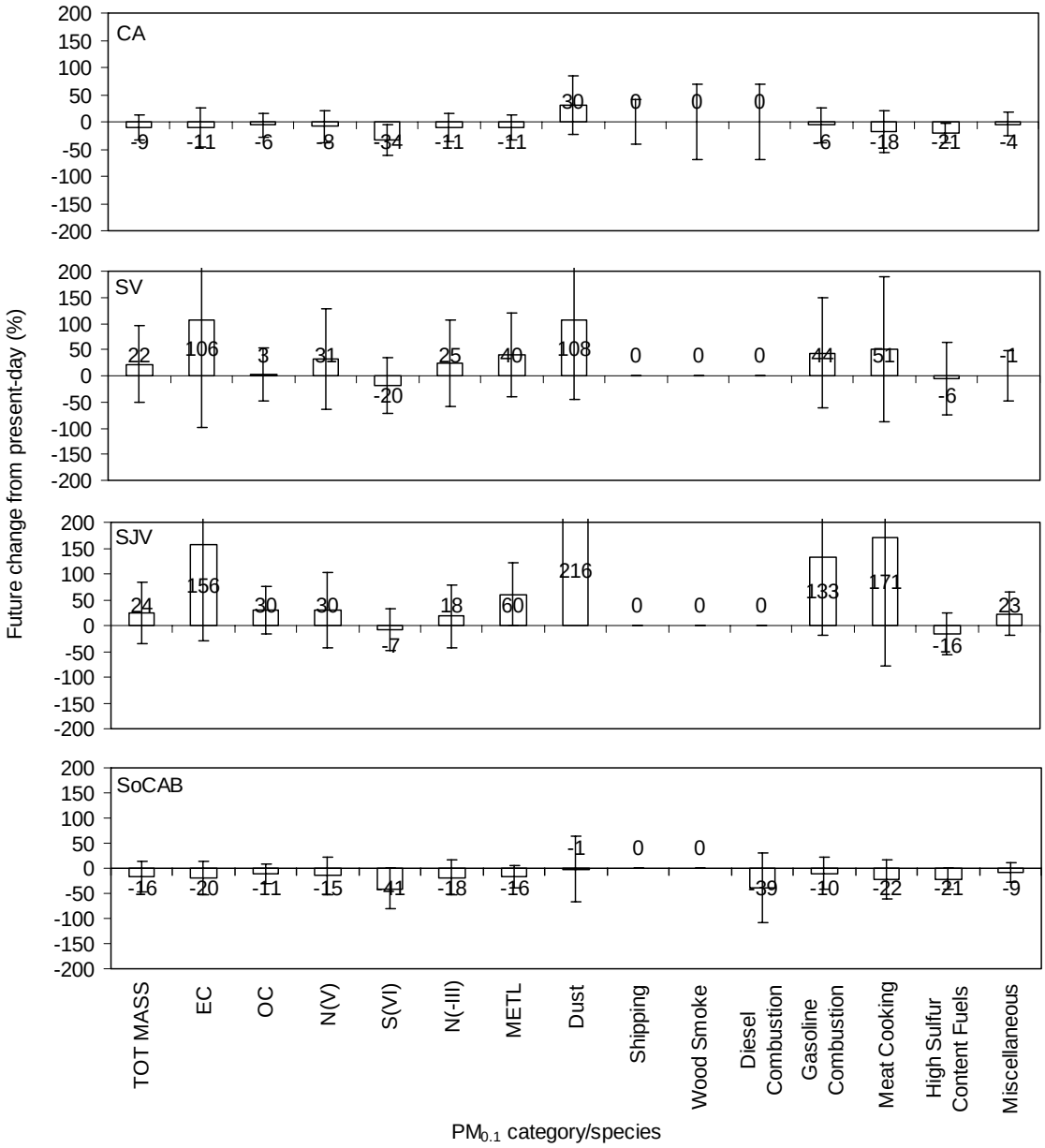

Figure 9-8: Future change (2047-53 vs. 2000-06) in population-weighted 99th percentile concentrations of $PM_{0.1}$ total mass / components / primary source contributions. Panels (top-down) show California state-wide average, Sacramento Valley (SV) air basin average, San Joaquin Valley (SJV) air basin average, and South Coast Air Basin (SoCAB) average results.

Figure 9-9 illustrates the difference between future and present population-weighted average concentrations of $PM_{2.5}$ during extreme 99th percentile concentration events using the 2050 emissions as a fixed reference point. Statistically significant trends for population-weighted 99th percentile $PM_{2.5}$ mass were not detected across any of the major air basins. Population-weighted concentrations of $PM_{2.5}$ trace metals (METL) and primary contributions from dust increased in all air basins, with statistical significance achieved in the SV and SJV. The dust category shown in Figures 9-9 and 9-10 includes contributions from fugitive/windblown + agricultural dust that were not changed between 2000 and 2050. The similarity of the 2050 vs. 2000 dust emissions yields consistent climate trends during 99th percentile extreme events (compare Figures 8-8 and 9-8). Population-weighted contributions from shipping and high-sulfur fuel combustion emissions to 99th percentile primary $PM_{2.5}$ mass were reduced in the future due to the effects of reduced wind speed during future stagnation events.

Figures 9-10 illustrate the difference between future and present population-weighted average concentrations of PM_{10} during extreme 99th percentile concentration events using the 2050 emissions as a fixed reference point. The 99th percentile population-weighted PM_{10} mass increased by 48% in the future (2047-53) SV relative current (2000-06) conditions. All primary components of the PM_{10} mass increased during the future extreme events in the SV, with statistically significant changes for elemental carbon (EC), and trace metals (METL). Likewise, local primary source contributions increased in the SV and SJV, with statistically significant changes for dust and wood smoke in the SV. Residential wood combustion for home heating was banned in the 2050 emissions inventory, and so the wood smoke contribution evident in Figure 9-10 largely reflects the impact of agricultural burns.

Population-weighted concentrations of primary diesel PM during extreme 99th percentile events were higher in 2047-53 than in 2000-06 based on 2000 emissions (Figures 8-8 and 8-9) but this trend was not present when 2050 emissions were used for the analysis (Figures 9-9 and 9-10). Diesel particle filters (DPFs) were applied to reduce primary on-road diesel PM emissions by 90% in the future inventory resulting in changes to the spatial distribution of diesel emission in California (compare Figure 7-3 to Figure 9-1 for EC as an indirect marker of diesel PM). This analysis suggests that DPFs or some other technology to eliminate primary diesel PM emissions will be required in California to prevent a climate-induced increase of population-weighted concentrations of primary diesel PM during future extreme (99th percentile) pollution events.

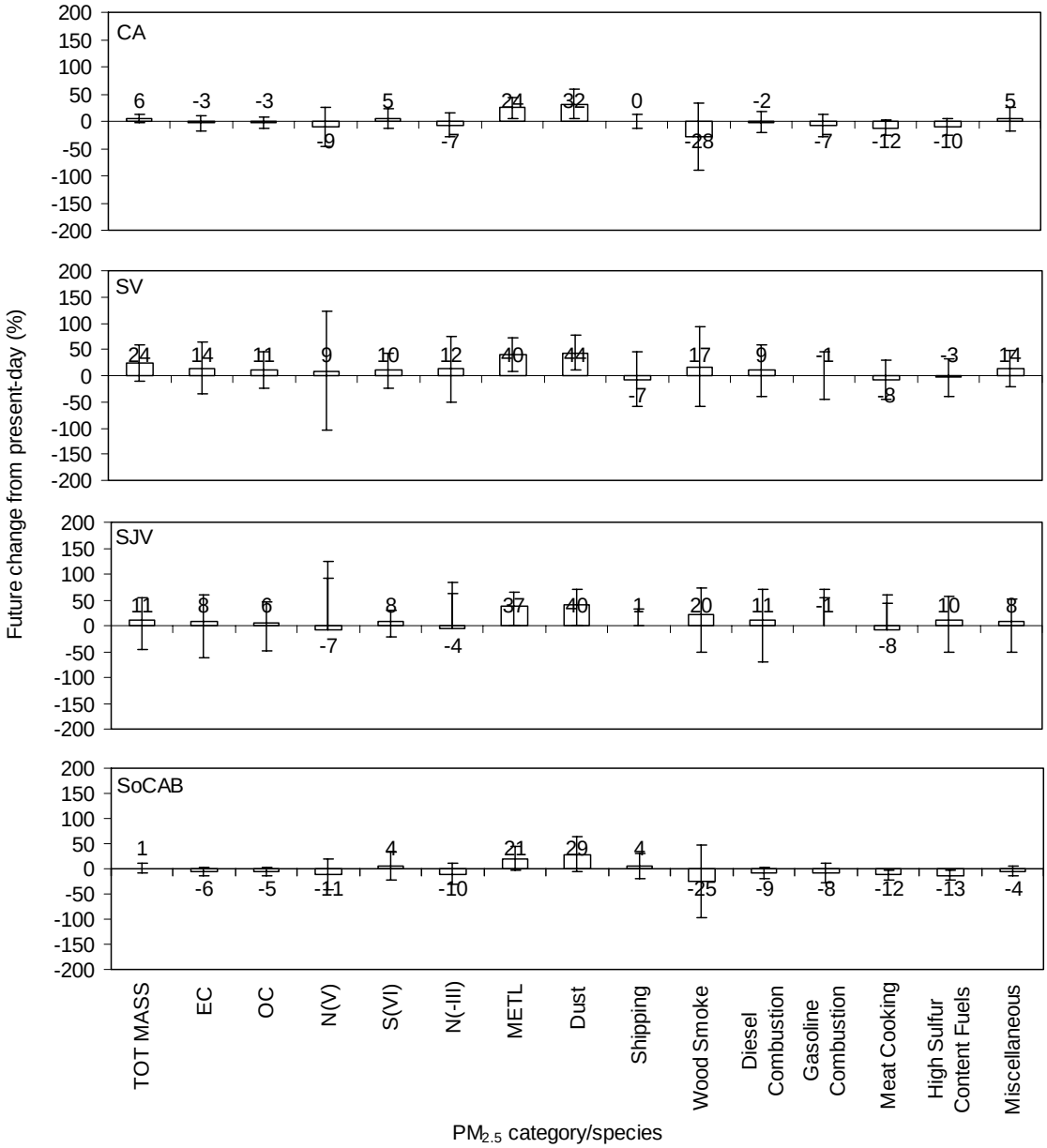

Figure 9-9: Future change (2047-53 vs. 2000-06) in population-weighted 99th percentile concentrations of $PM_{2.5}$ total mass / components / primary source contributions. Panels (top-down) show California state-wide average, Sacramento Valley (SV) air basin average, San Joaquin Valley (SJV) air basin average, and South Coast Air Basin (SoCAB) average results.

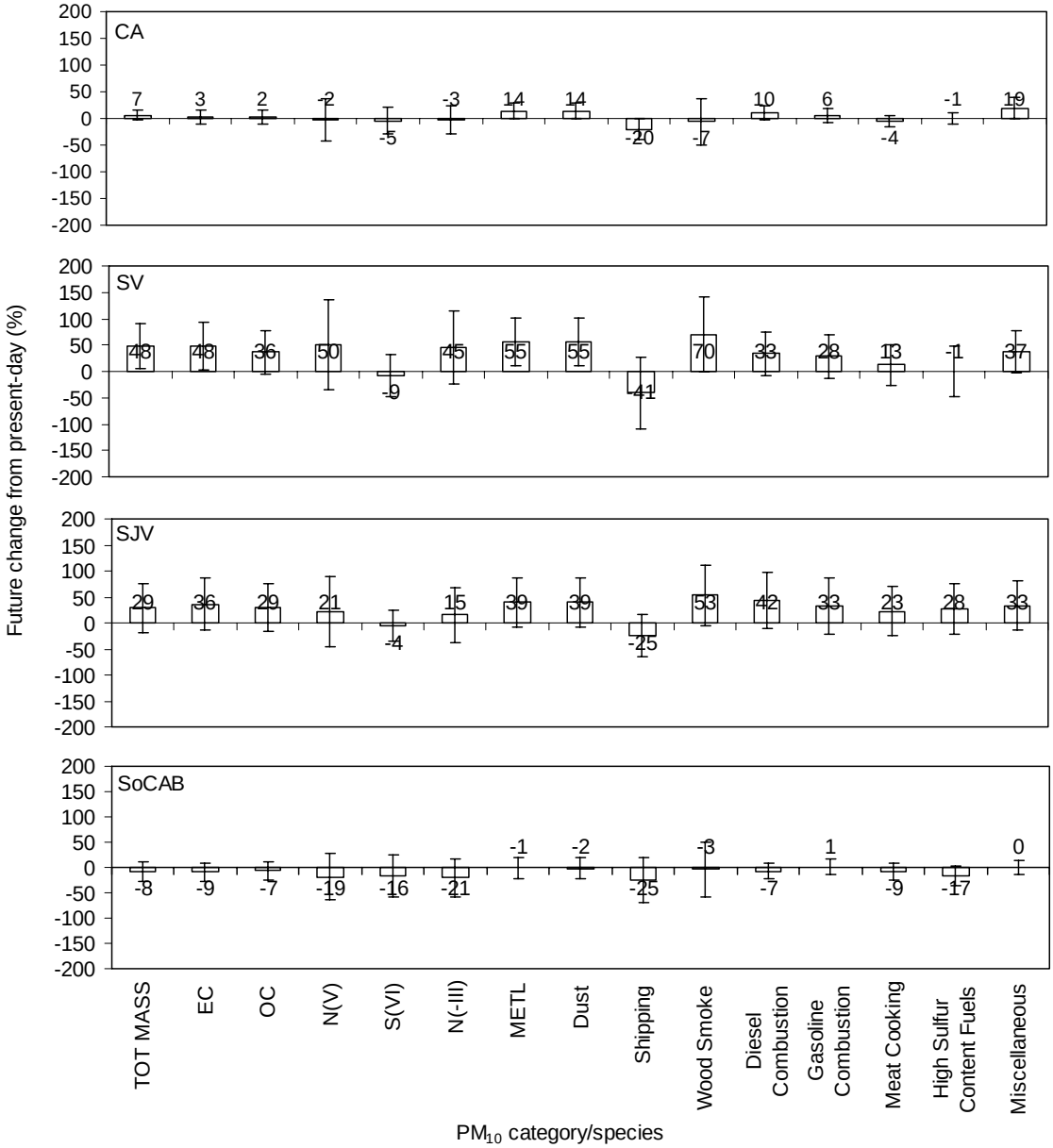

Figure 9-10: Future change (2047-53 vs. 2000-06) in population-weighted 99th percentile concentrations of PM_{10} total mass / components / primary source contributions. Panels (top-down) show California state-wide average, Sacramento Valley (SV) air basin average, San Joaquin Valley (SJV) air basin average, and South Coast Air Basin (SoCAB) average results.

9.4 Conclusions

The non-linear features of the atmospheric chemistry do not combine with changes in the emissions between 2000 and 2050 to produce a different annual-average outcome based on changing climate. Future studies comparing the climate response of annual-average $PM_{2.5}$ concentrations between 2000 and 2050 in California can focus on emissions from one period without the need for a full evaluation of present and future inventories under both sets of climatology.

The analysis of annual-average concentrations conducted with the 2050 emissions inventory indicates that population-weighted primary $PM_{2.5}$ concentrations will generally decrease in the future (2047-53) relative to present day (2000-06). This trend is especially true in the SoCAB. The primary driver for the decreased primary PM concentrations is increased average wind speed in the future, especially in coastal regions.

The analysis of extreme events conducted with the 2050 emissions inventory had the same qualitative behavior as the simulations conducted with the 2000 emissions inventory. Stagnation conditions are stronger in future extreme pollution episodes resulting in enhanced population-weighted concentrations of primary PM from sources located close to population centers. Controls that eliminate PM emissions from major sources such as wood combustion and diesel engines are needed to avoid higher population-weighted concentrations in the future.

The analysis presented in the previous sections confirms the results shown in Chapters 7 and 8. Based on the year 2050 emissions inventory, the impact of climate change on ground-level PM concentrations in California is smaller than the inter-annual variability during any seven year period in both current and future climate conditions. This makes the 95% confidence intervals for the effect of climate change on average ground-level PM concentrations broad when n=1000 sample days are used. Longer analysis periods are needed to quantify the climate impact with 95% confidence intervals that do not overlap zero.

10.0 COMBINED IMPACT OF CLIMATE CHANGE AND EMISSIONS CONTROLS ON PARTICULATE MATTER (PM) IN CALIFORNIA

10.1 Introduction

Climate and emissions will change simultaneously in the future, producing a net change to airborne particulate matter (PM) concentrations in California. The magnitudes of these combined changes and the signals contributed by climate vs. emissions are of interest since any climate "penalties" for $PM_{2.5}$ will require additional emissions controls. The present chapter compares the net effects of climate and emissions on airborne particulate matter concentrations.

10.2 Methods

Four sets of simulations with different climatology and emissions conditions were analyzed as shown in Table 10.1.

Table 10-1: Summary of climate and emissions cases analyzed.

Climatology\Emissions	**Present Emissions**	**Future Emissions**
Present Climate	2000-06 meteorology 2000 emissions	2000-06 meteorology 2050 emissions
Future Climate	2047-53 meteorology 2000 emissions	2047-53 meteorology 2050 emissions

Comparisons will be made between results associated with each of the four quadrants within Table 10-1. Chapters 7-9 compared results across climate conditions (vertically) for either present emissions or future emissions. The present chapter is the first to compare results across emissions conditions (horizontally) for present climate and future climate. The present chapter is also the first to compare results simultaneously across climate and emissions conditions (diagonally).

10.3 Results

Figure 10-1 illustrates the surface-level $PM_{2.5}$ concentration differences predicted using 2050 emissions and 2047-53 meteorology vs. 2000 emissions and 2000-06 meteorology. Regions offshore of California are predicted to experience an increase of 14 µg m^{-3} due to increased shipping activities associated with goods movement. Coastal inland regions including the San Francisco Bay Area and southern California are also predicted to experience increased $PM_{2.5}$ concentrations ranging from 5-14 µg m^{-3} higher than present-day values. In contrast, the $PM_{2.5}$ concentrations predicted in the future SV and SJV are lower than present-day values, with decreases of up to3- 4.4 µg m^{-3} predicted in the cities of Sacramento, Fresno and Bakersfield. These changes reflect the net effects of climate and emissions trends between 2000 and 2050.

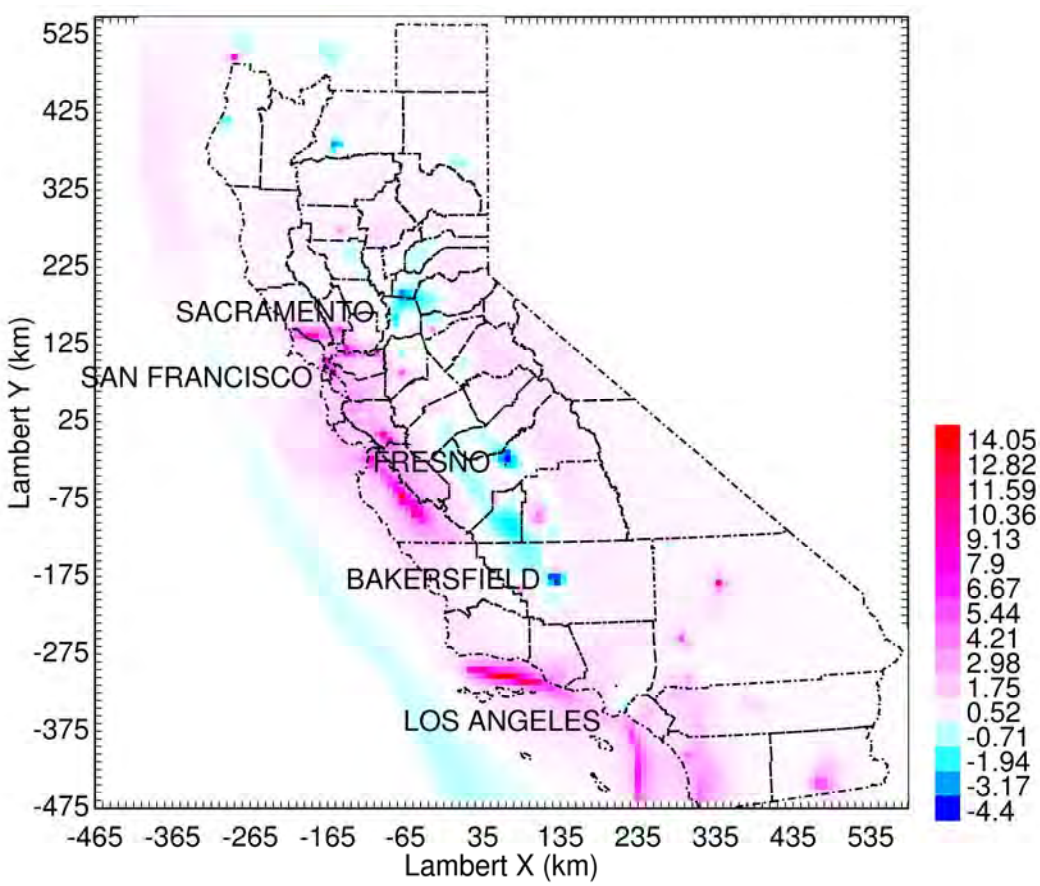

Figure 10-1: Annual average PM 2.5 mass difference (2047 to 2053) using 2050 emissions vs. (2000 – 2006) using 2000 emissions.

Figure 10-2 illustrates the effects of climate change, emissions change, and net changes to population-weighted $PM_{2.5}$ concentrations in California. Results are displayed for total $PM_{2.5}$ mass and the chemical components that make up the majority of that mass. Comparisons are shown for the effect of climate change (2047-53 vs. 2000-06) for the 2000 emissions (1st bar) and 2050 emissions (2nd bar) of each grouping. Comparisons are shown for the effect of emissions change (2000 vs. 2050) for the 2000-06 meteorology

(3rd bar) and 2047-53 meteorology (4th bar). Comparisons are shown for the combined effect of emissions and climate in the 5th bar. Uncertainty estimates shown in Figure 10-2 represent the 95% confidence interval. Simulations conducted with identical meteorology but altered emissions (3rd and 4th bars) were treated as a paired t-test with each day compared under two different emissions conditions yielding n>1000 and resulting in relatively small uncertainty ranges. The 1st, 2nd, and 5th bars compare differences between climate periods and so calculations were done as n=7 annual averages in both present and future climate periods yielding a paired t-test with 12 degrees of freedom. Note that crustal components were removed from all emissions comparisons (3rd, 4th, and 5th bars) outside of the SoCAB to avoid potential bias in the comparison. The 2000 emissions outside of the SoCAB were based on a winter emissions inventory while the 2050 emissions were based on an annual average emissions inventory, resulting in some biases between species that contribute to crustal components.

The results summarized in Figure 10-2 indicate that climate change has a similar effect on population-weighted concentrations under both the year 2000 and year 2050 emissions inventory. This result is also evident by comparing the results in chapters 7+8 with the results in chapter 9. The climate signal is shown in Figure 10-2 to aid in the comparison with emissions changes and net changes. The 3rd and 4th bars illustrated in Figure 10-2 indicate that the effects of emissions changes are very similar under both present and future climate conditions. Statewide population weighted $PM_{2.5}$ concentrations are predicted to increase by ~0.3-0.4 µg m^{-3}, largely due to increased concentrations of ammonium sulfate and metals even as statewide OC and EC population-weighted concentrations decrease due to the adoption of new emissions control measures such as diesel particle filters. Emissions comparisons in the SV and the SJV clearly reveal the benefits of a complete ban on residential wood combustion through a decrease in population-weighted OC concentrations of 0.5-1.5 µg m^{-3}. Population-weighted concentrations of nitrate decrease by ~0.1-0.2 µg m^{-3} in the SV and SJV due to a reduction in ammonia emissions from agricultural sources. Population-weighted $PM_{2.5}$ mass concentrations in the SoCAB are predicted to increase by ~1 µg m^{-3} due to increased exposure to OC, sulfate, and crustal material.

The 5th bar shown for each $PM_{2.5}$ concentration component in Figure 10-2 illustrates the combined differences between 2047-53 vs. 2000-06 driven by both climate changes and emissions changes. Not surprisingly, the emissions changes appear to be the larger of the two signals for almost all comparisons.

Figures 10-3 and 10-4 illustrate population-weighted concentrations of $PM_{0.1}$ and PM_{10} in various regions of California using the same format as Figure 10-2. The trends for the $PM_{0.1}$ and PM_{10} size fractions are in general agreement with those for $PM_{2.5}$.

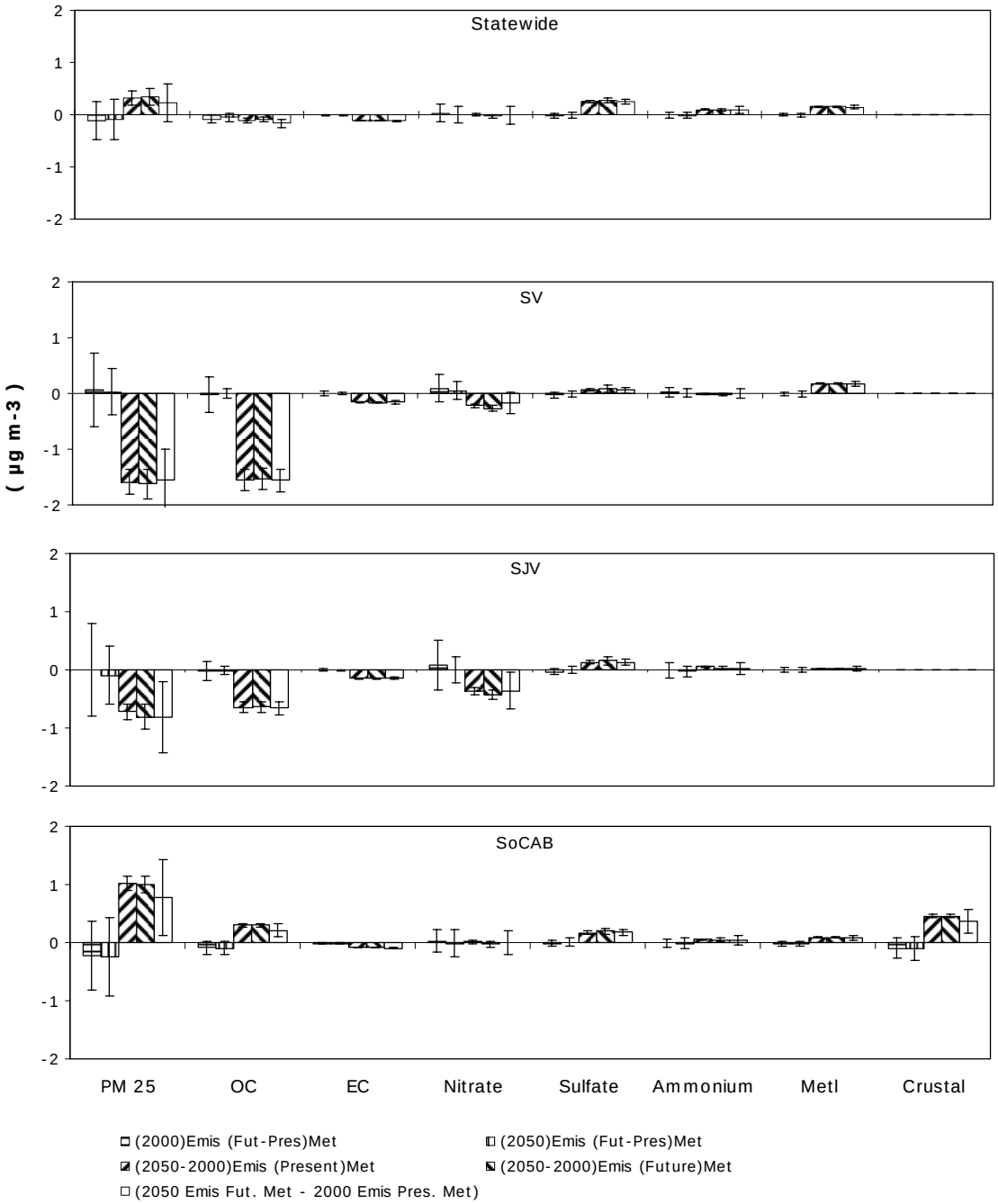

Figure 10-2: PM2.5 population-weighted concentration differences by chemical component. The first two bars of each group show the climate signal, the second two bars show the emissions signal, and the final bar shows the combined signal. Uncertainty bars represent the 95% confidence interval based on the inter-annual variability. The crustal signal has been removed from the (2050-2000) emissions comparisons (3rd – 5th bars) for all locations except the SoCAB to remove a bias in the calculation.

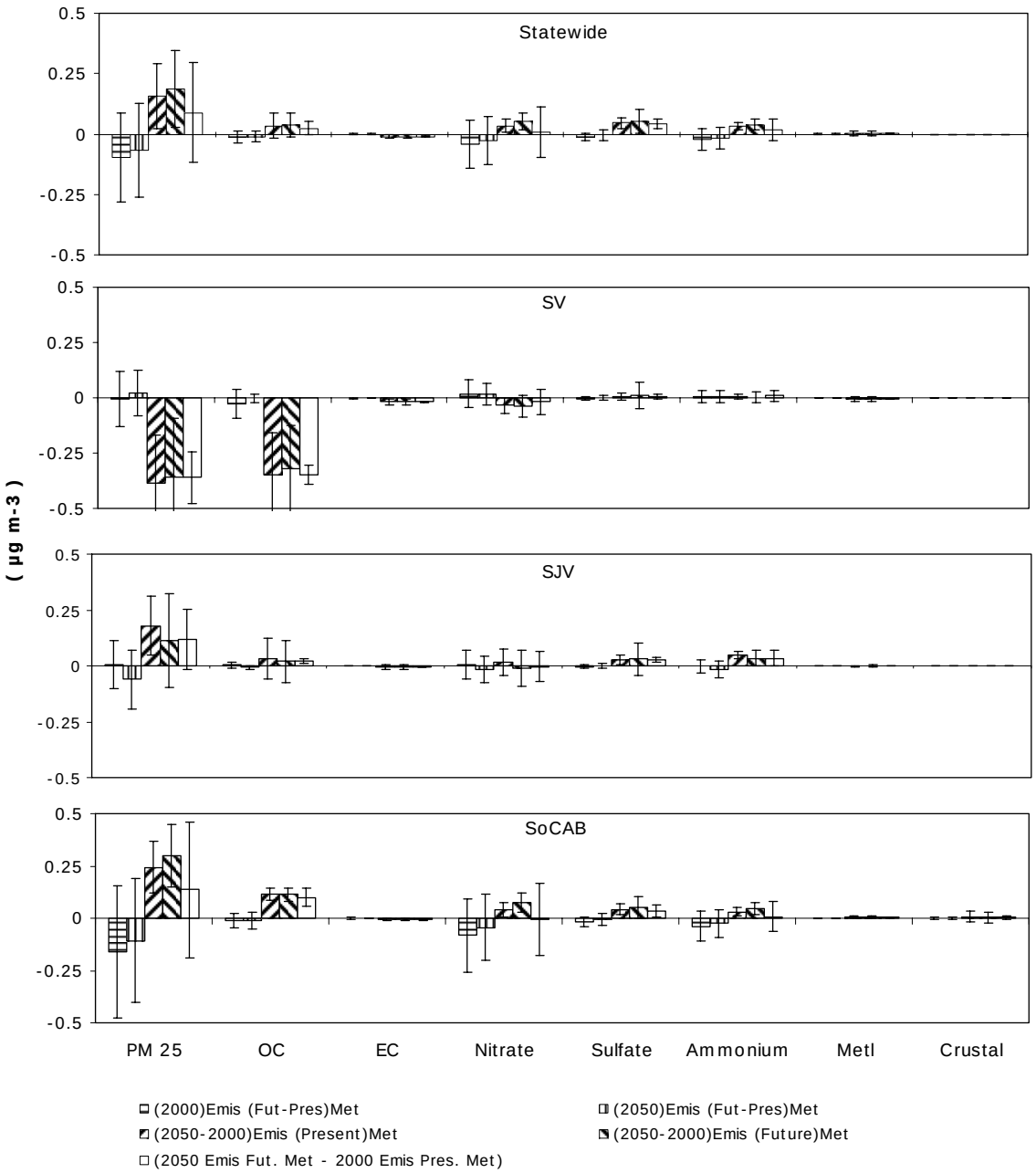

Figure 10-3: PM0.1 population-weighted concentration differences by chemical component. The first two bars of each group show the climate signal, the second two bars show the emissions signal, and the final bar shows the combined signal. Uncertainty bars represent the 95% confidence interval based on the inter-annual variability. The crustal signal has been removed from the (2050-2000) emissions comparisons (3rd – 5th bars) for all locations except the SoCAB to remove a bias in the calculation.

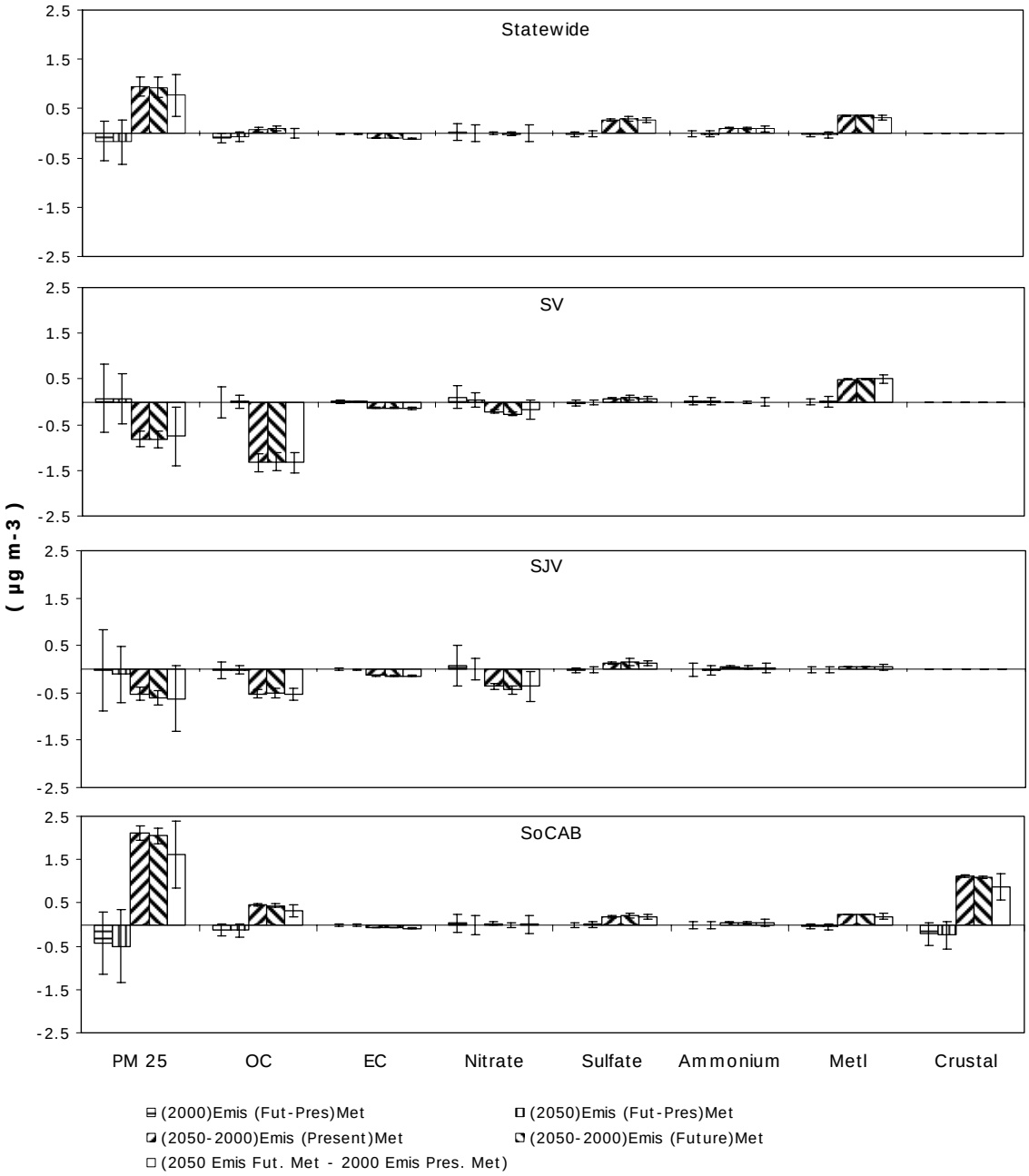

Figure 10-4: PM10 population-weighted concentration differences by chemical component. The first two bars of each group show the climate signal, the second two bars show the emissions signal, and the final bar shows the combined signal. Uncertainty bars represent the 95% confidence interval based on the inter-annual variability. The crustal signal has been removed from the (2050-2000) emissions comparisons (3rd – 5th bars) for all locations except the SoCAB to remove a bias in the calculation.

Figure 10-5 illustrates the effects of climate change, emissions change, and net changes to population-weighted primary source contributions to $PM_{2.5}$ concentrations using the same format that was employed for Figure 10-2. Note that Figure 10-5 presents results for primary mass only while Figure 10-2 presents results for total mass (=primary + secondary). Also note that dust and miscellaneous (Misc) source contributions were removed from all emissions comparisons (3rd, 4th, and 5th bars) outside of the SoCAB to avoid potential bias in the comparison.

The results shown in Figure 10-5 indicate a stronger signal associated with future changes to emissions than from the changes to climate in all regions of California. Future bans on residential wood combustion reduce population-weighted concentrations of primary wood smoke (Burns) while the application of diesel-particle filters reduces population-weighted concentrations of primary diesel particles. Uncontrolled sources such as meat cooking and gasoline engine combustion increase their primary population-weighted concentrations in the future as increased population puts upward pressure on these emissions. Likewise, population-weighted concentrations of primary ship exhaust increase in the future reflecting the projected increased movement of goods through California ports. The net changes to population-weighted annual-average $PM_{2.5}$ mass are predicted to be positive in the SoCAB and negative for all other regions of the state.

Figures 10-6 and 10-7 summarize population weighted concentrations of primary $PM_{2.5}$ source contributions to $PM_{0.1}$ and PM_{10} using the same format as Figure 10-5. The trends illustrated for the $PM_{0.1}$ and PM_{10} size fractions are similar to those for $PM_{2.5}$, with the importance of combustion sources slightly increased in the $PM_{0.1}$ size fraction and the importance of crustal dust sources slightly increased in the PM_{10} size fraction.

The results summarized in Figures 10-2 through 10-7 predict that population-weighted annual-average $PM_{2.5}$ concentrations are strongly influenced by future emissions changes in California. The 2050 emissions projections analyzed in the current project do not incorporate any reductions in criteria pollutants associated with rules designed to reduce greenhouse gas emissions. It is possible that efforts to control greenhouse gas emissions may not only mitigate climate change, but they will provide co-benefits of reduced criteria pollutant emissions and reduced population-weighted concentrations in California. A comprehensive analysis of this feedback is currently being conducted at UC Davis under funding from the US EPA.

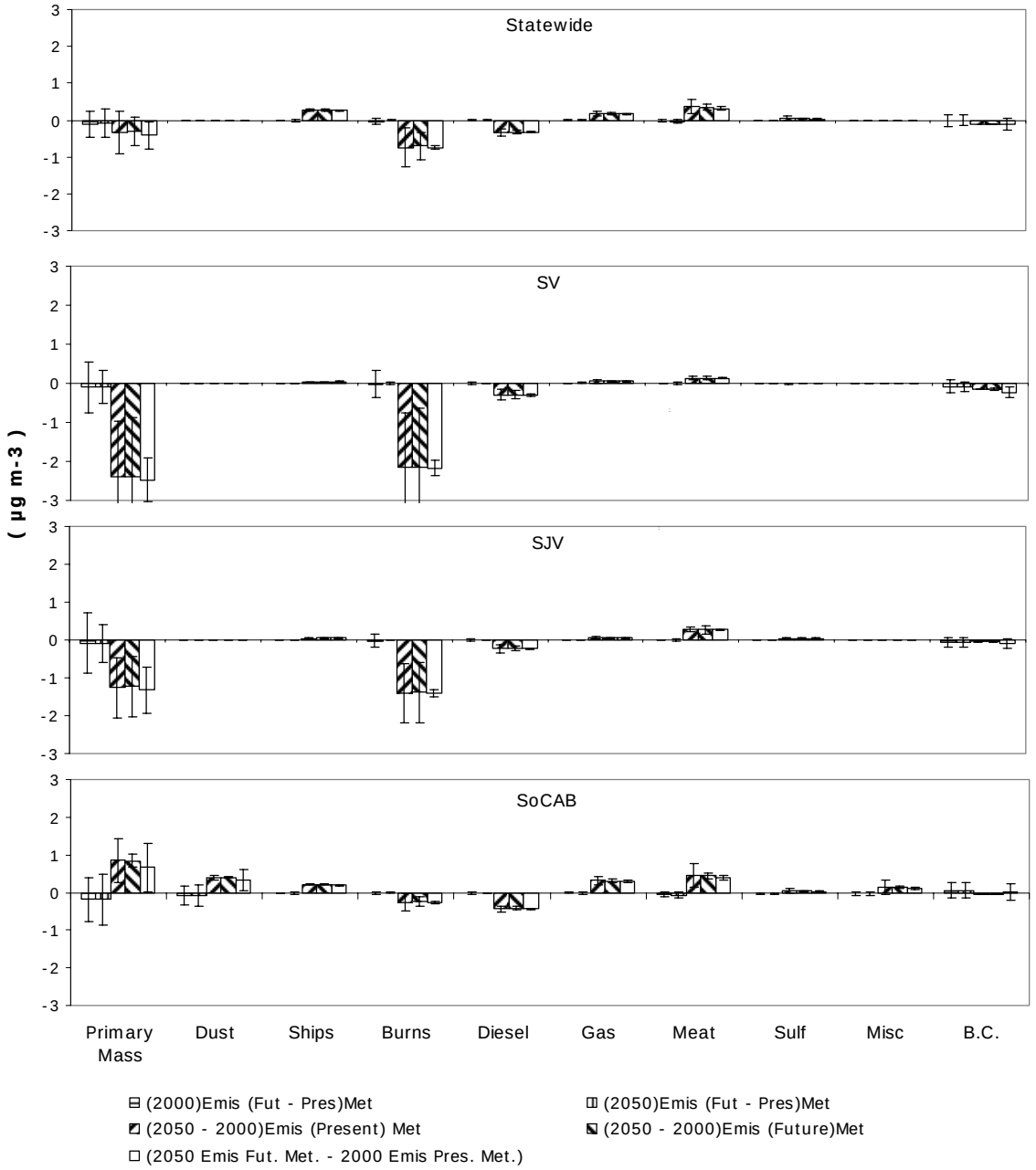

Figure 10-5: PM2.5 population-weighted concentration differences by primary source contribution. The first two bars of each group show the climate signal, the second two bars show the emissions signal, and the final bar shows the combined signal. Uncertainty bars represent the 95% confidence interval based on the inter-annual variability. The dust and miscellaneous (Misc) signals have been removed from the (2050-2000) emissions comparisons (3rd – 5th bars) for all locations except the SoCAB to remove a bias in the calculation.

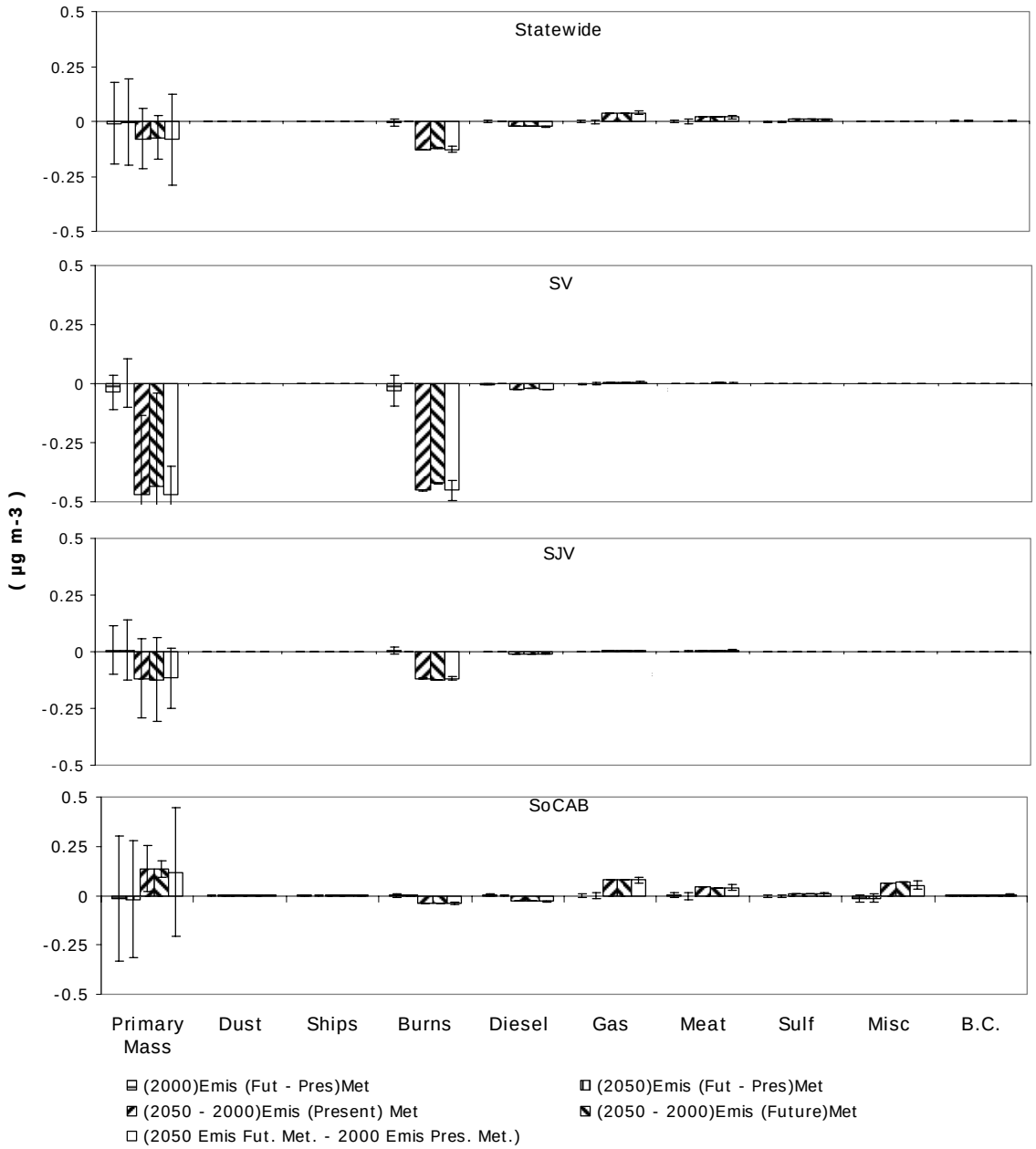

Figure 10-6: PM0.1 population-weighted concentration differences by primary source contribution. The first two bars of each group show the climate signal, the second two bars show the emissions signal, and the final bar shows the combined signal. Uncertainty bars represent the 95% confidence interval based on the inter-annual variability. The dust and miscellaneous (Misc) signals have been removed from the (2050-2000) emissions comparisons (3rd – 5th bars) for all locations except the SoCAB to remove a bias in the calculation.

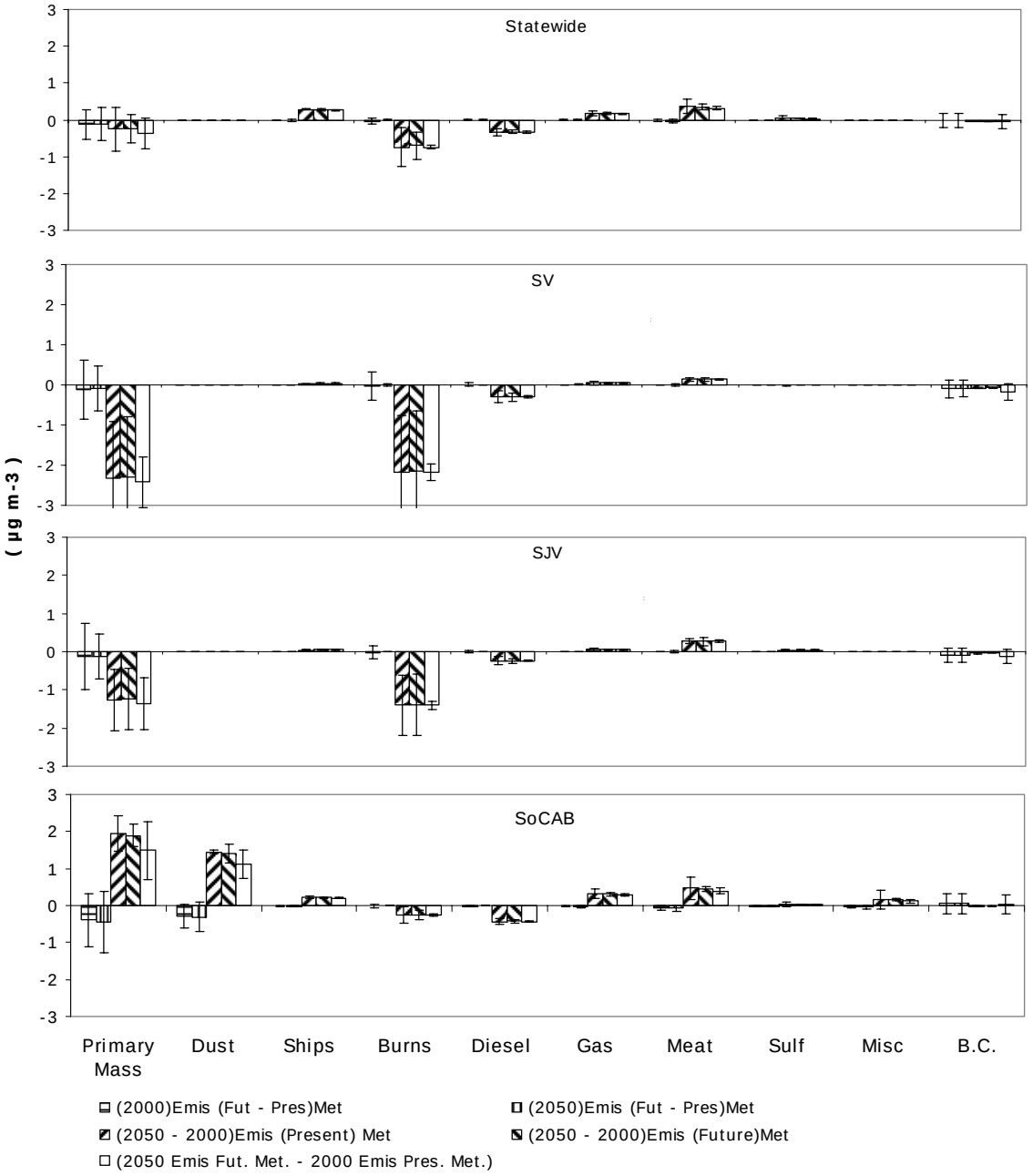

Figure 10-7: PM10 population-weighted concentration differences by primary source contribution. The first two bars of each group show the climate signal, the second two bars show the emissions signal, and the final bar shows the combined signal. Uncertainty bars represent the 95% confidence interval based on the inter-annual variability. The dust and miscellaneous (Misc) signals have been removed from the (2050-2000) emissions comparisons (3rd – 5th bars) for all locations except the SoCAB to remove a bias in the calculation.

10.4 Conclusions

The results of the present study do not detect a statistically significant climate "penalty" associated with annual-average concentrations of airborne particulate matter (PM). The changes to the annual-average population-weighted PM concentrations induced by the changes to the emissions inventories between 2000 and 2050 appear to be largely unmodified by the climate signal in each of California's major air basins.

Climate change does appear to impose a "penalty" on airborne PM in California during extreme (99th percentile) pollution episodes (see chapters 8 and 9). Although cross comparison figures are not shown in the current chapter, the results of chapters 8 and 9 indicate that population-weighted extreme PM concentrations increase in future climate relative to current conditions. Strict control measures can prevent a future increase in population-weighted concentrations of primary diesel PM and biomass PM. These necessary control measures may be considered a climate "penalty" for extreme PM concentrations.

The conclusions regarding climate "penalties" for annual-average population-weighted PM concentrations and extreme (99th percentile) population-weighted PM concentrations are subject to the qualifications inherent in the previous chapters of this report. The climate-weather-air quality modeling system under-predicts present-day $PM_{2.5}$ concentrations by 30-40% due to the inability of WRF to simulate low wind speeds in the surface layer during high pressure stagnation events. It is possible that low wind speed events will be influenced by future climate change, and this in turn will influence future $PM_{2.5}$ concentrations. Furthermore, the GCM used in the current study is one example of an ensemble of GCM's that have been employed to study future climate. Significant differences exist between predictions from GCM's, especially for wind speed, mixing depth, cloud cover, precipitation, etc that all influence PM concentrations. Further studies that employ ensembles of GCMs/RCMs/CTMs are needed to fully quantify the uncertainty in the climate air quality interactions.

11.0 SUMMARY AND CONCLUSIONS

The chapters presented in this report provide comprehensive analyses of climate change impact on air quality, especially on ozone and particulate matter (PM) with probable implications for public health in California. The results will benefit the scientific community, regulatory agencies and the general public in better understanding the impact of global climate change on regional air quality.

11.1 A Preliminary Assessment of the Sensitivity of Air Quality in California to Global Change

A regional air quality model was used to quantify the effect of temperature, humidity, mixing depth, and ozone (O_3) background concentrations on O_3 and airborne particulate matter (PM) during three air quality episodes in California. Increasing temperature with no change in absolute humidity promoted the formation of O_3 by +2 to +9 ppb K^{-1} through increased reaction rates. Increasing temperature with no change in relative humidity increased predicted O_3 concentrations by +2 to +15 ppb K^{-1} through enhanced production of hydroxyl radical combined with increased reaction rates. Increasing mixing depth promoted the formation of O_3 in regions with an over-abundance of fresh NO emissions (such as central Los Angeles) by providing extra dilution.

Increasing temperature with no change in absolute humidity reduced particle water content and promoted ammonium nitrate evaporation at a rate of -3 to -7 µg m^{-3} K^{-1}. Increasing temperature with no change in relative humidity maintained particle water content and moderated ammonium nitrate evaporation rates to a maximum value of -3 µg m^{-3} K^{-1} during warmer episodes and increased ammonium nitrate condensation by +1.5 µg m^{-3} K^{-1} during colder episodes. Increasing mixing depth reduced the concentration of primary particulate matter but increased the formation of secondary particulate matter in regions with an over-abundance of fresh NO emissions.

O_3 transported into California from upwind areas enhanced the formation of particulate nitrate by promoting the formation of N_2O_5 and HNO_3 at night. A 30 ppb increase in background O_3 concentrations (roughly doubling current levels) increased maximum $PM_{2.5}$ concentrations by +7 to +16 µg m^{-3} even when temperature was simultaneously increased by +5 K with no change in absolute humidity (most unfavorable conditions for nitrate formation).

11.2 Impact of Climate Change on Photochemical Air Pollution in Southern California

The effects of future climate and emissions-related perturbations on ozone air quality in Southern California was considered, with an assumed increase to 2x pre-industrial levels (280 ppm to 560 ppm) for global background levels of carbon dioxide. Effects of emission and climate-related forcings on air quality were superimposed on a summer 2005 high-ozone time period. Perturbations considered here included (a) effect of increased temperature on atmospheric reaction rates, (b) effect of increased temperature

on biogenic emissions, (c) effect of increased water vapor concentrations, (d) effect of increased pollutant levels at the inflow (western) boundary, and (e) effect of population growth and technology change on emissions within southern California. Various combinations of the above perturbations were also considered. The climate-related perturbations (a-c) led to combined peak 1-h ozone increases of up to 11 ppb. The effect on ozone was greatly reduced when the temperature increase was applied mostly during nighttime hours rather than uniformly throughout the day. Increased pollutant levels at the inflow boundary also led to ozone increases up to 5 ppb. These climate and inflow-related changes offset some of the anticipated benefits of emission controls within the air basin.

11.3 Statistical Downscaling of Climate Change Impacts on Ozone Concentrations in California

The statistical relationship between the daily 1-hr maximum ozone (O_3) concentrations and the daily maximum upper air temperature was explored for California's two most heavily polluted air basins: the South Coast Air Basin (SoCAB) and the San Joaquin Valley Air Basin (SJVAB). A coarse scale analysis of the temperature at an elevation of 850-millibar pressure (T850) for the period 1980 – 2004 was obtained from the National Center for Environmental Prediction (NCEP) / National Center for Atmospheric Research (NCAR) Reanalysis1 dataset for grid points near Upland (SoCAB) and Parlier (SJVAB). Daily 1-hr maximum ozone concentrations were obtained from the California Air Resources Board (CARB) for these locations over the same time period. The ozone concentrations measured at any given value of the Reanalysis T850 were approximately normally distributed. The 25%, 50%, and 75% quartile ozone concentrations increased linearly with T850, reflecting the effect of temperature on emissions and chemical reaction rates. A 2-D Lagrangian (trajectory) form of the UCD/CIT photochemical air quality model was used in a perturbation study to explain the variability of the ozone concentrations at each value of T850. Wind speed, wind direction, temperature, relative humidity, mixing height, initial concentrations for VOCs, background ozone concentrations, time of year (late spring – early fall) and overall emissions were perturbed in a realistic fashion during this study. A total of 62 model simulations were performed and the results were analyzed to show that long-term changes to emissions inventories were the largest sources of ozone variability at a fixed value of T850. Projections of future T850 values in California were obtained from the Geophysical Fluid Dynamics Laboratory (GFDL) model under the Intergovernmental Panel on Climate Change (IPCC) A2 and B1 emissions scenarios for the years from 2001 to 2100. The future temperature trends combined with the historical statistical relationships suggest that an additional 22-30 days year^{-1} in California would experience $O_3 \geq 90$ ppb under the A2 emissions scenario and an additional 6-13 days year^{-1} would experience $O_3 \geq 90$ ppb under the B1 emissions scenario by the year 2050 (assuming the emissions remained at 1990-2004 levels). These calculations help to quantify the climate "penalty" that must be overcome to improve air quality in California.

An extensive search for a robust statistical relationship between measured airborne particulate matter (PM) concentrations and meteorological variables did not identify a

suitable relationship for statistical downscaling. This finding suggests that either a strong climate-PM relationship does not exist in California or the climate-PM relationship is so non-linear that it could not be identified by multiple regression analysis of the measurements. Dynamic downscaling should be used to further investigate the relationship between climate and PM in California's major air basins.

11.4 The Impact of Climate Change on Air Quality Related Meteorological Conditions in California – Part I: Present Time Simulation Analysis

The impact of climate change on meteorology related to air quality conditions in California (CA) was investigated by dynamically downscaling Parallel Climate Model (PCM) results to 4km resolution using the Weather Research and Forecast (WRF) model. The analyses focused on wind speed, planetary boundary layer height (PBLH), surface temperature, and relative humidity between the years 2000-06. The accuracy of the PCM-WRF simulations was evaluated by comparing results to separate WRF simulations that used data from the National Center for Environmental Prediction (NCEP) Global Forecasting System (GFS) reanalysis data. Regionally-averaged performance statistics of the downscaling results were estimated for the South Coast Air Basin (SoCAB) and the San Joaquin Valley (SJV). This comparison indicated that two types of biases exist in the downscaling results – those inherited from PCM and those introduced by the WRF model itself. PCM-WRF biases were primarily caused by an imprecise prediction for the location and strength of the Pacific Subtropical High (PSH). Inherent WRF biases identified in the GFS-WRF predictions overestimated surface temperature and wind speed for most of the year, indicating that WRF has systematic errors in California's major air basins. The GFS-WRF simulations had lower bias during the summer vs. the winter. The overall analysis implies that PCM-WRF predictions used as input data for air quality models will likely cause underestimates for air pollution concentrations in CA.

11.5 The Impact of Climate Change on Air Quality Related Meteorological Conditions in California – Part II: Present versus Future Time Simulation Analysis

The Weather Research and Forecasting (WRF) model was applied to dynamically downscale the Parallel Climate Model (PCM) projection for the impact of climate change on the regional meteorological conditions in California (CA). Comparisons were made for meteorological fields that strongly influence regional air quality between the current (2000-06) and future (2047-53) climate periods. Analyses showed that stagnation events will occur more frequently and have stronger intensity in the future during summer and winter seasons (decreasing stagnation frequency during the spring and fall). This trend may intensify the concentrations of air pollutants during extreme episodes. Increases in surface wind and planetary boundary layer height (PBLH) were predicted for the coastal part of southern California during summer, suggesting stronger ventilation in this region. The analysis of the inter-annual variability indicates that future changes in temperature are statistically significant ($p<0.05$) throughout California, but future changes to surface wind and PBLH are not statistically significant ($p>0.1$) except in limited sub-regions along the coast. This suggests that the inter-annual variability in meteorological

conditions is larger than the climate signal between 2000 and 2050 for most variables except temperature.

11.6 Climate Impact on Airborne Particulate Matter Concentrations in California Using Seven Year Analysis Periods

The effect of global climate change on the annual average concentrations of fine particulate matter ($PM_{2.5}$) in California was studied using a climate – air quality modeling system composed of global through regional models. Meteorological output from the Parallel Climate Model (PCM) generated under the "business as usual" global emissions scenario was downscaled using the Weather Research and Forecasting (WRF) model followed by air quality simulations using the UCD/CIT airshed model. The air quality simulations were carried out for the entire state of California with a resolution of 8-km for the years 2000-06 (present climate) and 2047-53 (future climate). The 7-year windows were chosen to properly account for annual variability with the added benefit that the air quality predictions under the present climate could be compared to actual measurements. The climate – air quality modeling system successfully predicted the spatial pattern of present climate $PM_{2.5}$ concentrations in California but the absolute magnitude of the annual average $PM_{2.5}$ concentrations were under-predicted by ~35-40% in the major air basins. The majority of this under-prediction was caused by excess ventilation predicted by PCM-WRF that should be present to the same degree in the current and future time periods so that the net bias introduced into the comparison is minimized.

Surface temperature, relative humidity (RH), rain rate, and wind speed were predicted to increase in the future climate while the ultra violet (UV) radiation was predicted to decrease in major urban areas in the San Joaquin Valley (SJV) and South Coast Air Basin (SoCAB). These changes lead to a predicted decrease in $PM_{2.5}$ mass concentrations of ~0.3-0.7 $\mu g\ m^{-3}$ in the southern portion of the SJV and ~0.3-1.1 $\mu g\ m^{-3}$ along coastal regions of California including the heavily populated San Francisco Bay Area and the SoCAB surrounding Los Angeles. Annual average $PM_{2.5}$ concentrations were predicted to increase in the northern portion of the SJV and in the Sacramento Valley due to the effects of climate change, but a corresponding analysis of the annual variability showed that these predictions are not statistically significant (i.e. the choice of a different 7-year period could produce a different outcome for these regions).

11.7 Climate Impact on Population-Weighted Airborne Particulate Matter Concentrations in California during Short and Long Time Periods

The climate change effect on population-weighted concentrations of particulate matter (PM) was studied using the Parallel Climate Model (PCM), the Weather Research and Forecasting (WRF) model and the UCD/CIT 3-D photochemical air quality model. A "business as usual" climate emissions scenario was dynamically downscaled for the entire state of California between the years 2000-06 and 2047-53. Air quality simulations were carried out for 1008 days in each of the present-day and future climate conditions

using emissions at 2000 level. Population-weighted annual average concentrations of $PM_{0.1}$, $PM_{2.5}$, and PM_{10} total mass, components species, trace metal and primary source contributions were calculated for California and three air basins: the Sacramento Valley Air Basin (SV), the San Joaquin Valley Air Basin (SJV) and the South Coast Air Basin (SoCAB). Population-weighted concentrations during extreme events were also calculated for California and the three air basins of interest.

Population-weighted annual average concentrations of $PM_{2.5}$ showed mixed climate responses for California. The $PM_{2.5}$ total mass concentration was predicted to decrease by ~2% in the SoCAB with little change in the SV and SJV in the future. $PM_{2.5}$ elemental carbon, organic carbon, sulfate, ammonium ion and trace metal concentrations followed the trends of total mass for California and the sub-regions. Contributions from shipping, wood smoke, diesel combustion, gasoline combustion, meat cooking, high sulfur content fuels, and miscellaneous sources were predicted to decrease by ~2-6% in the SoCAB in the future. Population-weighted annual average concentrations of PM_{10} total mass, component species, trace metal, and sources generally had the same pattern as the $PM_{2.5}$ results. The uncertainty associated with the climate signal is large because the inter-annual variability within any climate period is greater than the mean difference between climate periods.

Extreme PM concentrations were examined by calculating the average concentration on the 10 most heavily polluted days during present and future climate conditions (99th percentile concentrations). Extreme $PM_{2.5}$ total mass was predicted to be ~20 $\mu g\ m^{-3}$ higher in the future compared to the present-day in the SJV and SV. Population-weighted concentrations for these extreme events were also calculated for $PM_{0.1}$, $PM_{2.5}$ and PM_{10} for the entire state of California and the three sub-regions of interest. Predicted extreme $PM_{2.5}$ and PM_{10} concentrations for total mass and almost all components and primary source contributions increased in the future vs. present climate in the SV and SJV. Statewide extreme population-weighted $PM_{2.5}$ primary diesel concentrations were higher in the future due to the effects of climate change, while $PM_{2.5}$ primary shipping concentrations decreased. These trends reflect the increased strength of future stagnation episodes which trap pollutants close to the locations where they were emitted.

11.8 Climate Impact on Particulate Matter (PM) in California for Emissions Projected in 2050

Emissions inventories for California in the year 2050 were projected from basecase inventories for 2029/2030 using population growth estimates obtained from the Department of Finance. The average PM concentrations between 2000-06 and 2047-53 were predicted using the year 2050 emissions inventories and the PCM/WRF/UCD-CIT models. PM concentrations predicted using the 2050 emissions and the meteorology between 2000-06 and 2047-53 were consistent with predictions using the year 2000 emissions inventory. Stated another way, the changes to the emission inventory between the year 2000 and 2050 did not expose any non-linear relationships between emissions and annual-average PM concentrations.

In contrast to the annual-average results, extreme PM concentrations did respond differently to the climate signal when the emissions were changed from year 2000 to year 2050. Future emissions generally produced lower climate sensitivity for extreme PM concentrations because emissions of primary diesel PM and wood smoke were greatly reduced in the future inventory. This finding suggests that diesel particle filters and similar control strategies that control primary PM emitted close to population centers are effective methods to avoid the climate penalty associated with extreme pollution events in the future.

11.9 Combined Impact of Climate Change and Emissions Controls on Particulate Matter in California

A cross-comparison of the simultaneous effects of climate change and emissions change on airborne particulate matter concentrations in California was carried out. Changes to the emissions inventories resulted in similar changes to annual-average airborne particulate matter concentrations under either current or future climate conditions. No climate "penalty" for annual-average airborne particulate matter was revealed in the current analysis, subject to the qualification that the biases in the downscaling system may be masking such an effect.

11.10 Future research

Chapters 4-10 of the current report analyze climate change under a moderate "business as usual" emissions scenario. The IPCC analyzes global climate change under a range of SRES emissions scenarios ranging from the lowest (B1) through to the highest (A2FI) emissions. It is recommended that further air quality simulations should be carried out under a high IPCC-SRES emissions scenario to complement the findings of the current study.

The current work utilized future climate predictions based on one Global climate Model (GCM) output in each of the statistical down-scaling (GFDL2) and dynamic down-scaling (PCM) techniques. In contrast, the IPCC analyzes results from multiple GCMs to generate an ensemble of results that are then used to create a "weight of science" estimate for future climate under each one of the SRES emissions scenarios. Air quality simulations should take the same approach. Air quality results produced by an ensemble of GCMs should be produced to create a "weight of science" estimate for the effects of climate change on air quality in California. A true assessment of the uncertainty in the calculations is impossible without going through this exercise.

Air quality simulations with fine spatial resolution (<10km) over climatologically relevant time periods (3-8 years) are computationally challenging. A possible approach to reduce the burden of these calculations would be to carry out air quality simulations using meteorological fields averaged over an analysis period for a base year instead of running the simulations using meteorological fields from individual years. A mechanism to quantify the uncertainty associated with this technique should be developed.

Reference

1. Jacob, D.J. and D.A. Winner, *Effect of climate change on air quality.* Atmospheric Environment, 2009. **43**(1): p. 51-63.
2. Adams, L., et al., *Climate Action Team Biennial Report to the Governor and Legislature*. 2009, California Environmental Protection Agency: Sacramento, CA.
3. Christensen, J.H., et al., *Regional Climate Projections. In: Climate Change 2007: The Physical Science Basis. Contribution of Working Group I to the Fourth Assessment Report of the Intergovernmental Panel on Climate Change, [Solomon, S., D. Qin, M. Manning, Z. Chen, M. Marquis, K.B. Averyt, M. Tignor and H.L. Miller (eds.)]*. Cambridge University Press, 2007. **Cambridge, United Kingdom and New York, NY, USA**.
4. Rubin, J.I., et al., *Temperature dependence of volatile organic compound evaporative emissions from motor vehicles.* Journal of Geophysical Research-Atmospheres, 2006. **111**(D3): p. -.
5. Steiner, A.L., et al., *Influence of future climate and emissions on regional air quality in California.* Journal of Geophysical Research-Atmospheres, 2006. **111**(D18): p. -.
6. Samet, J.M., et al., *On health effects of ozone exposure and exposing the epidemiologic process.* Epidemiology, 2005. **16**(4): p. 425-426.
7. Weschler, C.J., *Ozone's impact on public health: Contributions from indoor exposures to ozone and products of ozone-initiated chemistry.* Environmental Health Perspectives, 2006. **114**(10): p. 1489-1496.
8. Morland, K., et al., *Health effects associated with potential exposures to PM2.5 ozone and carbon monoxide in the RTP PM Panel Study.* Epidemiology, 2002. **13**(4): p. S84-S84.
9. Pope, C.A., et al., *Particulate Air-Pollution as a Predictor of Mortality in a Prospective-Study of Us Adults.* American Journal of Respiratory and Critical Care Medicine, 1995. **151**(3): p. 669-674.
10. Dockery, D.W., et al., *An Association between Air-Pollution and Mortality in 6 United-States Cities.* New England Journal of Medicine, 1993. **329**(24): p. 1753-1759.
11. Samet, J.M., et al., *Fine particulate air pollution and mortality in 20 US Cities, 1987-1994.* New England Journal of Medicine, 2000. **343**(24): p. 1742-1749.
12. Bernard, S.M., et al., *The potential impacts of climate variability and change on air pollution-related health effects in the United States.* Environmental Health Perspectives, 2001. **109**: p. 199-209.
13. Prather, M., et al., *Fresh air in the 21st century?* Geophysical Research Letters, 2003. **30**(2).
14. Mickley, L.J., et al., *Effects of future climate change on regional air pollution episodes in the United States.* Geophysical Research Letters, 2004. **31**(24).
15. Murazaki, K. and P. Hess, *How does climate change contribute to surface ozone change over the United States?* Journal of Geophysical Research, 2006. **111**(D5).
16. Liao, H., W.T. Chen, and J.H. Seinfeld, *Role of climate change in global predictions of future topospheric ozone and aerosols.* Journal of Geophysical Research, 2006. **111**: p. D12304.

17. Wu, S.L., et al., *Effects of 2000-2050 global change on ozone air quality in the United States.* Journal of Geophysical Research-Atmospheres, 2008. **113**(D6).
18. Tagaris, E., et al., *Potential Impact of Climate Change on Air Pollution-Related Human Health Effects.* Environmental Science & Technology, 2009. **43**(13): p. 4979-4988.
19. Jacobson, M.Z., *On the causal link between carbon dioxide and air pollution mortality.* Geophysical Research Letters, 2008. **35**(3): p. L03809, doi:10.1029/2007GL031101.
20. Jacobson, M.Z., *Enhancement of Local Air Pollution by Urban CO2 Domes.* Environmental Science & Technology, 2010. **44**(7): p. 2497-2502.
21. Avise, J., et al., *Attribution of projected changes in summertime US ozone and PM2.5 concentrations to global changes.* Atmospheric Chemistry and Physics, 2009. **9**(4): p. 1111-1124.
22. *Climate Change 2001: The Scientific Basis. Contribution of Working Group I to the Third Assessment Report of the Intergovernmental Panel on Climate Change (IPCC)*, ed. J.T. Houghton, et al. 2001, Cambridge: Cambridge University Press.
23. VanCuren, R.A. and T.A. Cahill, *Asian aerosols in North America: Frequency and concentration of fine dust.* Journal of Geophysical Research, 2002. **107**(D24).
24. Vingarzan, R., *A review of surface ozone background levels and trends.* Atmospheric Environment, 2004. **38**(21): p. 3431-3442.
25. Kim, B.M., S. Teffera, and M.D. Zeldin, *Characterization of PM2.5 and PM10 in the South Coast Air Basin of southern California: Part 1 - Spatial variations.* Journal of the Air & Waste Management Association, 2000. **50**(12): p. 2034-2044.
26. Hogrefe, C., et al., *Simulating changes in regional air pollution over the eastern United States due to changes in global and regional climate and emissions.* Journal of Geophysical Research, 2004. **109**(D22).
27. Langner, J., R. Bergstrom, and V. Foltescu, *Impact of climate change on surface ozone and deposition of sulphur and nitrogen in Europe.* Atmospheric Environment, 2005. **39**(6): p. 1129-1141.
28. Leung, L.R., et al., *Mid-century ensemble regional climate change scenarios for the western United States.* Climatic Change, 2004. **62**(1-3): p. 75-113.
29. Duffy, P.B., et al., *Simulations of present and future climates in the western United States with four nested regional climate models.* Journal of Climate, 2006. **19**(6): p. 873-895.
30. Klonecki, A. and H. Levy, *Tropospheric chemical ozone tendencies in CO-CH4-NOy-H2O system: Their sensitivity to variations in environmental parameters and their application to a global chemistry transport model study.* Journal of Geophysical Research, 1997. **102**(D17): p. 21221-21237.
31. Sillman, S. and F.J. Samson, *Impact Of Temperature On Oxidant Photochemistry In Urban, Polluted Rural And Remote Environments.* Journal of Geophysical Research, 1995. **100**(D6): p. 11497-11508.
32. Jacobson, M.Z., *Effects of soil moisture on temperatures, winds, and pollutant concentrations in Los Angeles.* Applied Meteorology, 1999. **38**(5): p. 607-616.

33. Aw, J. and M.J. Kleeman, *Evaluating the first-order effect of intraannual temperature variability on urban air pollution.* Journal of Geophysical Research-Atmospheres, 2003. **108**(D12).
34. Kleeman, M.J. and G.R. Cass, *A 3D Eulerian source-oriented model for an externally mixed aerosol.* Environmental Science & Technology, 2001. **35**(24): p. 4834-4848.
35. Held, T., et al., *Modeling particulate matter in the San Joaquin Valley with a source-oriented externally mixed three-dimensional photochemical grid model.* Atmospheric Environment Part a-General Topics, 2004. **38**(22): p. 3689-3711.
36. Ying, Q. and M.J. Kleeman, *Source contributions to the regional distribution of secondary particulate matter in California.* Atmospheric Environment, 2006. **40**(4): p. 736-752.
37. Mysliwiec, M.J. and M.J. Kleeman, *Source Apportionment of Secondary Airborne Particulate Matter in a Polluted Atmosphere.* Environmental Science and Technology, 2002. **36**(24): p. 5376-5384.
38. Carter, W.P.L., *A Detailed Mechanism for the Gas-Phase Atmospheric Reactions of Organic-Compounds.* Atmospheric Environment Part a-General Topics, 1990. **24**(3): p. 481-518.
39. Pandis, S.N., et al., *Secondary Organic Aerosol Formation and Transport.* Atmospheric Environment Part a-General Topics, 1992. **26**(13): p. 2269-2282.
40. Odum, J.R., et al., *Gas/particle partitioning and secondary organic aerosol yields.* Environmental Science & Technology, 1996. **30**(8): p. 2580-2585.
41. Griffin, R.J., D. Dabdub, and J.H. Seinfeld, *Secondary organic aerosol - 1. Atmospheric chemical mechanism for production of molecular constituents.* Journal of Geophysical Research-Atmospheres, 2002. **107**(D17).
42. Griffin, R.J., D. Dabdub, and J.H. Seinfeld, *Development and initial evaluation of a dynamic species-resolved model for gas phase chemistry and size-resolved gas/particle partitioning associated with secondary organic aerosol formation.* Journal of Geophysical Research, 2005. **110**(D5).
43. Pun, B.K., et al., *Secondary organic aerosol - 2. Thermodynamic model for gas/particle partitioning of molecular constituents.* Journal of Geophysical Research-Atmospheres, 2002. **107**(D17).
44. Kusik, C.L. and H.P. Meissner, *Electrolyte activity coefficients in inorganic processing.* Fundamental Aspects of Hydrometallurgical Processes AIChE Symposium Series, 1978. **74**: p. 14-20.
45. Fredenslund, A., J. Gmehling, and P. Rasmussen, *Vapor-liquid equilibrium using UNIFAC.* 1977, New York: Elsevier.
46. Kleeman, M.J., G.R. Cass, and A. Eldering, *Modeling the airborne particle complex as a source-oriented external mixture.* Journal of Geophysical Research-Atmospheres, 1997. **102**(SEP 20): p. 21355-21372.
47. Fraser, M.P., et al., *Modeling the atmospheric concentrations of individual gas-phase and particle-phase organic compounds.* Environmental Science & Technology, 2000. **V34 N7**(APR 1): p. 1302-1312.
48. Griffin, R.J., et al., *Secondary organic aerosol 3. Urban/regional scale model of size- and composition-resolved aerosols.* Journal of Geophysical Research, [Atmospheres], 2002. **107**(D17): p. AAC5/1-AAC5/14.

49. Ying, Q. and M. Kleeman, *Verification of a source-oriented external mixture air quality model during a severe photochemical smog event.* Atmospheric Environment Part a-General Topics, submitted for publication.
50. Held, A.E., et al., *A comparison of the UCD/CIT air quality model and the CMB source-receptor model for primary airborne particulate matter.* Atmospheric Environment Part a-General Topics, 2005. **39**: p. 2281-2297.
51. Kleeman, M.J., Q. Ying, and A. Kaduwela, *Control Strategies for the Reduction of Airborne Particulate Nitrate in California's San Joaquin Valley.* Atmospheric Environment, 2005. **39**(29): p. 5325-5341.
52. Kleeman, M.J., et al., *Source contributions to the size and composition distribution of atmospheric particles: Southern California in September 1996.* Environmental Science & Technology, 1999. **33**(23): p. 4331-4341.
53. Clark, T.L. and T.R. Karl, *Application of Prognostic Meteorological Variables to Forecasts of Daily Maximum One-Hour Ozone Concentrations in the Northeastern United-States.* Journal of Applied Meteorology, 1982. **21**(11): p. 1662-1671.
54. Lin, C.Y.C., D.J. Jacob, and A.M. Fiore, *Trends in exceedances of the ozone air quality standard in the continental United States, 1980-1998.* Atmospheric Environment, 2001. **35**(19): p. 3217-3228.
55. Sillman, S. and F.J. Samson, *Impact of Temperature on Oxidant Photochemistry in Urban, Polluted Rural and Remote Environments.* Journal of Geophysical Research-Atmospheres, 1995. **100**(D6): p. 11497-11508.
56. Brasseur, G.P., et al., *Impact of climate change on the future chemical composition of the global troposphere.* Journal of Climate, 2006. **19**(16): p. 3932-3951.
57. Racherla, P.N. and P.J. Adams, *Sensitivity of global tropospheric ozone and fine particulate matter concentrations to climate change.* Journal of Geophysical Research-Atmospheres, 2006. **111**(D24): p. D24103, doi: 10.1029/2005JD006939.
58. Stevenson, D., et al., *Impacts of climate change and variability on tropospheric ozone and its precursors.* Faraday Discussions, 2005. **130**: p. 1-17, Doi: 10.1039/b417412g.
59. Unger, N., et al., *Influences of man-made emissions and climate changes on tropospheric ozone, methane, and sulfate at 2030 from a broad range of possible futures.* Journal of Geophysical Research-Atmospheres, 2006. **111**(D12): p. D12313, doi: 10.1029/2005JD006518.
60. Racherla, P.N. and P.J. Adams, *The response of surface ozone to climate change over the Eastern United States.* Atmospheric Chemistry and Physics, 2008. **8**(4): p. 871-885.
61. Kleeman, M.J., *A preliminary assessment of the sensitivity of air quality in California to global change.* Climatic Change, 2008. **87**: p. S273-S292.
62. Leung, L.R. and W.I. Gustafson, *Potential regional climate change and implications to US air quality.* Geophysical Research Letters, 2005. **32**(16): p. L16711, doi: 10.1029/2005GL022911.

63. Duffy, P.B., C. Bonfils, and D. Lobell, *Interpreting Recent Temperature Trends in California.* EOS, Transactions, American Geophysical Union, 2006. **88**(41): p. 409-424.
64. Bonfils, C. and D. Lobell, *Empirical evidence for a recent slowdown in irrigation-induced cooling.* Proceedings of the National Academy of Sciences of the United States of America, 2007. **104**(34): p. 13582-13587.
65. Lobell, D.B. and C. Bonfils, *The effect of irrigation on regional temperatures: A spatial and temporal analysis of trends in California, 1934-2002.* Journal of Climate, 2008. **21**(10): p. 2063-2071.
66. Lebassi, B., et al., *Observed 1970-2005 Cooling of Summer Daytime Temperatures in Coastal California.* Journal of Climate, 2009: p. doi: 10.1175/2008JCLI2111.1 (in press).
67. SCAQMD, *Air Quality Management Plan, Southern California Air Quality Management District, Diamond Bar, CA, June.* 2007.
68. Byun, D. and K.L. Schere, *Review of the governing equations, computational algorithms, and other components of the models-3 Community Multiscale Air Quality (CMAQ) modeling system.* Applied Mechanics Reviews, 2006. **59**(1-6): p. 51-77.
69. Carter, W.P.L., *Implementation of the SAPRC-99 Chemical Mechanism into the Models-3 Framework, College of Engineering, University of California, Riverside, CA. Report to the United States Environmental Protection Agency.* 2000: p. 3-23, 56-60.
70. Nowak, J.B., et al., *Gas-phase chemical characteristics of Asian emission plumes observed during ITCT 2K2 over the eastern North Pacific Ocean.* Journal of Geophysical Research-Atmospheres, 2004. **109**(D23): p. D23S19, doi: 10.1029/2003JD004488.
71. SCAQMD, *Air Quality Management Plan, Appendix 5, Modeling and Attainment Demonstrations, Southern California Air Quality Management District, Diamond Bar, CA, June.* 2007: p. V-1-11, V-2-18, V-4-23 to V-4-29.
72. Jackson, B., *Planning and Technical Support Division, California Air Resources Board, Sacramento, CA, personal communication, Dec.* 2007: Sacramento, CA.
73. Scott, K.I. and M.T. Benjamin, *Development of a biogenic volatile organic compounds emission inventory for the SCOS97-NARSTO domain.* Atmospheric Environment, 2003. **37**: p. S39-S49.
74. Snyder, M.A., et al., *Climate responses to a doubling of atmospheric carbon dioxide for a climatically vulnerable region.* Geophysical Research Letters, 2002. **29, 11**: p. 10.1029/2001GL014431.
75. Guenther, A.B., et al., *Isoprene and Monoterpene Emission Rate Variability - Model Evaluations and Sensitivity Analyses.* Journal of Geophysical Research-Atmospheres, 1993. **98 (D7)**(D7): p. 12609-12617.
76. Harley, P., et al., *Emission of 2-methyl-3-buten-2-ol by pines: A potentially large natural source of reactive carbon to the atmosphere.* Journal of Geophysical Research-Atmospheres, 1998. **103 (D19)**(D19): p. 25479-25486.
77. DOF, *Population Projections for California and Its Counties 2000-2050, California Deptartment of Finance, Sacramento, CA, July*. 2007.

78. IPCC, *Intergovernmental Panel on Climate Change. Climate Change 2001: The Scientific Basis*, ed. J.T. Houghton, et al. 2001, Cambridge, UK and New York, NY, USA: Cambridge University Press. 63, 800-810.
79. Parrish, D.D., et al., *Changes in the photochemical environment of the temperate North Pacific troposphere in response to increased Asian emissions.* Journal of Geophysical Research-Atmospheres, 2004. **109**(D23): p. D23S18, doi:10.1029/2004JD004978.
80. Parrish, D.D., D.B. Millet, and A.H. Goldstein, *Increasing ozone in marine boundary layer inflow at the west coasts of North America and Europe.* Atmospheric Chemistry and Physics, 2009. **9**(4): p. 1303-1323.
81. Jaffe, D., et al., *Increasing background ozone during spring on the west coast of North America.* Geophysical Research Letters, 2003. **30**(12): p. doi:10.1029/2003GL017024.
82. Bonfils, C., et al., *Identification of external influences on temperatures in California.* Climatic Change, 2008. **87**: p. S43-S55.
83. Brown, T.J., B.L. Hall, and A.L. Westerling, *The impact of twenty-first century climate change on wildland fire danger in the western United States: An applications perspective.* Climatic Change, 2004. **62**(1-3): p. 365-388.
84. Cox, P., M. Johnson, and J. Auyeung, *The California Almanac of Emissions and Air Quality.* Planning and Technical Support Division, the California Air Resources Board, 2006.
85. Seinfeld, J.H. and S.N. Pandis, *Atmospheric chemistry and physics: from air pollution to climate change*. 2006, New York: Wiley.
86. Constable, J.V.H., et al., *Modelling changes in VOC emission in response to climate change in the continental United States.* Global Change Biology, 1999. **5**(7): p. 791-806.
87. Fuentes, J.D., et al., *Biogenic hydrocarbons in the atmospheric boundary layer: A review.* Bulletin of the American Meteorological Society, 2000. **81**(7): p. 1537-1575.
88. Sanderson, M.G., et al., *Effect of climate change on isoprene emissions and surface ozone levels.* Geophysical Research Letters, 2003. **30**(18): p. -.
89. Dawson, J.P., P.J. Adams, and S.N. Pandis, *Sensitivity of ozone to summertime climate in the eastern USA: A modeling case study.* Atmospheric Environment, 2007. **41**(7): p. 1494-1511.
90. Snyder, M.A., L.C. Sloan, and J.L. Bell, *Modeled regional climate change in the hydrologic regions of California: A CO2 sensitivity study.* Journal of the American Water Resources Association, 2004. **40**(3): p. 591-601.
91. Bell, M.L., et al., *Climate change, ambient ozone, and health in 50 US cities.* Climatic Change, 2007. **82**(1-2): p. 61-76.
92. Kalnay, E., et al., *The NCEP/NCAR 40-year reanalysis project.* Bulletin of the American Meteorological Society, 1996. **77**(3): p. 437-471.
93. Delworth, T.L., et al., *GFDL's CM2 global coupled climate models. Part I: Formulation and simulation characteristics.* Journal of Climate, 2006. **19**(5): p. 643-674.

94. Cayan, D.R., et al., *Climate Change Scenarios for the California Region.* Climatic Change(Special Issue on Climate Change Scenarios), accepted for publication, 2007.
95. Kleeman, M.J. and G.R. Cass, *Source Contributions to the Size and Composition Distribution of Urban Particulate Air Pollution.* Atmospheric Environment
1998. **32**: p. 2803--2816.
96. Kleeman, M.J. and G.R. Cass, *Effect of Emission Control Strategies on the Size and Composition Distribution of Urban Particulate Air Pollution.* Environmental Science & Technology, 1999. **33**: p. 177-189.
97. Kleeman, M.J. and G.R. Cass, *Identifying the Effect of Individual Emissions Sources on Particulate Air Quality Within a Photochemical Aerosol Processes Trajectory Model.* Atmospheric Environment 1999. **33**: p. 4597-4613.
98. Ying, Q., et al., *Verification of a source-oriented externally mixed air quality model during a severe photochemical smog episode.* Atmospheric Environment, 2007. **41**(7): p. 1521-1538.
99. Harley, R.A., et al., *Photochemical Modeling of the Southern California Air-Quality Study.* Environmental Science & Technology, 1993. **27**(2): p. 378-388.
100. Bergin, M.S., et al., *Formal Uncertainty Analysis of a Lagrangian Photochemical Air Pollution Model.* Environmental Science & Technology 1999. **33**: p. 1116--1126.
101. Guenther, A.B., et al., *Isoprene and Monoterpene Emission Rate Variability - Model Evaluations and Sensitivity Analyses.* Journal of Geophysical Research-Atmospheres, 1993. **98**(D7): p. 12609-12617.
102. Hancock, B., *California Air Resources Board.* Personal communication, 2007.
103. Mahmud, A., et al., *Statistical downscaling of climate change impacts on ozone concentrations in California.* Journal of Geophysical Research-Atmospheres, 2008. **113**(D21): p. -.
104. Geron, C., et al., *Temporal variability in basal isoprene emission factor.* Tree Physiology, 2000. **20**(12): p. 799-805.
105. Caldwell, P., et al., *Evaluation of a WRF dynamical downscaling simulation over California.* Climatic Change, 2009. **95**(3-4): p. 499-521.
106. Bell, J.L., L.C. Sloan, and M.A. Snyder, *Regional changes in extreme climatic events: A future climate scenario.* Journal of Climate, 2004. **17**(1): p. 81-87.
107. Leung, L.R. and S.J. Ghan, *Pacific northwest climate sensitivity simulated by a regional climate model driven by a GCM. Part II: 2xCO(2) simulations.* Journal of Climate, 1999. **12**(7): p. 2031-2053.
108. Washington, W.M., et al., *Parallel climate model (PCM) control and transient simulations.* Climate Dynamics, 2000. **16**(10-11): p. 755-774.
109. Barnett, T.P., D.W. Pierce, and R. Schnur, *Detection of anthropogenic climate change in the world's oceans.* Science, 2001. **292**(5515): p. 270-274.
110. Hay, L.E. and M.P. Clark, *Use of statistically and dynamically downscaled atmospheric model output for hydrologic simulations in three mountainous basins in the western United States.* Journal of Hydrology, 2003. **282**(1-4): p. 56-75.
111. Skamarock, W.C., et al., *A description of the advanced research WRF version 2.* NCAR Tech. Note, NCAR/TN—468+STR, 2005: p. pp 100, Natl. Cent. for Atmos. Res., Boulder, Colo.

112. Dai, A., et al., *The ACPI climate change simulations.* Climatic Change, 2004. **62**(1-3): p. 29-43.
113. Michalakes, J., et al., *Development of a next generation regional weather research and forecast model, in Developments in Teracomputing.* Proceedings of the Ninth ECMWF Workshop on the Use of High Performance Computing in Meteorology :edited by W. Zwieflhofer, and N. Kreitz, 2001: p. 269–276.
114. Hong, S.Y., Y. Noh, and J. Dudhia, *A new vertical diffusion package with an explicit treatment of entrainment processes.* Monthly Weather Review, 2006. **134**(9): p. 2318-2341.
115. Janjic, Z.I., *Nonsingular Implementation of the Mellor–Yamada Level 2.5 Scheme in the NCEP Meso model.* NCEP Office Note, 2002. **No. 437**: p. 61.
116. Mellor, G.L. and T. Yamada, *Development of a Turbulence Closure-Model for Geophysical Fluid Problems.* Reviews of Geophysics, 1982. **20**(4): p. 851-875.
117. Kain, J.S., *The Kain-Fritsch convective parameterization: An update.* Journal of Applied Meteorology, 2004. **43**: p. 170–181.
118. Grell, G.A. and D. Devenyi, *A generalized approach to parameterizing convection combining ensemble and data assimilation techniques.* Geophysical Research Letters, 2002. **29**(14): p. -.
119. Thompson, G., R.M. Rasmussen, and K. Manning, *Explicit forecasts of winter precipitation using an improved bulk microphysics scheme. Part I: Description and sensitivity analysis.* Monthly Weather Review, 2004. **132**(2): p. 519-542.
120. Hong, S.Y., J. Dudhia, and S.H. Chen, *A revised approach to ice microphysical processes for the bulk parameterization of clouds and precipitation.* Monthly Weather Review, 2004. **132**(1): p. 103-120.
121. Mlawer, E.J., et al., *Radiative transfer for inhomogeneous atmospheres: RRTM, a validated correlated-k model for the longwave.* Journal of Geophysical Research-Atmospheres, 1997. **102**(D14): p. 16663-16682.
122. Dudhia, A., *Noise Characteristics of the Avhrr Infrared Channels.* International Journal of Remote Sensing, 1989. **10**(4-5): p. 637-644.
123. Singal, S.P., et al., *Studies of the Marine Boundary-Layer at Tarapur.* Boundary-Layer Meteorology, 1986. **37**(4): p. 371-384.
124. Mölders, N. and G. Kramm, *A case study on wintertime inversions in Interior Alaska with WRF.* Atmospheric Research, 2009. **doi:10.1016/j.atmosres.2009.06.002.**
125. Zhang, Y., et al., *Comparisons of WRF/Chem simulations in Mexico City with ground-based RAMA measurements during the 2006-MILAGRO.* Atmospheric Chemistry and Physics, 2009. **9**(11): p. 3777-3798.
126. Whiteman, D., *Breakup of Temperature Inversions in Deep Mountain Valleys .1. Observations.* Journal of Applied Meteorology, 1982. **21**(3): p. 270-289.
127. De Wekker, S., et al., *The performance of RAMS in representing the convective boundary layer structure in a very steep valley.* Environmental Fluid Mechanics, 2005. **5**: p. 35–62.
128. Kuwagata, T. and F. Kimura, *Daytime boundary layer evolution in a deep valley .2. Numerical simulation of the cross-valley circulation.* Journal of Applied Meteorology, 1997. **36**(7): p. 883-895.

129. Zorita, E., V. Kharin, and H. Vonstorch, *The Atmospheric Circulation and Sea-Surface Temperature in the North-Atlantic Area in Winter - Their Interaction and Relevance for Iberian Precipitation.* Journal of Climate, 1992. **5**(10): p. 1097-1108.
130. Houghton, J.T., et al., *Climate change 2001: The scientific basis. contribution of working group I to the third assessment report of the intergovernmental panel on climate change. Human influences will continue to change atmospheric composition throughout the 21st century* Intergovernmental Panel on Climate Change, 2001
http://www.grida.no/climate/ipcc_tar/wg1/008.htm. Retrieved 2007-12-03.
131. Emanuel, K., *Increasing destructiveness of tropical cyclones over the past 30 years.* Nature, 2005. **436**(7051): p. 686-688.
132. Liang, X.Z., et al., *Regional climate model downscaling of the U.S. summer climate and future change.* Journal of Geophysical Research-Atmospheres, 2006. **111**(D10): p. -.
133. Castro, C.L., R.A. Pielke, and G. Leoncini, *Dynamical downscaling: Assessment of value retained and added using the regional atmospheric modeling system (RAMS).* Journal of Geophysical Research-Atmospheres, 2005. **110**(D5): p. -.
134. Rockel, B., et al., *Dynamical downscaling: Assessment of model system dependent retained and added variability for two different regional climate models.* Journal of Geophysical Research-Atmospheres, 2008. **113**(D21): p. -.
135. Whetton, P.H., et al., *Developing scenarios of climate change for Southeastern Australia: an example using regional climate model output.* Climate Research, 2001. **16**(3): p. 181-201.
136. Cubasch, U., G. , et al., *Projections of future climate change*, in *Climate Change 2001: The Scientific Basis*. 2001, Intergovernmental Panel on Climate Change. p. 881.
137. Leung, L.R., et al., *Simulations of the ENSO hydroclimate signals in the Pacific Northwest Columbia River basin.* Bulletin of the American Meteorological Society, 1999. **80**(11): p. 2313-2329.
138. Simpson, J.E., *Sea-Breeze and Local Winds*. 1995, Cambridge University Press. p. 234.
139. Zhong, S.Y., C.D. Whiteman, and X.D. Bian, *Diurnal evolution of three-dimensional wind and temperature structure in California's Central Valley.* Journal of Applied Meteorology, 2004. **43**(11): p. 1679-1699.
140. Kitada, T., *Turbulence Structure of Sea Breeze Front and Its Implication in Air-Pollution Transport - Application of K-Epsilon Turbulence Model.* Boundary-Layer Meteorology, 1987. **41**(1-4): p. 217-239.
141. Novitsky, M., D.D. Reible, and B.M. Corripio, *Modeling the Dynamics of the Land-Sea Breeze Circulation for Air-Quality Modeling.* Boundary-Layer Meteorology, 1992. **59**(1-2): p. 163-175.
142. Koo, Y. and D.D. Reibel, *Flow and transport modeling in the sea breeze. Part II: Flow model application and pollutant transport.* Boundary-Layer Meteorology, 1995b. **76**: p. 209–234.

143. Bao, J.W., et al., *Observed and WRF-simulated low-level winds in a high-ozone episode during the Central California Ozone Study.* Journal of Applied Meteorology and Climatology, 2008. **47**(9): p. 2372-2394.
144. Mahmud, A., et al., *Climate impact on airborne particulate matter concentrations in California using seven year analysis periods.* Atmospheric Chemistry and Physics Discussions, 2010. **10**: p. 1-36.
145. Pope, C.A., *Review: Epidemiological basis for particulate air pollution health standards.* Aerosol Science and Technology, 2000. **32**(1): p. 4-14.
146. Tran, H.T., et al., *Methodology for Estimating Premature Deaths Associated with Long-term Exposure to Fine Airborne Particulate Matter in California*. 2008, California Environmental Protection Agency, Air Resources Board: Sacramento, CA.
147. Tagaris, E., et al., *Impacts of global climate change and emissions on regional ozone and fine particulate matter concentrations over the United States.* Journal of Geophysical Research-Atmospheres, 2007. **112**(D14): p. -.
148. Chen, J., et al., *The effects of global changes upon regional ozone pollution in the United States.* Atmospheric Chemistry and Physics, 2009. **9**(4): p. 1125-1141.
149. Dawson, J.P., et al., *Impacts of climate change on regional and urban air quality in the eastern United States: Role of meteorology.* Journal of Geophysical Research-Atmospheres, 2009. **114**: p. -.
150. Liao, K.J., et al., *Quantification of the impact of climate uncertainty on regional air quality.* Atmospheric Chemistry and Physics, 2009. **9**(3): p. 865-878.
151. Rind, D., et al., *Use of on-line tracers as a diagnostic tool in general circulation model development 2. Transport between the troposphere and stratosphere.* Journal of Geophysical Research-Atmospheres, 1999. **104**(D8): p. 9151-9167.
152. Grell, G., J. Dudhia, and D.R. Stauffer, *A description of the fifth generation Penn State/NCAR mesoscale model (MM5).* NCAR Tech. Note, 1994. **NCAR/TN-398+STR**(Natl. Cent for Atmos. Res., Boulder, Colo.).
153. Skamarock, W.C., *Evaluating mesoscale NWP models using kinetic energy spectra.* Monthly Weather Review, 2004. **132**(12): p. 3019-3032.
154. Zhao, Z., et al., *The impact of climate change on air quality related meteorological conditions in California – Part I: Present time simulation analysis.* submit to J. Climate., 2010.
155. Ying, Q., et al., *Modeling air quality during the California Regional PM10/PM2.5 Air Quality Study (CRPAQS) using the UCD/CIT source-oriented air quality model - Part I. Base case model results.* Atmospheric Environment, 2008. **42**(39): p. 8954-8966.
156. Menut, L., I. Coll, and S. Cautenet, *Impact of meteorological data resolution on the forecasted ozone concentrations during the ESCOMPTE IOP2a and IOP2b.* Atmospheric Research, 2005. **74**(1-4): p. 139-159.
157. Martien, P.T. and R.A. Harley, *Adjoint sensitivity analysis for a three-dimensional photochemical model: Application to Southern California.* Environmental Science & Technology, 2006. **40**(13): p. 4200-4210.
158. Kleeman, M.J., et al., *Source apportionment of secondary organic aerosol during a severe photochemical smog episode.* Atmospheric Environment, 2007. **41**(3): p. 576-591.

159. Jaffe, D., S. Tamura, and J. Harris, *Seasonal cycle and composition of background fine particles along the west coast of the US.* Atmospheric Environment, 2005. **39**(2): p. 297-306.
160. Liang, J.Y., et al., *Seasonal budgets of reactive nitrogen species and ozone over the United States, and export fluxes to the global atmosphere.* Journal of Geophysical Research-Atmospheres, 1998. **103**(D11): p. 13435-13450.
161. Mcrae, G.J., W.R. Goodin, and J.H. Seinfeld, *Development of a 2nd-Generation Mathematical-Model for Urban Air-Pollution .1. Model Formulation.* Atmospheric Environment, 1982. **16**(4): p. 679-696.
162. Ying, Q. and M.J. Kleeman, *Effects of aerosol UV extinction on the formation of ozone and secondary particulate matter.* Atmospheric Environment, 2003. **37**(36): p. 5047-5068.
163. Byun, D.W., *Dynamically consistent formulations in meteorological and air quality models for multiscale atmospheric studies. Part II: Mass conservation issues.* Journal of the Atmospheric Sciences, 1999. **56**(21): p. 3808-3820.
164. Hu, Y.T., M.T. Odman, and A.G. Russell, *Mass conservation in the Community Multiscale Air Quality model.* Atmospheric Environment, 2006. **40**(7): p. 1199-1204.
165. Lee, S.M., S.C. Yoon, and D.W. Byun, *The effect of mass inconsistency of the meteorological field generated by a common meteorological model on air quality modeling.* Atmospheric Environment, 2004. **38**(18): p. 2917-2926.
166. Odman, M.T. and A.G. Russell, *Mass conservative coupling of non-hydrostatic meteorological models with air quality models.* In: S.E. Gryning and E. Batchvarova, Editors, Air Pollution Modeling and its Application XIII, Kluwer/Plenum, New York (2000), pp. 651-660., 2000.
167. Sportisse, B., D. Quelo, and V. Mallet, *Impact of mass consistency errors for atmospheric dispersion.* Atmospheric Environment, 2007. **41**(29): p. 6132-6142.
168. Jacobson, M.Z., *A solution to the problem of nonequilibrium acid/base gas-particle transfer at long time step.* Aerosol Science and Technology, 2005. **39**(2): p. 92-103.
169. Wexler, A.S. and J.H. Seinfeld, *Analysis of Aerosol Ammonium-Nitrate - Departures from Equilibrium during Scaqs.* Atmospheric Environment Part a-General Topics, 1992. **26**(4): p. 579-591.
170. Clegg, S.L., et al., *Effects of uncertainties in the thermodynamic properties of aerosol components in an air quality model - Part 1: Treatment of inorganic electrolytes and organic compounds in the condensed phase.* Atmospheric Chemistry and Physics, 2008. **8**(4): p. 1057-1085.
171. Fountoukis, C. and A. Nenes, *ISORROPIA II: a computationally efficient thermodynamic equilibrium model for K+-Ca2+-Mg2+-Nh(4)(+)-Na+-SO42--NO3--Cl--H2O aerosols.* Atmospheric Chemistry and Physics, 2007. **7**(17): p. 4639-4659.
172. Nenes, A., S.N. Pandis, and C. Pilinis, *ISORROPIA: A new thermodynamic equilibrium model for multiphase multicomponent inorganic aerosols.* Aquatic Geochemistry, 1998. **4**: p. 123-152.

173. Cerro, C., et al., *Modeling raindrop size distribution and Z(R) relations in the Western Mediterranean area.* Journal of Applied Meteorology, 1997. **36**(11): p. 1470-1479.
174. Loosmore, G.A. and R.T. Cederwall, *Precipitation scavenging of atmospheric aerosols for emergency response applications: testing an updated model with new real-time data.* Atmospheric Environment, 2004. **38**(7): p. 993-1003.
175. Gong, S.L., *A parameterization of sea-salt aerosol source function for sub- and super-micron particles.* Global Biogeochemical Cycles, 2003. **17**(4): p. -.
176. de Leeuw, G., et al., *Production of sea spray aerosol in the surf zone.* Journal of Geophysical Research-Atmospheres, 2000. **105**(D24): p. 29397-29409.
177. Hu, J., et al., *Particulate Air Quality Model Predictions using Prognostic vs. Diagnostic Meteorology in Central California.* Atmospheric Environment, 2009. **accepted for publication**.
178. Huffman, J.A., et al., *Chemically-Resolved Volatility Measurements of Organic Aerosol from Different Sources.* Environmental Science and Technology, 2009. **43**(14): p. 5351-5357.
179. Presto, A.A., et al., *Intermediate-Volatility Organic Compounds: A Potential Source of Ambient Oxidized Organic Aerosol.* Environmental Science and Technology, 2009. **43**(13): p. 4744-4749.
180. Robinson, A.L., et al., *Rethinking organic aerosols: Semivolatile emissions and photochemical aging.* Science, 2007. **315**(5816): p. 1259-1262.
181. Mokdad, A.H., et al., *Actual causes of death in the United States, 2000 (vol 291, pg 1238, 2004).* Jama-Journal of the American Medical Association, 2005. **293**(3): p. 293-294.
182. Kinney, P.L., *Climate Change, Air Quality, and Human Health.* American Journal of Preventive Medicine, 2008. **35**(5): p. 459-467.
183. *State of California, Department of Finance, Population Projections for California and Its Counties 2000-2050.* July, 2007: Sacramento, California.
184. Hixson, M., et al., *Influence of regional development policies and clean technology adoption on future air pollution exposure.* Atmospheric Environment, 2010. **44**(4): p. 552-562.
185. Flannigan, M.D. and C.E. Vanwagner, *Climate Change and Wildfire in Canada.* Canadian Journal of Forest Research-Revue Canadienne De Recherche Forestiere, 1991. **21**(1): p. 66-72.
186. Fried, J.S., M.S. Torn, and E. Mills, *The impact of climate change on wildfire severity: A regional forecast for northern California.* Climatic Change, 2004. **64**(1-2): p. 169-191.
187. Stocks, B.J., et al., *Climate change and forest fire potential in Russian and Canadian boreal forests.* Climatic Change, 1998. **38**(1): p. 1-13.
188. Westerling, A.L., et al., *Warming and earlier spring increase western US forest wildfire activity.* Science, 2006. **313**(5789): p. 940-943.